



Performance of Direct Power Controlled Grid-connected Voltage Source Converters

Francis Mulolani

School of Electrical and Electronic Engineering

A thesis submitted for the degree of Doctor of Philosophy

April, 2017

Abstract

In this thesis the performance of direct power controlled grid-connected voltage source converters (VSCs) is investigated. Of particular interest is the stability of the controller with the third-order LCL filter employed as the grid filter, effect of grid impedance variations and grid voltage distortion, and current limitation during voltage dips. The control scheme implemented is virtual-flux direct power control with space vector modulation (VF-DPC-SVM). By mathematical modelling and stability analysis, it is found that the closed-loop power control system is stable for all values of proportional gain when the current sensors are on the inverter side of the LCL filter. The inverter current together with the estimated grid virtual-flux is used to estimate the active power and the reactive power. The difference between the estimated reactive power and the reactive power on the grid side is compensated for, using a new reactive power error compensation scheme based on the estimated capacitor current. The control system is found to be robust to changes in grid inductance, and remains stable for a range of grid inductance values, and controller proportional gain. It is demonstrated in simulation and experimentally that the total harmonic distortion (THD) of the current injected by the VSC is less than the limit of 5 %, set by standards, for all different values of grid inductance and proportional gain. This is true even in the presence of significant grid voltage distortion. To control the VSC during voltage dips without damaging the semiconductor devices, a new current limiting algorithm is proposed and implemented. The positive-sequence component of the virtual-flux is used for synchronization and power estimation to achieve balanced, undistorted currents during unsymmetrical voltage dips. Experimental results show that the current achieved during unsymmetrical voltage dips is balanced and has a THD of less than 3 %.

In memory of my late mother, Elena Chanda

Acknowledgments

The work that led to the writing of this thesis was made possible by the financial support of the UK government through the Commonwealth Scholarship and Fellowship Plan, which I gratefully acknowledge. I am grateful to my employers, the Copperbelt University for granting me study leave for the duration of my studies and financial support for the latter part of my studies.

I am very grateful to my main supervisor Dr Matthew Armstrong for his kindness, patience, support and guidance throughout the project. I am also grateful to my second supervisor Dr Mohammed Elgendy for his useful advice and for helping me to get a better understanding of code composer studio. I am thankful to Dr Bashar Zahawi who was my second supervisor at the beginning of the project.

I am grateful to Darren Mackie from the electronics workshop for building all the electronic circuits and for his kindness and patience every time he had to replace some components which I had blown. Many thanks to Jack Noble, Alan Wheatley, Samuel Burn and Chris Manning from the mechanical workshop for their help with preparing the enclosure for the circuits and all the mechanical aspects of setting up the rig. I would also like to acknowledge the contribution of James Richardson, Gordon Marshall and Stephen Mitchel, who provided all the electrical equipment needed during the setting up of the rig and during the experiments. To my fellow PhD students in the Electrical Power Lab, I am grateful for the company, and the interesting discussions. Many thanks go to the academic staff, and the administrative staff, particularly Gill Webber, who assisted me in different ways during my studies.

I am very grateful to my wife Yakiwe, for putting her career on hold and supporting me throughout my studies; my children Precious, Francis II and Jaden for making my life away from the lab enjoyable when they were in Newcastle, and for enduring many months of my absence when they were in Zambia. I am grateful to my parents in law, my brothers Abraham and John, and my sister Angela and their families for their constant help and encouragement.

Table of Contents

Abstract.....	i
Acknowledgments	v
Table of Contents	vii
List of Figures.....	xi
List of Symbols and Abbreviations.....	xvii
Chapter 1 Introduction.....	1
1.1 Background.....	1
1.2 Classification of Grid-connected PV Systems	3
1.3 Main Control Functions in Grid-connected Converters.....	5
1.3.1 Common Functions	5
1.3.2 PV Specific Functions	7
1.3.3 Ancillary Functions	8
1.4 Scope and Objectives of the Thesis.....	8
1.5 Main Contributions of the Thesis	9
1.6 Publications	10
1.7 Outline of the Thesis	10
Chapter 2 Review of Control Techniques for Grid-connected Voltage Source Converters	
13	
2.1 Introduction	13
2.2 Current Control Basics	14
2.3 Hysteresis Current Control.....	15
2.4 Voltage Based Control	17
2.4.1 Voltage-Oriented Current Control.....	17
2.4.2 Direct Power Control.....	20
2.4.3 Direct power Control with Space Vector Modulation.....	22
2.5 Virtual-Flux Based Control	24

2.5.1	Virtual-Flux Oriented Current Control	24
2.5.2	Virtual-Flux Direct Power Control	26
2.5.3	Virtual flux Direct Power Control with Space Vector Modulation	28
2.6	Predictive Control.....	29
2.7	Comparison of the Reviewed Control Schemes	30
2.8	Conclusion	32
Chapter 3 Modelling and Stability Analysis of Grid-connected Converter with LCL Filter		
35		
3.1	Introduction.....	35
3.2	Models of Grid-connected Converter with LCL Filter.....	36
3.2.1	Natural Reference Frame Model	39
3.2.2	Stationary Reference Frame Model	41
3.2.3	Synchronous Reference Frame Model	43
3.3	Stability Analysis of Power Control Loop.....	45
3.3.1	With Current Sensors on the Grid-side with No Damping.....	47
3.3.2	With Current Sensors on the Grid-side with Passive Damping	50
3.3.3	With Current Sensors on the Grid-side with Notch-filter Active Damping .	54
3.3.4	With Current Sensors on the Inverter-side with No Damping.....	57
3.4	Conclusion	62
Chapter 4 Implementation of Virtual Flux Direct Power Control with Space Vector		
Modulation 63		
4.1	Introduction.....	63
4.2	Simulation Model.....	63
4.3	Experimental Setup	65
4.4	Virtual Flux Estimation.....	69
4.4.1	Overview of Virtual Flux Estimation Methods.....	69
4.4.2	Simulation and Practical Results for Virtual Flux Estimation	70
4.5	Synchronization	72

4.6	Power Estimation.....	77
4.7	Modified Power Estimation with LCL Filter	80
4.7.1	Phasor Diagram for Grid-connected VSC.....	81
4.7.2	Derivation of an Expression for the Error	83
4.7.3	Simulation Results for Reactive Power Error Compensation Scheme.....	86
4.7.4	Experimental Results for Power Estimation.....	89
4.8	Conclusion.....	90
Chapter 5	Effect of Grid Impedance Variation and Grid Voltage Distortion.....	93
5.1	Introduction	93
5.2	Harmonic Limits	94
5.3	Effect of Grid Impedance Variation on Controller Stability	95
5.3.1	Variation of Resonance Frequency with Grid Inductance	95
5.3.2	Stability Analysis.....	97
5.4	Power Estimation with Distorted Voltage and Current	101
5.4.1	Classical Power Theories for Distorted Voltage and Current.....	101
5.4.2	Modern Instantaneous Power Theories for Distorted Voltage and Current 103	
5.5	Simulation Results with Ideal Grid Voltage.....	105
5.5.1	With $L_g = 0.1$ mH	106
5.5.2	With $L_g = 0.5$ mH.....	107
5.6	Simulation Results with Distorted Grid Voltage	108
5.6.1	With $L_g = 0.1$ mH	109
5.6.2	With $L_g = 0.5$ mH.....	110
5.7	Experimental Results.....	112
5.7.1	With Nominal Grid Impedance.....	112
5.7.2	With Additional Grid Inductance.....	115
5.8	Conclusion.....	117
Chapter 6	Current Limitation during Grid Voltage Disturbances.....	119

6.1	Introduction.....	119
6.2	Over-currents in Direct Power Controlled VSCs during Grid Disturbances	121
6.3	Proposed Current Limitation Method	124
6.4	Current Limitation during Unsymmetrical Voltage Dips	129
6.4.1	Symmetrical Components.....	129
6.4.2	Instantaneous Power Equations with Unsymmetrical Voltages and Currents 131	
6.4.3	Positive-sequence Virtual-flux Based Instantaneous Power Estimation... 133	
6.4.4	Positive-sequence Virtual-flux Estimation.....	133
6.5	Experimental System for Unsymmetrical Voltage Dips.....	135
6.6	Experimental Results	136
6.7	Conclusion	140
Chapter 7	Thesis Conclusions and Suggestions for Further Work.....	143
7.1	Conclusions	143
7.2	Suggestions for Further Work.....	144
References.....		147
Appendix A.	Transformations for Three-Phase Systems.....	158
A.1	Three-phase to Stationary Reference Frame Transformation.....	158
A.2	Stationary to Rotating Reference Frame Transformation	159
A.3	Transformations for Unsymmetrical Systems	160
Appendix B.	Per-unit System.....	162
Appendix C.	LCL Filter Design.....	164
Appendix D.	Power Flow between the VSC and the Grid.....	167
Appendix E.	List of Equipment	171

List of Figures

Figure 1.1 Global PV installed capacity between 2000 and 2014.....	2
Figure 1.2 Structure of a grid-connected PV system.....	3
Figure 1.3 Classification of PV systems.....	4
Figure 1.4 Control functions of grid-connected converters.....	6
Figure 1.5 PV array characteristic for different values of irradiation (a) current-voltage characteristics (b) power-voltage characteristics.....	7
Figure 2.1 Single-phase equivalent circuit of grid-connected converter.....	14
Figure 2.2 Vector diagram of grid-connected converter.....	15
Figure 2.3 Block diagram of hysteresis current control.....	16
Figure 2.4 Principle of hysteresis control: current (upper) and converter output voltage (lower).....	17
Figure 2.5 Block diagram of voltage oriented control.....	18
Figure 2.6 Vector diagram of voltage-oriented control.....	19
Figure 2.7 Current controller with decoupling and feedforward terms.....	20
Figure 2.8 Block diagram of direct power control.....	21
Figure 2.9 Block diagram of direct power control with space vector modulation.....	23
Figure 2.10 Block diagram of virtual-flux oriented control.....	25
Figure 2.11 Vector diagram of virtual-flux oriented control.....	26
Figure 2.12 Block diagram of virtual-flux direct power control.....	27
Figure 2.13 Block diagram of virtual-flux direct power control with space vector modulation.....	28
Figure 2.14 Block diagram of predictive control.....	29
Figure 3.1 Grid-connected VSC with LCL filter.....	37
Figure 3.2 Equivalent single-phase circuit of grid-connected VSC.....	37
Figure 3.3 Voltage vectors for different switching states.....	38
Figure 3.4 Block diagram of the natural reference frame model.....	41
Figure 3.5 Block diagram of stationary reference frame model.....	43
Figure 3.6 Block diagram of synchronous reference frame model.....	45
Figure 3.7 Grid-connected VSC with (a) current sensors on the grid side (b) current sensors on the inverter side.....	46
Figure 3.8 Block diagram of power control loop with current sensors on the grid-side.....	47

Figure 3.9 Pole-zero plots for the power control loop with undamped LCL filter with current sensors on the grid-side and varying K_p (arrows indicate increasing K_p).	50
Figure 3.10 Block diagram of power control loop with current sensors on the grid-side and passively damped LCL filter.....	51
Figure 3.11 Pole-zero plots for the power control loop with passively damped LCL filter with varying K_p for a damping resistor of $R_d = 1/(3\omega_{res}C_f)$.	52
Figure 3.12 Pole-zero plots for the power control loop with passively damped LCL filter with varying K_p for a damping resistor of $R_d = 10/(3\omega_{res}C_f)$.	53
Figure 3.13 Step response for $K_p = 1$ with two different damping resistors.....	54
Figure 3.14 Block diagram of power control loop with current sensors on the grid-side and notch filter active damping.....	55
Figure 3.15 Pole-zero plots for the power control loop with notch-filter actively damped LCL filter with varying K_p	56
Figure 3.16 Step response of closed-loop discrete system with notch filter for stable range of K_p values.....	57
Figure 3.17 Block diagram of power control loop with current sensors on the inverter side with no damping.....	58
Figure 3.18 Pole-zero plots for the power control loop for undamped LCL filter with current sensors on the inverter side for varying K_p	59
Figure 3.19 Step response of closed-loop discrete system with current sensors on the inverter side for different values of K_p	60
Figure 3.20 (a) Pole-zero plot and (b) step response, for passively damped LCL filter with current sensors on the inverter side.....	61
Figure 4.1 Block diagram of experimental system.....	66
Figure 4.2 Photograph of experimental rig.....	68
Figure 4.3 Photograph of the enclosure's interior.....	68
Figure 4.4 Variation of magnitude and phase with frequency for cascaded low-pass filters.....	70
Figure 4.5 Simulation results for virtual flux estimation (a) $v_{g\alpha}$ and $\psi_{g\alpha}$ (b) $v_{g\beta}$ and $\psi_{g\beta}$	71

Figure 4.6 Experimental results for virtual flux estimation (a) $v_{g\alpha}$ and $\psi_{g\alpha}$ (b) $v_{g\beta}$ and $\psi_{g\beta}$ [scale: 20 V/div].....	71
Figure 4.7 SRF-PLL.....	72
Figure 4.8 VF-PLL.....	73
Figure 4.9 Orientation of voltage vector and virtual flux vectors.....	74
Figure 4.10 Performance of SRF-PLL and VF-PLL with balanced undistorted grid voltage (a) phase voltages (b) SRF-PLL angle (c) VF-PLL angle.....	75
Figure 4.11 Performance of SRF-PLL and VF-PLL with distorted grid voltage (a) phase voltages (b) SRF-PLL angle (c) VF-PLL angle.....	76
Figure 4.12 Experimental results for (a) SRF-PLL. Phase voltages (40 V/div); angle (120°/div) (b) VF-PLL. Phase voltages (40 V/div); angle (120°/div).....	77
Figure 4.13 Single-phase equivalent circuit of grid-connected VSC.....	81
Figure 4.14 Phasor diagram of grid-connected VSC (not to scale).....	82
Figure 4.15 Variation of grid current phase angle with filter capacitance for different values of active power.....	83
Figure 4.16 Block diagram of reactive power error compensation scheme.....	85
Figure 4.17 Block diagram of VF-DPC SVM control.....	86
Figure 4.18 Simulation results for reactive power calculation (a) inverter side currents (b) grid side current (c) filter capacitor current (d) reactive power error (e) filtered reactive power error.....	87
Figure 4.19 Simulation results for uncompensated reactive power error (a) grid virtual fluxes (b) inverter side currents (c) active power and reactive power.....	88
Figure 4.20 Simulation results for compensated reactive power error (a) grid virtual fluxes (b) inverter side currents (c) active power and reactive power.....	89
Figure 4.21 Experimental results showing inverter side current (top, 10 A/div), filter capacitor current (middle, 1 A/div) and grid side current (bottom, 10 A/div).....	90
Figure 4.22 Experimental results for power estimation. Virtual flux (25 V/div), inverter side current (10 A/div) and active power and reactive power (200 W/div).....	90
Figure 5.1 Single-phase equivalent circuit of grid-connected VSC with grid impedance.....	95
Figure 5.2 Variation of resonance frequency with grid inductance.....	97
Figure 5.3 Pole-zero plot for variable grid inductance with $K_p = 1$	98
Figure 5.4 Pole-zero plot for variable grid inductance with $K_p = 2$	99
Figure 5.5 Pole-zero plot for variable grid inductance with $K_p = 3$	100

Figure 5.6 Power tetrahedron showing the four power components defined by Budeanu [62].	103
Figure 5.7 Variation of current THD with K_p for $L_g = 0.1$ mH with ideal grid voltage.	106
Figure 5.8 Frequency spectra of the grid current for $L_g = 0.1$ mH with ideal grid voltage.	107
Figure 5.9 Variation of current THD with K_p for $L_g = 0.5$ mH with ideal grid voltage.	107
Figure 5.10 Frequency spectra of the grid current for $L_g = 0.5$ mH with ideal grid voltage.	108
Figure 5.11 Variation of current THD with K_p for $L_g = 0.1$ mH with distorted grid voltage.	109
Figure 5.12 Frequency spectra of the grid current for $L_g = 0.1$ mH with distorted grid voltage.	110
Figure 5.13 Variation of current THD with K_p for $L_g = 0.5$ mH with distorted grid voltage.	111
Figure 5.14 Frequency spectra of the grid current for $L_g = 0.5$ mH with distorted grid voltage.	111
Figure 5.15 Experimental voltage (50V/div), current (5A/div) and power (200W/div) waveforms for VF-DPC-SVM with nominal grid impedance.	113
Figure 5.16 Experimental voltage (50V/div), current (5A/div) and power (200W/div) waveforms for voltage based DPC-SVM with nominal grid impedance.	113
Figure 5.17 Experimental variation of current THD with K_p for a nominal grid inductance of $L_g = 0.3$ mH.	114
Figure 5.18 Frequency spectra of the grid current for a nominal grid inductance of $L_g = 0.3$ mH.	114
Figure 5.19 Experimental voltage (50V/div), current (5A/div) and power (200W/div) waveforms for VF-DPC-SVM with high grid inductance.	115
Figure 5.20 Experimental variation of current THD with K_p for a high grid inductance of $L_g = 0.6$ mH.	116
Figure 5.21 Frequency spectrum of the grid current for VF-DPC-SVM for a high grid inductance of $L_g = 0.6$ mH.	116
Figure 6.1 Theoretical current rise due to voltage dip.	122

Figure 6.2 Simulated voltage dip of 50% showing current rise.	123
Figure 6.3 Experimental voltage dip of 50% showing current rise Upper: grid voltage (50V/div), middle: inverter current (10A/div), lower: active power and reactive power (200W/div).	123
Figure 6.4 Flowchart of current limiter algorithm	127
Figure 6.5 Simulation of 50% voltage dip with current limitation.....	128
Figure 6.6 Experimental results of 50% voltage dip with current limitation. Upper: grid voltage (50V/div), middle: inverter current (10A/div), lower: active power and reactive power (250W/div).....	128
Figure 6.7 Symmetrical Components (a) positive-sequence (b) negative-sequence.....	129
Figure 6.8 Positive-sequence VF estimation.....	134
Figure 6.9 Modified connection to create single-phase voltage dips.....	135
Figure 6.10 Block diagram of positive-sequence virtual-flux control with current limitation.	136
Figure 6.11 Grid voltage [30 V/div] and synchronization angle [$2\pi/3$ rad/div] during unsymmetrical voltage dip (a) virtual-flux PLL (b) positive-sequence virtual-flux PLL.	137
Figure 6.12 Grid currents [5 A/div] during unsymmetrical voltage dip when supplying active power (a) conventional control with no current limitation (b) conventional control with current limitation (c) positive-sequence control with no current limitation (d) positive-sequence control with current limitation.....	138
Figure 6.13 Grid currents [5 A/div] during unsymmetrical voltage dip when supplying reactive power (a) conventional control with no current limitation (b) conventional control with current limitation (c) positive-sequence control with no current limitation (d) positive-sequence control with current limitation.....	139
Figure 6.14 Grid currents [5 A/div] during unsymmetrical voltage dip when supplying active power and reactive power (a) conventional control with no current limitation (b) conventional control with current limitation (c) positive-sequence control with no current limitation (d) positive-sequence control with current limitation.	139
Figure A.1 Vector diagram space vector transformation of three-phase quantities	159
Figure A.2 Vector diagram showing the stationary and rotating reference frames	160
Figure C.1 Flow chart of LCL Filter Design.....	165
Figure D.1.....	167

Figure D.2 Variation of voltage with active and reactive power with inductive grid
impedance 170

Figure D.3 Variation of voltage with active and reactive power with resistive grid
impedance 170

List of Symbols and Abbreviations

Symbols

C_d	DC link capacitance
\underline{i}_{L1}	Inverter-side current space vector
\underline{i}_{L2}	Grid-side current space vector
\underline{v}_{inv}	Inverter voltage space vector
\underline{v}_g	Grid voltage space vector
\underline{v}_{Cf}	Filter capacitor voltage space vector
$\underline{\psi}_{inv}$	Inverter virtual-flux space vector
$\underline{\psi}_g$	Grid virtual flux space vector
v_{dc}	DC link voltage
i_{dc}	DC current
i_{Cdc}	DC link capacitor current
θ_v	Grid voltage angle
θ_ψ	Grid virtual-flux angle
v_{dcref}	Reference DC link voltage
$v_{inv\alpha}, v_{inv\beta}$	Inverter voltage in alpha-beta coordinates
$v_{g\alpha}, v_{g\beta}$	Grid voltage in alpha-beta coordinates
$v_{Cf\alpha}, v_{Cf\beta}$	Filter capacitor voltage in alpha-beta coordinates
$i_{L1\alpha}, i_{L1\beta}$	Inverter-side current in alpha-beta coordinates
$i_{L2\alpha}, i_{L2\beta}$	Grid-side current in alpha-beta coordinates

$i_{Cf\alpha}, i_{Cf\beta}$	Filter capacitor current in alpha-beta coordinates
v_{invd}, v_{invq}	Inverter voltage in d-q coordinates
v_{gd}, v_{gq}	Grid voltage in d-q coordinates
v_{Cfd}, v_{Cfq}	Filter capacitor voltage in d-q coordinates
i_{L1d}, i_{L1q}	Inverter-side current in d-q coordinates
i_{L2d}, i_{L2q}	Grid-side current in d-q coordinates
i_{Cfd}, i_{Cfq}	Filter capacitor current in d-q coordinates
$\Psi_{inv\alpha}, \Psi_{inv\beta}$	Inverter virtual-flux in alpha-beta coordinates
$\Psi_{g\alpha}, \Psi_{g\beta}$	Grid virtual-flux in alpha-beta coordinates
p, q	Instantaneous active power and reactive power
i_{dref}, i_{qref}	Reference currents in d-q coordinates
p_{ref}, q_{ref}	Reference active power and reactive power
K_p, K_i	PI controller proportional gain and integral gain
v_{dref}, v_{qref}	Modulator reference voltages in d-q coordinates
$v_{\alpha ref}, v_{\beta ref}$	Modulator reference voltages in alpha-beta coordinates
$v_{inva}, v_{invb}, v_{invc}$	Inverter phase voltages in abc coordinates
v_{ga}, v_{gb}, v_{gc}	Grid phase voltages in abc coordinates
$v_{Cfa}, v_{Cfb}, v_{Cfc}$	Filter capacitor voltage in abc coordinates
$i_{L1a}, i_{L1b}, i_{L1c}$	Inverter-side currents in abc coordinates
$i_{L2a}, i_{L2b}, i_{L2c}$	Grid-side currents in abc coordinates
$i_{Cfa}, i_{Cfb}, i_{Cfc}$	Filter capacitor currents in abc coordinates

C_f	Filter capacitance of LCL filter
L_1	Inverter-side inductance of LCL filter
L_2	Grid-side inductance of LCL filter

Abbreviations

AC	Alternating Current
ADC	Analogue to Digital Converter
DAC	Digital to Analogue Converter
DC	Direct Current
DG	Distributed Generation
DPC	Direct Power Control
DPC-SVM	Direct Power Control with Space Vector Modulation
DSC	Digital Signal Controller
EPIA	European Photovoltaic Industry Association
FFT	Fast Fourier Transform
FOC	Field Oriented Control
IEA	International Energy Agency
IGBT	Insulated Gate Bipolar Transistor
MPP	Maximum Power Point
MPPT	Maximum Power Point Tracking
PCC	Point of Common Coupling
PI	Proportional-plus-Integral
PLL	Phase Locked Loop
PR	Proportional-plus- Resonant

PV	Photovoltaic
PVPS	Photovoltaic Power Systems
PWM	Pulse-width Modulation
RAM	Random Access Memory
RMS	Root Mean Square
SRF-PLL	Synchronous Reference Frame Phase Locked Loop
STATCOM	Static Synchronous Compensator
SVM	Space Vector Modulation
VF	Virtual Flux
VF-DPC	Virtual Flux Direct Power Control
VF-DPC-SVM	Virtual Flux Direct Power Control with Space Vector Modulation
VFOC	Virtual Flux Oriented Control
VF-PLL	Virtual Flux Phase Locked Loop
VOC	Voltage Oriented Control
VSC	Voltage Source Converter
WWEA	World Wind Energy Association
ZCD	Zero-crossing Detector

Chapter 1 Introduction

1.1 Background

For many years, most of the world's energy requirements were met by large centralized fossil fuel based thermal power stations. The abundance and relatively low price of fossil fuels, and the use of well-established and understood synchronous machine technology meant that there was no immediate need to deviate from this technology. However, factors such as increasing energy demand, depletion of fossil fuel reserves, gradually increasing fuel prices, and environmental concerns have led to increased interest in renewable energy sources. Renewable energy provides a clean source of energy and can be installed close to consumer as distributed generation (DG). Wind energy and photovoltaics are the fastest growing renewable energy sources in DG applications. Wind energy is the leading renewable source with the World Wind Energy Association(WWEA) reporting 63,690 MW of new wind installation in 2015, bringing the total installed wind capacity to 435 GW with a global growth rate of 17.2 % [1]. While solar photovoltaic (PV) has a lower total installed capacity than wind energy, with 177 GW reported at the end of 2014 [2], it had a growth rate of 55.9 % between 2002 and 2012, with the highest annual growth of 65.1 % between 2011 and 2012 [3]. For the same period wind energy had a growth rate of 26.1 % and an annual growth rate of 18.3 % for the years 2011 to 2012 [3]. In 2014, the European Photovoltaic Industry Association (EPIA) projected that by 2018, the global cumulative installed capacity of PV could be as high as 430 GW[4], while the International Energy Agency (IEA) projects that PV could account for 16 % of the global electricity production in the process leading to a reduction in carbon dioxide emissions of 4 Gt annually [5].

Large scale PV power plants are now common, with over forty-one PV plants with capacities ranging from 40 MW to 290 MW commissioned worldwide between 2008 and 2012 [6]. While most of the growth in PV has been reported from European countries, the USA and China, African countries are also reporting new developments with an 85 MW PV plant reported to be under construction in Rwanda [7]. The cumulative global installed capacity of PV from 2000 to 2014 is shown in Figure 1.1.

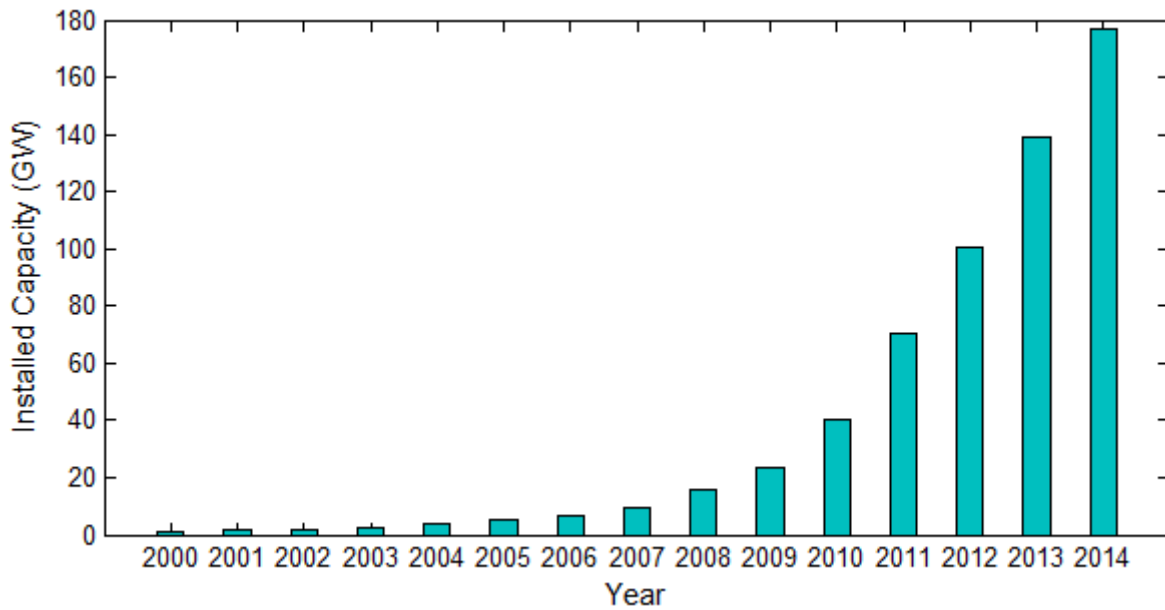


Figure 1.1 Global PV installed capacity between 2000 and 2014.

For grid connection of renewable energy sources, a power electronic converter is present between the energy source and the grid. This is commonly a voltage source converter (VSC) but current source converters have also been reported in [8], [9],[10]. Many different topologies exist for three-phase VSCs. For low distribution voltage applications and powers up to a few MW, the most common topology is the three-phase two-level VSC. For higher voltages applications, multi-level VSCs are preferred because they give a staircase output voltage waveform resulting in reduced filter requirements at lower switching frequencies, lower switching losses and they eliminate the need to connect devices in series [11], [12]. This study focuses on VSCs interfacing renewable energy with the low voltage distribution grid and therefore only the two-level VSC will be considered.

A low-pass filter between the VSC and the grid ensures that the harmonics in the output current of the VSC are attenuated and the current injected to the grid meets the requirements set out by standards such as IEEE 1547, IEEE 519 and IEC 61000 [13], [14], [15]. Commonly used filter types are the first-order L filter, the second-order LC filter and the third-order LCL filter. The LCL filter is becoming the preferred choice particularly in high power applications with low switching frequencies because it can achieve a higher harmonic attenuations at frequencies higher than its resonance frequency using relatively smaller filter components [16]. The choice of filter will play a significant role in the performance of the system.

The other factor that determines the performance of the system is the control scheme employed to control the VSC. The reduced cost and size of powerful digital signal controllers (DSCs) and microprocessors has led to improvements in the control of VSCs. Modern DSCs such as Texas Instruments®' TMS320F28335® have fast processing speed, and have multiple peripherals such as a multichannel Analogue to Digital Converter (ADC), multiple PWM outputs etc. and can be programmed using high level programming language like C/C++, thus making them more user-friendly [17]. With improvements in control and power electronics, the VSC has become very widely used in applications such as electric motor drives, PWM rectifiers, active filters and static synchronous compensators (STATCOM) in addition to renewable energy systems. The control schemes used in grid-connected applications are similar and have their foundation in the more established electric drives technology.

The general structure of a grid-connected photovoltaic converter is shown in Figure 1.2.

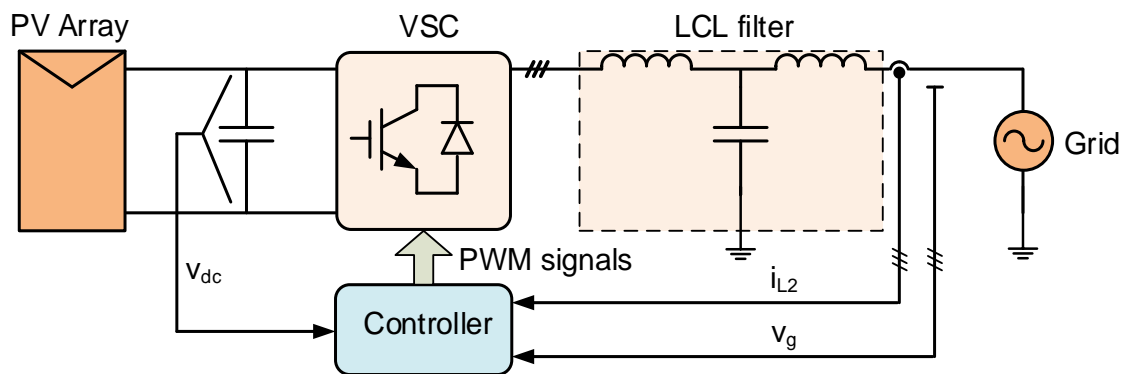


Figure 1.2 Structure of a grid-connected PV system.

1.2 Classification of Grid-connected PV Systems

PV systems are broadly classified as stand-alone or grid-connected systems. Stand-alone systems supply a local load and have no interaction with the grid. They usually require some form of energy storage to be able to supply the load during periods of low irradiation and during night-time and batteries are normally used for this purpose. Stand-alone PV systems are outside the scope of this study.

The different classifications of PV converters are shown in Figure 1.3.

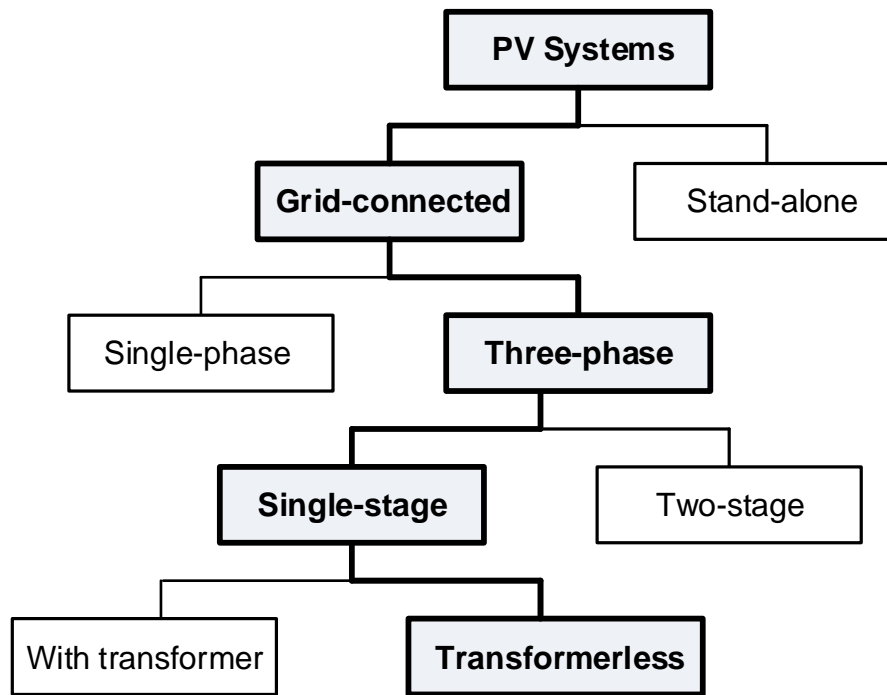


Figure 1.3 Classification of PV systems.

Grid-connected PV converters can also be classified as either single-phase or three-phase converters. Single-phase systems are usually small, low power domestic roof based systems, connected to the low-voltage distribution grid. Three-phase units are preferred for higher power systems which could be connected to the low-voltage or medium voltage distribution grid.

Grid-connected PV systems can further be classified based on the number of converter stages they have. A two-stage system includes a DC to DC boost converter connected between the PV array and the inverter [18]. The boost converter performs two functions; increasing the DC voltage from the PV array to allow grid-connection of systems with a low PV array voltage and extracting maximum power from the PV array using a maximum power point tracking (MPPT) algorithm. Two-stage PV converters are able to operate with a wide range of PV voltages and provide a DC link voltage with low ripple content with a relatively small DC link capacitor particularly in single-phase systems [19]. However, they have more components making them more bulky and costly and have higher conversion losses [20], [21]. The alternative is the single-stage converter, where the PV array is connected directly to the DC side of the inverter[22], [23]. This requires a higher PV array voltage meaning that more PV modules have to be connected in series. With single-stage PV converters, the MPPT algorithm is implemented as part of the control for the inverter

and this makes its overall control more complex, but with increased power conversion efficiency compared to two-stage converters.

For both single-stage and two-stage grid-connected PV converters, a grid-frequency isolation transformer may be used to prevent DC current injection into the grid, and to provide galvanic isolation for safety reasons [24]. In some systems, the transformer also steps up the voltage to the grid-voltage at the point of common coupling. However, the transformer is bulky, heavy, and costly and increases the system losses. Transformerless systems are more attractive due to lower cost and higher efficiency [25] but may require modifications to the controller to mitigate the dc current injection [26], [27], [28].

In this study, three-phase, single-stage transformerless grid-connected converters will be considered.

1.3 Main Control Functions in Grid-connected Converters

Grid-connected converter control schemes can be divided into a number of different functions as shown in Figure 1.4. Some of these functions are common to all grid-connected converters regardless of its specific purpose while others depend on the specific purpose of the converter [29].

1.3.1 Common Functions

The following functions are common to all grid-connected converters.

- Grid current control

The grid current control is a closed-loop controller that regulates the converter output current and hence the power-flow between the converter and the grid. A common current control scheme is voltage-oriented current control where the currents are converted to a synchronous reference frame and controlled as DC quantities using proportional-plus-integral (PI) controllers [30], [31]. The stationary reference frame proportional-plus-resonant (PR) controller is another common current control scheme which is becoming increasingly popular for grid-connected converters [32], [33]. The current can also be controlled indirectly by using direct power control schemes, in which the active power and reactive power are estimated and regulated by PI controllers [34], [35]. The current control provides the modulation index or reference voltage for the PWM module. Apart from regulating the power flow, the current control should also ensure the current meets the THD limits imposed by standards and it should be robust to grid impedance variations.

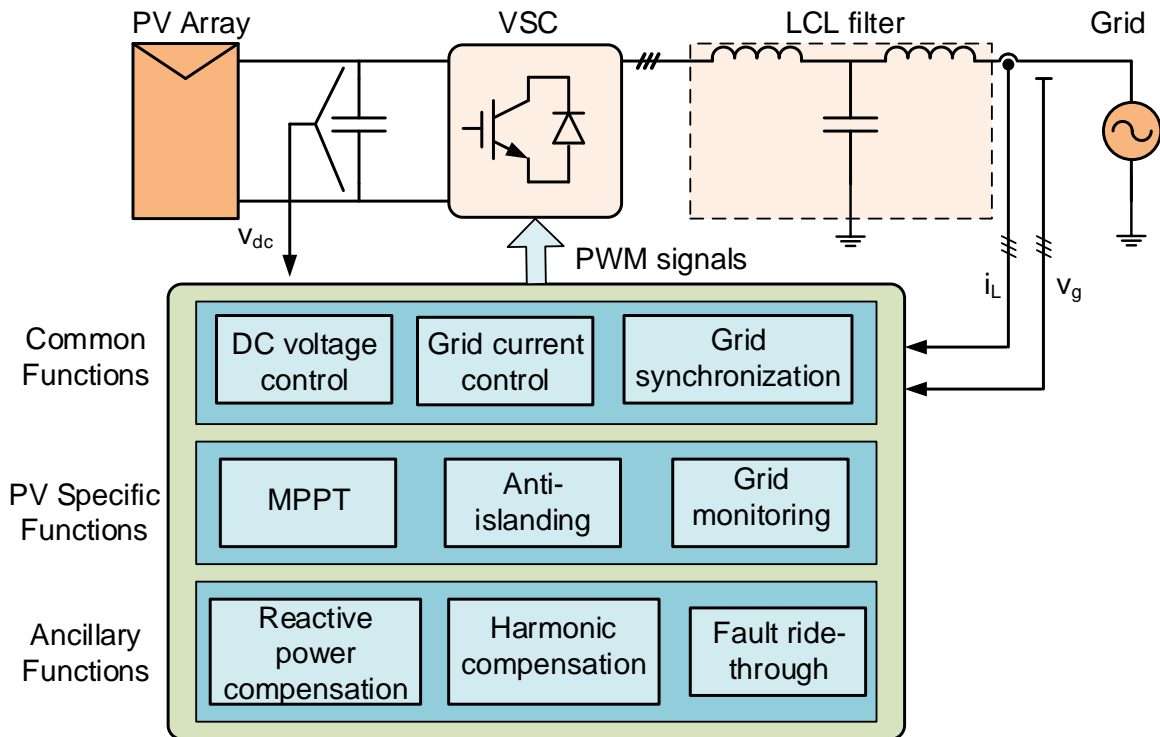


Figure 1.4 Control functions of grid-connected converters.

- DC voltage control

The DC voltage controller is implemented as an outer control loop with the current controller as the inner loop [36], [37], [38]. It maintains the active power balance between the DC side and the grid side of the converter by maintaining the voltage across the DC capacitor equal to a specified reference and providing the reference value for the active component of the current in the current controller or the active power in the case of direct power control [39], [40].

- Grid synchronization

Grid synchronization is an essential control function in a grid-connected converter. The grid synchronization function extracts the phase angle of the grid voltage which is needed for reference frame transformations, synchronized switching of the power semiconductor devices and correct calculation and control of the active and reactive power flow [41], [42]. There are many grid synchronization methods, the most common of which are based on the phase-locked loop (PLL) [43], [44].

1.3.2 PV Specific Functions

The following functions are specific to PV and other forms of grid-connected renewable energy sources. Their description here is with respect to their application to PV systems, which form the main topic of this thesis.

- Maximum power point tracking (MPPT)

It is important to extract maximum power from the PV array under different operating conditions. The output power of a PV array varies with irradiation and cell temperature. The relationship between the cell voltage and current is non-linear and maximum power is extracted at one point for each value of irradiation and temperature. This point is called the maximum power point (MPP). MPPT control ensures that the operating point of the PV array is at the MPP for each value of temperature and irradiation. Thus it should be able to track fast irradiation changes and should be stable at low irradiation values. Some popular MPPT methods with tracking efficiencies of up to 99% include the constant voltage, perturb and observe, and incremental conductance algorithms [45], [46], [47], [48], [49]. The current-voltage and power-voltage characteristics of a PV array for different values of irradiation are shown in Figure 1.5.

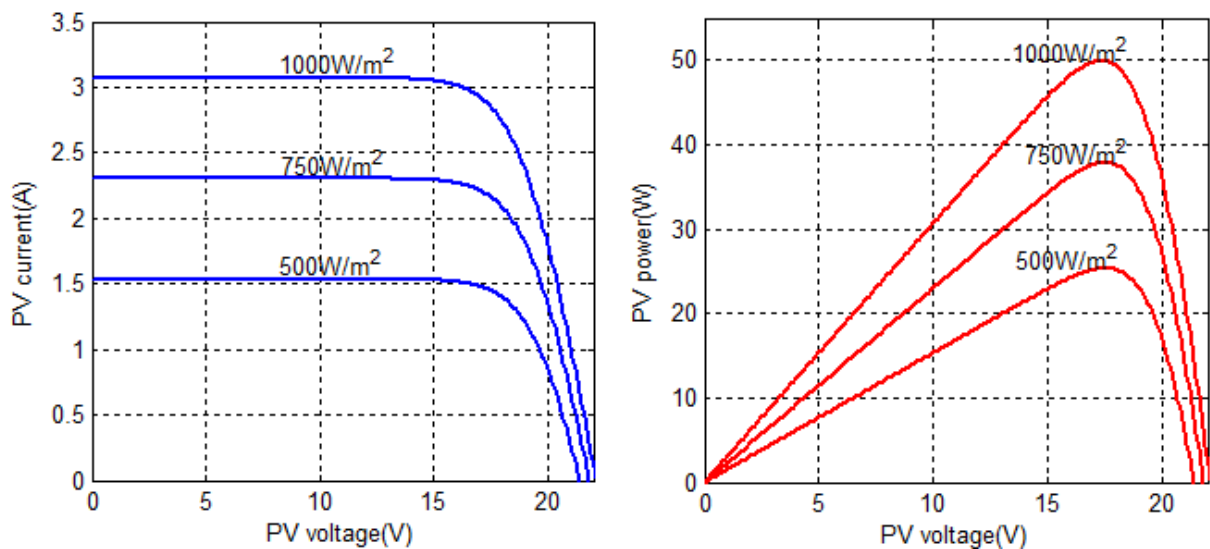


Figure 1.5 PV array characteristic for different values of irradiation (a) current-voltage characteristics (b) power-voltage characteristics.

- Anti-islanding

Islanding occurs when part of the utility system containing distributed generation and a local load becomes isolated from the main grid. This could be caused unintentionally by a

fault that leads to opening of protection devices, or accidental opening of the devices due to equipment failure or human error. It could also be caused intentionally when the utility shuts down part of the system for maintenance. In the case of PV systems, this is undesirable because it can lead to damage to customer equipment due to loss of control of voltage and frequency by the utility, it is hazardous to utility workers, and it could lead to damage of the PV converter upon re-closure of the isolating device. To prevent a PV system forming an island, it must be equipped with an anti-islanding mechanism [24]. Many methods of islanding detection have been discussed in literature and they are broadly classified as either passive, active or hybrid islanding detection [50], [51], [52]. Passive methods are based on the monitoring of the voltage, current, or frequency at the output of the converter. Active methods are based on the introduction of a disturbance in the system and measuring its effect on the voltage, current or frequency. Hybrid methods use a combination of passive and active methods.

- Grid Monitoring and Plant Monitoring

Grid monitoring is an optional function that can be used to monitor the grid parameters. These parameters are useful in the implementation of islanding detection algorithms. Plant monitoring is another optional function that can be used to monitor the state of the PV array. It is useful for diagnostic of the PV array and to detect partial shading of the array [29].

1.3.3 Ancillary Functions

Ancillary or grid support functions increase the security and reliability of the grid. They include local voltage support, reactive power compensation, frequency control, harmonic compensation and low-voltage ride-through. Traditionally ancillary services are provided by conventional synchronous generators. However, with the increasing penetration of distributed generation and changes in the grid-codes governing their operation, converter based generation systems such as PV, are required to participate in the provision of ancillary services [53], [54], [55]. Non-active power ancillary functions can be carried out by the PV converter during periods of low irradiation and during night-time [56].

1.4 Scope and Objectives of the Thesis

In this thesis, the performance of direct power controlled grid-connected voltage source converters is investigated. The research is focused on the interaction between the VSC, the grid filter and the control system under variable grid conditions. The instability

problem caused by the LCL filter is well known and many researchers have suggested solutions based on passive and active damping. Achieving stability of the LCL filter based VSC for a wide range of operating conditions is therefore, an integral part of this thesis.

The main aim of the work is to research improvements to the existing direct power control algorithms to achieve improved controller stability without using damping for the LCL filter, increased robustness to grid condition changes, and improved control during balanced and unbalanced grid faults to protect the converter from damage and allow it to ride-through grid faults.

The following are the specific objectives of the thesis:

- To study the stability of the power control loop in order to determine the conditions needed to achieve stability of the control loop with an LCL filter. The effect of passive damping, active damping and current sensor position on the stability of the system is considered.
- To study the performance of the system under conditions of varying grid inductance and distorted grid voltage. The stability of the system and the quality of the current it injects in the grid are used to determine its robustness to changes in grid impedance and grid voltage distortion.
- To study the performance of the system during balanced and unbalanced grid faults. The response of the system to the voltage dips resulting from grid faults is investigated and modifications are proposed to improve its performance.

1.5 Main Contributions of the Thesis

The following points summarize the original contributions presented in this thesis.

- ❖ Stability analysis of the closed-loop direct power control system shows that the system is stable without any damping, when the current sensors are on the inverter side of the LCL filter.
- ❖ A reactive power error compensation scheme is developed to make the reactive power at the grid side equal to the controlled reactive power. This error occurs when the grid virtual flux (or voltage) and the inverter current are used to estimate the power. The error compensation scheme corrects the error caused by the reactive power contribution of the filter capacitor of the LCL filter.

- ❖ Virtual-flux based direct power control is shown to be more stable and robust to grid inductance variations and grid voltage distortion than voltage based direct power control. This reinforces the earlier findings that virtual-flux based control schemes are superior to voltage-based control schemes in grids with distorted voltages.
- ❖ A new current limitation algorithm based on power limitation to protect the VSC from excessive currents during voltage dips is developed and implemented. The proposed current limitation algorithm limits the current by decreasing the power references proportionally to the voltage dip. The algorithm is demonstrated for both symmetrical and unsymmetrical voltage dips. For the latter, it is combined with a positive-sequence control scheme to achieve balanced and sinusoidal currents during unsymmetrical voltage dips. Unlike other existing current limiting algorithms, there is no recalculation of the reference current, and it is flexible enough to be adapted to different grid code requirements.

1.6 Publications

The following papers have been written during the course of this project.

- I. F. Mulolani and M. Armstrong, "Space vector modulation direct power control of grid-connected photovoltaic converter with reactive power compensation," *Power Electronics, Machines and Drives (PEMD 2014), 7th IET International Conference on, Manchester, 2014*, pp. 1-6.
- II. F. Mulolani, M. Armstrong and B. Zahawi, "Modeling and simulation of a grid-connected photovoltaic converter with reactive power compensation," *Communication Systems, Networks & Digital Signal Processing (CSNDSP), 2014 9th International Symposium on, Manchester, 2014*, pp. 888-893.

1.7 Outline of the Thesis

The thesis is divided into seven Chapters.

Chapter 1 presents the background of the most common renewable energy sources and the importance of PV in the global energy sector. The voltage source converter is introduced as a key component of grid-connected PV systems, and a brief overview of its control is presented. A review of control techniques for grid-connected VSCs is presented

in Chapter 2. Among the techniques reviewed is virtual-flux direct power control with space vector modulation (VF-DPC-SVM), which is the focus of the thesis. The mathematical models of grid-connected converters with LCL filters are presented in Chapter 3. The closed-loop control system based on VF-DPC-SVM is derived and its stability is analyzed for different types of damping, and different current sensor positions. The system is found to be stable without any damping when the current sensors are on the inverter side. The main issues in the implementation of VF-DPC-SVM in a real system are described in Chapter 4. Implementation of a discrete virtual flux estimation method, virtual flux based grid synchronization and power estimation are described. A new method is proposed to compensate for the error in the reactive power caused by having the current sensors on the inverter side of the LCL filter. In Chapter 5 the effect of grid impedance variation and grid voltage distortion on the performance of the system is investigated. Specifically the effect on system stability and current quality is investigated for voltage based DPC-SVM and virtual-flux based DPC-SVM. Simulation and experimental results obtained using the two control schemes are compared. The control of the VSC during grid faults is the main subject of Chapter 6. To protect the VSC during voltage dips, a new current limiting algorithm based on the reduction of the power references during voltage dips is proposed and implemented. The algorithm is demonstrated to effectively limit the current during both symmetrical and unsymmetrical voltage dips. It is shown that during unsymmetrical voltage dips, it can be combined with a positive-sequence control scheme to maintain balanced and sinusoidal currents. In Chapter 7 the thesis conclusions and suggestions for future work are presented.

Chapter 2 **Review of Control Techniques for Grid-connected Voltage Source Converters**

2.1 Introduction

Three-phase voltage source converters (VSCs) are widely used in variable speed AC electric drives and grid-connected systems. Grid-connected systems include active filters, PWM rectifiers, static synchronous compensators (STATCOMs), and converters for renewable energy sources. The VSC is able to operate with bi-directional power flow, low current distortion, controllable power factor and a relatively small AC filter, making it a good choice for many applications. Regardless of the application, the performance of the VSC will largely depend on the applied current control technique [57], [58], [30]. The main function of the current controller is to force the instantaneous three-phase current to follow the current reference signals [59], [60]. The current controller also determines the appropriate switching states to minimize the error between the reference and the actual current [59], [60]. The switching states determine the state of the semiconductor switches either directly or through a suitable modulator [59]. Control techniques for most VSC applications are similar, and most of them are based on techniques which were initially developed for the control of AC drives.

In this chapter the main control methods for grid-connected voltage source converters are reviewed and analyzed. The control methods will be broadly divided into hysteresis control, voltage based control schemes, virtual-flux based control schemes, and predictive control schemes. Voltage based and virtual flux based control schemes are further divided into current control and direct power control schemes [61]. It should be noted that there is no universally accepted method of classifying the different types of current controllers because most of the control methods are related in a way; for example some direct power control and predictive control schemes use some form of hysteresis controllers. But for the intended purpose of this review, the above classification will suffice.

In the context of this review, the performance of the current control schemes will be evaluated based on how they meet the following criteria:

- Fast dynamic response
- Constant switching frequency
- Low harmonic distortion in the output current

- Decoupled control of active and reactive power
- Ease of implementation of the algorithm
- Stability over a wide range of operating conditions

2.2 Current Control Basics

To develop the basis for current control of a grid-connected VSC, the single-phase equivalent circuit of Figure 2.1 is considered. For simplicity, throughout this chapter a first order inductive filter is assumed. This is a reasonable assumption because at frequencies less than half of its resonance frequency, the higher order LCL filter has the same characteristics as the L filter [29].

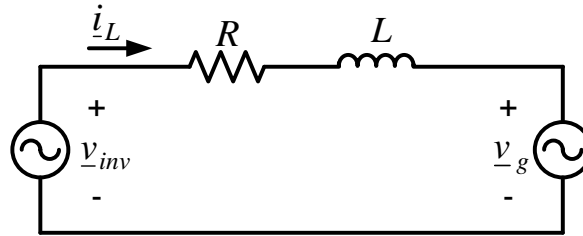


Figure 2.1 Single-phase equivalent circuit of grid-connected converter.

In space vector form, the phase voltage of the inverter is related to the grid phase voltage by the equation below.

$$\underline{v}_{inv} = L \frac{d\underline{i}_L}{dt} + R\underline{i}_L + \underline{v}_g \quad (2.1)$$

where $\underline{v}_{inv} = \begin{bmatrix} v_{inva} \\ v_{invb} \\ v_{invc} \end{bmatrix}$ is the inverter voltage space vector, $\underline{v}_g = \begin{bmatrix} v_{ga} \\ v_{gb} \\ v_{gc} \end{bmatrix}$ is the grid voltage

space vector, $\underline{i}_L = \begin{bmatrix} i_{La} \\ i_{Lb} \\ i_{Lc} \end{bmatrix}$ is the line current space vector, L is the inductance of the filter

and R is the resistance of the filter.

The vector diagram of the phase voltage and current is shown in Figure 2.2. The voltage across the filter resistance is depicted as \underline{v}_R and the voltage across the filter inductance is depicted as \underline{v}_L .

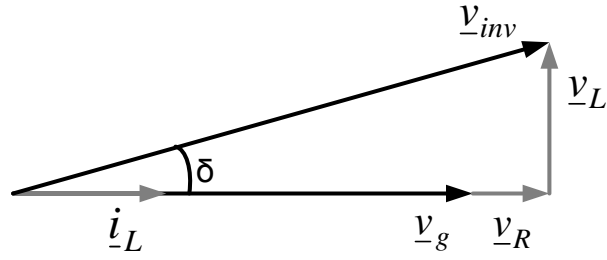


Figure 2.2 Vector diagram of grid-connected converter.

Since the grid voltage vector is essentially constant, the line current can be controlled by controlling the inverter voltage magnitude and phase angle between the inverter voltage and the grid voltage, δ . By regulating both the magnitude and phase angle of the inverter voltage relative to the current demand, the inverter behaves like a controlled current source. The current controller and the modulator set the correct switching sequence of the inverter devices to give the required current.

In terms of the phase voltages and line currents, the instantaneous active power and the instantaneous reactive power (or imaginary power) are respectively defined in [62] as

$$p = v_{ga}i_{La} + v_{gb}i_{Lb} + v_{gc}i_{Lc} \quad (2.2)$$

and

$$q = \frac{1}{\sqrt{3}} \left[(v_{gb} - v_{gc})i_{La} + (v_{gc} - v_{ga})i_{Lb} + (v_{ga} - v_{gb})i_{Lc} \right] \quad (2.3)$$

Equations (2.2) and (2.3) show that the active power is a scalar product of the grid voltage vector and the current vector and the reactive power is their vector product. Therefore, if the grid voltage vector is constant, by regulating the current, the power is indirectly regulated and vice versa. Therefore, both current control and direct power control achieve the same objective of controlling the current output of the VSC.

2.3 Hysteresis Current Control

One of the simplest methods of current control in voltage source converters is hysteresis current control [63], [64]. It consists of three independent hysteresis controllers; one for each phase leg of the VSC. The actual current is compared to the desired reference current and the error is fed to a hysteresis comparator which generates the appropriate switching

signal to keep the error between the actual current and the reference current within a fixed hysteresis band. No separate modulator is required with hysteresis control as this type of current control directly generates the switching signals [65]. The block diagram of hysteresis current control is shown in Figure 2.3 and its operating principle is shown in Figure 2.4. It is easy to implement, robust to load changes and has a very fast dynamic response. However, the output voltage has a variable switching frequency, which makes it difficult to design a filter if used to control a grid-connected VSC. A high switching frequency is required for the controller to compensate for its inherent drawbacks [66]. A further drawback is that it does not have the possibility of controlling the active power and the reactive power independently which other methods typically do. Improvements to the basic hysteresis controller, by operating with a constant switching frequency, have been suggested in [67], [68].

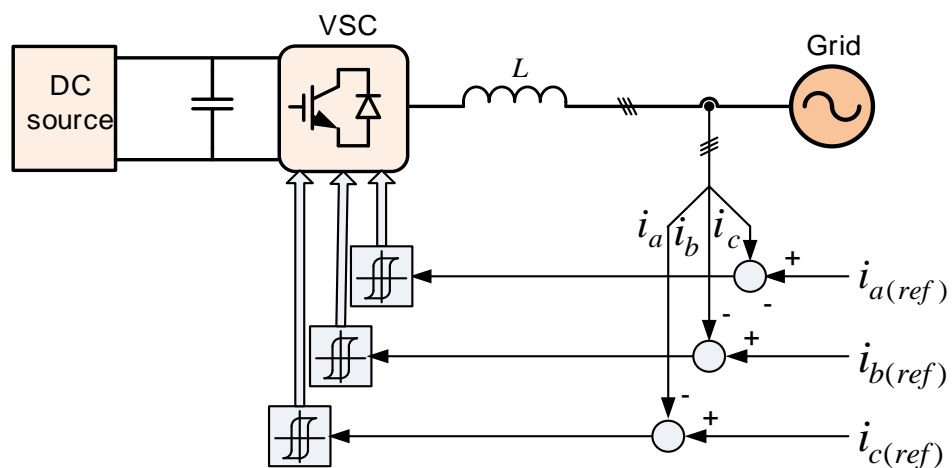


Figure 2.3 Block diagram of hysteresis current control.

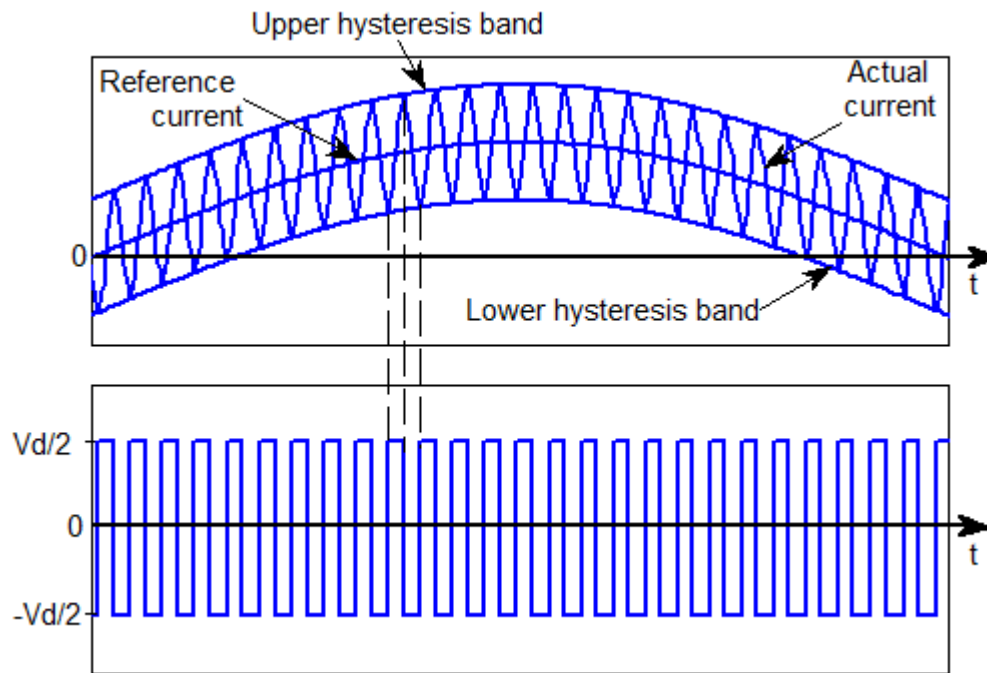


Figure 2.4 Principle of hysteresis control: current (upper) and converter output voltage (lower).

2.4 Voltage Based Control

A common feature of voltage based control schemes is that the grid voltage plays a role in the correct implementation of the controller. Typically the grid voltage angle is used as the reference for the orientation of the control scheme to achieve synchronization [38].

2.4.1 Voltage-Oriented Current Control

Voltage oriented control is a popular current control method, based on the field-oriented control (FOC) method of electric drives [69]. It is characterized by reference frame transformations to a synchronous rotating reference frame in which AC quantities are viewed as DC quantities. This makes it possible to use PI controllers without encountering the problem of steady-state errors, which is the case when PI controllers are used to regulate sinusoidal quantities [38]. The block diagram of a voltage-oriented current control scheme is shown in Figure 2.5.

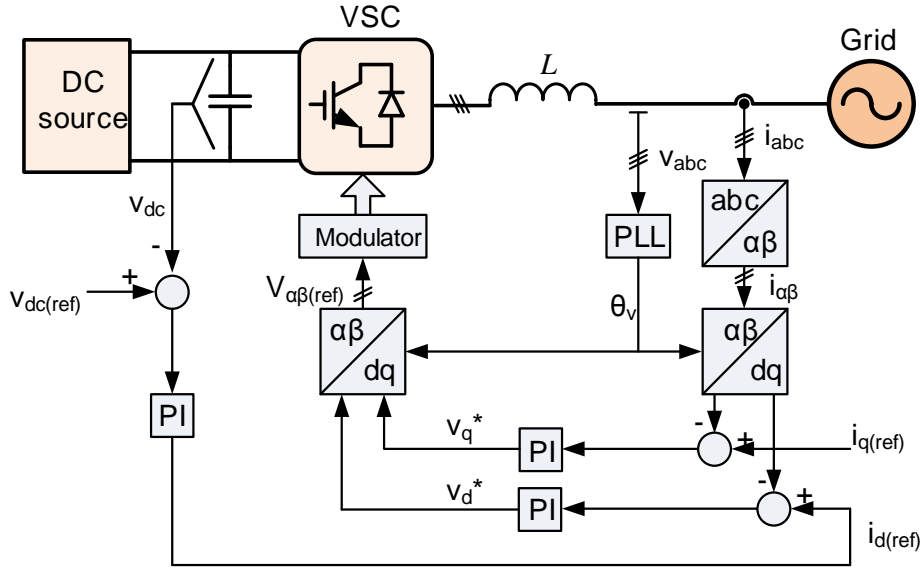


Figure 2.5 Block diagram of voltage oriented control.

The measured three-phase currents are transformed to equivalent two-phase currents in a stationary reference frame using the Clarke transformation given below.

$$\begin{bmatrix} i_{L\alpha} \\ i_{L\beta} \end{bmatrix} = \frac{2}{3} \begin{bmatrix} 1 & -\frac{1}{2} & -\frac{1}{2} \\ 0 & \frac{\sqrt{3}}{2} & \frac{\sqrt{3}}{2} \end{bmatrix} \begin{bmatrix} i_{La} \\ i_{Lb} \\ i_{Lc} \end{bmatrix} \quad (2.4)$$

Where $i_{L\alpha}$ and $i_{L\beta}$ are the orthogonal components of the currents in the stationary reference frame. The currents are then transformed to the synchronous reference frame using the Park transformation given below.

$$\begin{bmatrix} i_{Ld} \\ i_{Lq} \end{bmatrix} = \begin{bmatrix} \cos \theta_v & \sin \theta_v \\ -\sin \theta_v & \cos \theta_v \end{bmatrix} \begin{bmatrix} i_{L\alpha} \\ i_{L\beta} \end{bmatrix} \quad (2.5)$$

where i_{Ld} and i_{Lq} are the orthogonal current components in the synchronous reference frame and θ_v is the angle of the grid voltage.

The vector diagram of VOC showing the orientation of the voltages and currents in the stationary reference frame and the synchronous reference frame is shown in Figure 2.6. In the diagram the phase angle between the voltage and the current is φ .

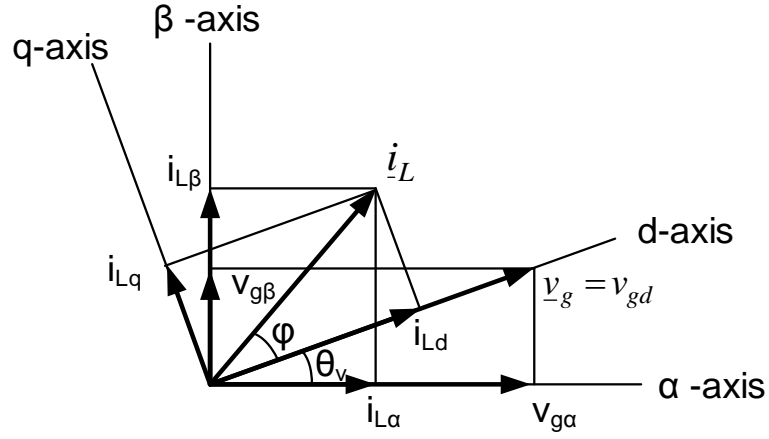


Figure 2.6 Vector diagram of voltage-oriented control.

From Figure 2.6, it can be seen that the grid voltage vector is oriented along the d-axis of the synchronous reference frame and the component of the grid voltage on the q-axis is zero. Therefore, the d-axis voltage is equal to the magnitude of the grid voltage vector as given by the equation below.

$$v_{gd} = |v_g| \quad (2.6)$$

By applying the definition of instantaneous power, the active power and the reactive power in the synchronous reference frame are obtained as

$$p = \frac{3}{2} v_{gd} i_{Ld} \quad (2.7)$$

$$q = -\frac{3}{2} v_{gd} i_{Lq} \quad (2.8)$$

From equations (2.7) and (2.8) it is apparent that, the d-axis current is used to control active power and the q-axis current is used to control reactive power. However, if equation (2.1) is rewritten in terms of the synchronous reference frame components, the equations obtained are

$$v_{invd} = v_{gd} + L \frac{di_{Ld}}{dt} + Ri_{Ld} - \omega Li_{Lq} \quad (2.9)$$

$$v_{invq} = 0 + L \frac{di_{Lq}}{dt} + Ri_{Lq} + \omega Li_{Ld} \quad (2.10)$$

where $\omega = d\theta_v/dt$ is the angular frequency of the grid voltage.

Equations (2.9) and (2.10) show that there is cross-coupling of the d-axis and the q-axis currents. To eliminate this cross-coupling, the current controller is implemented as shown in Figure 2.7. The voltage feedforward is added to improve the dynamic response of the controller and improve its grid voltage disturbance rejection [29].

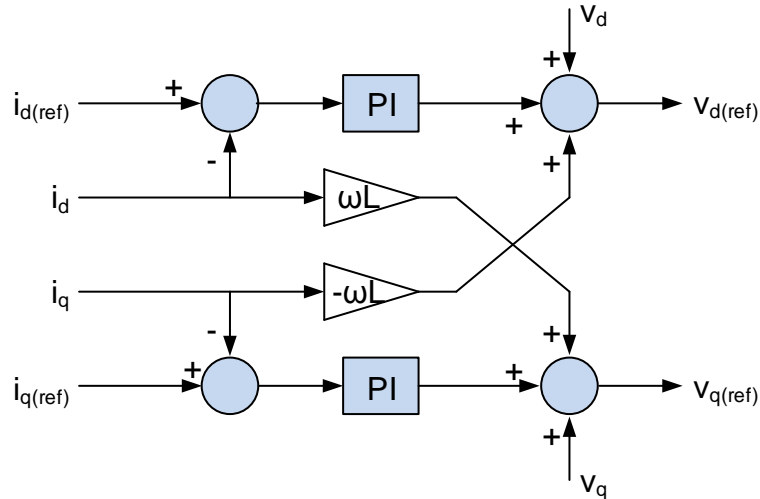


Figure 2.7 Current controller with decoupling and feedforward terms

The output of the current controller is converted to the stationary reference frame using the inverse Park transformation and forms the input to the modulator.

VOC has the following advantages:

- It has a constant switching frequency which makes it easy to design the grid filter.
- It allows decoupled control of active and reactive power through the SRF current components.
- It does not require a very high sampling frequency.

It has the following disadvantages:

- It needs reference frame transformations to the synchronous reference frame.
- It has a slow dynamic performance.

2.4.2 Direct Power Control

Direct power control (DPC), which is based on direct torque control (DTC) developed earlier for the control of electrical machines [70], [71], was first proposed by Ohnishi in [72], and developed as an AC voltage sensorless control technique for three-phase PWM rectifiers [34], [73]. In DPC, the active power and the reactive power are regulated directly

without using a current control loop. This requires accurate estimation of the instantaneous powers. The power estimation is based on the instantaneous power theory [62], in which the instantaneous powers are given by

$$p = \frac{3}{2}(v_{g\alpha}i_{L\alpha} + v_{g\beta}i_{L\beta}) \quad (2.11)$$

$$q = \frac{3}{2}(v_{g\alpha}i_{L\beta} - v_{g\beta}i_{L\alpha}) \quad (2.12)$$

The block diagram of a direct power control scheme with grid voltage sensors is shown in Figure 2.8. Some differences with voltage oriented control include the absence of reference frame transformation to the synchronous reference frame, use of hysteresis controllers instead of PI controllers, and use of a switching table to determine the switching sequence of the switches instead of a modulator.

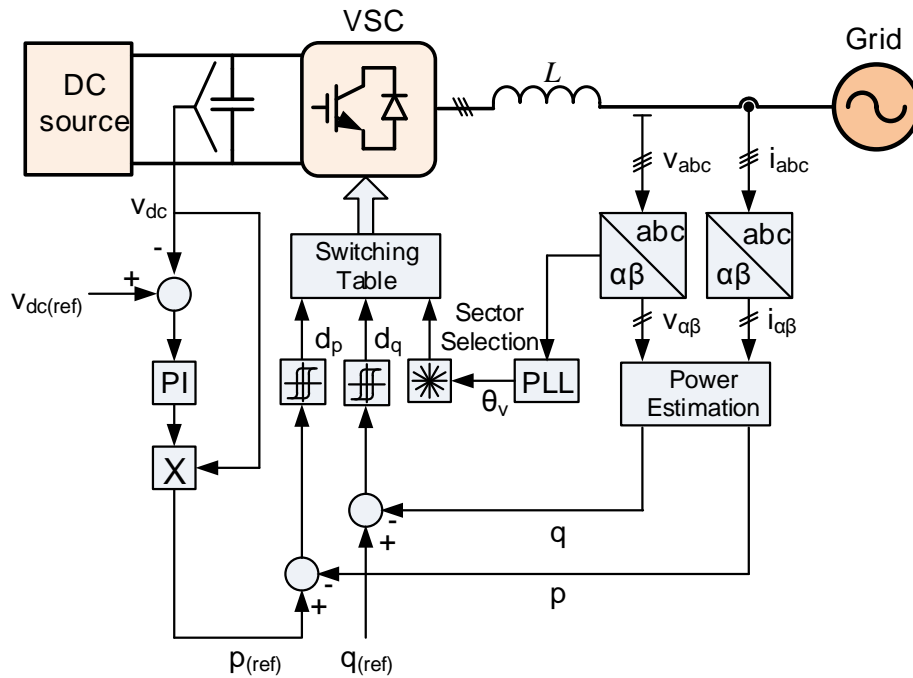


Figure 2.8 Block diagram of direct power control.

The DC voltage controller sets the active power reference, while the reactive power reference is usually set to zero for unit power factor operation. The reference powers are compared to the actual estimated powers and the errors fed to hysteresis controllers. The outputs of the hysteresis comparators and the angular position of the voltage vector given by the PLL are used to select the most suitable voltage vector from the switching table.

The switching table affects the performance of the control scheme and many different types of switching tables can be found in literature [74], [75], [76].

DPC has the following advantages:

- It has a very fast dynamic response due to the use of hysteresis comparators.
- It is a relatively simple algorithm with no reference frame transformation to the synchronous reference frame.

It has the following disadvantages:

- Due to the use of hysteresis comparators, it has a variable switching frequency which makes it difficult to design the grid filter.
- A high value of the filter inductance is needed to obtain a smooth current.
- A high sampling frequency is needed for accurate power estimation.
- Its implementation requires a fast microprocessor and ADC due to its high sampling frequency requirement.

2.4.3 Direct power Control with Space Vector Modulation

The simplicity and fast dynamic response of DPC makes it a practical alternative to VOC current control. However, its main drawbacks which include the need for a fast sampling frequency and a variable switching frequency makes its implementation on a large scale more difficult. While most modern DSPs and microcontrollers are capable of handling high sampling frequencies, the switching frequency will still be variable. The disadvantages of a variable switching frequency can be overcome by replacing the hysteresis controllers with linear PI controllers and the switching table with any suitable modulation technique such as space vector modulation (SVM).

When space vector modulation (SVM) is used, the technique is referred to as direct power control with space vector modulation [77], [78]. It can be implemented as a voltage-based control scheme as in [78], [79], although it is more commonly implemented as a virtual-flux based control scheme [80]. The block diagram of virtual flux direct power control with space vector modulation is shown in Figure 2.9.

The main feature of the control is that the active and reactive powers are controlled directly without a current control loop. The power estimation is performed in the same way as for DPC. Synchronization can be achieved by using the virtual flux angle. Unlike VOC where two reference frame transformations are performed, only one reference frame

transformation is performed in transforming the outputs of the power controllers from the synchronous reference frame to the stationary reference frame required for space vector modulation.

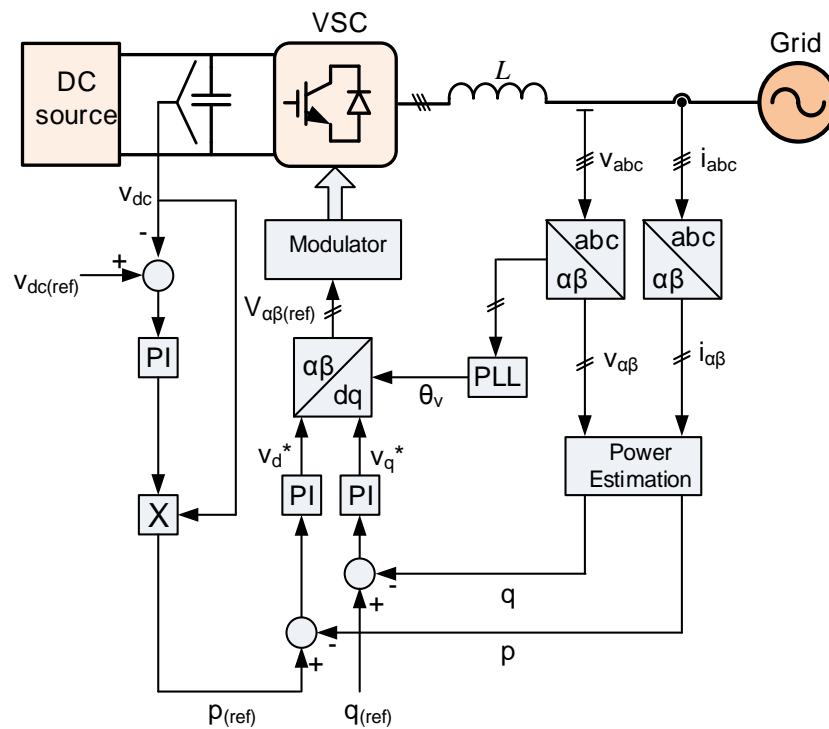


Figure 2.9 Block diagram of direct power control with space vector modulation.

DPC-SVM combines the advantages of a fast dynamic response of direct power control, and the constant switching frequency current control. While it retains most of the advantages of both control schemes, it also retains some of their disadvantages such as the complexity of reference frame transformation needed to convert the modulator's reference voltages from the synchronous reference frame to the stationary reference frame.

The advantages of DPC-SVM are summarized below:

- It has a constant switching frequency like VOC.
- It requires a lower sampling frequency than DPC.

It has the following disadvantages:

- It requires reference frame transformation making the control algorithm more complicated than DPC.
- It has a slower dynamic response than DPC.

2.5 Virtual-Flux Based Control

The concept of using virtual-flux in the control of grid-connected converters makes use of the analogy between inverter-fed AC machine drives and grid-connected converters [81]. In this analogy, the grid is viewed as a virtual AC machine and the grid voltage is induced by the time variation of a flux, similar to the back emf in a machine, as given by

$$\underline{v}_g = \frac{d\underline{\psi}_g}{dt} \quad (2.13)$$

The flux is called the virtual-flux and its vector is represented by $\underline{\psi}_g$ in equation (2.13).

In virtual-flux based control schemes, the virtual-flux is used in place of the voltage for synchronization and power estimation in direct power control schemes.

The virtual-flux cannot be measured directly and is estimated from the grid voltage using

$$\underline{\psi}_g = \underline{\psi}_{g0} + \int \underline{v}_g dt \quad (2.14)$$

where $\underline{\psi}_{g0}$ is the initial value of the virtual-flux.

In practice, direct integration of the grid voltage to obtain the virtual-flux is not used because of possible integrator drift and saturation if there is an offset in the measured voltage [82]. The virtual-flux estimation methods in literature are based on filters which give a phase shift of 90° at the fundamental frequency [73], [81], [82], [83], [84], [85]. Due to the use of filters, the distortion in the grid voltage is damped and the virtual-flux vector rotates more smoothly than the grid voltage vector. Thus, the virtual-flux angle can be tracked more easily than the voltage angle even without using a PLL [86]. Virtual-flux based control schemes tend to perform better than voltage based control schemes in distorted grids [35].

2.5.1 Virtual-Flux Oriented Current Control

Virtual flux oriented control (VFOC) is an improvement to VOC based on the virtual-flux concept [73], [81]. The block diagram of the VFOC scheme is shown in Figure 2.10.

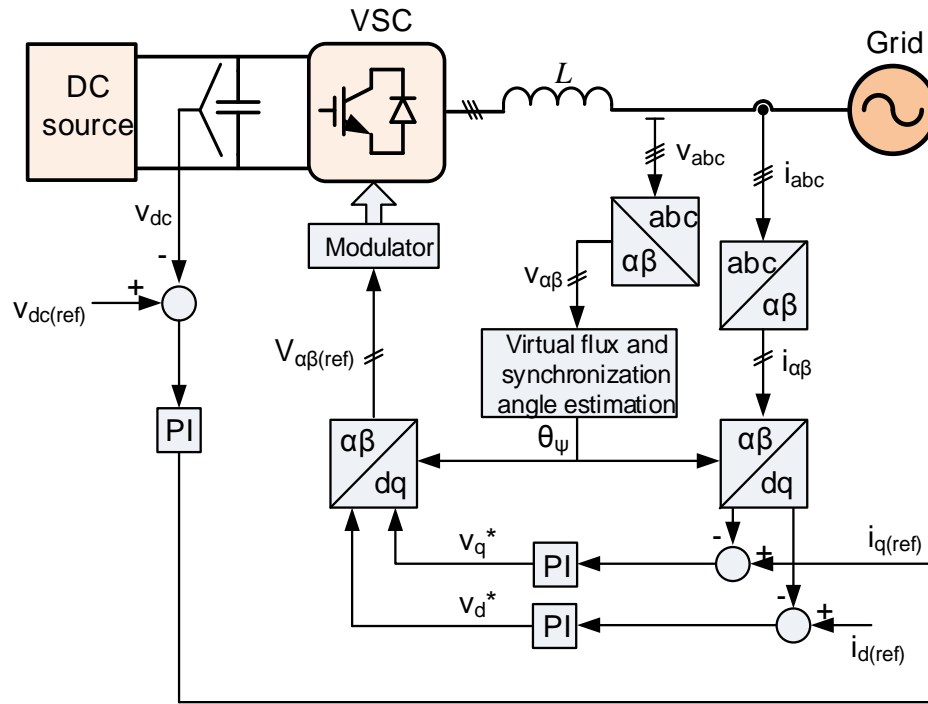


Figure 2.10 Block diagram of virtual-flux oriented control.

The virtual-flux angle, θ_ψ , is used for reference frame transformation, and can be obtained either by using a PLL or using the arctangent of its stationary reference frame components as shown by the equation below.

$$\theta_\psi = \tan^{-1} \left(\frac{\psi_{g\beta}}{\psi_{g\alpha}} \right) \quad (2.15)$$

Using the definitions of instantaneous power, and virtual-flux, the instantaneous powers in the synchronous reference frame are given by

$$p = \frac{3}{2} \omega (\psi_{gd} i_{Lq} - \psi_{gq} i_{Ld}) \quad (2.16)$$

$$q = \frac{3}{2} \omega (\psi_{gd} i_{Ld} + \psi_{gq} i_{Lq}) \quad (2.17)$$

If the virtual-flux vector is oriented along the d-axis as shown in the vector diagram in Figure 2.11, the component of current along the q-axis is used to control active power, and the components along the d-axis is used to control reactive power.

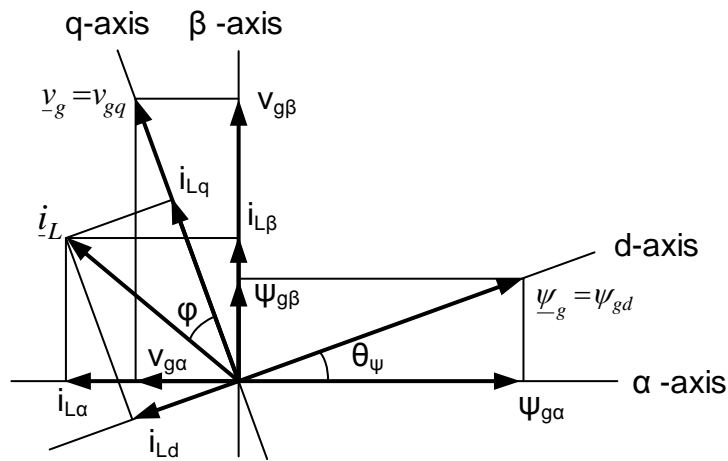


Figure 2.11 Vector diagram of virtual-flux oriented control.

VFOC has the same advantages and disadvantages as VOC. One advantage it has over VOC is better performance when the grid voltage is distorted [87].

2.5.2 Virtual-Flux Direct Power Control

Virtual-flux direct power control (VF-DPC) was proposed to improve the performance of the performance of the original voltage-based DPC [40]. In VF-DPC, the estimated virtual-flux is used to estimate the powers and the virtual-flux angle is used to select the correct switching sector in the switching table. The block diagram of VF-DPC is shown in Figure 2.12.

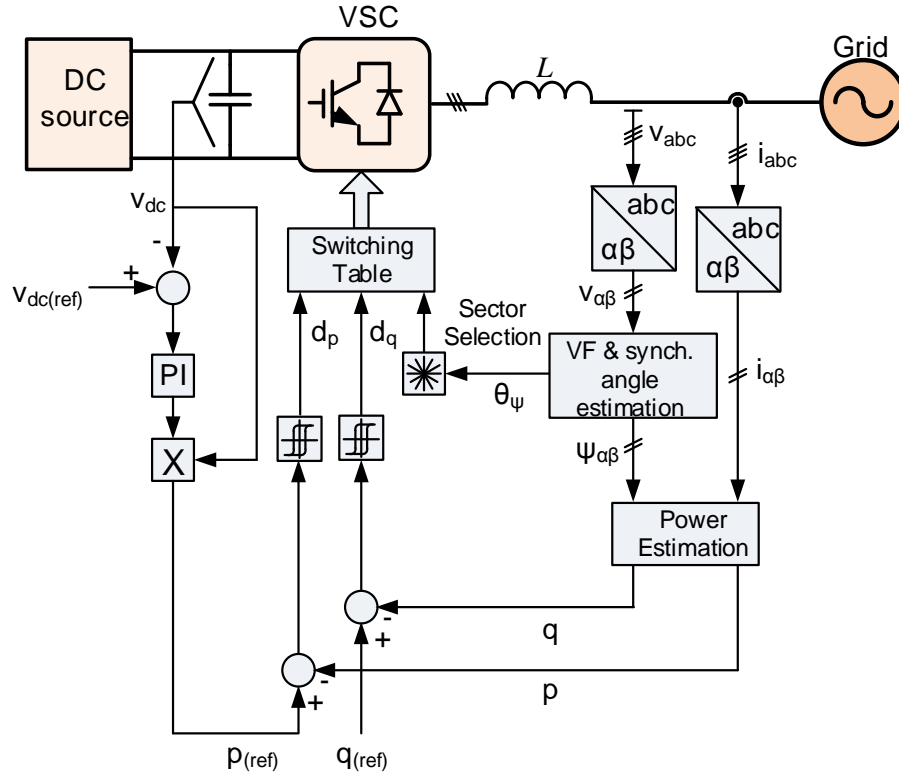


Figure 2.12 Block diagram of virtual-flux direct power control.

The active power and the reactive power are calculated from the estimated virtual flux, and the measured current using the equations below, [40], [88].

$$p = \frac{3}{2} \omega (\psi_{g\alpha} i_{L\beta} - \psi_{g\beta} i_{L\alpha}) \quad (2.18)$$

$$q = \frac{3}{2} \omega (\psi_{g\alpha} i_{L\alpha} + \psi_{g\beta} i_{L\beta}) \quad (2.19)$$

Due to the reduced distortion in the virtual-flux the power estimation is less noisy than it is for voltage-based DPC and the output current is less distorted [61]. This makes it possible to use a lower sampling frequency than that used in DPC. However, the required sampling frequency is still much higher than that needed for VOC and VFOC [59].

The main advantages of VF-DPC over DPC can be summarized as

- Less noisy power estimation.
- Lower distortion in the output current with distorted grid voltage.
- Lower sampling frequency than DPC.

Compared to VOC and VFOC it still has the disadvantages of

- Variable switching frequency.
- Fast sampling frequency.

2.5.3 Virtual flux Direct Power Control with Space Vector Modulation

Virtual flux direct power control with space vector modulation (VF-DPC-SVM) is the virtual flux based version of the voltage based DPC-SVM described earlier. The virtual flux based DPC-SVM was actually the first version of DPC-SVM to be introduced [77] and is usually referred to as DPC-SVM. To differentiate it from the voltage based DPC-SVM, in this thesis it will be referred to as VF-DPC-SVM. The block diagram of VF-DPC-SVM is shown in Figure 2.13.

VF-DPC-SVM has all the advantages of DPC-SVM. In addition it also has all the advantages of VF-DPC and VFOC compared to DPC and VOC. It has similar drawbacks to DPC-SVM.

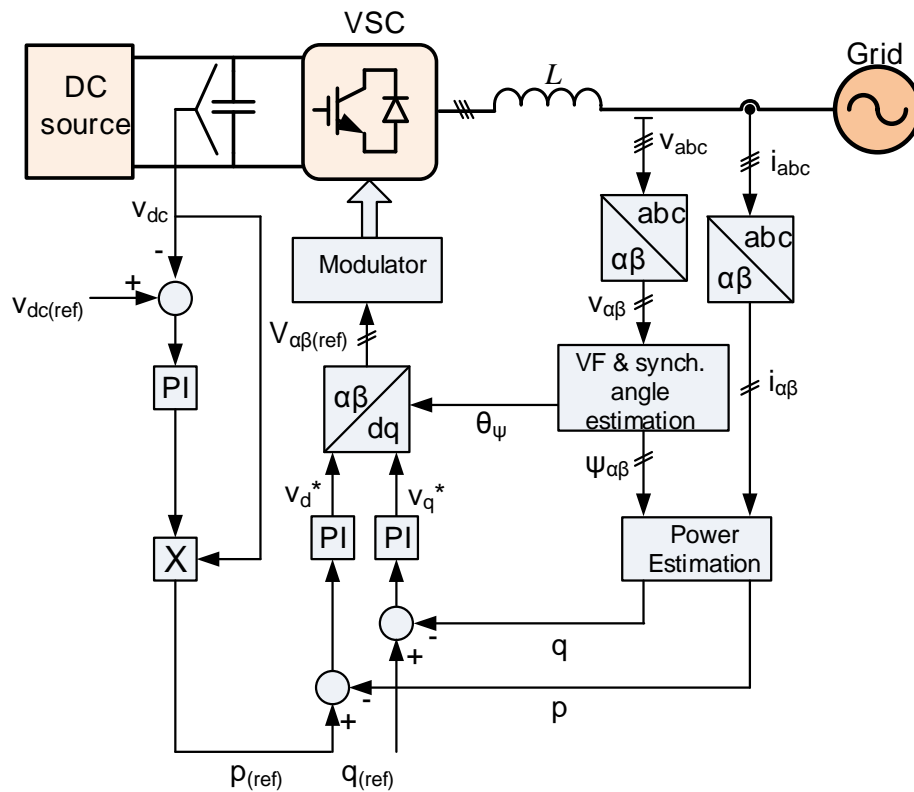


Figure 2.13 Block diagram of virtual-flux direct power control with space vector modulation.

2.6 Predictive Control

Predictive control schemes have gained popularity in the control of grid-connected converters and electric drives. The term refers to a range of controllers which use the model of the controlled system to predict the behaviour of the controlled variables [89]. By minimizing a selected parameter or cost function, the most suitable switching voltage vector is selected in every sampling period. Predictive control can be implemented as a current control scheme or a direct power control scheme [90], [91]. Predictive control is characterized by fast dynamic response but the controller has to perform a high amount of mathematical computations, thus requiring a fast DSC for implementation. The performance is affected by the parameters used in the load model and accurate knowledge of the model parameters is needed for good performance. The block diagram of a predictive control scheme of a grid-connected VSC is shown in Figure 2.14.

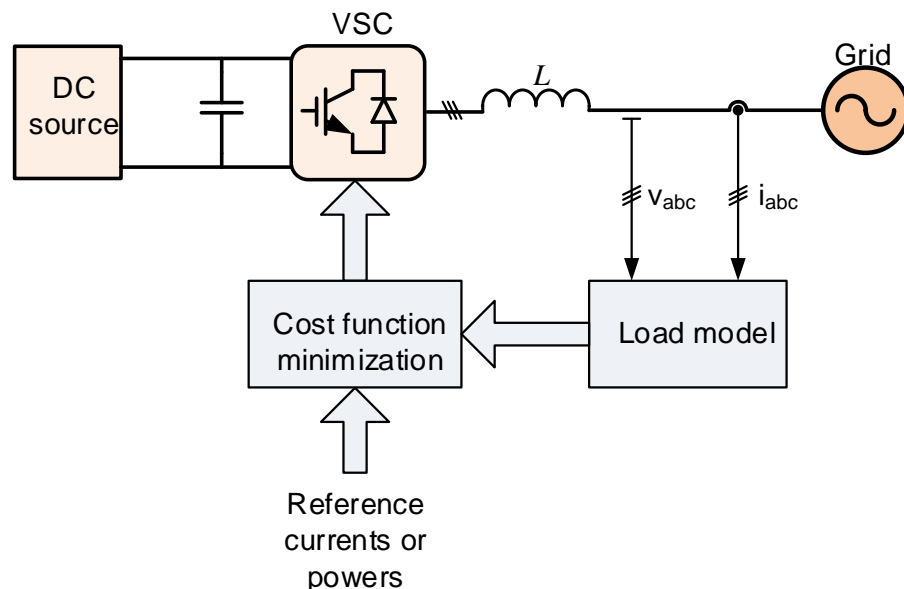


Figure 2.14 Block diagram of predictive control.

One of the earliest and most well-known predictive control methods is deadbeat control [92], [93], [94]. In this method, the objective is to select the switching voltage vector which will make the error between the predicted and the actual current equal to zero at the end of each sampling period. Deadbeat control has a fast dynamic response. However, computational delays, errors in parameter values used in the model and external disturbances reduce the quality of its performance.

Another type of predictive control is hysteresis based predictive control [89], [90], [95] where the controlled variables are kept within hysteresis bands. It is based on the basic hysteresis band (bang-bang) control scheme. The switch states are determined directly by selecting the voltage vector which would keep the current within a suitable error boundary without using a modulator. As a consequence the switching frequency is variable, and this is a major drawback of hysteresis based predictive control.

Trajectory based predictive control is another type of predictive control which is based on the principle of forcing the system variables to follow pre-calculated trajectories. Examples of trajectory based predictive control include direct self-control [96], direct mean torque control [97], and direct torque control [70].

Model predictive control is another predictive control method that has been widely used in the control of converters. It is based on using a model of the system to predict the switching state of the converter. When a modulator is used to determine the switching states, it is known as model predictive control with continuous control sets; and when the switch states are determined directly without using a modulator it is called finite control set method. The finite control set method is more popular with converters because it takes into consideration the non-linear nature of the converter and the switch states are determined by minimizing a given cost function [98], [99]. Both constant switching frequency and variable switching frequency have been reported [100]. The advantage of model predictive control is that it has fast transient response because it does not have a cascaded structure. The disadvantage is that it requires a high number of computations and requires a powerful DSC for practical implementation. Another disadvantage is that its performance depends on the accuracy of the parameters used in the model.

2.7 Comparison of the Reviewed Control Schemes

The performance of the various control techniques has been compared in a number of publications [57], [58], [30], [59], [87], [101]. Based on the criteria set out at the beginning of this chapter, the reviewed control schemes are compared in table 2.1.

Table 2.1 Comparison of various control systems

	Hysteresis	VOC/VFOC	DPC/VF-DPC	DPC-SVM/VF-DPC-SVM	Predictive
Dynamic response	Very Fast	Slow	Very Fast	Fast	Very fast
Switching frequency	Variable	Fixed	Variable	Fixed	Variable or fixed
Output current THD	High	Load dependent	High	Load dependent	Load dependent
Decoupled p, q control	No	Yes	Yes	Yes	Yes
Ease of implementation	Very Simple	Complicated	Simple	Simple	Very complicated
Stability	Stable	Load dependent	Stable	Load dependent	Load dependent

From the reviewed methods, it can be seen that each method has advantages and disadvantages when compared to other methods. Therefore, in the selection of a control scheme for a particular application the most important performance criterion for that application should be given priority over other criteria. In grid-connected converter applications, a low THD of the output current is a necessity in order to meet the harmonic requirements specified by international standards. A constant switching frequency makes the design of the grid filter which reduces the harmonics in the current easier. Stability over a wide range of grid operating conditions is also an important criterion because the grid parameters such as voltage magnitude, frequency and grid impedance are not constant and the control scheme should be robust to these changes. Ease of implementation of a control scheme is important because a simpler scheme will be less costly and will take less time to implement in practice. Decoupled control of active power and reactive power makes it possible to use the active power controller to balance the

active power flow from the renewable source to the grid and use the reactive power control as an ancillary function.

As seen from Table 2.1, there is no control scheme that can be said to be better than the other control schemes in all aspects. Therefore, in the selection of a control scheme, certain trade-offs have to be made depending on the particular application. Among the reviewed control schemes, DPC-SVM is found to be the most suitable for the objectives of this thesis. Although it is not as simple as hysteresis control, it has better performance in steady state with a constant switching frequency and low harmonic distortion of the output current.

2.8 Conclusion

In this chapter the main current control techniques for voltage source converters have been reviewed. From the reviewed techniques, the following conclusions were drawn.

- Hysteresis based techniques, such as hysteresis current control and direct power control, and predictive control schemes have good dynamic performance. This is because of the absence of the modulator which increases the execution time of the control algorithm.
- Control techniques which use a modulator have a constant switching frequency, and the output current has a well-defined frequency spectrum. In addition, they can be operated with a lower sampling frequency than hysteresis based and predictive control techniques.
- Virtual-flux based control techniques have a lower output current THD compared to voltage based control techniques. This makes them a better option for grid-connected converters, connected to a distorted grid.
- Direct power control schemes and current control schemes based on the synchronous reference frame, have decoupled control of active power and reactive power.
- Hysteresis based control techniques are easier to implement than other control techniques.
- The stability of each control technique will depend on factors such as the type of filter used, the presence of harmonics and the variation of the grid parameters such

as grid impedance and frequency. Hysteresis based control techniques are generally more robust to these changes than modulator based control techniques.

Chapter 3 **Modelling and Stability Analysis of Grid-connected Converter with LCL Filter**

3.1 Introduction

Mathematical models of three-phase voltage source converters connected to the grid through an L filter have been presented in [31], [102]. The models are developed in the stationary reference frame and the synchronous rotating reference frame. In the stationary reference frame, the three-phase system is presented as an equivalent two-phase system by transforming the three-phase quantities into two-phase quantities using the Clarke transformation. In the synchronous reference frame, the two-phase quantities are transformed into DC quantities using the Park transformation. The models are useful in understanding the behaviour of the system and designing a suitable control scheme. In a similar way, the mathematical models of a grid-connected voltage source converter with an LCL filter can be developed and analyzed. In this chapter mathematical models are developed in the natural reference frame, stationary reference frame and the synchronous rotating reference frame. The synchronous reference frame model is used to develop a closed-loop control scheme for the converter, for stability analysis.

The stability analysis is necessary due to the tendency of the LCL filter to cause controller instability at its resonance frequency. On the other hand the LCL filter provides higher harmonic attenuation using smaller filter components than corresponding L or LC filters [103] which is a big advantage in high-power converters where the switching frequency is kept low to minimize the switching losses. The instability caused by the LCL filter resonance can be mitigated by damping, which can be passive or active. Passive damping refers to the use of passive elements such as resistors connected in series or in parallel with the filter capacitor [104], [105], [106]. A disadvantage of passive damping is that it leads to reduced efficiency due to increased losses in the damping resistors [104]; and reduced performance of the filter at frequencies higher than the resonance frequency because it is not frequency-selective [105]. Active damping involves modification of the control structure to introduce damping at the resonance frequency. Many active damping methods have been proposed, among them virtual resistor [107], [108], capacitor current feedback [109], [110], lead-lag elements [111], low-pass filters [111], and notch filters [111], [112], [113], [114]. Active damping makes the controller design more complicated

and some active damping methods such as capacitor current feedback need the capacitor current to be measured, therefore requiring extra current sensors, making the system more complicated and costly.

Another option of achieving stable operation of the LCL filter based VSC, is by careful selection of the filter components and the current sensor position as proposed in [115] and [116]. In both of these publications, the system is reported to be stable without using passive or active damping. This is an interesting solution because it avoids the added losses of passive damping and the complexity of active damping.

The stability analysis is performed for a grid-connected VSC with an LCL filter controlled using virtual-flux based direct-power control with space vector modulation, which is the control scheme adopted in this thesis. In this control scheme which is introduced in chapter two, the measured current is multiplied by the virtual flux to obtain the active power and reactive power which are controlled using PI controllers. The stability is investigated for four cases: with the current sensors on the grid side without damping; with the current sensors on the grid side with passive damping; with the current sensors on the grid side with active damping and with the current sensors on the inverter side with no damping. For each case the continuous-time closed-loop transfer function of the power controlled system is derived. This is then discretized to allow for the stability analysis to be performed in the z-domain using the pole-zero maps.

3.2 Models of Grid-connected Converter with LCL Filter

The circuit of a grid-connected voltage-source converter with an LCL filter is shown in Figure 3.1. The PV array is the energy source on the DC side and converter acts as a controlled current source with the grid absorbing the injected current. The converter consists of three single-phase IGBT half-bridge legs connected across the DC link capacitor. The LCL filter provides an interface between the VSC and the grid.

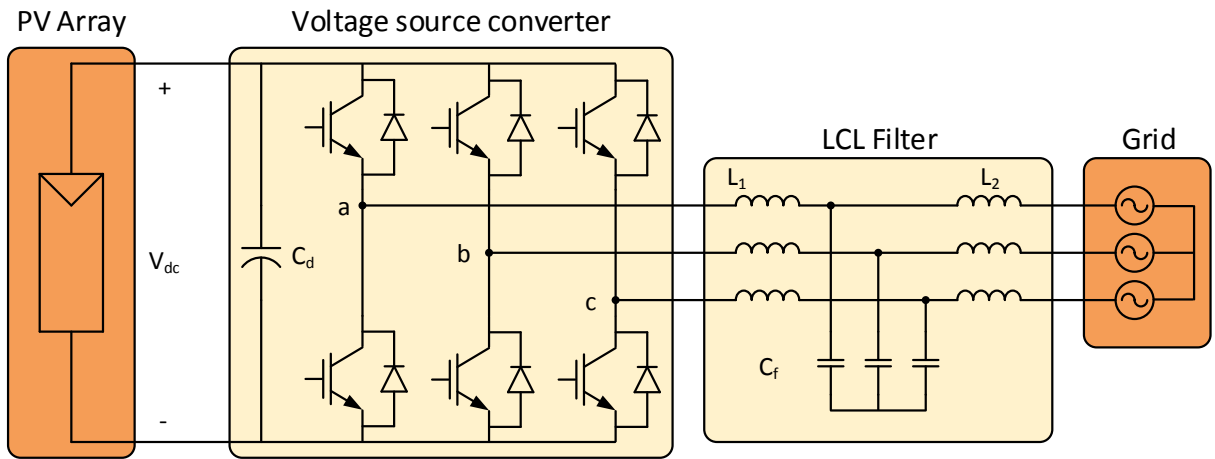


Figure 3.1 Grid-connected VSC with LCL filter.

For modelling purposes the IGBTs are assumed to be ideal switches. The output of each phase leg is then determined by the switching state of that leg. The switching state is given by S_k , where $k = a, b, c$. A switching state equal to 1 means the upper switch is on while the lower switch is off, and a switching state equal to 0 means the upper switch is off while the lower switch is on. The two switches in a phase leg cannot be on at the same time.

The equivalent single-phase circuit is shown in Figure 3.2. In the figure, R_1 , R_2 , L_1 and L_2 are the resistances and inductances of the inverter-side and grid-side filter inductors, respectively.

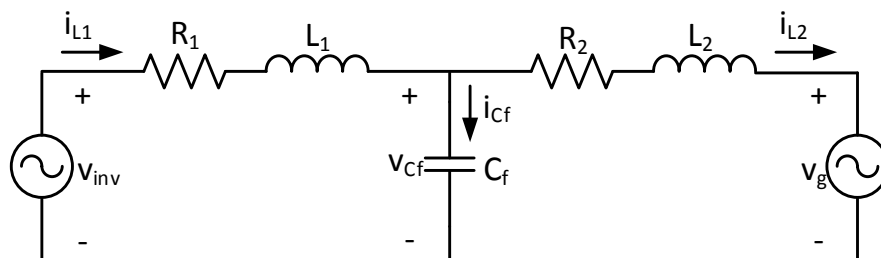


Figure 3.2 Equivalent single-phase circuit of grid-connected VSC.

In space vector notation, the inverter voltage vector can be written in terms of the switching function as shown in the equation below.

$$\underline{v}_{inv} = \frac{2}{3} \left(S_a + S_b e^{j\frac{2\pi}{3}} + S_c e^{-j\frac{2\pi}{3}} \right) \quad (3.1)$$

There are eight possible combinations of the switching states as shown in Table 3.1 and the resultant voltage vectors for each state are shown in Figure 3.3.

Table 3.1 Switching states for three-phase VSC

Voltage vector	S_a	S_b	S_c
v_0	0	0	0
v_1	1	0	0
v_2	1	1	0
v_3	0	1	0
v_4	0	1	1
v_5	0	0	1
v_6	1	0	1
v_7	1	1	1

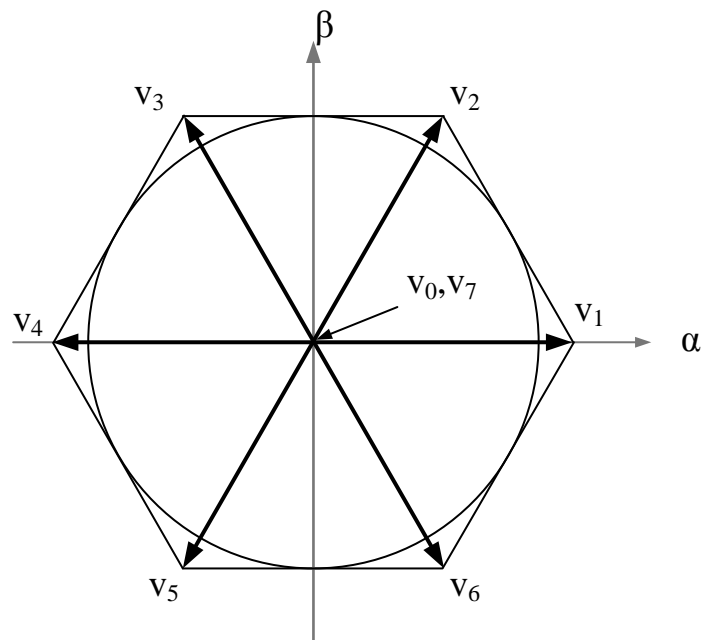


Figure 3.3 Voltage vectors for different switching states.

3.2.1 Natural Reference Frame Model

In the natural reference frame, the instantaneous grid phase voltages are defined as

$$\begin{bmatrix} v_{ga} \\ v_{gb} \\ v_{gc} \end{bmatrix} = \sqrt{\frac{2}{3}} V_L \begin{bmatrix} \cos \omega t \\ \cos(\omega t - 2\pi/3) \\ \cos(\omega t + 2\pi/3) \end{bmatrix} \quad (3.2)$$

where V_L is the rms value of the grid line-to-line voltage.

The inverter phase voltages are given by

$$\begin{bmatrix} v_{inva} \\ v_{invb} \\ v_{invc} \end{bmatrix} = \frac{1}{2} v_{dc} \begin{bmatrix} S_a \\ S_b \\ S_c \end{bmatrix} \quad (3.3)$$

The voltage across the filter capacitor is given by

$$\begin{bmatrix} v_{Cfa} \\ v_{Cfb} \\ v_{Cfc} \end{bmatrix} = \begin{bmatrix} v_{inva} \\ v_{invb} \\ v_{invc} \end{bmatrix} - R_1 \begin{bmatrix} i_{L1a} \\ i_{L1b} \\ i_{L1c} \end{bmatrix} - L_1 \frac{d}{dt} \begin{bmatrix} i_{L1a} \\ i_{L1b} \\ i_{L1c} \end{bmatrix} \quad (3.4)$$

It can also be given by

$$\begin{bmatrix} v_{Cfa} \\ v_{Cfb} \\ v_{Cfc} \end{bmatrix} = \begin{bmatrix} v_{ga} \\ v_{gb} \\ v_{gc} \end{bmatrix} + R_2 \begin{bmatrix} i_{L2a} \\ i_{L2b} \\ i_{L2c} \end{bmatrix} + L_2 \frac{d}{dt} \begin{bmatrix} i_{L2a} \\ i_{L2b} \\ i_{L2c} \end{bmatrix} \quad (3.5)$$

where $\begin{bmatrix} i_{L1a} \\ i_{L1b} \\ i_{L1c} \end{bmatrix}$ is the inverter side current vector, $\begin{bmatrix} i_{L2a} \\ i_{L2b} \\ i_{L2c} \end{bmatrix}$ is the grid side current vector.

The filter capacitor current is given by

$$\begin{bmatrix} i_{Cfa} \\ i_{Cfb} \\ i_{Cfc} \end{bmatrix} = C_f \frac{d}{dt} \begin{bmatrix} v_{Cfa} \\ v_{Cfb} \\ v_{Cfb} \end{bmatrix} \quad (3.6)$$

Alternatively it can be given by

$$\begin{bmatrix} i_{Cfa} \\ i_{Cfb} \\ i_{Cfc} \end{bmatrix} = \begin{bmatrix} i_{L1a} \\ i_{L1b} \\ i_{L1c} \end{bmatrix} - \begin{bmatrix} i_{L2a} \\ i_{L2b} \\ i_{L2c} \end{bmatrix} \quad (3.7)$$

Assuming the power losses are negligible, the current from the PV array is related to the current through the dc link capacitor and the current through the inverter side inductor by

$$i_{PV} = C_d \frac{dv_{dc}}{dt} + S_a i_{L1a} + S_b i_{L1b} + S_c i_{L1c} \quad (3.8)$$

The differential equations (3.4) to (3.8) are converted from the time domain to the frequency domain using the Laplace transform. The frequency domain equations are given below.

The voltage across the filter capacitor can be expressed in terms of the inverter voltage as

$$\begin{bmatrix} V_{Cfa}(s) \\ V_{Cfb}(s) \\ V_{Cfc}(s) \end{bmatrix} = \begin{bmatrix} V_{inva}(s) \\ V_{invb}(s) \\ V_{invc}(s) \end{bmatrix} - R_1 \begin{bmatrix} I_{L1a}(s) \\ I_{L1b}(s) \\ I_{L1c}(s) \end{bmatrix} - sL_1 \begin{bmatrix} I_{L1a}(s) \\ I_{L1b}(s) \\ I_{L1c}(s) \end{bmatrix} \quad (3.9)$$

It can also be expressed in terms of the grid voltage as

$$\begin{bmatrix} V_{Cfa}(s) \\ V_{Cfb}(s) \\ V_{Cfc}(s) \end{bmatrix} = \begin{bmatrix} V_{ga}(s) \\ V_{gb}(s) \\ V_{gc}(s) \end{bmatrix} + R_2 \begin{bmatrix} I_{L2a}(s) \\ I_{L2b}(s) \\ I_{L2c}(s) \end{bmatrix} + sL_2 \begin{bmatrix} I_{L2a}(s) \\ I_{L2b}(s) \\ I_{L2c}(s) \end{bmatrix} \quad (3.10)$$

The filter capacitor current can be expressed in terms of the capacitor voltage as

$$\begin{bmatrix} I_{Cfa}(s) \\ I_{Cfb}(s) \\ I_{Cfc}(s) \end{bmatrix} = sC_f \begin{bmatrix} V_{Cfa}(s) \\ V_{Cfb}(s) \\ V_{Cfc}(s) \end{bmatrix} \quad (3.11)$$

It can also be expressed in terms of the inverter current and the grid current as

$$\begin{bmatrix} I_{Cfa}(s) \\ I_{Cfb}(s) \\ I_{Cfc}(s) \end{bmatrix} = \begin{bmatrix} I_{L1a}(s) \\ I_{L1b}(s) \\ I_{L1c}(s) \end{bmatrix} - \begin{bmatrix} I_{L2a}(s) \\ I_{L2b}(s) \\ I_{L2c}(s) \end{bmatrix} \quad (3.12)$$

The PV current, the DC link capacitor currents and the AC currents are related by

$$I_{PV}(s) = sC_d V_{dc}(s) + S_a I_{L1a}(s) + S_b I_{L1b}(s) + S_c I_{L1c}(s) \quad (3.13)$$

Using equations (3.9) to (3.13) the block diagram of the grid-connected VSC in the natural reference frame is developed and given in Figure 3.4.

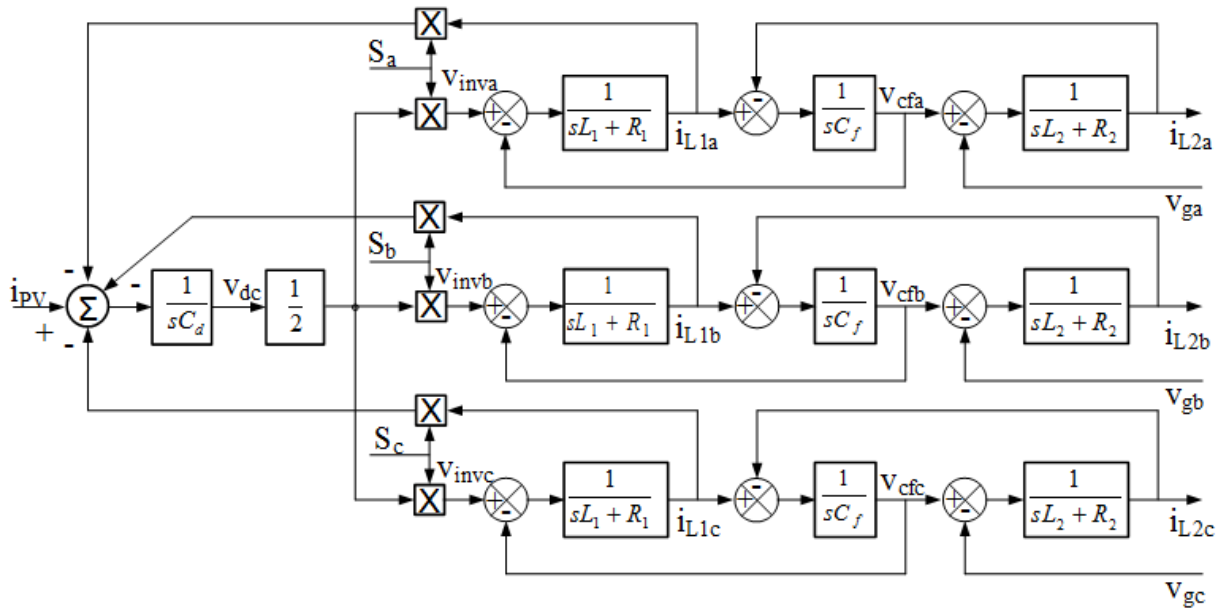


Figure 3.4 Block diagram of the natural reference frame model.

3.2.2 Stationary Reference Frame Model

The model can be simplified by applying the Clarke transformation to obtain the model in the stationary reference frame. The general form of the amplitude invariant Clarke transformation is

$$\begin{bmatrix} x_\alpha \\ x_\beta \end{bmatrix} = \frac{2}{3} \begin{bmatrix} 1 & -\frac{1}{2} & -\frac{1}{2} \\ 0 & \frac{\sqrt{3}}{2} & -\frac{\sqrt{3}}{2} \end{bmatrix} \begin{bmatrix} x_a \\ x_b \\ x_c \end{bmatrix} \quad (3.14)$$

The inverter voltage is given in terms of the DC voltage and the switching functions as shown below.

$$\begin{bmatrix} v_{inv\alpha} \\ v_{inv\beta} \end{bmatrix} = \frac{1}{2} v_{dc} \begin{bmatrix} S_\alpha \\ S_\beta \end{bmatrix} \quad (3.15)$$

where $\begin{bmatrix} S_\alpha \\ S_\beta \end{bmatrix} = \begin{bmatrix} 1/3(2S_a - S_b - S_c) \\ 1/\sqrt{3}(S_b - S_c) \end{bmatrix}$ is the switching function vector.

The voltage across the filter capacitor is given in terms of the inverter voltage by

$$\begin{bmatrix} v_{Cf\alpha} \\ v_{Cf\beta} \end{bmatrix} = \begin{bmatrix} v_{inv\alpha} \\ v_{inv\beta} \end{bmatrix} - L_1 \frac{d}{dt} \begin{bmatrix} i_{L1\alpha} \\ i_{L1\beta} \end{bmatrix} - R_1 \begin{bmatrix} i_{L1\alpha} \\ i_{L1\beta} \end{bmatrix} \quad (3.16)$$

It can also be given in terms of the grid voltage by

$$\begin{bmatrix} v_{Cf\alpha} \\ v_{Cf\beta} \end{bmatrix} = \begin{bmatrix} v_{g\alpha} \\ v_{g\beta} \end{bmatrix} + L_2 \frac{d}{dt} \begin{bmatrix} i_{L2\alpha} \\ i_{L2\beta} \end{bmatrix} + R_2 \begin{bmatrix} i_{L2\alpha} \\ i_{L2\beta} \end{bmatrix} \quad (3.17)$$

The filter capacitor current is given in terms of the capacitor voltage by

$$\begin{bmatrix} i_{Cf\alpha} \\ i_{Cf\beta} \end{bmatrix} = C_f \frac{d}{dt} \begin{bmatrix} v_{Cf\alpha} \\ v_{Cf\beta} \end{bmatrix} \quad (3.18)$$

It can also be given in terms of the inverter current and the grid current as

$$\begin{bmatrix} i_{Cf\alpha} \\ i_{Cf\beta} \end{bmatrix} = \begin{bmatrix} i_{L1\alpha} \\ i_{L1\beta} \end{bmatrix} - \begin{bmatrix} i_{L2\alpha} \\ i_{L2\beta} \end{bmatrix} \quad (3.19)$$

The PV current, the DC capacitor current and the AC currents are related by

$$i_{PV} = C_d \frac{dv_{dc}}{dt} + S_\alpha i_{L1\alpha} + S_\beta i_{L1\beta} \quad (3.20)$$

Applying the Laplace transform to the differential equations (3.16) to (3.20) the frequency domain equations below are obtained.

The filter capacitor voltage is given in terms of the inverter voltage by

$$\begin{bmatrix} V_{Cf\alpha}(s) \\ V_{Cf\beta}(s) \end{bmatrix} = \begin{bmatrix} V_{inv\alpha}(s) \\ V_{inv\beta}(s) \end{bmatrix} - sL_1 \begin{bmatrix} I_{L1\alpha}(s) \\ I_{L1\beta}(s) \end{bmatrix} - R_1 \begin{bmatrix} I_{L1\alpha}(s) \\ I_{L1\beta}(s) \end{bmatrix} \quad (3.21)$$

It is also given in terms of the grid voltage by

$$\begin{bmatrix} V_{Cf\alpha}(s) \\ V_{Cf\beta}(s) \end{bmatrix} = \begin{bmatrix} V_{g\alpha}(s) \\ V_{g\beta}(s) \end{bmatrix} + sL_2 \begin{bmatrix} I_{L2\alpha}(s) \\ I_{L2\beta}(s) \end{bmatrix} + R_2 \begin{bmatrix} I_{L2\alpha}(s) \\ I_{L2\beta}(s) \end{bmatrix} \quad (3.22)$$

The filter capacitor current is given in terms of the capacitor voltage by

$$\begin{bmatrix} I_{Cf\alpha}(s) \\ I_{Cf\beta}(s) \end{bmatrix} = sC_f \begin{bmatrix} V_{Cf\alpha}(s) \\ V_{Cf\beta}(s) \end{bmatrix} \quad (3.23)$$

It is also given in terms of the inverter current and the grid current by

$$\begin{bmatrix} I_{Cf\alpha}(s) \\ I_{Cf\beta}(s) \end{bmatrix} = \begin{bmatrix} I_{L1\alpha}(s) \\ I_{L1\beta}(s) \end{bmatrix} - \begin{bmatrix} I_{L2\alpha}(s) \\ I_{L2\beta}(s) \end{bmatrix} \quad (3.24)$$

Assuming the power losses are negligible, the source current, the DC capacitor current and the inverter currents are related by

$$I_{PV}(s) = sC_d V_{dc}(s) + S_\alpha I_{L1\alpha}(s) + S_\beta I_{L1\beta}(s) \quad (3.25)$$

The block diagram of the stationary reference frame model obtained using the equations (3.21) to (3.25) is given in Figure 3.5

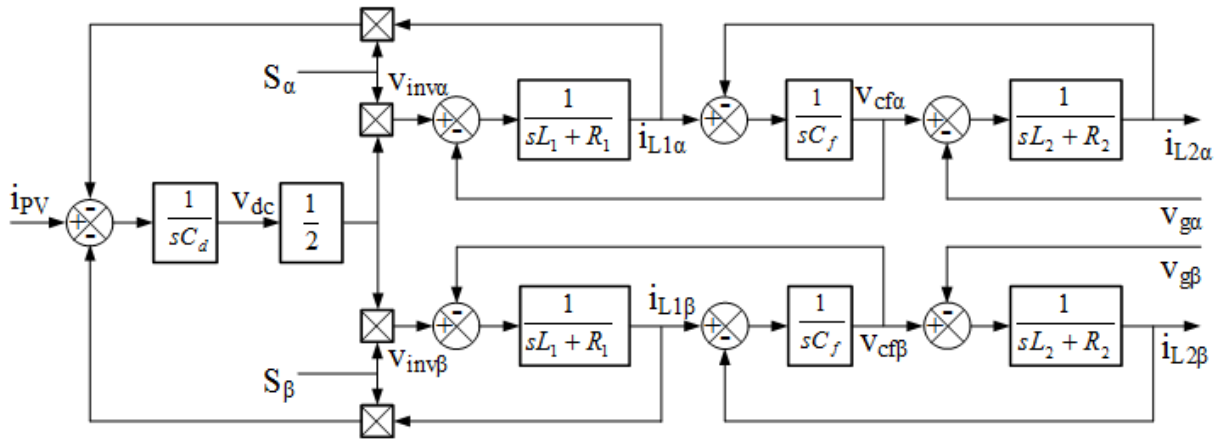


Figure 3.5 Block diagram of stationary reference frame model.

3.2.3 Synchronous Reference Frame Model

The synchronous reference frame model is obtained by multiplying the space vectors in the stationary reference frame by $e^{-j\theta_v}$, where θ_v is the angle of the grid voltage vector. This aligns the grid voltage vector with the d-axis, and the component of the grid voltage vector on the q-axis is zero. Both axes rotate at synchronous speed hence the name. This is called the Park transformation and in matrix form it is given by

$$\begin{bmatrix} x_d \\ x_q \end{bmatrix} = \begin{bmatrix} \cos \theta_v & \sin \theta_v \\ -\sin \theta_v & \cos \theta_v \end{bmatrix} \begin{bmatrix} x_\alpha \\ x_\beta \end{bmatrix} \quad (3.26)$$

The equations for the voltages and currents in the rotating reference frame are given below.

The inverter voltage is given by

$$\begin{bmatrix} v_{invd} \\ v_{invq} \end{bmatrix} = \frac{1}{2} v_{dc} \begin{bmatrix} S_d \\ S_q \end{bmatrix} \quad (3.27)$$

where S_d and S_q are the switching functions in the synchronous reference frame.

The voltage across the filter capacitor is given in terms of the inverter voltage by

$$\begin{bmatrix} v_{Cfd} \\ v_{Cfq} \end{bmatrix} = \begin{bmatrix} v_{invd} \\ v_{invq} \end{bmatrix} - L_1 \frac{d}{dt} \begin{bmatrix} i_{L1d} \\ i_{L1q} \end{bmatrix} + \omega L_1 \begin{bmatrix} -i_{L1q} \\ i_{L1d} \end{bmatrix} - R_1 \begin{bmatrix} i_{L1d} \\ i_{L1q} \end{bmatrix} \quad (3.28)$$

Alternatively it can be given in terms of the grid voltage by

$$\begin{bmatrix} v_{Cfd} \\ v_{Cfq} \end{bmatrix} = \begin{bmatrix} v_{gd} \\ 0 \end{bmatrix} + L_2 \frac{d}{dt} \begin{bmatrix} i_{L2d} \\ i_{L2q} \end{bmatrix} - \omega L_2 \begin{bmatrix} -i_{L2q} \\ i_{L2d} \end{bmatrix} + R_2 \begin{bmatrix} i_{L2d} \\ i_{L2q} \end{bmatrix} \quad (3.29)$$

The terms $\omega L_1 i_{L1d}$ and $\omega L_1 i_{L1q}$, in equation (3.28) and $\omega L_2 i_{L2d}$ and $\omega L_2 i_{L2q}$, in equation (3.29) are called the cross-coupling terms and show the coupling between the d-axis and the q-axis components.

The filter capacitor current is given in terms of the capacitor voltage by

$$\begin{bmatrix} i_{Cfd} \\ i_{Cfq} \end{bmatrix} = C_f \frac{d}{dt} \begin{bmatrix} v_{Cfd} \\ v_{Cfq} \end{bmatrix} \quad (3.30)$$

It is also given in terms of the inverter current and the grid current by

$$\begin{bmatrix} i_{Cfd} \\ i_{Cfq} \end{bmatrix} = \begin{bmatrix} i_{L1d} \\ i_{L1q} \end{bmatrix} - \begin{bmatrix} i_{L2d} \\ i_{L2q} \end{bmatrix} \quad (3.31)$$

The PV current and the inverter current are related by the equation below.

$$i_{PV} = C_d \frac{dv_{dc}}{dt} + S_d i_{L1d} + S_q i_{L1q} \quad (3.32)$$

Applying the Laplace transform to the differential equations (3.28) to (3.32) we obtain the frequency domain equations below.

The filter capacitor voltage is given in terms of the inverter voltage by

$$\begin{bmatrix} V_{Cfd}(s) \\ V_{Cfq}(s) \end{bmatrix} = \begin{bmatrix} V_{invd}(s) \\ V_{invq}(s) \end{bmatrix} - sL_1 \begin{bmatrix} I_{L1d}(s) \\ I_{L1q}(s) \end{bmatrix} + \omega L_1 \begin{bmatrix} I_{L1d}(s) \\ -I_{L1q}(s) \end{bmatrix} - R_1 \begin{bmatrix} I_{L1d}(s) \\ I_{L1q}(s) \end{bmatrix} \quad (3.33)$$

It can also be given in terms of the grid voltage by

$$\begin{bmatrix} V_{Cfd}(s) \\ V_{Cfq}(s) \end{bmatrix} = \begin{bmatrix} V_{gd}(s) \\ 0 \end{bmatrix} + sL_2 \begin{bmatrix} I_{L2d}(s) \\ I_{L2q}(s) \end{bmatrix} - \omega L_2 \begin{bmatrix} I_{L2d}(s) \\ -I_{L2q}(s) \end{bmatrix} + R_2 \begin{bmatrix} I_{L2d}(s) \\ I_{L2q}(s) \end{bmatrix} \quad (3.34)$$

The filter capacitor current is given in terms of the capacitor voltage by

$$\begin{bmatrix} I_{Cfd}(s) \\ I_{Cfq}(s) \end{bmatrix} = sC_f \begin{bmatrix} V_{Cfd}(s) \\ V_{Cfq}(s) \end{bmatrix} \quad (3.35)$$

It can also be given in terms of the inverter current and the grid current by

$$\begin{bmatrix} I_{Cfd}(s) \\ I_{Cfq}(s) \end{bmatrix} = \begin{bmatrix} I_{L1d}(s) \\ I_{L1q}(s) \end{bmatrix} - \begin{bmatrix} I_{L2d}(s) \\ I_{L2q}(s) \end{bmatrix} \quad (3.36)$$

The PV current and the inverter currents are related by

$$I_{PV}(s) = sC_d V_{dc}(s) + S_d I_{L1d}(s) + S_q I_{L1q}(s) \quad (3.37)$$

The block diagram of the synchronous reference frame model derived from equations (3.33) to (3.37) is given in Figure 3.6.

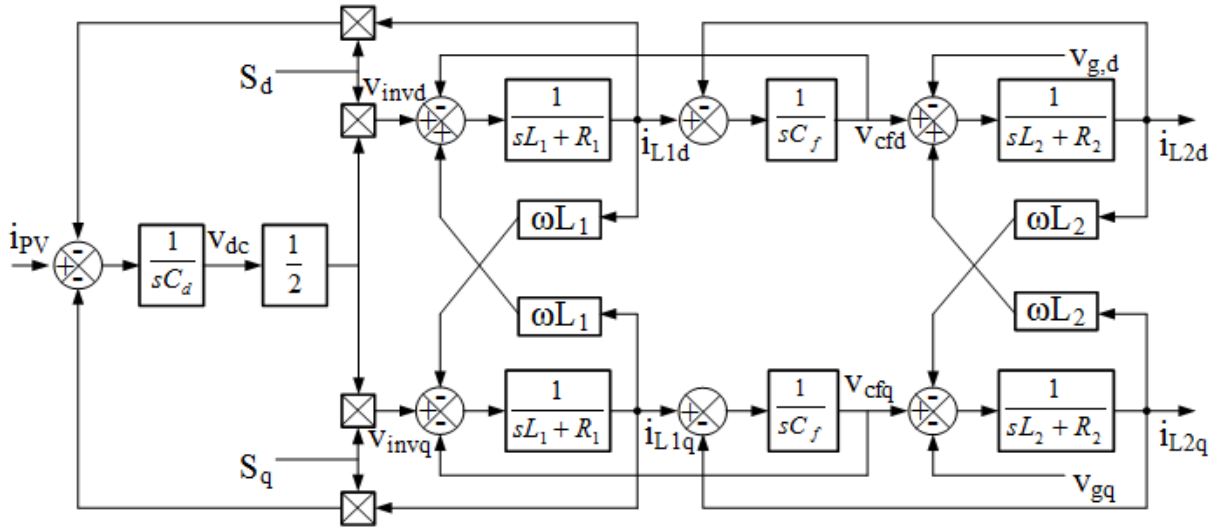


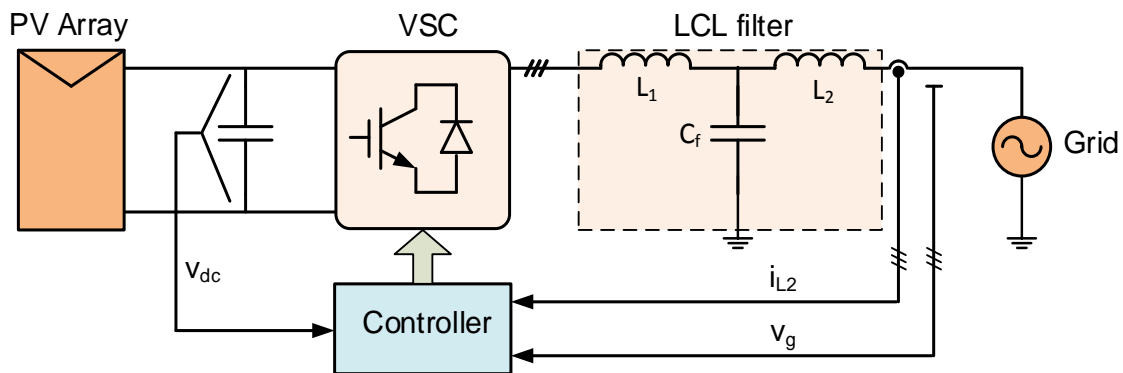
Figure 3.6 Block diagram of synchronous reference frame model.

3.3 Stability Analysis of Power Control Loop

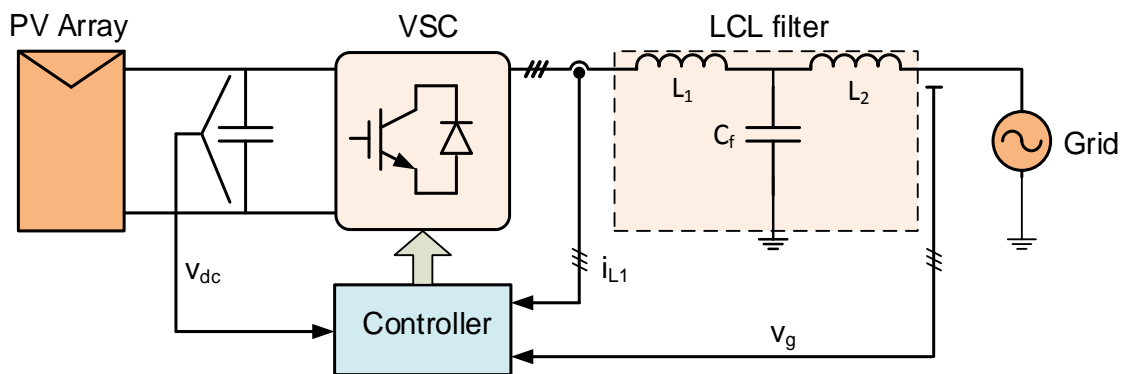
In a grid-connected VSC with an LCL filter, the current sensors can be on the grid side or on the inverter side as shown in Figure 3.7 (a) and Figure 3.7 (b), respectively. For each choice of current sensor position it is important to thoroughly investigate the stability of the system, as the LCL filter causes controller instability at the resonance frequency. In literature, stable operation without damping has been reported for current sensors on the grid-side for a PWM rectifier [115], and with current sensors on the inverter-side for a single-phase inverter [116], and a three-phase inverter [117]. However, there is no detailed stability analysis in [116] and [117] and a notch-filter is used to enhance the damping in [117]. In [115] stability analysis is performed and compared to the passively damped case. In this section the stability analysis of the power control loop is performed to independently verify the stability for both current sensor positions. The closed-loop transfer function for the active power control loop is derived in the Laplace domain, and

converted to the z-domain for stability analysis using pole-zero plots. The following assumptions are made in the analysis:

- The system is linear and time-invariant.
- The effect of the grid voltage and the grid impedance is neglected so the system can be considered as a single-input, single-output system.
- The resistance of the filter inductors is neglected.
- The dead time of the converter PWM is neglected.
- The dynamics of the dc link are not included.
-



(a)



(b)

Figure 3.7 Grid-connected VSC with (a) current sensors on the grid side (b) current sensors on the inverter side.

3.3.1 With Current Sensors on the Grid-side with No Damping

Having the current sensors on the grid side allows for accurate estimation of the instantaneous active and reactive powers at the point of common coupling and is, therefore, a good choice of the current sensor position. This is because the voltage sensors are located on the grid side to synchronize the control with the grid voltage vector. Therefore, the estimated powers will be equal to the actual powers at the point of common coupling (PCC).

The block diagram of the power control loop is shown in Figure 3.8. This is based on the virtual-flux direct power control with space vector modulation. The active power which is the controlled variable is calculated by multiplying the grid-side current and the grid virtual-flux, which is assumed to have constant amplitude. The calculated active power is given by [118]

$$p = \frac{3}{2} |\underline{\Psi}_g| I_{L2}(s) \quad (3.38)$$

where $|\underline{\Psi}_g|$ is the magnitude of the grid virtual flux vector scaled to be equal to the grid voltage.

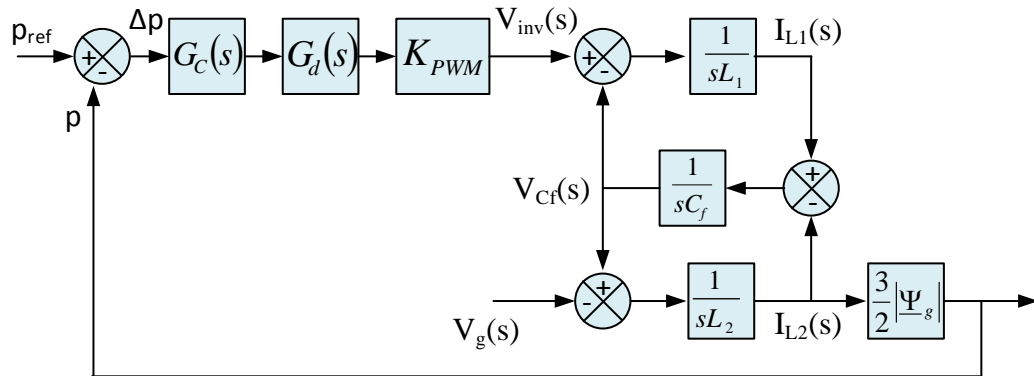


Figure 3.8 Block diagram of power control loop with current sensors on the grid-side.

The reference active power p_{ref} is compared to the calculated active power p and the difference Δp is fed to a PI controller.

The transfer function of the PI controller, $G_C(s)$ is expressed as

$$G_C(s) = \frac{K_p s + K_i}{s} \quad (3.39)$$

where K_p is the proportional gain and K_i is the integral gain.

The controller is implemented in digital form and the delay due to the sampling, computations and PWM has to be accounted for. The total delay is assumed to be $1.5T_s$, where T_s is the sample time, with the sampling and computation accounting for a delay of T_s and the PWM accounting for a delay of $0.5T_s$ [29]. The transfer function for the delay is given by

$$G_d(s) = \frac{1}{1.5T_s s + 1} \quad (3.40)$$

The VSC is represented as a unit gain, given by K_{PWM} in Figure 3.8.

The transfer function of the LCL filter with the inverter voltage as the input and the grid-side current as the output is derived to give

$$G_{LCL}(s) = \frac{I_{L2}(s)}{V_{inv}(s)} = \frac{1}{L_1 s} \frac{\omega_{LC}^2}{s^2 + \omega_{res}^2} \quad (3.41)$$

where $\omega_{res} = \sqrt{\frac{L_1 + L_2}{L_1 L_2 C_f}}$ is the resonance frequency of the LCL filter and $\omega_{LC} = \frac{1}{\sqrt{L_2 C_f}}$.

The open-loop transfer function is given by

$$G_{OL}(s) = \frac{p(s)}{\Delta p(s)} = G_C(s) G_d(s) K_{PWM} G_{LCL}(s) \frac{3}{2} |\underline{\Psi}_g| \quad (3.42)$$

Setting the integral gain of the PI controller to zero, and substituting equations (3.38) to (3.41) into equation (3.42) we obtain

$$G_{OL}(s) = \frac{1.5K_p K_{PWM} \omega_{LC}^2 |\underline{\Psi}_g| s}{L_1 (1.5T_s s^5 + s^4 + 1.5T_s \omega_{res}^2 s^3 + \omega_{res}^2 s^2)} \quad (3.43)$$

The closed-loop transfer function is given by

$$G_{CL}(s) = \frac{p(s)}{p_{ref}(s)} = \frac{G_{OL}(s)}{1 + G_{OL}(s)} \quad (3.44)$$

Substituting equation (3.43) into equation (3.44) and recalling that $K_{PWM} = 1$, the closed-loop transfer function is obtained as

$$G_{CL}(s) = \frac{1.5K_p \omega_{LC}^2 \left| \underline{\Psi}_g \right|_s}{1.5T_s L_1 s^5 + L_1 s^4 + 1.5T_s L_1 \omega_{res}^2 s^3 + L_1 \omega_{res}^2 s^2 + 1.5K_p \omega_{LC}^2 \left| \underline{\Psi}_g \right|_s} \quad (3.45)$$

To analyze the stability of the closed-loop transfer function in the z-plane it is converted from continuous form to discrete form. This can be done using the 'c2d' function in Matlab with a suitable discretization method. Common methods include, zero-order hold, first-order hold, impulse-invariant mapping, Tustin approximation (bilinear transformation) and zero-pole matching equivalents [119]. The Tustin approximation is chosen due to its ability to produce a good match in the frequency domain between the continuous and the discrete models, and the left-hand side of the s-plane is mapped within the unit circle in the z-plane [120]. The discretization is given by

$$G_{CL}(z) = G_{CL}(s) \Big|_{s = \frac{2}{T_s} \frac{z-1}{z+1}} \quad (3.46)$$

where T_s is the sample time.

The pole-zero plot of the resulting discrete transfer function is shown in Figure 3.9 for values of K_p increasing from 0.1 to 1. The closed-loop transfer function is a fifth order system with a pole on the boundary of the unit circle, a pole-pair inside the unit circle, and a pole-pair outside the unit circle. The pole-pair outside the unit circle causes the system to be unstable and increasing K_p causes the poles to move further outside the unit circle, thus the PI controller cannot be tuned to obtain stability in this case.

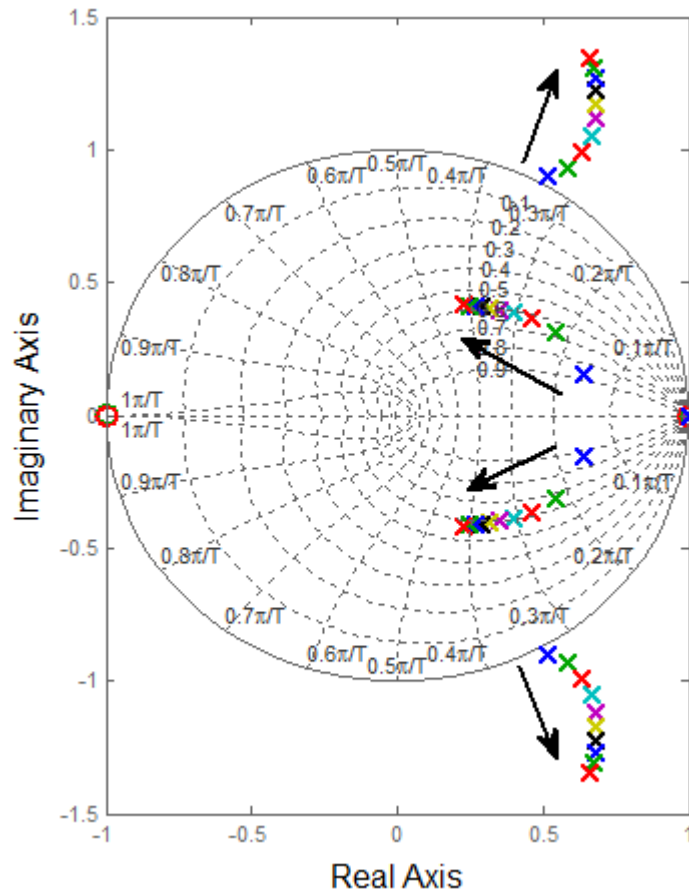


Figure 3.9 Pole-zero plots for the power control loop with undamped LCL filter with current sensors on the grid-side and varying K_p (arrows indicate increasing K_p).

3.3.2 With Current Sensors on the Grid-side with Passive Damping

A common method used to improve the system stability is to connect a damping resistor in series with the filter capacitor. This is called passive damping. The block diagram of power control loop with a passively damped LCL filter is shown in Figure 3.10.

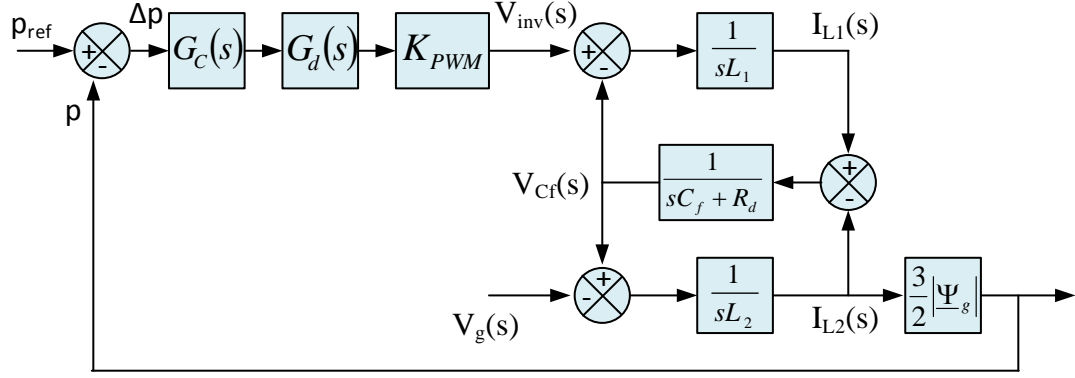


Figure 3.10 Block diagram of power control loop with current sensors on the grid-side and passively damped LCL filter.

The transfer function of the passively damped LCL filter is given by

$$G_{LCD}(s) = \frac{I_{L2}(s)}{V_{inv}(s)} = \frac{1}{L_1} \frac{C_f R_d \omega_{LC}^2 s + \omega_{LC}^2}{s^2 + C_f R_d \omega_{res}^2 s + \omega_{res}^2} \quad (3.47)$$

With the integral gain set to zero, the open-loop transfer function is obtained in the same way as in sub-section 3.3.1, to give

$$G_{OLD} = \frac{1.5 |\underline{\Psi}_g| (K_p C_f R_d \omega_{LC}^2 s^2 + K_p \omega_{LC}^2 s)}{L_1 [1.5 T_s s^5 + (1.5 T_s C_f R_d \omega_{res}^2 + 1) s^4 + (1.5 T_s + C_f R_d) \omega_{res}^2 s^3 + \omega_{res}^2 s^2]} \quad (3.48)$$

Similarly the closed-loop transfer function is obtained as

$$G_{CLD}(s) = \frac{1.5 |\underline{\Psi}_g| (K_p C_f R_d \omega_{LC}^2 s^2 + K_p \omega_{LC}^2 s)}{1.5 T_s L_1 s^5 + A L_1 s^4 + B L_1 \omega_{res}^2 s^3 + C s^2 + 1.5 |\underline{\Psi}_g| K_p \omega_{LC}^2 s} \quad (3.49)$$

where $A = 1.5 T_s C_f R_d \omega_{res}^2 + 1$; $B = 1.5 T_s + C_f R_d$; $C = \omega_{res}^2 L_1 + 1.5 |\underline{\Psi}_g| K_p C_f R_s \omega_{LC}^2$.

The closed-loop transfer function is converted to discrete form and the stability of the system is analyzed using pole-zero plots for different values of gain K_p . To further illustrate the effect of the chosen value of damping resistor on the system stability, the system is analyzed for different values of damping resistor. There is no universally agreed method of determining the damping resistor, with some publications such as [121], [122] proposing a damping resistance of

$$R_d = \frac{1}{3 \omega_{res} C_f} \quad (3.50)$$

Starting with the resistance given by equation (3.50), the proportional gain is varied from 1 to 10. The resulting pole-zero plot are shown in Figure 3.11. With the low resistance of equation (3.50) the system is only stable for low values of K_p and becomes unstable for $K_p > 2$. This is because a pair of complex poles which is inside the unit circle for low values of K_p moves outside the unit circle as K_p is increased. Another pair of complex poles stays within the unit circle for all values of K_p and a real pole at the boundary of the unit circle is not affected by the variation of K_p .

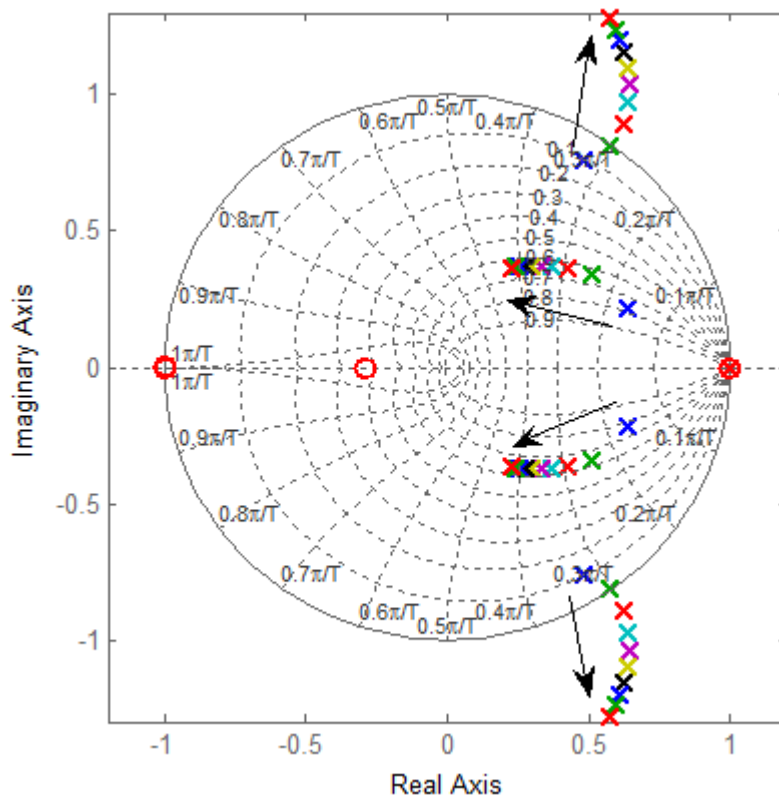


Figure 3.11 Pole-zero plots for the power control loop with passively damped LCL filter with varying K_p for a damping resistor of $R_d = 1/(3\omega_{res} C_f)$.

To determine the effect of a bigger damping resistor on the stability, the damping resistance given by equation (3.50) is increased by 10 times. The proportional gain is varied from 1 to 10 and the pole-zero plot is given in Figure 3.12.

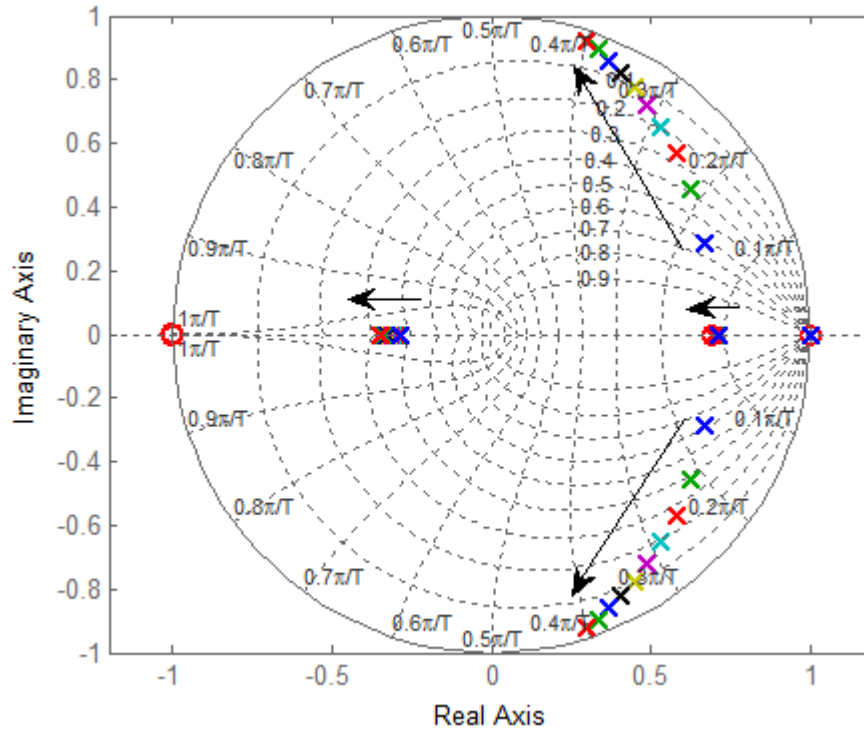


Figure 3.12 Pole-zero plots for the power control loop with passively damped LCL filter with varying K_p for a damping resistor of $R_d = 10/(3\omega_{res}C_f)$.

With the higher damping resistor, the stability of the system is improved, and it is stable for the range of K_p values used. However, at higher values of K_p , the resonant pole-pair is close to the boundary of the unit circle and there will be oscillations with low damping in the system response. The variation of K_p shows little effect on the other poles.

The step response for the same value of $K_p = 1$ for each of the two damping resistor values is shown in Figure 3.13. The step response for both resistors has the same rise time and the same overshoot. However, with the higher damping resistor, the settling time is shorter. This shows that the stability and dynamic performance of the system will be better with a higher damping resistor. But this is not an optimum solution because of the increased losses and degradation of the filter performance at higher frequencies.

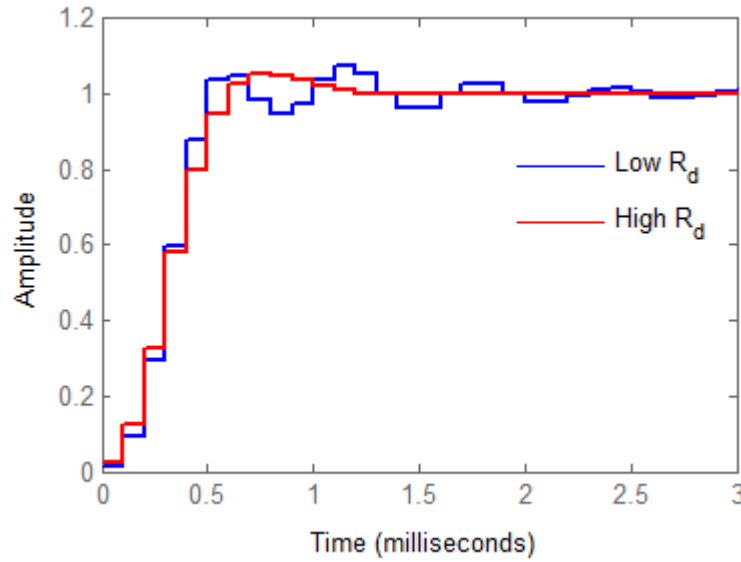


Figure 3.13 Step response for $K_p = 1$ with two different damping resistors.

This shows that using passive damping is effective in making the system stable. The damping resistance should be carefully selected and the PI controller carefully tuned to obtain the required performance. However, care should be taken to minimize the power losses due to the additional resistance. The effect on the frequency response should also be analyzed so that the filter performance does not deteriorate especially at higher frequencies higher than the resonance frequency.

3.3.3 With Current Sensors on the Grid-side with Notch-filter Active Damping

A notch filter can be used as an active damping method, without using any additional sensors. The general transfer function of a second order notch filter is given by

$$G_N(s) = \frac{s^2 + 2\zeta_1\omega_n s + \omega_n^2}{s^2 + 2\zeta_2\omega_n s + \omega_n^2} \quad (3.51)$$

where ζ_1 and ζ_2 are the damping coefficients and ω_n is the natural frequency.

By putting $\omega_n = \omega_{res}$ and $\zeta_1 = 0$, it is possible to cancel out the resonant peak of the LCL filter[112]. The notch filter is positioned between the PI controller and the modulator to eliminate any resonant frequency components from the reference voltage. The transfer function of the implemented notch filter is given by

$$G_N(s) = \frac{s^2 + \omega_{res}^2}{s^2 + 2\zeta_2 \omega_{res} s + \omega_{res}^2} \quad (3.52)$$

The block diagram of the power control loop with the notch filter is shown in Figure 3.14.

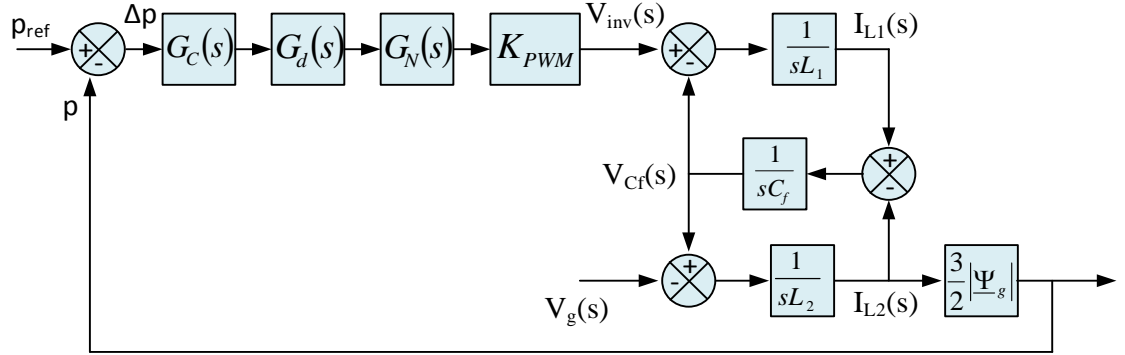


Figure 3.14 Block diagram of power control loop with current sensors on the grid-side and notch filter active damping.

The open-loop transfer function is given by

$$G_{OLN}(s) = \frac{p(s)}{\Delta p(s)} = G_C(s)G_d(s)G_N(s)K_{PWM}G_{LCL}(s)\frac{3}{2}|\underline{\Psi}_g| \quad (3.53)$$

Inserting the individual transfer functions into equation (3.53) we get

$$G_{OLN}(s) = \frac{1.5|\underline{\Psi}_g|K_p\omega_{LC}^2(s^3 + \omega_{res}^2s)}{1.5T_sL_1s^7 + Ds^6 + Gs^5 + Hs^4 + Js^3 + L_1\omega_{res}^4s^2} \quad (3.54)$$

where $D = 3T_s\zeta_2L_1\omega_{res} + L_1$; $G = 3T_sL_1\omega_{res}^2 + 2\zeta_2L_1\omega_{res}$; $H = 3T_s\zeta_2L_1\omega_{res}^3 + 2L_1\omega_{res}^2$;

$$J = 1.5T_sL_1\omega_{res}^2 + 2\zeta_2L_1\omega_{res}^2.$$

Using equation (3.54) the closed-loop transfer function is obtained as

$$G_{CLN}(s) = \frac{1.5|\underline{\Psi}_g|K_p\omega_{LC}^2(s^3 + \omega_{res}^2s)}{1.5T_sL_1s^7 + Ds^6 + Gs^5 + Hs^4 + Ms^3 + L_1\omega_{res}^4s^2} \quad (3.55)$$

where $M = J + 1.5|\underline{\Psi}_g|K_p\omega_{LC}^2$.

To preserve the behaviour of the system at the resonant frequency, the Tustin method with frequency pre-warping is used to discretize the closed-loop transfer function. The transformation is given by

$$G_{CLN}(z) = G_{CLN}(s) \Big|_{s = \frac{\omega}{\tan(\omega T_s/2)} \frac{z-1}{z+1}} \quad (3.56)$$

Where $\omega = \omega_{res}$ is the pre-warping frequency.

The stability of the discrete system is analyzed for values of K_p increasing from 1 to 10 in steps of 1. The pole-zero plot of the discrete transfer function is shown in Figure 3.15.

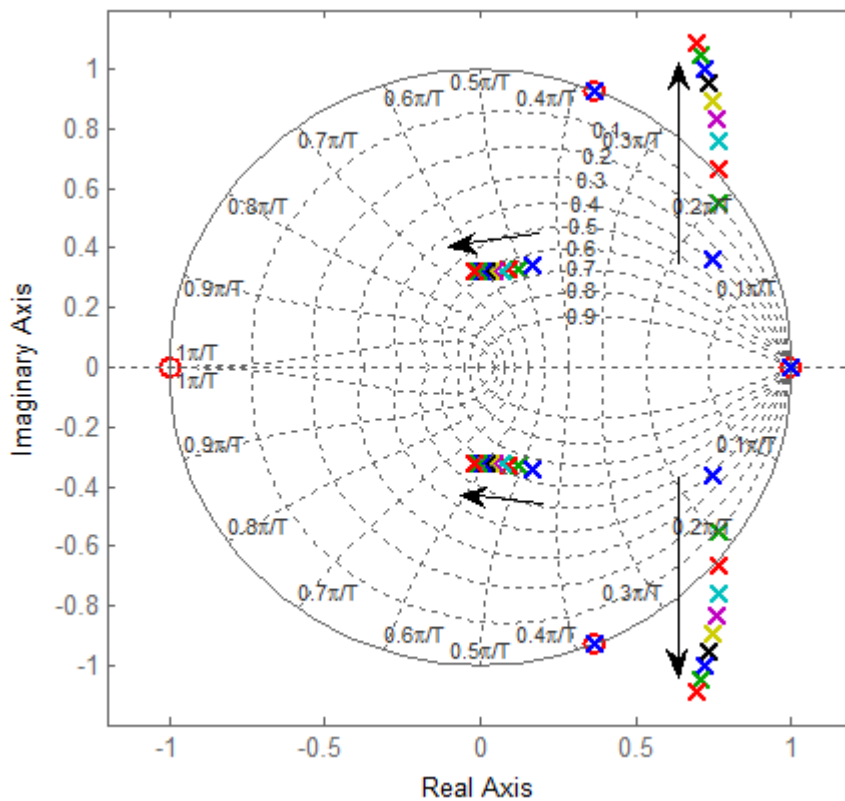


Figure 3.15 Pole-zero plots for the power control loop with notch-filter actively damped LCL filter with varying K_p .

The pole-zero plots shows that there is real pole and a complex pole-pair on the boundary of the unit circle which are not affected by the variation of K_p . The complex poles at the boundary will cause undamped oscillations in the step response of the system. There is a

pair of complex poles which stays within the unit circle for all value of K_p , indicating damped oscillations in the step response. The last pair of complex poles is within the unit circle for low values of K_p but is outside the unit circle for higher values of K_p . This indicates that the system is only stable for values of K_p less than 3. This shows that while the notch filter is able to provide active damping and achieve closed-loop system stability, it only does so within a small range of values of K_p and the tuning process for both the PI controller and the notch filter is tedious.

The step response of the discrete closed-loop system for the stable range of K_p is shown in Figure 3.16. It shows that the oscillations and the overshoot increase as K_p is increased. The increase in the oscillations is because as K_p is increased there is a pair of complex poles getting close to the boundary of the unit circle.

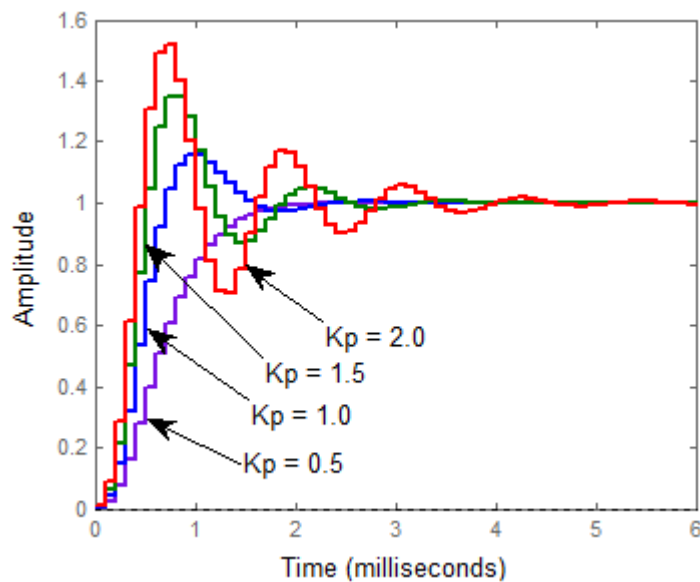


Figure 3.16 Step response of closed-loop discrete system with notch filter for stable range of K_p values.

3.3.4 With Current Sensors on the Inverter-side with No Damping

The fourth case is when the current sensors are on the inverter side with no passive or active damping. The block diagram of the power control loop is shown in Figure 3.17.

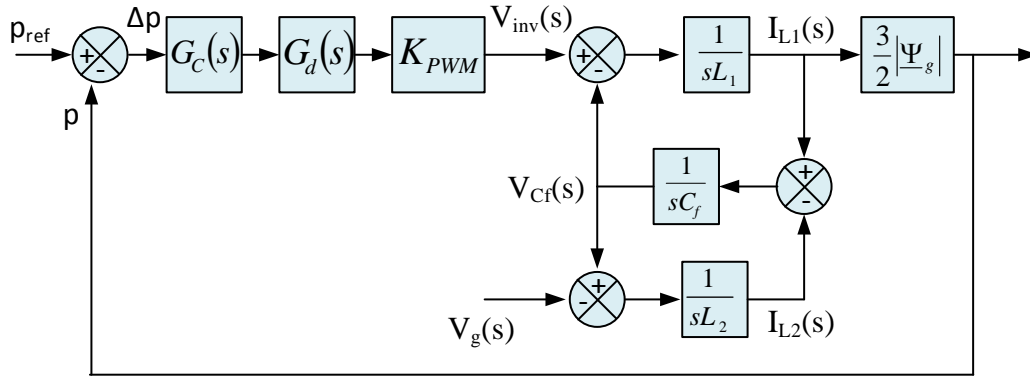


Figure 3.17 Block diagram of power control loop with current sensors on the inverter side with no damping.

The transfer function of the LCL filter when the inverter current is used is given by

$$G_{LCL}(s) = \frac{I_{L1}(s)}{V_{inv}(s)} = \frac{1}{L_1 s} \frac{s^2 + \omega_{LC}^2}{s^2 + \omega_{res}^2} \quad (3.57)$$

The power calculation is performed using the inverter current and the grid virtual flux as shown in the equation below.

$$p = \frac{3}{2} |\underline{\Psi}_g| I_{L1}(s) \quad (3.58)$$

The other components of the system are as defined in section 3.3.1. The open-loop transfer function is given by

$$G_{OLi}(s) = \frac{1.5 |\underline{\Psi}_g| K_p (s^3 + \omega_{LC}^2)}{1.5 L_1 T_s s^5 + L_1 s^4 + 1.5 L_1 T_s \omega_{res}^2 s^3 + \omega_{res} s^2} \quad (3.59)$$

The closed-loop transfer function is given by

$$G_{CLi}(s) = \frac{1.5 |\underline{\Psi}_g| K_p (s^3 + \omega_{LC}^2)}{1.5 L_1 T_s s^5 + L_1 s^4 + N s^3 + \omega_{res} s^2 + 1.5 |\underline{\Psi}_g| K_p \omega_{LC}^2} \quad (3.60)$$

where $N = 1.5(L_1 T_s \omega_{res}^2 + |\underline{\Psi}_g| K_p)$.

The closed-loop transfer function is converted to discrete form using the Tustin method. The pole-zero plots of the discretized transfer function for values of K_p ranging from 1 to 10 is shown in Figure 3.18. There is a real pole at the boundary of the unit circle which is not affected by the variation of K_p . Two complex pole pairs are affected by the variation

in K_p . The first pair of poles is at the boundary of the unit circle for low values of K_p and increasing K_p causes the poles to move away from the boundary of the unit circle. This pole pair will cause undamped oscillations in the step response of the system for low values of K_p . The second complex pair of poles is inside the unit circle for low values of K_p and moves towards the boundary with increasing values of K_p . This would cause undamped oscillations for higher values of K_p . The system will therefore be stable for all values of K_p considered, but care should be taken when tuning the controller to avoid excessive oscillations in the dynamic response.

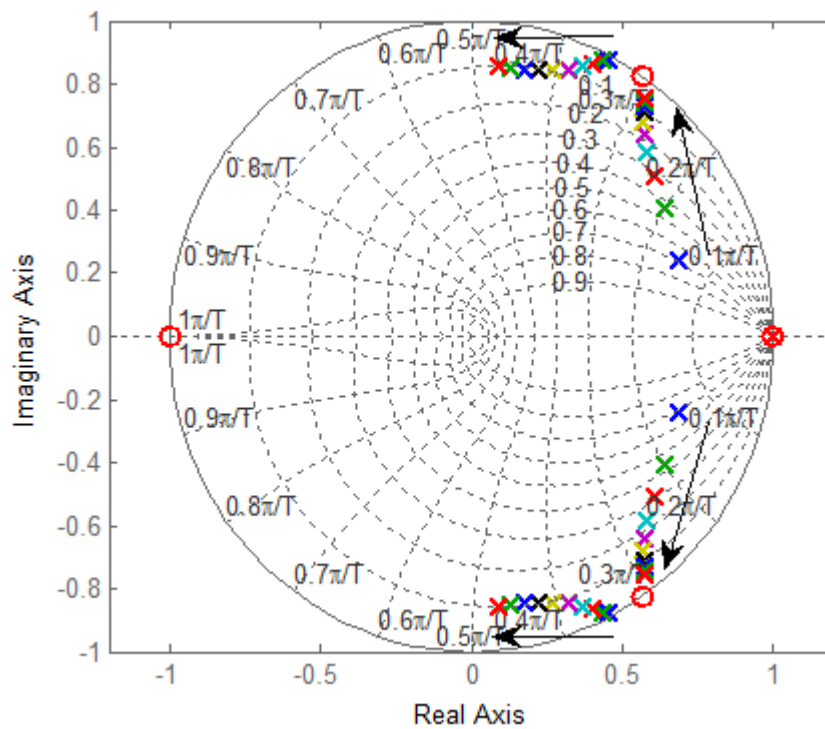


Figure 3.18 Pole-zero plots for the power control loop for undamped LCL filter with current sensors on the inverter side for varying K_p .

The step response of the discrete closed-loop system is shown in Figure 3.19 for four different values of K_p . For the range of values of K_p considered, the step response shows oscillations due to the complex poles near the boundary of the unit circle. The settling of the oscillations between $t = 5\text{ms}$ and $t = 7\text{ms}$ is shown in the zoomed in rectangle. For $K_p = 1$, there are sustained oscillations of amplitude 1.8%. For $K_p = 4$ there are damped

oscillations whose amplitude decreases from 2 % at $t = 5 \text{ ms}$, to 0.71 % at $t = 7 \text{ ms}$. For $K_p = 7$ the oscillations are negligible while for $K_p = 10$, the oscillations decrease from 1 % at $t = 5 \text{ ms}$ to 0.25 % at $t = 7 \text{ ms}$. Thus, for the range of K_p values considered, it can be concluded that lower values result in more sustained oscillations than higher values. The best performance in terms of damping of oscillations is obtained with $K_p = 7$.

From the analysis in this section it can be concluded that having the current sensors on the inverter side leads to stable operation of the system without any damping. There is no added complexity to the system, and the tuning process of the controller is relatively easy.

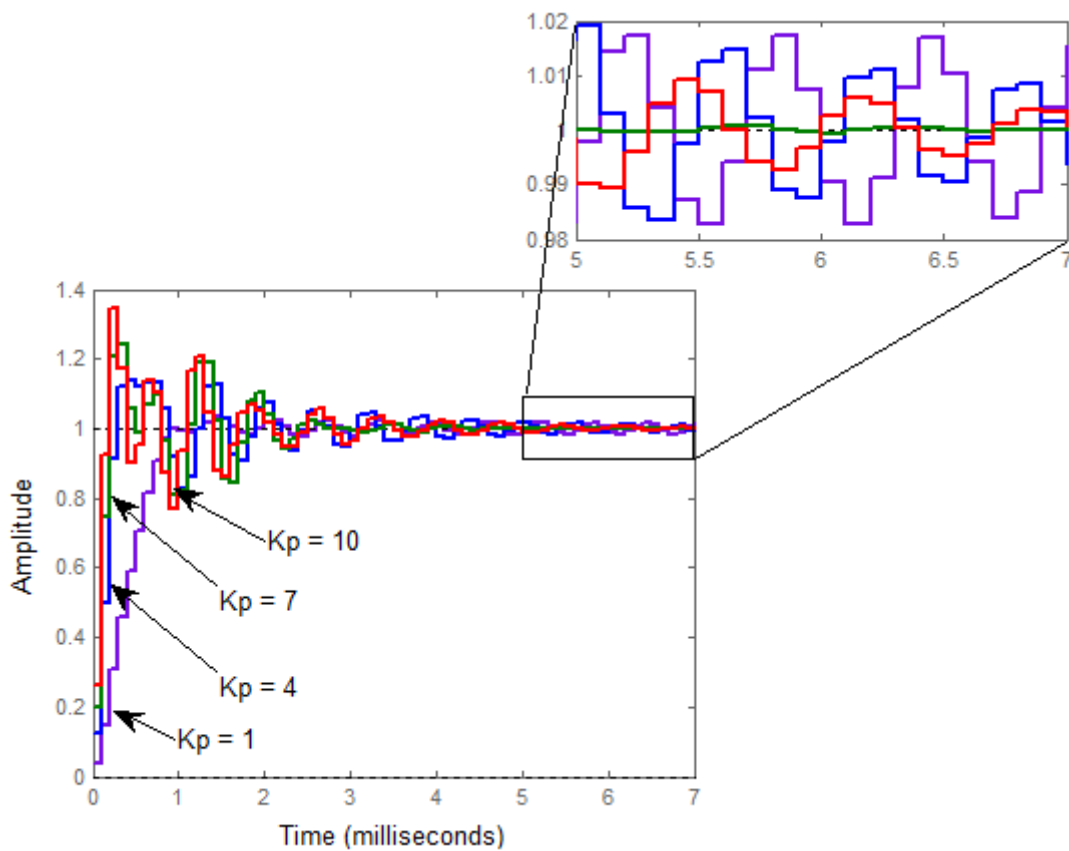


Figure 3.19 Step response of closed-loop discrete system with current sensors on the inverter side for different values of K_p .

Adding a damping resistance of $R_d = 1/(3\omega_{res}C_f)$ will reduce the oscillations in the step response and reduce the settling time as shown in Figure 3.20(b). This is because there are no complex poles at the boundary of the unit circle as shown in the pole-zero plot of Figure 3.20(a). However, the power losses will be increased. Increasing the damping

resistance will further increase the losses without a corresponding improvement in performance; therefore, it is not a good option.

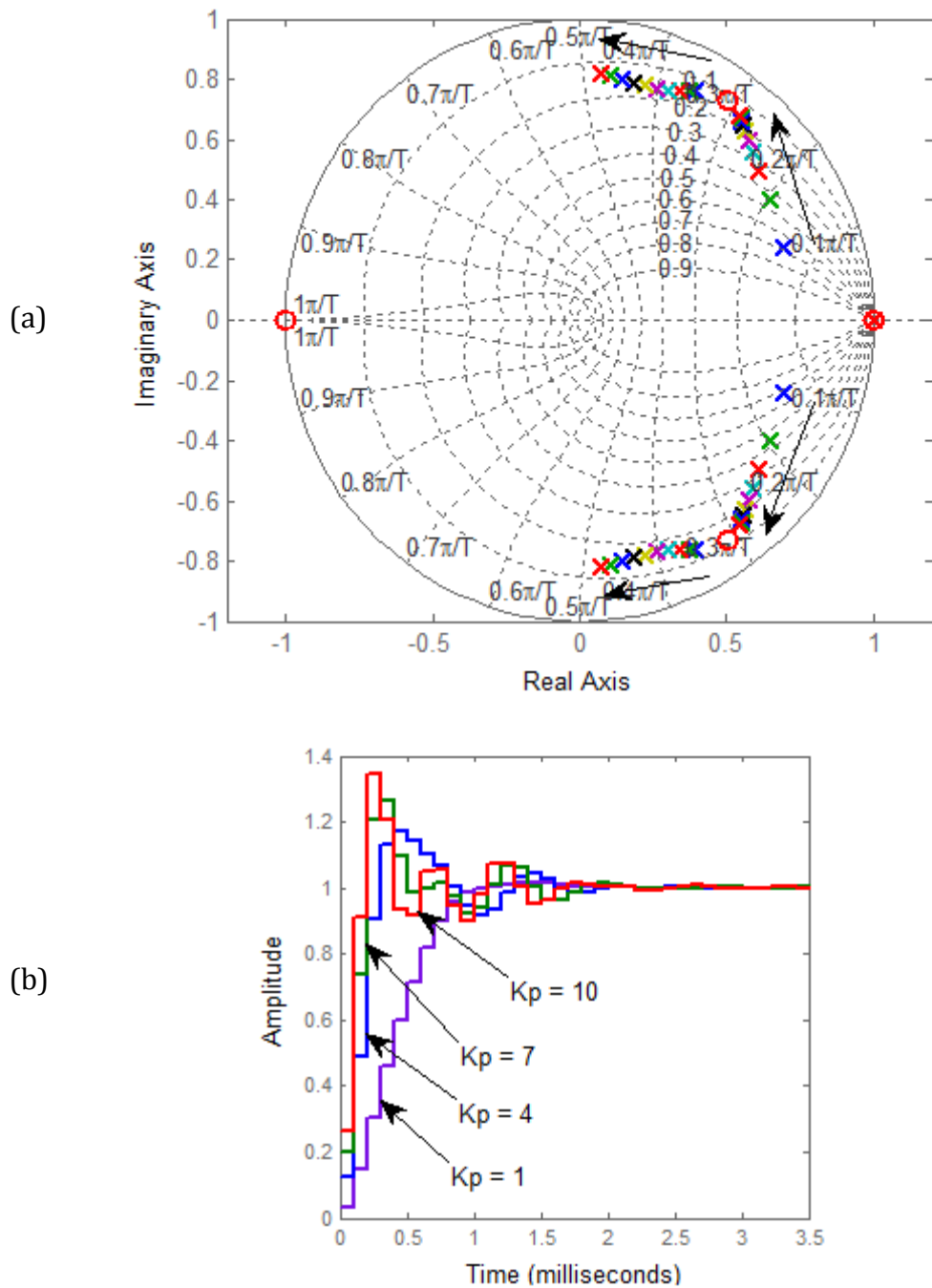


Figure 3.20 (a) Pole-zero plot and (b) step response, for passively damped LCL filter with current sensors on the inverter side.

3.4 Conclusion

In this chapter, the mathematical models of the grid-connected VSC with an LCL filter have been developed. Based on the synchronous reference frame model, the continuous-time closed-loop transfer function of the active power control loop is derived in the continuous-time domain and converted to discrete-time domain. Stability analysis was performed in the z-plane. The findings of the stability analysis are summarized below.

- When the current sensors are on the grid side, the system is unstable for all values of PI controller proportional gain and thus, the controller cannot be tuned to obtain stability.
- When passive damping is used, it is found that the system stability depends on the value of damping resistor used, and the value of the proportional gain.
- With notch filter active damping it is found that the system is stable for low values of gain but becomes unstable for higher values.
- When the current sensors are on the inverter side, the system is found to be stable for all values of gain considered.

Thus, it can be concluded that having the current sensors on the inverter side is a good solution to the problem of LCL filter instability. It does not require any additional passive elements or additional current sensors and modification of the controller.

Chapter 4 Implementation of Virtual Flux Direct Power Control with Space Vector Modulation

4.1 Introduction

Virtual-flux based direct power control with space vector modulation (VF DPC-SVM) is introduced in chapter two, and based on its favourable comparison to other VSC control techniques it was chosen for further investigation. In this chapter, the main issues involved in the implementation of DPC-SVM will be discussed. Of particular importance is the virtual flux estimation, the grid synchronization and the power estimation. The error in the reactive power at the PCC caused by having the current sensors on the inverter side of the LCL filter is derived and a new, simple scheme to compensate for this error is derived.

The complete control scheme is implemented in simulations of a 100 kW grid-connected photovoltaic converter and experimentally verified in a scaled down 1 kW laboratory set up. The chapter starts with a description of the simulation model and the experimental setup. The principle of virtual flux estimation is explained and different methods of virtual flux estimation are investigated. Grid synchronization methods are reviewed and a virtual flux phase-locked loop (VF-PLL) is implemented and compared to a voltage based synchronous reference frame PLL (SRF-PLL). Virtual flux based power estimation is derived from first principles based on the instantaneous power theory. The error in the reactive power at the PCC due to the reactive power output of the filter capacitor is derived analytically and a simple reactive power error compensation scheme is derived.

Simulation and experimental results are presented to support the analysis and derivations at all stages.

4.2 Simulation Model

A model of a grid-connected VSC is developed in Simulink using Simulink library blocks for the control elements and SimPowerSystems library blocks for the power electronics and power system elements.

The DC side is supplied by a PV array modeled based on the single diode model of a PV cell [123], [124]. The model is written in a Matlab s-function with the irradiation and cell temperature as inputs and the cell current as an output. The cell current is used to drive a controlled current source which represents a PV array giving an open circuit voltage of 995 V, and a short-circuit current of 138 A. The nominal power of the array at the standard test conditions of irradiation of 1000 W/m² and temperature of 25°C is 100 kW. The PV array voltage is kept constant at 760V. The VSC is modeled using the universal bridge available in SimPowerSystems™ power electronics library. The bridge is set to three IGBT/diode legs for three-phase operation. A DC link capacitor is connected across the DC input of the VSC. An LCL filter is connected between the VSC and the grid. The filter is designed following the guidelines in [103], [104]. The main considerations are reduction of the inverter side current ripple, grid side current harmonic attenuation and filter capacitor reactive power rating. The details of the design procedure for the LCL filter are given in Appendix C. The grid is modeled using a programmable three-phase source available in the sources library of SimPowerSystems™. The grid impedance is modeled as a resistive-inductive impedance in line with standard IEC/TR 60725:2012 [125].

The voltage and current measurements for control purposes are converted to per-unit using the rated power of the converter and the peak value of the phase voltage as the base values. A zero-order hold block for each measurement represents the sample and hold function in a real system. The control scheme is implemented using Simulink blocks and user-defined functions.

The parameters used in the simulation are summarized in Table 4.1.

Table 4.1 Simulation parameters

Parameters	Value
Nominal power, P_n	100 kW
Grid voltage (line-to-line), V_{gL}	415 V
Grid frequency, f_0	50 Hz
DC voltage, V_{dc}	760 V
DC capacitor, C_d	2200 μ F
Inverter side inductor, L_1	0.35 mH
Grid side inductor, L_2	0.10 mH
Filter capacitor, C_f	100 μ F
Sampling frequency, f_s	10 kHz
Switching frequency, f_{sw}	10 kHz
Base power, P_{base}	100 kW
Base voltage, V_{base}	339 V

4.3 Experimental Setup

Experimental verification of the simulation results was performed on a low-power prototype of a grid-connected VSC. The block diagram of the experimental system is shown in Figure 4.1. The system is supplied with a DC voltage of 120 V from a 3 kW, 300 V LAB/SM variable DC power supply and feeds into the utility grid through a variac and an isolation transformer at a voltage of 50 V (line-to-line). The variac allows the voltage at the point of connection of the VSC to the grid to be varied and the isolation transformer is included for safety reasons and to prevent DC current injection.

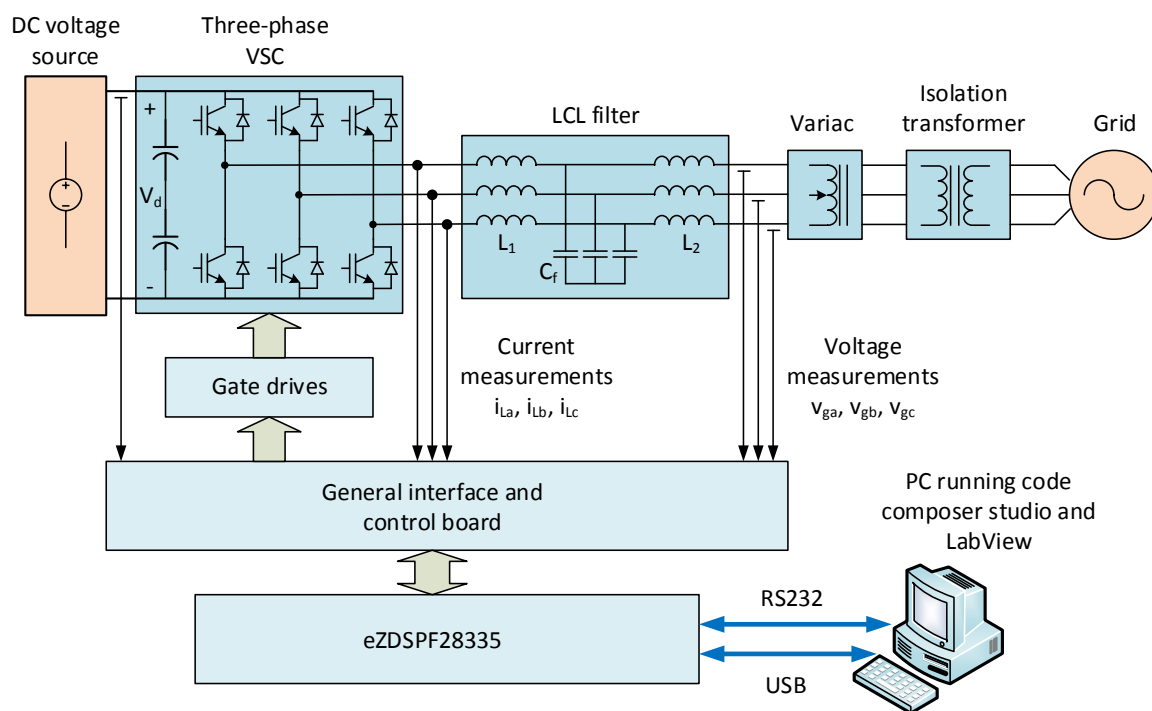


Figure 4.1 Block diagram of experimental system.

The three-phase VSC used in the experiments is a four-leg flexible inverter developed at Newcastle University. In this case the fourth leg was redundant as only three legs were required for the three-phase two-level VSC. The DC link of the VSC consists of two series-connected 2700 $\mu\text{F}/250\text{V}$ electrolytic capacitors to filter the low-frequency oscillations from the DC voltage and a 150 nF ceramic capacitor connected across the DC link to remove the high-frequency oscillations. International rectifier IRG4PH50UD IGBTs are used as the switching devices, with the switching signals provided by SN75372 gate drivers designed for the flexible inverter.

The LCL filter is connected between the VSC and the variac. The design procedure used to determine the values of the LCL filter components is similar to the one used for the simulation model. Current sensors are placed on the inverter side of the filter, while voltage sensors are on the grid side.

The control algorithms are implemented on the Spectrum Digital eZdspTMF28335 evaluation board based on the Texas Instruments TMS320F28335 digital signal controller (DSC). The TMS320F28335 DSC is a 150 MHz, 32-bit floating point DSC suitable for control applications such as converter control. The evaluation board comes with a 12-bit analogue/digital converter (ADC) with 16 input channels. The code is written in C

language using Texas Instruments Code Composer Studio Integrated Development Environment Version 6.0.1. An RS232 interface connects the DSC to a LabView control panel running on a computer. The LabView user control panel enables the user to change control parameters such as current/power demand and tune controller parameters in real time. The LabView panel also has a data transfer interface which is used to transfer variables stored in the eZdsp™F28335 Random Access Memory (RAM) to the computer for further analysis and processing using Matlab.

The general interface and control board is designed and developed within Newcastle University to interface the eZdsp™F28335 board to the power electronics and the various sensors. The board has a variety of interfaces suitable for power electronics and drives applications. The main interfaces used in this project include the gate drive interface which links the PWM signals from the DSC to the gate drivers; the sensor interface which connects the output signals from the voltage and current sensors to the ADC; a digital/analogue converter (DAC) which enables the real time monitoring of parameters from the DSC on an oscilloscope.

The parameters used in the experimental setup are given in Table 4.2

Table 4.2 Parameters used in the experimental setup

Parameters	Value
Nominal power, P_n	1 kW
Grid voltage (line-to-line), V_{gL}	50 V
Grid frequency, f_0	50 Hz
DC voltage, V_{dc}	120 V
DC capacitor, C_d	1350 μ F
Inverter side inductor, L_1	0.5 mH
Grid side inductor, L_2	0.15 mH
Filter capacitor, C_f	20 μ F
Sampling frequency, f_s	10 kHz
Switching frequency, f_{sw}	10 kHz

Photographs of the experimental rig are shown in Figure 4.2 and Figure 4.3.

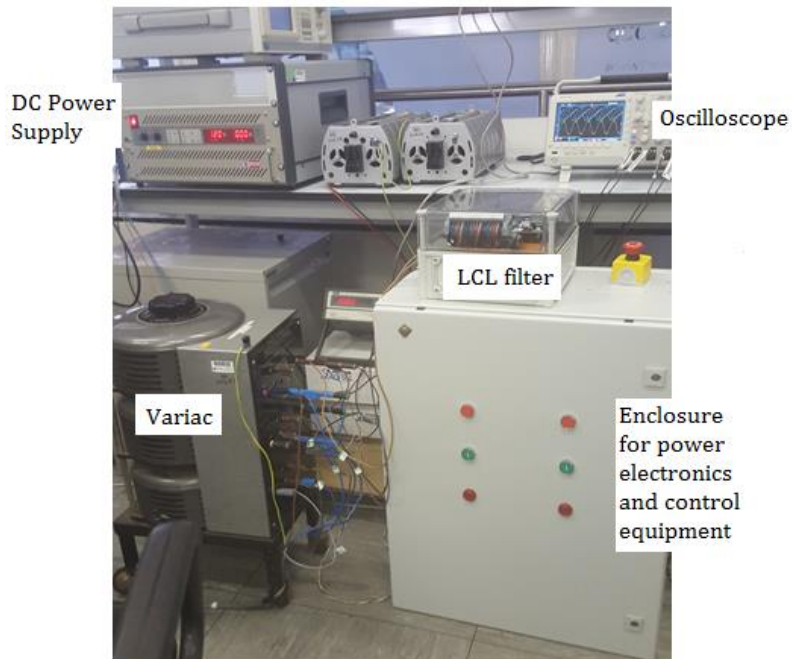


Figure 4.2 Photograph of experimental rig.

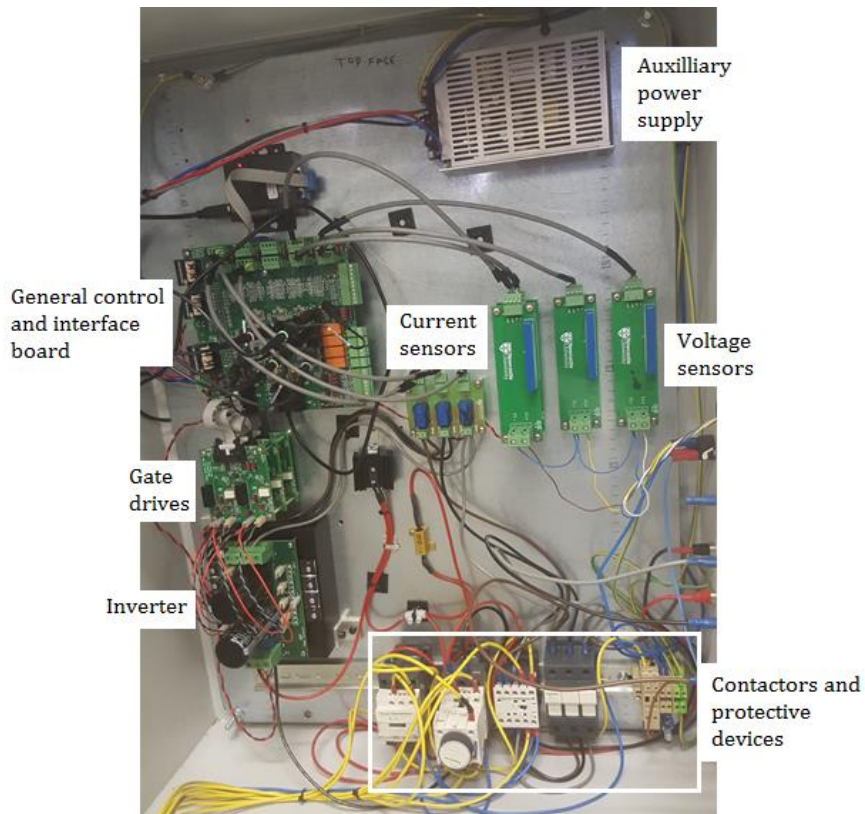


Figure 4.3 Photograph of the enclosure's interior.

4.4 Virtual Flux Estimation

4.4.1 Overview of Virtual Flux Estimation Methods

By definition the virtual flux is the integral of the voltage. Thus, the grid virtual flux is given in terms of the grid voltage as

$$\underline{\psi}_g = \int \underline{v}_g dt + \underline{\psi}_{g0} \quad (4.1)$$

Where $\underline{\psi}_g$ the grid is virtual flux vector, \underline{v}_g is the grid voltage vector and $\underline{\psi}_{g0}$ is the initial value of the grid virtual flux vector.

Equation (4.1) assumes that the virtual flux is calculated from the measured grid voltage using a pure integrator. However, in practice a pure integrator is not used because it could lead to integrator drift and saturation, if there is an offset in the measured voltage due to converter dead time, sensor offset or inaccuracies in the analogue to digital conversion [82]. To avoid the problem of drift and integrator saturation, the integration is performed using filters which provide a phase shift of 90° at the fundamental frequency. Among the filter types presented in literature, there are first order low-pass filters [73]; second order band-pass filters [81], [83] and cascaded first-order low-pass filters [82], [84], [85]. However, filter based integration suffers from magnitude and phase errors due to frequency variations away from the nominal grid frequency. The performance of the filter can be improved by adding phase and magnitude error compensation [126], [88] or adaptive compensation [127]. Other proposed improvements include making the filter frequency adaptive, as in [128] where a second-order generalized integrator (SOGI) based method is used.

In this study, the cascaded first-order low-pass filter method is adopted. This is because in a grid-connected application the expected frequency variation is $\pm 1\%$ of the nominal grid frequency [129], [130]. Within this range of variation, using cascaded low-pass filters give a maximum magnitude error of $\pm 1\%$ and a maximum phase error is $\pm 0.5^\circ$ as shown in Figure 4.4.

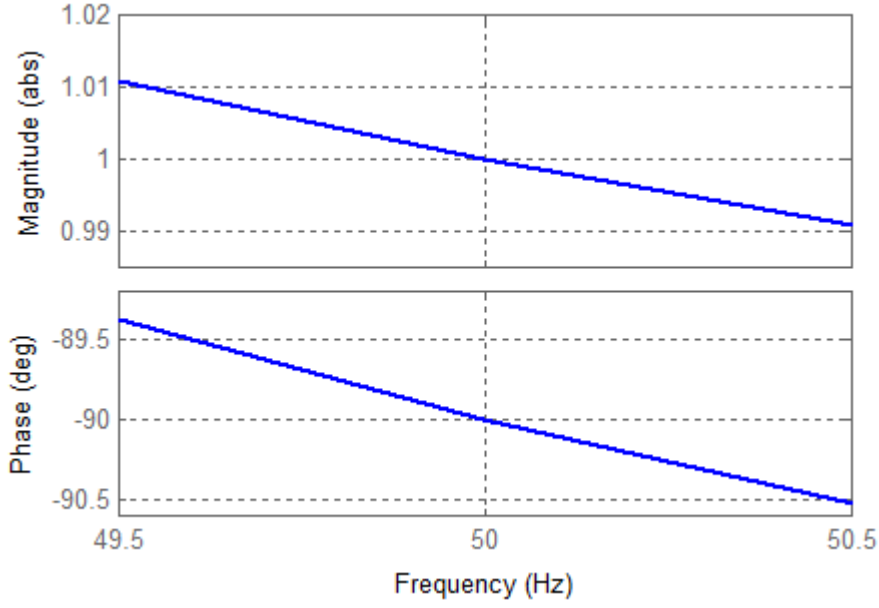


Figure 4.4 Variation of magnitude and phase with frequency for cascaded low-pass filters.

The transfer function of the cascaded low-pass filters is given by

$$G_{LP}(s) = \frac{\psi_{g\alpha\beta}}{v_{g\alpha\beta}} = \left(\frac{2\omega_0}{s + \omega_0} \right) \left(\frac{\omega_0}{s + \omega_0} \right) \quad (4.2)$$

where ω_0 is the nominal grid frequency.

The multiplication factor of 2 is needed to make the magnitude of the estimated virtual-flux equal to the magnitude of the voltage. The output of the filter is therefore not equal to the virtual flux measured in Wb , but it is equal to the virtual flux multiplied by the angular frequency, and its unit is $Wb.rad.s^{-1}$ (same as voltage). In [128] the symbol χ is adopted to differentiate it from the conventional virtual flux. However, in this thesis, the common symbol for virtual-flux will be used.

4.4.2 Simulation and Practical Results for Virtual Flux Estimation

The results of the virtual flux estimation in simulations and experiments are shown in Figure 4.5 and Figure 4.6 respectively. In both cases the voltage and the virtual flux are scaled to the same amplitude with the virtual flux which has a phase shift of -90° with respect to the voltage. The results show that the implemented virtual flux estimation method meets the requirements of obtaining the virtual flux with minimal amplitude and

phase errors. The estimated virtual flux will be used in the controller for synchronization and power estimation.

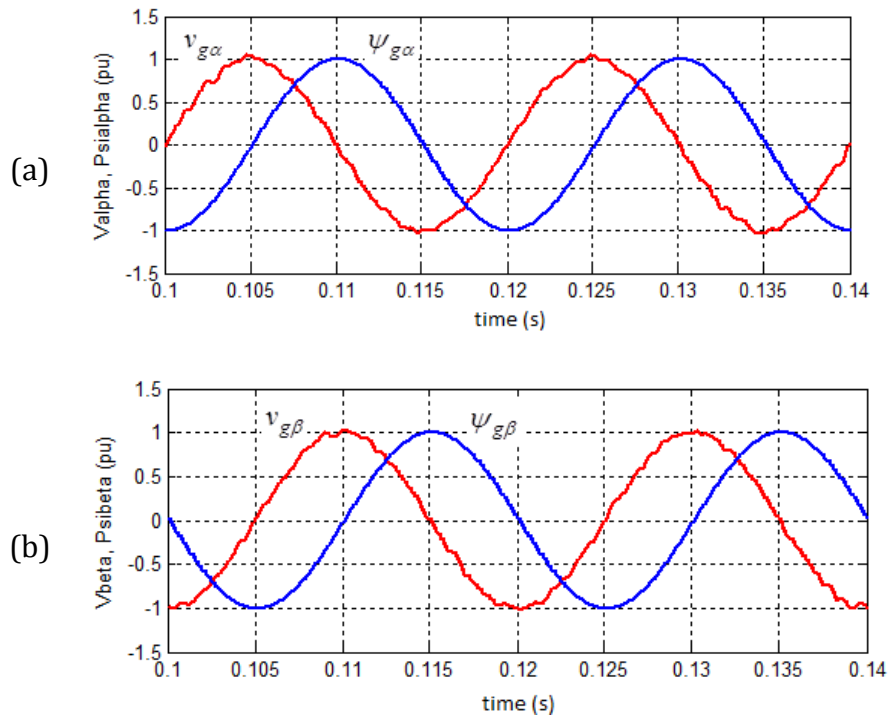


Figure 4.5 Simulation results for virtual flux estimation (a) $v_{g\alpha}$ and $\psi_{g\alpha}$ (b) $v_{g\beta}$ and $\psi_{g\beta}$.

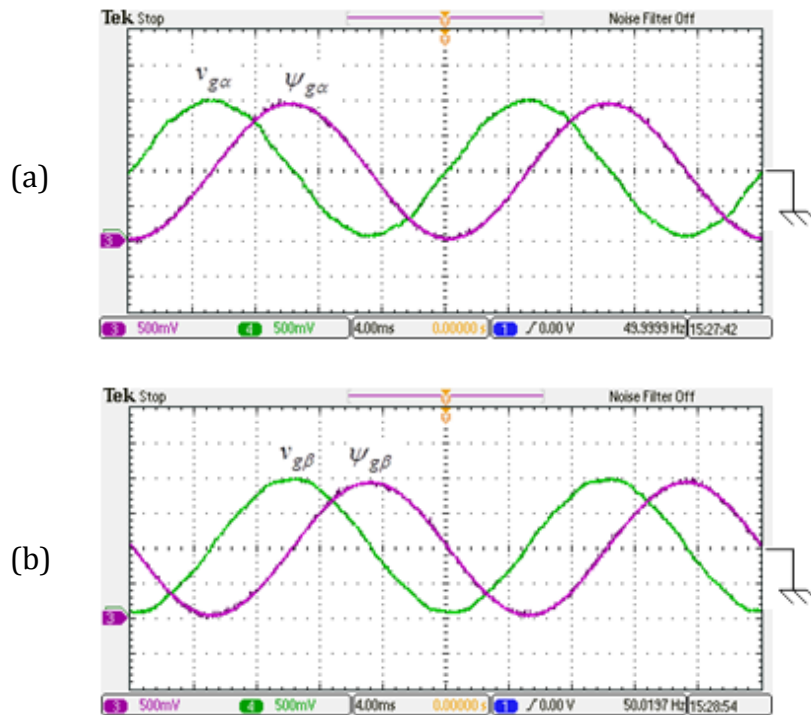


Figure 4.6 Experimental results for virtual flux estimation (a) $v_{g\alpha}$ and $\psi_{g\alpha}$ (b) $v_{g\beta}$ and $\psi_{g\beta}$ [scale: 20 V/div].

4.5 Synchronization

Synchronization is one of the important control functions in a grid-connected VSC. It involves obtaining information about the grid voltage such as the magnitude, the phase angle and the frequency. The phase angle of the grid voltage is useful in synchronizing the switching on and off of the semiconductor devices, reference frame transformation of the feedback variables and the determination and control of the active and reactive power flow [41]. The quality of the synchronization affects the quality of the control [41]. The main synchronization techniques found in literature are the zero-crossing detector (ZCD) [131],[132] and the phase-locked loop (PLL) [41], [44],[133],[134],[42].

The zero-crossing detector is a simple synchronization method which detects the zero-crossing points of the grid voltage. By counting the number of zero crossings, the frequency is estimated and by integrating the estimated frequency the phase angle is obtained. One of the drawbacks of the ZCD is that the zero-crossing can only be detected every half-cycle and there is no phase detection between the zero-crossing points which makes the dynamic performance of the ZCD poor [135]. Another drawback is that it is sensitive to noise and distortions in the grid voltage such as notches and low-frequency harmonics can negatively affect the output the output of the ZCD [132], [136].

A phase-locked loop is another method of grid synchronization. Originally used in telecommunications as a device whose output signal tracks its input signal, it has become very popular in grid-connected applications [137]. The most common PLL is the synchronous reference frame PLL (SRF-PLL) which is shown in Figure 4.7.

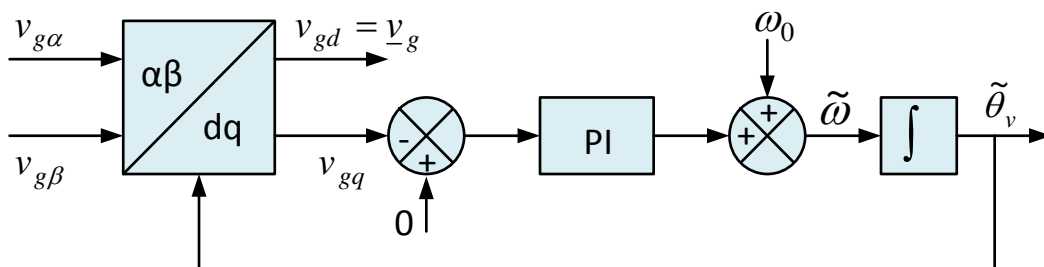


Figure 4.7 SRF-PLL.

It consists of a reference frame transformation to obtain the synchronous reference frame voltages which are dc quantities. The lock is achieved by setting one of the synchronous

frame voltages to zero. In Figure 4.7 v_{gq} is controlled to be zero by using a PI controller. This aligns the grid voltage vector with the d-axis. The output of the PI controller is added to the nominal value of the grid angular frequency to obtain the grid angular frequency. The frequency is integrated to obtain the voltage angle, which is fed back and used in the reference frame transformation. The SRF-PLL gives a satisfactory performance with balanced grid voltages, even in the presence of high-order harmonic distortion [138].

When a virtual flux based control technique is implemented, the virtual flux can be used for synchronization [81]. Due to the low-pass filters used for the virtual flux estimation, the virtual flux vector rotates more smoothly than the voltage vector and can be tracked more easily without using a PLL [81]. In this case, the virtual flux angle is calculated using the arctan function for the virtual flux components in the stationary reference frame. This is given by

$$\theta_{\psi} = \arctan\left(\frac{\psi_{g\beta}}{\psi_{g\alpha}}\right) \quad (4.3)$$

The virtual flux vector lags the voltage by 90° and the voltage angle can be calculated from the virtual flux angle using

$$\theta_v = \theta_{\psi} + \frac{\pi}{2} \quad (4.4)$$

The performance of virtual flux based synchronization can be improved for operation with distorted and unbalanced grid voltages by using a PLL [40], [88].

A virtual flux PLL (VF-PLL) is implemented in this study. The overall structure and operation of the VF-PLL is similar to the SRF-PLL. The block diagram of the VF-PLL is shown in Figure 4.8.

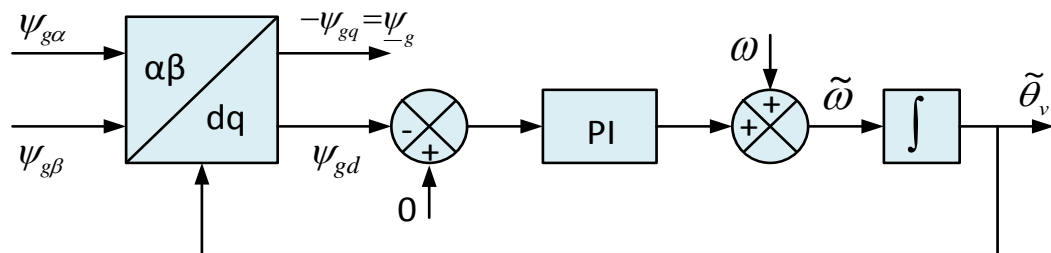


Figure 4.8 VF-PLL.

A notable difference between the SRF-PLL and the VF-PLL is that while for the SRF-PLL the q-component of the voltage is set to zero, for the VF-PLL the d-component of the virtual flux is set to zero. This is because of the -90° phase difference between the voltage vector and the virtual flux vector. With this orientation the virtual flux vector is aligned with the q-axis i.e. $\underline{\psi}_g = \psi_{gq}$. With this orientation, the estimated angle of the VF-PLL is equal to the voltage vector angle. The orientation of the voltage vector and the virtual flux vector are shown in the vector diagram in Figure 4.9.

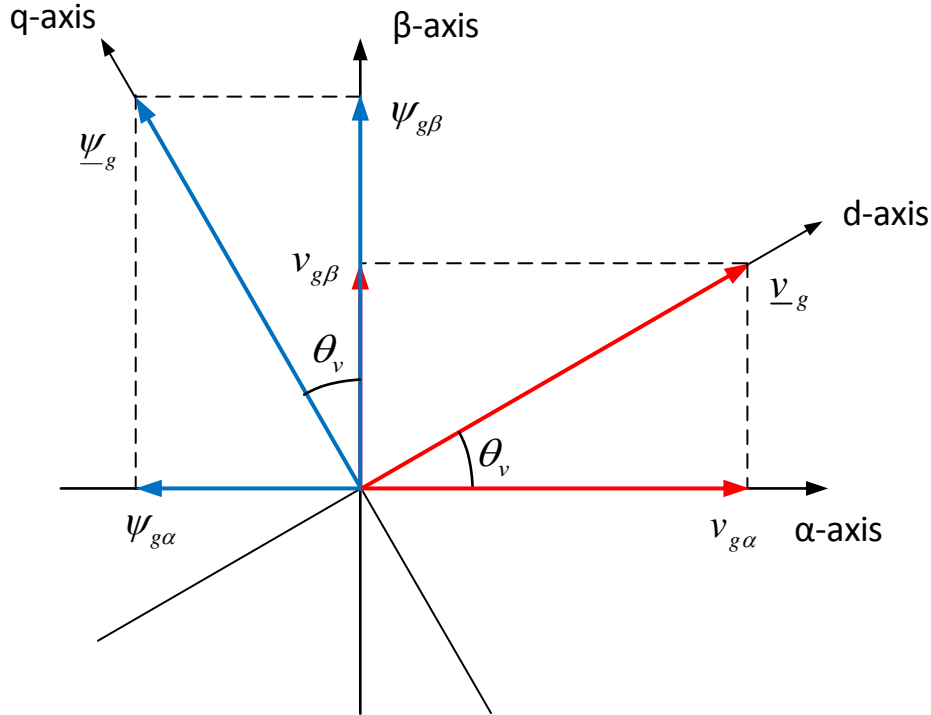


Figure 4.9 Orientation of voltage vector and virtual flux vectors.

The other difference is the performance of the two PLLs when the grid voltage is distorted with low-order harmonics. The performance of the SRF-PLL with distorted grid voltage is better when its feedback loop has a low bandwidth. This is because when the bandwidth is low, the PI controller which acts as the loop filter is able to reject the low-order harmonics. However, this reduces the dynamic response and the accuracy of the detected angle [29], [42]. In a high bandwidth SRF-PLL the effect of the low-order harmonics will be visible in the detected angle. The VF-PLL is more robust to low-order harmonics because its input is the virtual flux which is estimated using low-pass filters. Therefore, even with low-order harmonics present on the grid voltage, it gives a good performance.

The performance of the SRF-PLL and the VF-PLL are compared in the simulation results below. In Figure 4.10 the performance of the two PLLs is shown for a purely sinusoidal grid voltage. This is the ideal case, and is rarely encountered in practice, though a strong grid does not deviate too far from this ideal case. The two PLLs are tuned to have the same bandwidth for comparison and both of them show good accuracy in tracking the grid voltage angle.

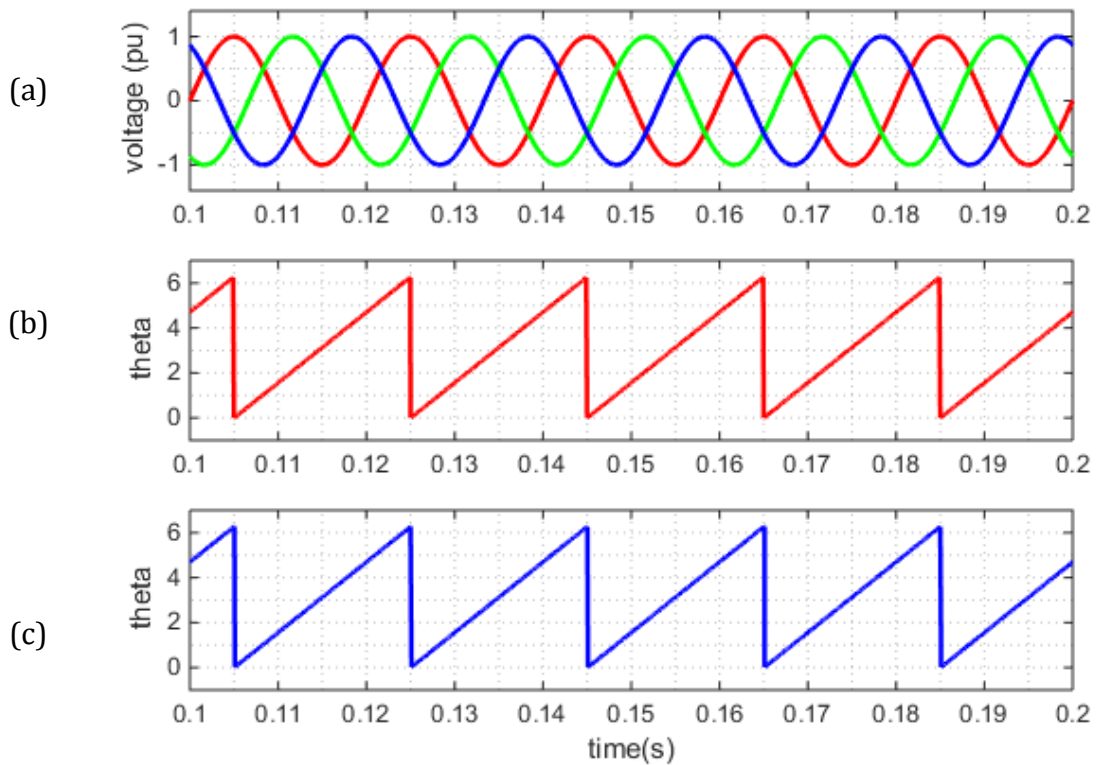


Figure 4.10 Performance of SRF-PLL and VF-PLL with balanced undistorted grid voltage
 (a) phase voltages (b) SRF-PLL angle (c) VF-PLL angle.

In Figure 4.11 a distorted grid voltage is applied to both PLLs tuned to the same bandwidth. The distortion is created by adding a positive-sequence fifth harmonic voltage of magnitude 20% of the fundamental grid voltage, and a positive-sequence seventh harmonic voltage of magnitude 15% of the fundamental grid voltage to the fundamental grid voltage. This is an extreme case of distortion which is not likely to be encountered in practice but it gives a good test of the robustness of the two PLLs. The SRF-PLL shows oscillations in its detected angle which show a deviation from the actual angle. The VF-PLL shows a better performance and the detected angle does not have any oscillations.

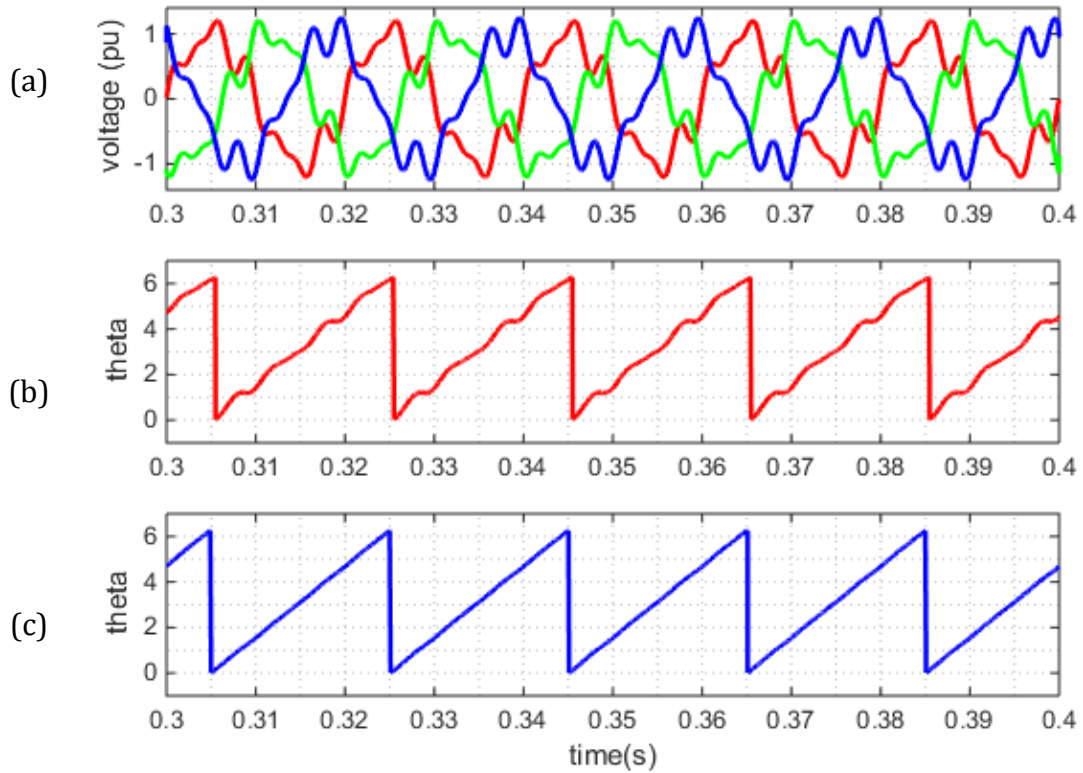


Figure 4.11 Performance of SRF-PLL and VF-PLL with distorted grid voltage (a) phase voltages (b) SRF-PLL angle (c) VF-PLL angle.

Therefore, the VF-PLL and the SRF-PLL have comparable performance in strong grids with almost sinusoidal voltages. However, in weak grids with highly distorted voltages consisting of low-order harmonics, the VF-PLL performs better.

The SRF-PLL and the VF-PLL were both implemented practically and the results are shown in Figure 4.12. The practical results verify the simulation results for undistorted grid voltage.

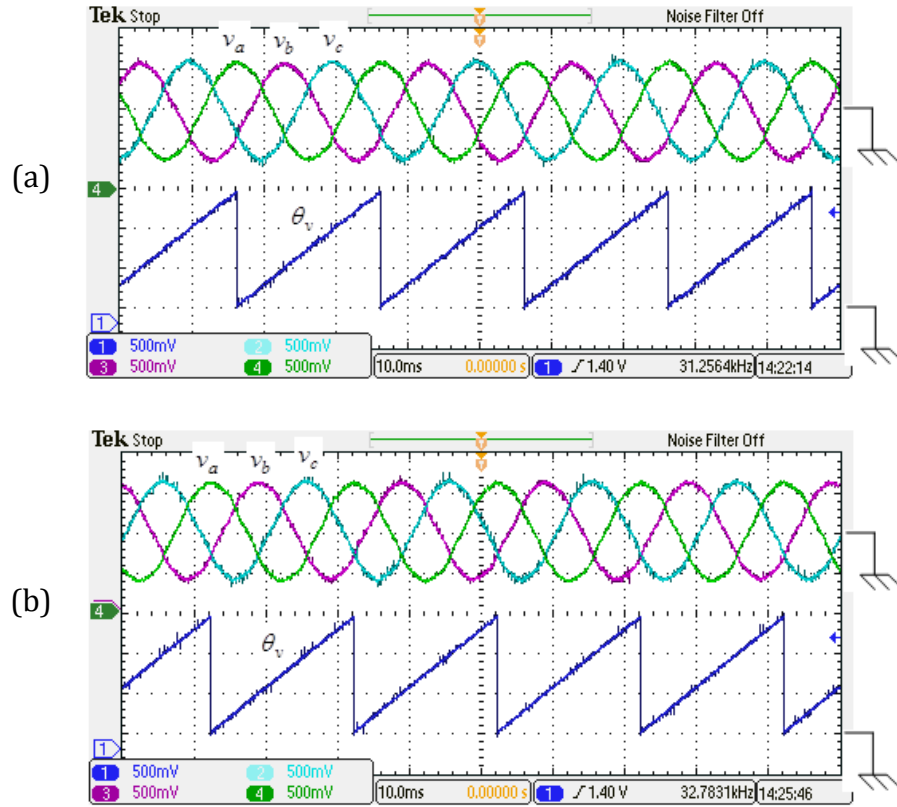


Figure 4.12 Experimental results for (a) SRF-PLL. Phase voltages (40 V/div); angle (120°/div) (b) VF-PLL. Phase voltages (40 V/div); angle (120°/div).

4.6 Power Estimation

In direct power control schemes, the inner control loop controls the active power and the reactive power, which are estimated using the current and the voltage or the virtual flux [72], [34], [77]. The power estimation is based on the instantaneous power theory or p-q theory. There are many definitions of instantaneous power in literature [62], [139], [140], [141], [142], [143]. While there is no generally agreed definition of instantaneous power in literature, various authors agree that the instantaneous power consists of at least two different components. These are the active or real power and the imaginary or reactive power.

Akagi *et al* defines the instantaneous active power, p for three-phase systems as “the total energy flow per second between two subsystems” [62].

Mathematically this is given by

$$p = v_a i_a + v_b i_b + v_c i_c \quad (4.5)$$

The definition of instantaneous imaginary power according to Akagi *et al* is that it is a component of the power proportional to the quantity of energy that is being exchanged between the phases of a three phase system and does not contribute to the energy transfer between the source and the load [62]. The instantaneous reactive power is the same as the instantaneous imaginary power.

Mathematically this is given by

$$q = \frac{1}{\sqrt{3}}(v_{ab}i_c + v_{bc}i_a + v_{ca}i_b) \quad (4.6)$$

Using space vectors of the voltage and the current, the active power and the reactive power are respectively given by

$$p = \frac{3}{2} \text{Re}[\underline{v} \cdot \underline{i}^*] \quad (4.7)$$

$$q = \frac{3}{2} \text{Im}[\underline{v} \cdot \underline{i}^*] \quad (4.8)$$

where \underline{i}^* is the complex conjugate of the current.

Using the stationary reference frame components of the voltage and the current, equations (4.7) and (4.8) can be written as

$$p = \frac{3}{2}(v_\alpha i_\alpha + v_\beta i_\beta) \quad (4.9)$$

$$q = \frac{3}{2}(v_\beta i_\alpha - v_\alpha i_\beta) \quad (4.10)$$

Using the virtual flux for power estimation has been shown to improve the quality of the converter current even in the presence of distorted grid voltage [40], [87].

Assuming sinusoidal balanced voltages, we can write the stationary reference frame voltages as

$$v_\alpha = V_m \cos \theta_v \quad (4.11)$$

$$v_\beta = V_m \sin \theta_v \quad (4.12)$$

Similarly, the estimated virtual flux scaled to the same amplitude as the voltage can be written as

$$\psi_{\alpha} = \Psi_m \sin \theta_v \quad (4.13)$$

$$\psi_{\beta} = -\Psi_m \cos \theta_v \quad (4.14)$$

where $\theta_v = \omega t$ is the voltage angle; V_m is the amplitude of the voltage and Ψ_m is the amplitude of the virtual flux.

The voltage can be written as the derivative of the virtual flux.

$$v_{\alpha} = \frac{d\psi_{\alpha}}{d\theta_v} \quad (4.15)$$

$$v_{\beta} = \frac{d\psi_{\beta}}{d\theta_v} \quad (4.16)$$

Substituting equations (4.15) and (4.16) into equations (4.9) and (4.10) we get

$$p = \frac{3}{2} \left(\frac{d\psi_{\alpha}}{d\theta_v} i_{\alpha} + \frac{d\psi_{\beta}}{d\theta_v} i_{\beta} \right) \quad (4.17)$$

$$q = \frac{3}{2} \left(\frac{d\psi_{\beta}}{d\theta_v} i_{\alpha} - \frac{d\psi_{\alpha}}{d\theta_v} i_{\beta} \right) \quad (4.18)$$

From equations (4.13) and (4.14), we get

$$\frac{d\psi_{\alpha}}{dt} = -\psi_{\beta} \quad (4.19)$$

$$\frac{d\psi_{\beta}}{dt} = \psi_{\alpha} \quad (4.20)$$

Substituting equations (4.19) and (4.20), into equations (4.17) and (4.18) we get

$$p = \frac{3}{2} (\psi_{\alpha} i_{\beta} - \psi_{\beta} i_{\alpha}) \quad (4.21)$$

$$q = \frac{3}{2} (\psi_{\alpha} i_{\alpha} + \psi_{\beta} i_{\beta}) \quad (4.22)$$

Equations (4.21) and (4.22) form the basis of active and reactive power estimation in virtual-flux based direct power control.

4.7 Modified Power Estimation with LCL Filter

The control objective in grid-connected VSCs is to control the flow of active and reactive power into the grid. This can be done directly, as in direct power control, or indirectly, as in voltage oriented current control. In direct power control the current is used to estimate the active power and the reactive power which are the regulated variables, and in current control it is regulated by the current controller. In both cases the control is synchronized with the grid voltage angle, and for unity power factor operation the current flowing into the grid should be in phase with the voltage at the PCC. If an L filter is used, the position of the current sensors can be on the inverter side or the grid side, since the same current flows through the inductor. However, if an LCL filter is used, there is a phase shift between the inverter side current and the grid side current, which is caused by the current drawn by the filter capacitor. Therefore, the current measured by the current sensors on the inverter side will not be equal to the current measured by current sensors on the grid side. It appears that the best position for the current sensors is on the grid side because that will give the actual current flowing into the grid. However, for stability reasons, the current sensors can be on the inverter side, and in this case the measured current will not be equal to the actual current flowing into the grid. In terms of the powers, the reactive power estimated using the inverter side current will not be equal to the reactive power at the PCC because of the reactive power output of the filter capacitor. If the losses in the inductor windings and the connecting cables are ignored, the estimated active power will be the same as the active power at the PCC, since the current drawn by the filter capacitor is purely reactive. This is a reasonable assumption in high power converters. If the error between the regulated reactive power and the actual reactive power is small, which is the case in low-power converters with low value filter capacitors, it can be neglected. However, in high power converters with high value filter capacitors the error is quite significant and it should be compensated for to achieve correct regulation of the reactive power.

A number of publications have presented various strategies of compensating for the error in the regulated reactive power and the reactive power at the PCC when the current sensors are on the inverter side. An example of reactive power error compensation in virtual flux direct power control is found in [88] where the inverter virtual flux and the inverter side current are used to estimate the powers. The reactive power error which is equal to the filter capacitor reactive power is estimated using the estimated filter

capacitor virtual flux and the measured capacitor current. A different approach for voltage based direct power control is presented in [144], where the filter capacitor reactive power is estimated using the measured capacitor voltage and the filter capacitance. A compensation scheme for a single-phase grid-connected converter is given in [116] where the inverter side current is measured. The grid side current reference is created by estimating the capacitor current and adding it to the inverter side reference current. The drawback of the methods in [88] and [144] is that they require additional sensors to measure the capacitor current and the capacitor voltage respectively.

In the following sub-sections, a new simple analytical method of compensating for the error in the estimated reactive power is developed and implemented. The method is based on the estimated virtual flux and the measured inverter side current. The advantages of the developed method are that it does not need any additional voltage or current sensors, and does not add complexity to the overall control scheme.

4.7.1 Phasor Diagram for Grid-connected VSC

The single-phase equivalent circuit of the grid-connected VSC is shown in Figure 4.13.

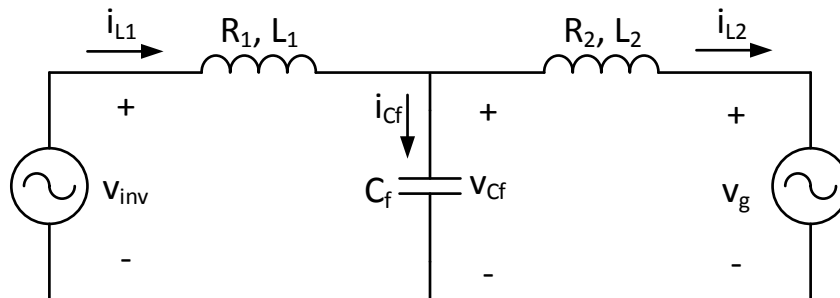


Figure 4.13 Single-phase equivalent circuit of grid-connected VSC.

The inverter voltage, the filter capacitor voltage and the grid voltage are related by

$$\underline{v}_{inv} = L_1 \frac{di_{L1}}{dt} + R_1 i_{L1} + \underline{v}_{Cf} \quad (4.23)$$

and

$$\underline{v}_{Cf} = L_2 \frac{di_{L2}}{dt} + R_2 i_{L2} + \underline{v}_g \quad (4.24)$$

The inverter side current, the filter capacitor current and the grid side current are related by

$$\dot{i}_{L1} = \dot{i}_{L2} + \dot{i}_{Cf} \quad (4.25)$$

The graphical relationship between the voltages and the currents is shown in the phasor diagram of Figure 4.14 which shows the fundamental frequency components of the voltages and currents. The grid voltage, V_g is taken as the reference phasor and the grid side current, I_{L2} is assumed to be lagging the voltage by an angle, φ_{L2} . The resistive voltage drops across the winding resistances of the inverter side inductor and the grid side inductor are given by $R_1 I_{L1}$ and $R_2 I_{L2}$ respectively. The inductive voltage drops across the inverter side inductor and the grid side inductor are given by $j\omega L_1 I_{L1}$ and $j\omega L_2 I_{L2}$ respectively. The filter capacitor current, I_{Cf} leads the filter capacitor voltage, V_{Cf} by 90° . The inverter side current, I_{L1} is the sum of the grid side current and the filter capacitor current and has a phase angle of φ_{L1} with respect to the grid voltage. The phasor diagram shows that there is a phase difference between the grid side current and the inverter side current which is given by

$$\Delta\varphi = \varphi_{L1} - \varphi_{L2} \quad (4.26)$$

Due to this difference in phase shift, caused by the current in the filter capacitor, when the inverter side current is regulated or used to estimate the powers, there is need to compensate for the error in the regulated current or the reactive power.

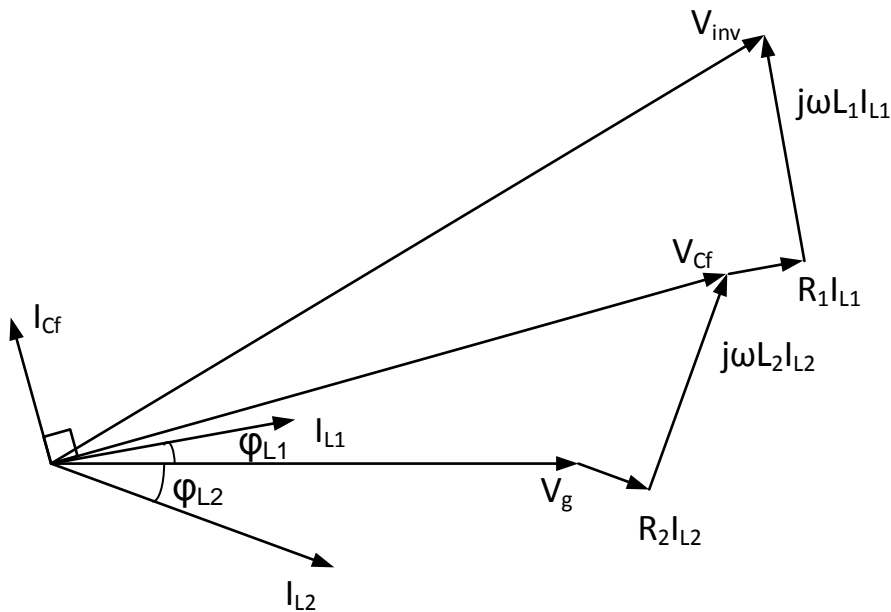


Figure 4.14 Phasor diagram of grid-connected VSC (not to scale).

The variation of the phase angle of the grid current with filter capacitance at different values of active power is shown in Figure 4.15. The graphs show that the phase angle is bigger at higher values of capacitance and low values of active power. For a grid-connected PV converter this is significant because the active power output is not always high, and if unity power factor is preferred during periods of low active power output there is need to compensate for the error due to the capacitive reactive power.

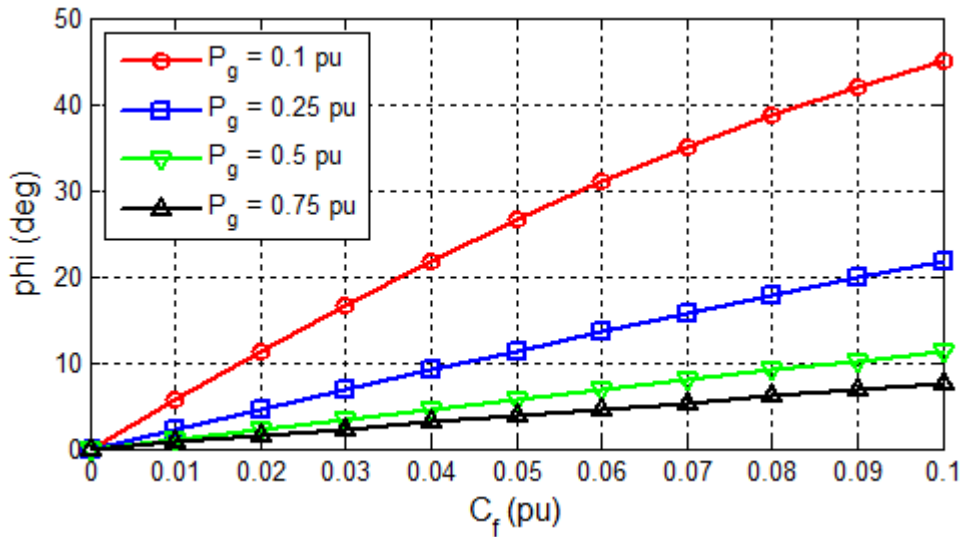


Figure 4.15 Variation of grid current phase angle with filter capacitance for different values of active power.

4.7.2 Derivation of an Expression for the Error

If the current sensors are on the inverter side, and the grid voltage is measured for synchronization, the regulated active power p_c and the regulated reactive power q_c are estimated using the inverter side current and the grid virtual flux as given by the equations below.

$$p_c = \frac{3}{2}(\psi_{g\alpha}i_{L1\beta} - \psi_{g\beta}i_{L1\alpha}) \quad (4.27)$$

$$q_c = \frac{3}{2}(\psi_{g\alpha}i_{L1\alpha} + \psi_{g\beta}i_{L1\beta}) \quad (4.28)$$

The active power and reactive power at the PCC are given by

$$p_g = \frac{3}{2}(\psi_{g\alpha}i_{L2\beta} - \psi_{g\beta}i_{L2\alpha}) \quad (4.29)$$

$$q_g = \frac{3}{2}(\psi_{g\alpha}i_{L2\alpha} + \psi_{g\beta}i_{L2\beta}) \quad (4.30)$$

It the capacitor current is assumed to be purely reactive, and if the resistive losses in the inductors are neglected, the controlled active power and the active power at the PCC can be assumed to be equal.

The difference between the controlled reactive power in (4.28) and the reactive power at the PCC in (4.30) is given by

$$\Delta q = q_c - q_g = \frac{3}{2}[\psi_{g\alpha}(i_{L1\alpha} - i_{L2\alpha}) + \psi_{g\beta}(i_{L1\beta} - i_{L2\beta})] \quad (4.31)$$

Rearranging equation (4.25), and using the stationary reference frame components of the currents we get the filter capacitor current as

$$i_{Cf\alpha} = i_{L1\alpha} - i_{L2\alpha} \quad (4.32)$$

$$i_{Cf\beta} = i_{L1\beta} - i_{L2\beta} \quad (4.33)$$

Substituting equations (4.32) and (4.33) in equation (4.31) we obtain the reactive power error as

$$\Delta q = \frac{3}{2}(\psi_{g\alpha}i_{Cf\alpha} + \psi_{g\beta}i_{Cf\beta}) \quad (4.34)$$

Implementation of equation (4.34) in the controller will need the capacitor current to be measured or estimated. To avoid using additional current sensors, the capacitor current can be estimated. To estimate the capacitor current, the inverter side current and the grid side current are needed. The inverter side current is available from the current sensors, while the grid side current can be estimated using the reference powers (which are the required powers at the PCC) and the grid virtual flux.

By rearranging equations (4.29) and (4.30) and substituting the grid side powers with the reference powers we obtain the equations for the grid side current below.

$$i_{L2\alpha} = \frac{2}{3} \left(\frac{q_{ref}\psi_{g\alpha} - p_{ref}\psi_{g\beta}}{\psi_{g\alpha}^2 + \psi_{g\beta}^2} \right) \quad (4.35)$$

$$i_{L2\beta} = \frac{2}{3} \left(\frac{p_{ref}\psi_{g\alpha} + q_{ref}\psi_{g\beta}}{\psi_{g\alpha}^2 + \psi_{g\beta}^2} \right) \quad (4.36)$$

Equations (4.32) to (4.36) are implemented to estimate the error in the reactive power, Δq . This error is then subtracted from the reactive power reference to make the reactive power at the PCC equal to the reference reactive power. This is expressed using the equation below.

$$q_{ref}' = q_{ref} - \Delta q \quad (4.37)$$

where q_{ref}' is the corrected reactive power reference.

The block diagram of the reactive power error compensation scheme is shown in Figure 4.16. A low-pass filter is used to remove the ripple in the estimated Δq .

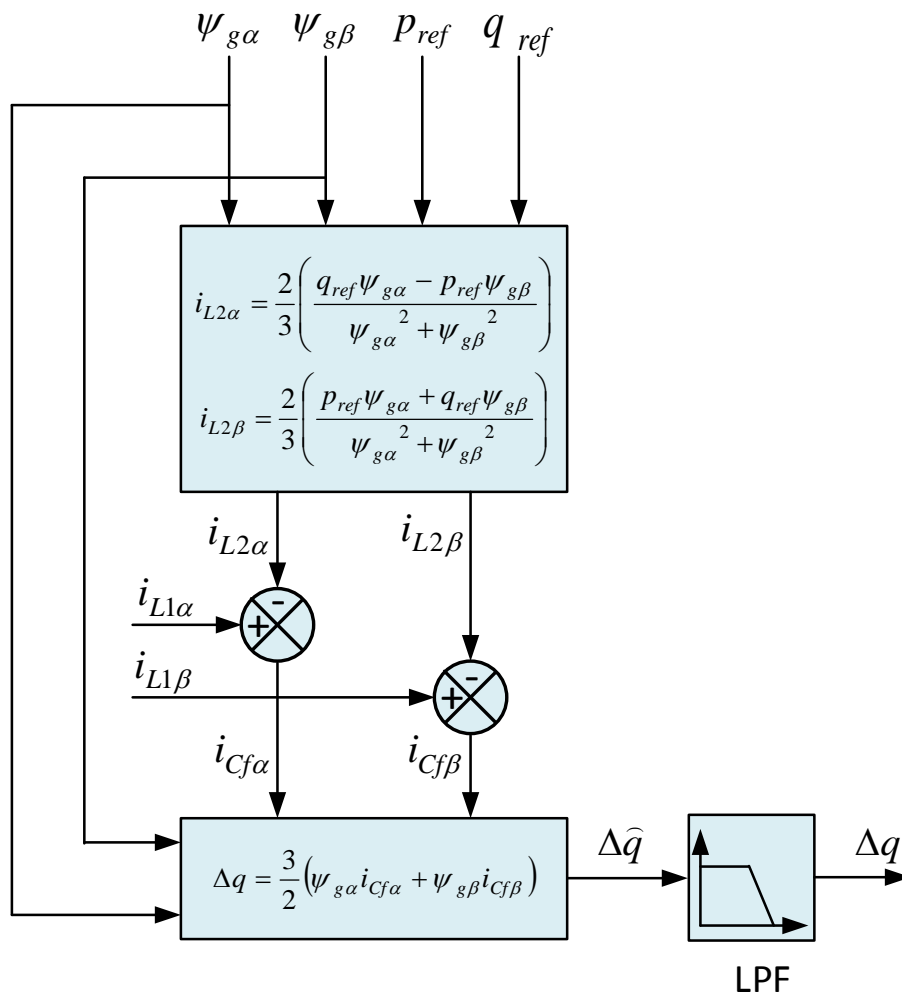


Figure 4.16 Block diagram of reactive power error compensation scheme.

The block diagram of the complete control scheme is shown in Figure 4.17.

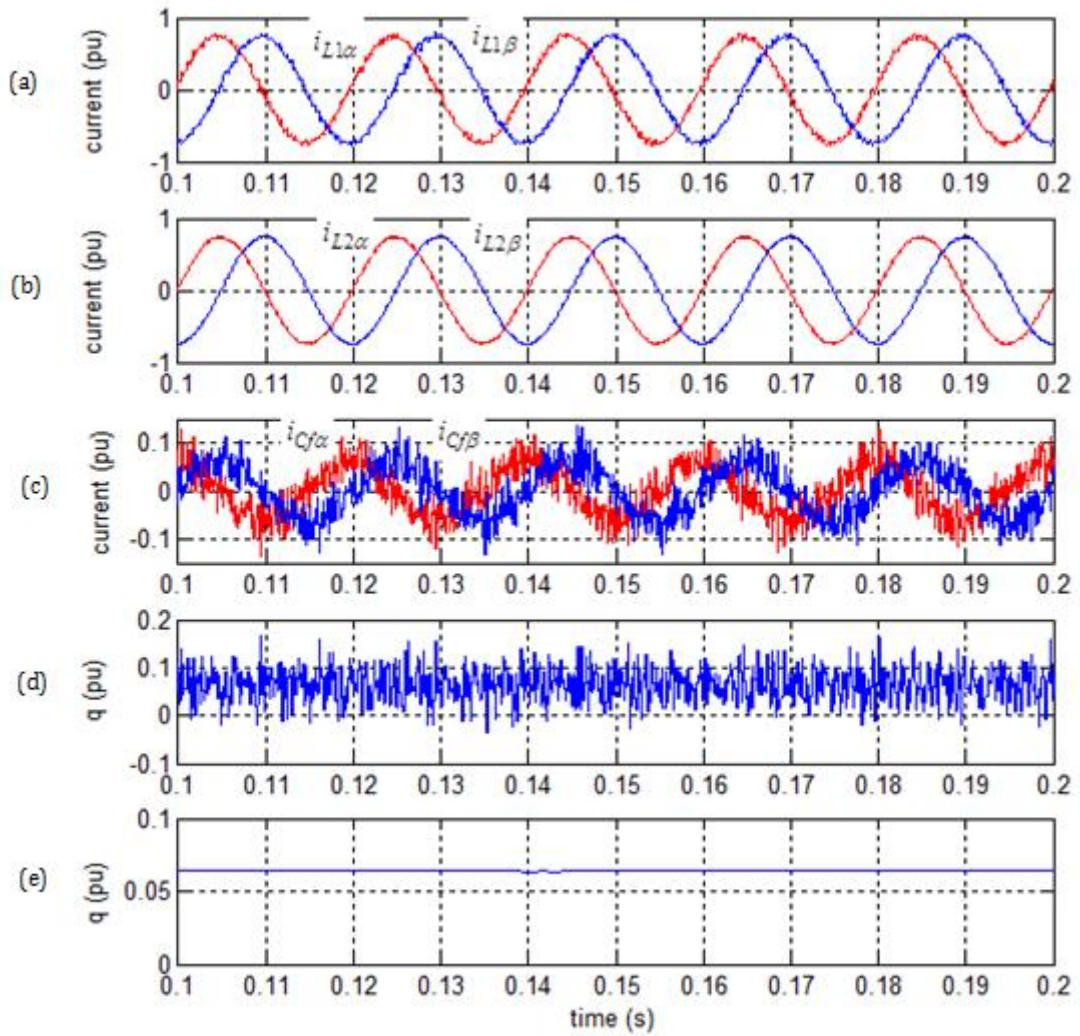


Figure 4.18 Simulation results for reactive power calculation (a) inverter side currents (b) grid side current (c) filter capacitor current (d) reactive power error (e) filtered reactive power error.

Simulation results showing the active power and the reactive power at the PCC without compensation for the reactive power are shown in Figure 4.19. The reference active power is 0.75 pu, and the reference reactive power is 0. The results show that the reactive power at the PCC is not equal to the reference reactive power.

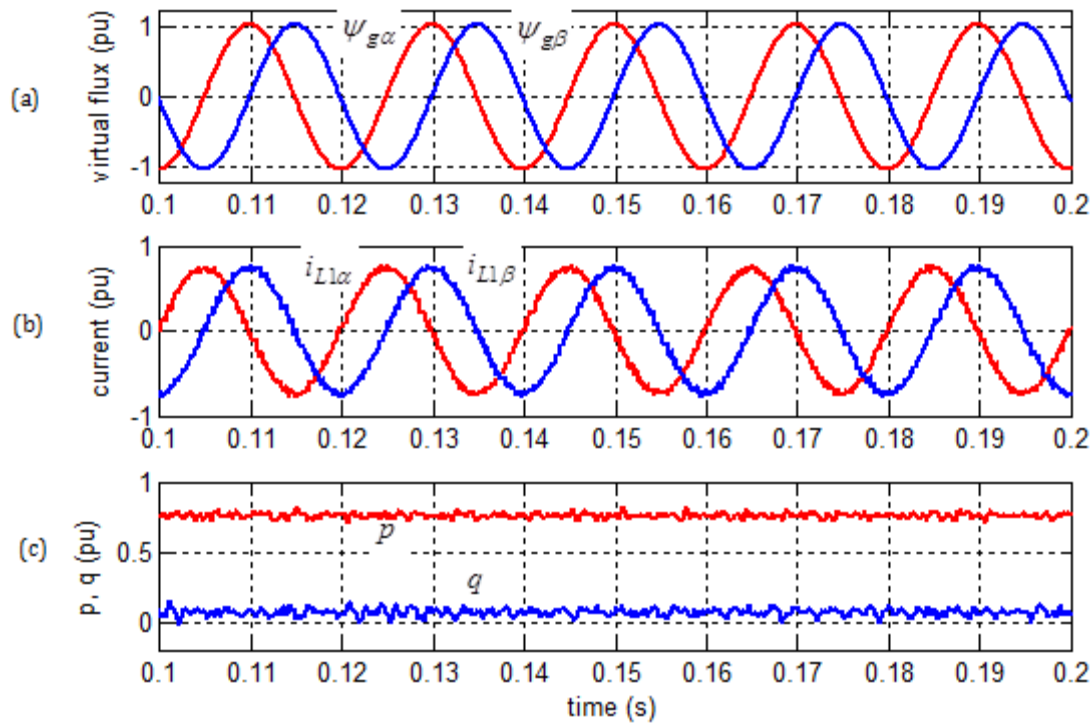


Figure 4.19 Simulation results for uncompensated reactive power error (a) grid virtual fluxes (b) inverter side currents (c) active power and reactive power.

Simulation results showing the active power and the reactive power at the PCC when the reactive power error compensation scheme is applied are shown in Figure 4.20. The error compensation is applied without changing the reference active power and reactive power. The reactive power at the PCC is equal to zero after compensation. Therefore, when the compensation scheme is applied, it is possible to make the reactive power at the PCC equal to the reference. This improves the power factor if unit power factor is desired, and it makes the reactive power control more accurate.

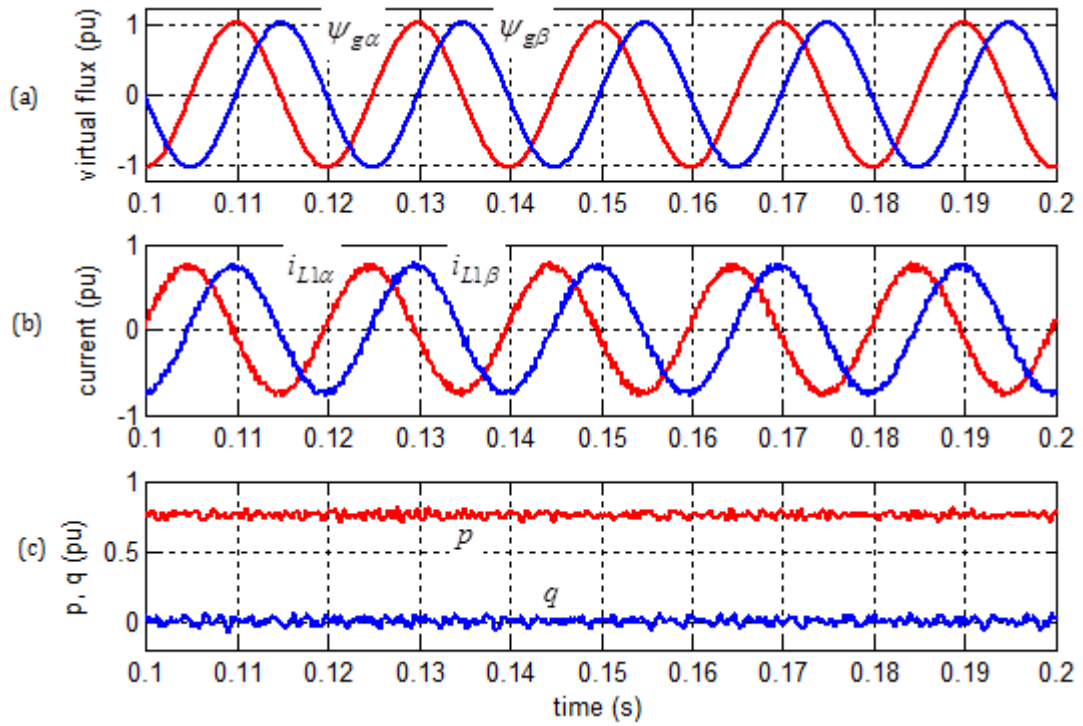


Figure 4.20 Simulation results for compensated reactive power error (a) grid virtual fluxes (b) inverter side currents (c) active power and reactive power.

4.7.4 Experimental Results for Power Estimation

The power estimation and the reactive power error compensation scheme described above were implemented in the practical set up. The inverter side current, grid side current and the filter capacitor current are shown in Figure 4.21. The experimental results in Figure 4.21, support the simulation results in Figure 4.18. The experimental results of the estimated powers are shown in Figure 4.22. The results show the grid virtual flux, the inverter side current and the estimated active power and reactive power. The experimental results of Figure 4.22, validate the simulation results of Figure 4.20.

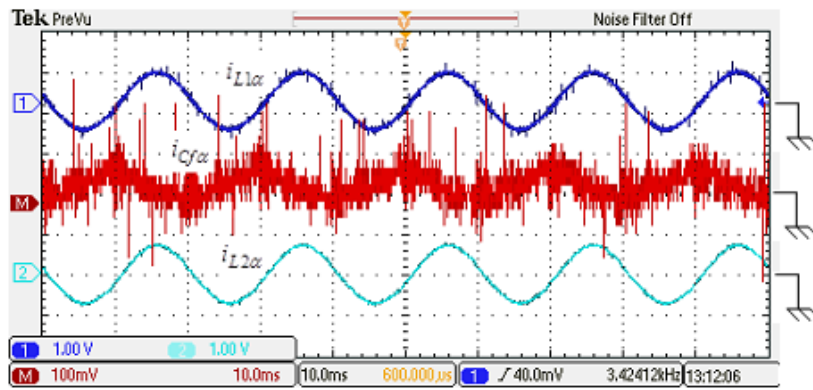


Figure 4.21 Experimental results showing inverter side current (top, 10 A/div), filter capacitor current (middle, 1 A/div) and grid side current (bottom, 10 A/div).

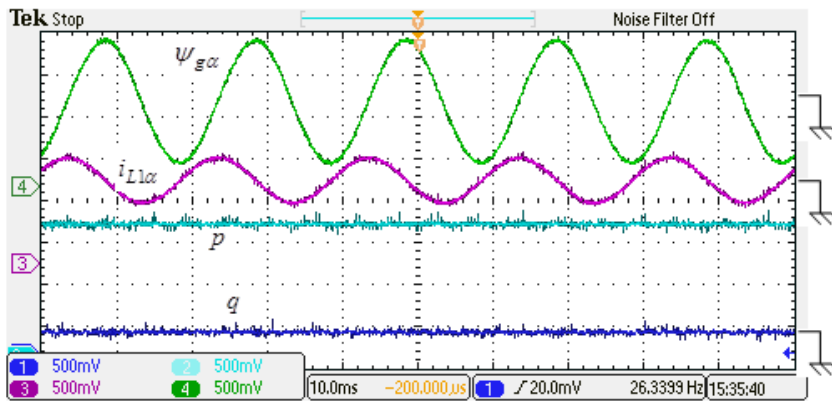


Figure 4.22 Experimental results for power estimation. Virtual flux (25 V/div), inverter side current (10 A/div) and active power and reactive power (200 W/div).

4.8 Conclusion

In this chapter the main issues involved in the implementation of virtual flux based direct power control with space vector modulation are presented. The simulation model and the experimental setup are described. The main contents of the chapter are summarized below.

- Virtual-flux estimation based on cascaded low-pass filter is described.
- An alternative synchronization method, the virtual-flux PLL is implemented and simulation results show that it has better performance than the common voltage based PLL in tracking the angle of the fundamental frequency voltage if the grid voltage is distorted with low order harmonics.

- It is proved mathematically that the reactive power estimated using the inverter side current of the LCL filter is not equal to the reactive power at the PCC, with the error being equal to the filter capacitor's reactive power output.
- A reactive power error compensation scheme is proposed and implemented to eliminate the error between the estimated reactive power and the reactive power at the PCC. The compensation scheme cancels out the reactive power output of the filter capacitor and ensures that the reactive power at the PCC is equal to the reference reactive power.

Chapter 5 Effect of Grid Impedance Variation and Grid Voltage Distortion

5.1 Introduction

In Chapter 3, it was established that, the power control loop of a grid-connected VSC with an LCL filter is stable without any damping if the current sensors are on the inverter side. The stability analysis was performed with the assumption that the grid voltage has no effect on the control loop, and the grid impedance was represented by a short circuit. These assumptions are reasonable if the VSC is connected to a strong grid, which is characterized by constant voltage magnitude and frequency, and low grid impedance. In practice, the VSC, particularly when used as a renewable energy interface, could be connected to a weak grid, where the voltage magnitude and grid impedance fluctuates. The grid impedance is the Thévenin equivalent impedance at the PCC and it fluctuates, as loads and sources are continuously being connected and disconnected from the grid. The variation of the grid impedance affects the stability and performance of the controller and the quality of the current injected by the VSC [145], [146], [147], [148].

The performance of the controller and the quality of the current injected into the grid by the VSC is also affected by the presence of harmonics in the grid voltage [149]. The main sources of harmonics in the grid include power electronic equipment, arcing equipment and devices with saturated magnetic cores [150]. In direct power controlled VSCs, grid voltage harmonics affect the instantaneous power estimation, and the quality of the grid current [62], [34]. The distortion in the current can be reduced by using individual harmonic current PI controllers [151], [88]. However, this adds to the complexity of the controller. Weak grids are more prone to harmonics than strong grids, and the controller should be robust enough to inject a sinusoidal current when the grid voltage is distorted.

In this chapter, the performance of the virtual-flux based direct power control with space vector modulation (VF-DPC-SVM) is investigated. The stability of the system when connected to a grid with variable grid impedance is verified by including the grid inductance in the closed-loop transfer function. The effect of variable grid inductance on the quality of the injected current is investigated for different values of power controller proportional gain. The effect of harmonics on the current quality and the controller tuning

is also investigated. Simulation and experimental results are presented to verify the investigation, and compared with the results obtained using voltage based DPC-SVM.

5.2 Harmonic Limits

The allowable distortion in the injected current of the VSC is limited by international standards. The most quoted standards are IEEE 519 [14] and IEC 61000-3-12:2011/BS EN 61000-3-12: 2011 [15]. Standards dealing specifically with limiting the harmonic distortion caused by distributed generation are IEEE 1547 [13] and IEC61000-3-15:2011 [152]. The IEEE standards give the maximum allowed total demand distortion (TDD) for systems rated from 120 V to 69 kV for a range of short-circuit current ratios from less than 20 to greater than 1000. The TDD gives a measure of the harmonic distortion in the system as a ratio of the full-load current. The IEC standards give the allowable individual harmonic distortion for systems with a rated current up to 75 A/phase and a voltage rating up to 400V. Due to the higher voltages considered, the IEEE standards are more rigorous than the IEC standards, and will be used as a bench mark in this investigation.

The main points of the IEC and IEEE standards are summarized in Table 5.1.

Table 5.1 Harmonic Limits for grid-connected VSC [14], [152]

Harmonic order (n)	IEC Limit (%)	IEEE Limit (%)
2	1.0	Not specified
3	21.6	4.0
5	10.7	
7	7.2	
9	3.8	
11	3.1	
13	2.0	2.0
$13 \leq n \leq 17$	1.0	
$17 \leq n \leq 23$		1.5
$23 \leq n \leq 35$		0.6
$35 \leq n \leq 50$		0.3
Even harmonics	1.0	25% of odd harmonics
TDD	Not specified	5.0

5.3 Effect of Grid Impedance Variation on Controller Stability

5.3.1 Variation of Resonance Frequency with Grid Inductance

The single-phase equivalent circuit of the grid-connected converter with a non-zero grid impedance is shown in Figure 5.1.

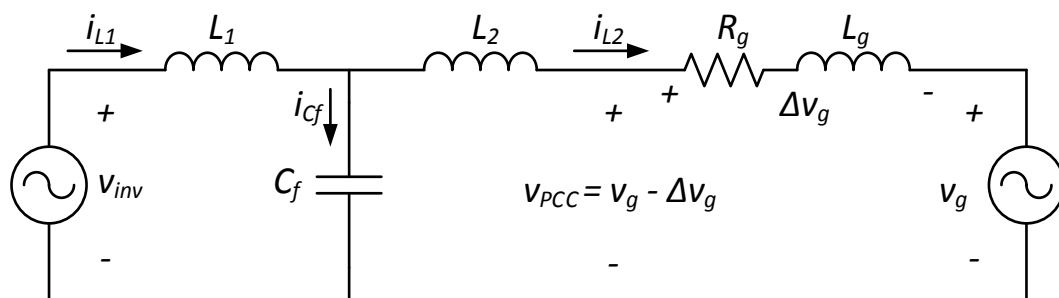


Figure 5.1 Single-phase equivalent circuit of grid-connected VSC with grid impedance.

Due to the variation in grid impedance, the magnitude of the voltage at the PCC will vary as shown by the grid impedance voltage drop, Δv_g in Figure 5.1. The grid impedance voltage drop depends on the grid current and is given by

$$\Delta v_g = i_{L2} (R_g + j\omega L_g) \quad (5.1)$$

where R_g is the resistive component of the grid impedance and L_g is the inductive component of the grid impedance.

The variation of the grid impedance will have an effect on the closed-loop stability of the control system. This is because the grid impedance is in series with the grid-side inductor of the LCL filter and it will change the attenuation of harmonics in the grid current and the resonance frequency of the filter. The added inductance will increase the harmonic attenuation, but it will decrease the resonance frequency, which could affect the controller bandwidth and stability.

The transfer function of the LCL filter with the current sensors on the inverter side and with the grid inductance taken into consideration is given by

$$G_{LCL, L_g}(s) = \frac{I_{L1}(s)}{V_{inv}(s)} = \frac{1}{L_1 s} \frac{s^2 + 1/[(L_2 + L_g)C_f]}{s^2 + (L_1 + L_2 + L_g)/[L_1(L_2 + L_g)C_f]} \quad (5.2)$$

The resonance frequency is given by

$$\omega_{res} = \sqrt{\frac{L_1 + (L_2 + L_g)}{L_1(L_2 + L_g)C_f}} \quad (5.3)$$

The effect of the grid inductance variation on the resonance frequency is shown in Figure 5.2. There is a steep reduction in resonance frequency for a small change in grid inductance at low values of grid inductance whereas for higher values of grid inductance the reduction in resonance frequency is not very steep. Considering a grid inductance increase from 0.1 mH to 0.5 mH, the corresponding reduction in resonance frequency is from 1.48 kHz to 1.13 kHz, which is a reduction of 24.1%. Further increase in the grid inductance will yield a lower relative reduction in the resonance frequency; therefore, the grid inductance variation will be limited to the range 0.1 mH to 0.5 mH.

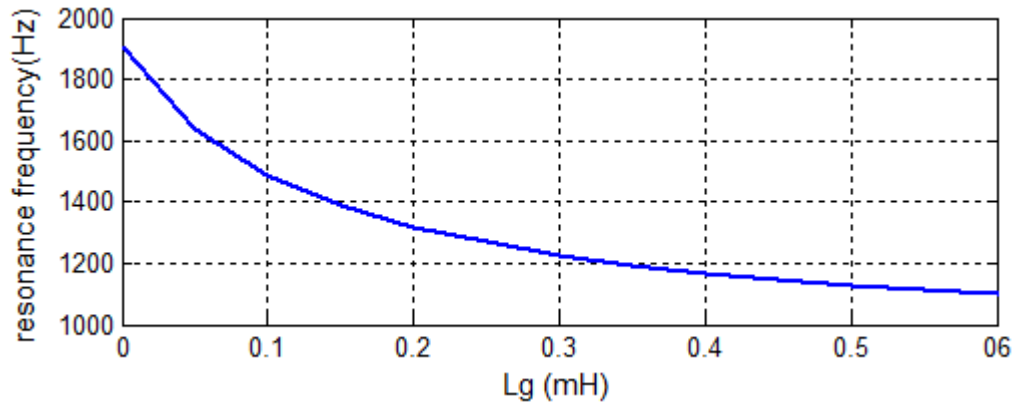


Figure 5.2 Variation of resonance frequency with grid inductance.

5.3.2 Stability Analysis

The transfer function of the LCL filter given in equation (5.2) is inserted in the closed-loop transfer function of the power control system and the discrete form of the transfer function is used to plot the poles and zeros of the system. To determine the effect of the grid inductance on the stability of the system the proportional gain, K_p is kept constant in turn and the grid inductance is varied from 0 to 0.5 mH for each value of K_p .

The pole-zero plot with $K_p = 1$ and the grid inductance varying from 0 to 0.5 mH is shown in Figure 5.3.

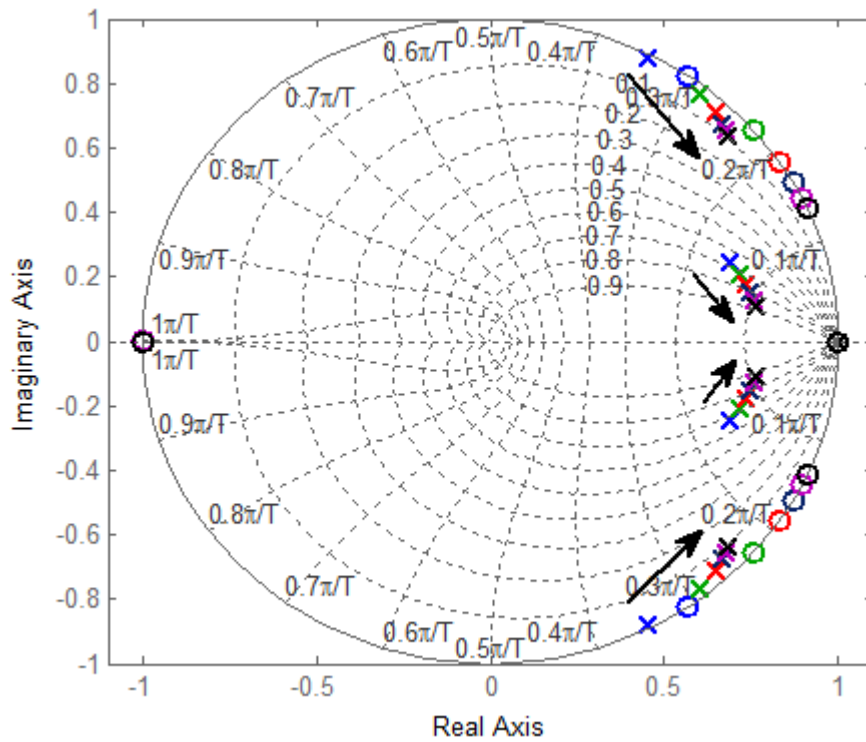


Figure 5.3 Pole-zero plot for variable grid inductance with $K_p = 1$.

The closed-loop system has five poles, a real pole at the boundary of the unit circle and two complex pole-pairs. The real pole is not affected by the variation of grid inductance, while the complex poles are affected. The complex pole pairs can be divided into the higher frequency resonance pole pair and the lower frequency anti-resonance pole pair.

For low values of grid inductance, the resonance pole-pair on the edge of the unit circle has very low damping of almost zero, and could cause undamped oscillations in the step response of the system. At higher values of grid inductance, the damping of the poles increases to 0.1, and this will improve the damping of the oscillations. The other complex pole-pair is deeper within the unit circle and has a high damping, ranging from 0.7 to 0.9 for the lowest and highest values of grid inductance, respectively. Oscillations due to this pole-pair will be of low frequency, ranging from 0.74 kHz to 0.46 kHz, and will be sufficiently damped.

The pole-zero plot with $K_p = 2$ and the grid inductance varying from 0 to 0.5 mH is shown in Figure 5.4.

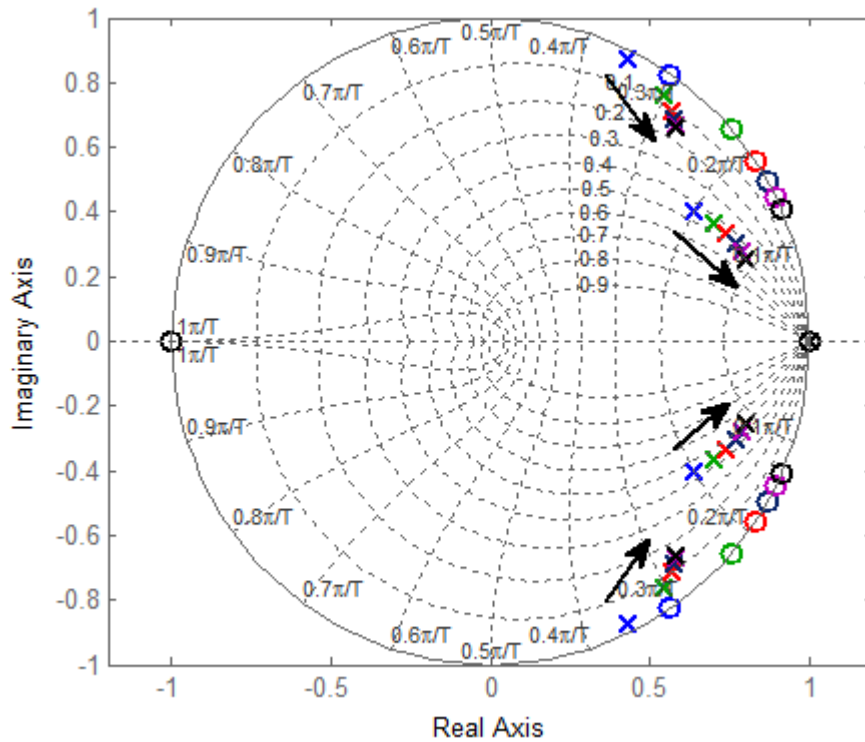


Figure 5.4 Pole-zero plot for variable grid inductance with $K_p = 2$.

The resonance pole-pair on the edge of the unit circle has very low damping for low values of grid inductance and the damping increases as the grid inductance increases. The highest damping achieved is 0.15 at a grid inductance of 0.5 mH. There will still be under-damped oscillations in the system response but they will have better damping than that achieved for $K_p = 1$. The anti-resonance pole-pair lying deeper within the unit circle has a higher damping which increases from 0.44 to 0.49 as the grid inductance increases. This is lower than the damping achieved with $K_p = 1$ but the low-frequency oscillations, ranging from 1 kHz to 0.56 kHz as grid inductance increases, will be sufficiently damped. The pole-zero plot with $K_p = 3$ and the grid inductance varying from 0 to 0.5 mH is shown in Figure 5.5.

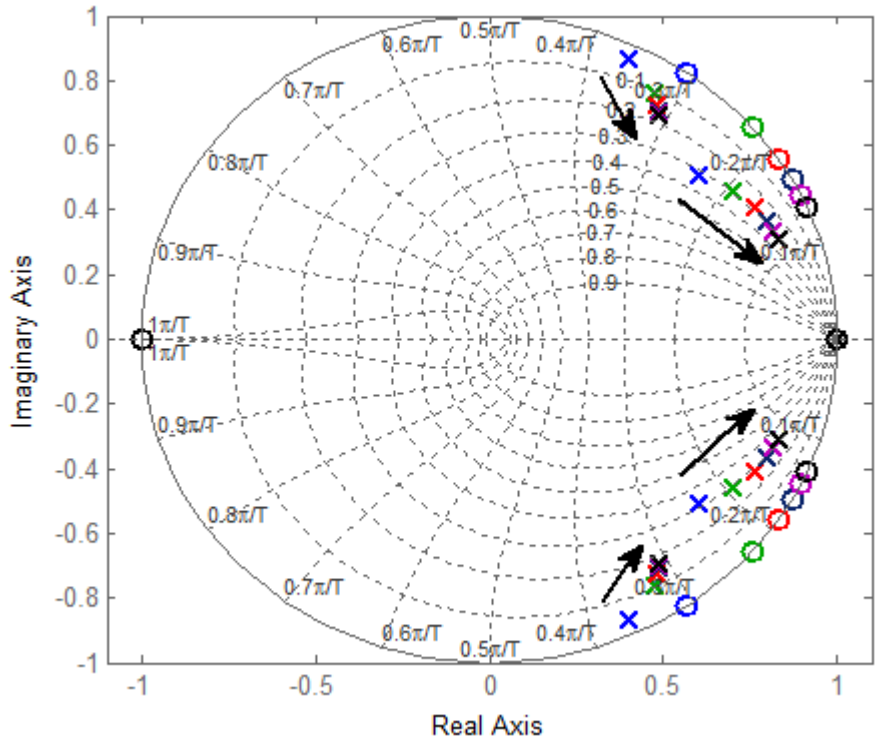


Figure 5.5 Pole-zero plot for variable grid inductance with $K_p = 3$.

There is a noticeable increase in the damping of the resonance pole-pair at the edge of the unit circle. The damping ranges from 0.04, for $L_g = 0$ to 0.17 for $L_g = 0.5$ mH; with the frequency ranging from 1.55 kHz to 1.8 kHz. The anti-resonance pole-pair lying deeper within the unit circle has a damping of 0.3 which does not vary much with the variation of grid inductance. This is lower than the damping achieved with lower values of K_p . The frequency of the oscillations will range from 1.2 kHz to 0.59 kHz as the grid inductance increases.

From the foregoing analysis, it can be concluded that any further increase in K_p will not have much effect on the resonance pole-pair, and will drive the anti-resonance pole-pair closer to the boundary of the unit circle, which will result in increased oscillations with low damping.

Of the range of K_p values considered, $K_p = 2$ gives the best stability in terms of damping of both the resonance and anti-resonance pole-pairs.

5.4 Power Estimation with Distorted Voltage and Current

In a direct power control scheme the power estimation plays an important part in the performance of the system. The principle of instantaneous power estimation based on voltage and virtual flux has been reviewed in Chapter 4. The voltages and currents are assumed to be purely sinusoidal, with no harmonics, and the effect of voltage and current distortion was not considered. In this section, the power estimation with distorted voltage and current will be considered. Classical power theories for distorted voltages and currents are reviewed. Due to the limitations of the classical power theories based on rms values of voltage and current, modern power theories based on instantaneous values of voltage and current are considered, and found to be more suitable for power estimation because they cater for distorted and unbalanced voltages and currents. Finally, virtual flux based power estimation with distorted current is presented with the virtual-flux assumed to be purely sinusoidal.

5.4.1 Classical Power Theories for Distorted Voltage and Current

A distorted grid voltage waveform, consists of the fundamental frequency component and harmonics whose frequencies are usually integer multiples of the fundamental frequency. Mathematically this is expressed as

$$v_g = \sum_{n=1}^{\infty} \sqrt{2} V_{gn} \cos(\omega_n t + \theta_n) \quad (5.4)$$

where V_{gn} is the rms value of the n th harmonic voltage, ω_n is its angular frequency and θ_n is its phase angle.

Similarly, the current can be written as

$$i_L = \sum_{n=1}^{\infty} \sqrt{2} I_{Ln} \cos(\omega_n t + \theta_n - \varphi_n) \quad (5.5)$$

where I_{Ln} is the rms value of the n th harmonic current, and φ_n is the phase angle between the n th harmonic voltage and the n th harmonic current.

The rms value of the distorted voltage is given by

$$V_g = \sqrt{\frac{1}{T} \int_0^T v_g^2 dt} = \sqrt{\sum_{n=1}^{\infty} V_{gn}^2} \quad (5.6)$$

where $T = 2\pi/\omega$ is the periodic time of the fundamental frequency voltage and v_g is the instantaneous value of the voltage.

In the same way, the rms value of the distorted current is given by

$$I_L = \sqrt{\frac{1}{T} \int_0^T i_L^2 dt} = \sqrt{\sum_{n=1}^{\infty} I_{Ln}^2} \quad (5.7)$$

where i_L is the instantaneous value of the current.

The instantaneous power is the product of the instantaneous voltage and the instantaneous current and is given by

$$p = v_g i_L \quad (5.8)$$

According to the classical definition of active power by Fryze [153], [154], it is the average of the instantaneous power and is given by

$$P = \frac{1}{T} \int_0^T p dt \quad (5.9)$$

Using equations (5.4) to (5.9), the active power for distorted voltage and current is obtained as

$$P = \sum_{n=1}^{\infty} V_{gn} I_{Ln} \cos \varphi_n \quad (5.10)$$

The apparent power is defined as the product of the rms values of the voltage and the current.

$$S = V_g I_L = \sqrt{\sum_{n=1}^{\infty} V_{gn}^2 \sum_{n=1}^{\infty} I_{Ln}^2} \quad (5.11)$$

The reactive power is given by

$$Q = \sum_{n=1}^{\infty} V_{gn} I_{Ln} \sin \varphi_n \quad (5.12)$$

Using these definitions of active power, reactive power and apparent power, the apparent power cannot be expressed, in a power triangle, as the square root of the sum of the squares of the active power and the reactive power, as is the case for sinusoidal voltages and current. Thus, a new form of power called the “distortion power” was introduced by Budeanu [155], [156]. The distortion power is given by

$$D = \sqrt{S^2 - P^2 - Q^2} \quad (5.13)$$

The relationship of distortion power to apparent power, active power and reactive power is shown graphically in the power tetrahedron in Figure 5.6.

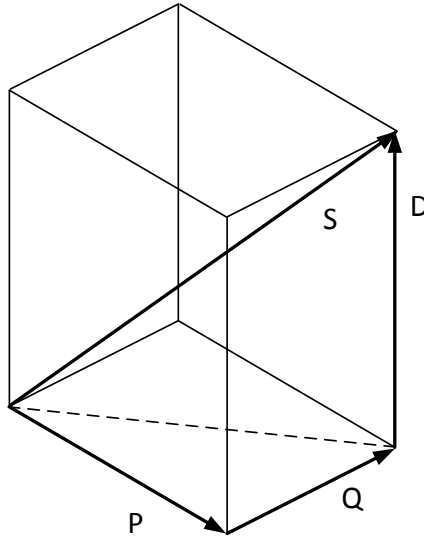


Figure 5.6 Power tetrahedron showing the four power components defined by Budeanu [62].

5.4.2 Modern Instantaneous Power Theories for Distorted Voltage and Current

Classical power theories have been found to be inadequate for application in power electronic equipment due to a lack of physical meaning of the reactive and distortion powers [157]. The modern instantaneous power theories by Akagi [140] and Peng [142], [158] are more general and take into consideration the harmonics and imbalances in the voltage and current.

The distorted grid voltage is given as

$$\underline{v}_g = \sum_{n=1}^{\infty} (v_{gcn} + jv_{g\beta n}) \quad (5.14)$$

where v_{gcn} and $v_{g\beta n}$ are the orthogonal components of the n th harmonic voltage in the stationary reference frame.

And the distorted current is given by

$$\underline{i}_L = \sum_{n=1}^{\infty} (i_{Lcn} + ji_{L\beta n}) \quad (5.15)$$

where $i_{L\alpha n}$ and $i_{L\beta n}$ are the orthogonal components of the n th harmonic current in the stationary reference frame.

The instantaneous power calculated using the distorted voltage and current will have a constant component and oscillating components. The constant component is due to the product of the fundamental frequency voltage and current, and harmonics with the same frequency. The oscillating components are due to the products of harmonics with different frequencies and positive and negative sequence components if they are present.

The instantaneous active power estimated using distorted voltage and current is given by

$$p = \bar{p} + \tilde{p} \quad (5.16)$$

Similarly, the reactive power is given by

$$q = \bar{q} + \tilde{q} \quad (5.17)$$

where \bar{p} and \bar{q} are the constant components of the power; \tilde{p} and \tilde{q} are the oscillating components.

If the distorted voltage and current are assumed to be balanced, so that only positive-sequence components are present, the power components are expressed in terms of the voltage and current as

$$\bar{p} = \frac{3}{2} \sum_{n=1}^{\infty} (v_{g\alpha n} i_{L\alpha n} + v_{g\beta n} i_{L\beta n}) \quad (5.18)$$

$$\bar{q} = \frac{3}{2} \sum_{n=1}^{\infty} (v_{g\alpha n} i_{L\beta n} - v_{g\beta n} i_{L\alpha n}) \quad (5.19)$$

$$\tilde{p} = \frac{3}{2} \sum_{\substack{m=1 \\ m \neq n}}^{\infty} \left[\sum_{n=1}^{\infty} (v_{g\alpha m} i_{L\alpha n} + v_{g\beta m} i_{L\beta n}) \right] \quad (5.20)$$

$$\tilde{q} = \frac{3}{2} \sum_{\substack{m=1 \\ m \neq n}}^{\infty} \left[\sum_{n=1}^{\infty} (v_{g\alpha m} i_{L\beta n} - v_{g\beta m} i_{L\alpha n}) \right] \quad (5.21)$$

The oscillating power components will be superimposed on the constant power components and will be visible as ripples in the output power of the VSC.

When the virtual flux is used for power estimation, only the current will be significantly distorted because the virtual flux has a very low distortion due to its estimation method outlined in detail in Chapter 4. Assuming the virtual flux is purely sinusoidal, with only

the fundamental frequency component present, the power components will be defined as shown below.

$$\bar{p} = \frac{3}{2}(\psi_{g\alpha}i_{L\beta 1} - \psi_{g\beta}i_{L\alpha 1}) \quad (5.22)$$

$$\bar{q} = \frac{3}{2}(\psi_{g\alpha}i_{L\alpha 1} + \psi_{g\beta}i_{L\beta 1}) \quad (5.23)$$

$$\tilde{p} = \frac{3}{2} \sum_{n=2}^{\infty} (\psi_{g\alpha}i_{L\beta n} - \psi_{g\beta}i_{L\alpha n}) \quad (5.24)$$

$$\tilde{q} = \frac{3}{2} \sum_{n=2}^{\infty} (\psi_{g\alpha}i_{L\alpha n} + \psi_{g\beta}i_{L\beta n}) \quad (5.25)$$

Equations (5.20), (5.21), (5.24) and (5.25) show that there are oscillations in the estimated powers regardless of whether voltage or virtual flux is used. It cannot be concluded from these equations which one will give better performance between voltage based power estimation and virtual flux power estimation in a direct power control scheme. The performance of the control scheme will also depend on other factors, such as the controller tuning, the grid impedance and the synchronization. In the following sections, the performance of the voltage based and virtual flux based direct power control schemes will be investigated for a range of control parameters, grid inductance and grid voltage distortion.

5.5 Simulation Results with Ideal Grid Voltage

The effect of grid inductance variation on the performance of the system is investigated further by varying the grid inductance in the simulation model for different values of proportional gain, K_p . Fast Fourier Transform (FFT) analysis of the grid current waveform is used to investigate the harmonics present in the current. In the simulation model, the resistance of the filter inductors, capacitors and grid impedance is neglected. This is to remove any damping that may be caused by these resistances. The simulation results are presented for two values of grid inductance, 0.1 mH and 0.5 mH. Two control schemes are used namely VF-DPC-SVM and voltage-based DPC-SVM.

For the first part of the analysis, the grid is modelled as an “ideal” grid, whose voltage is purely sinusoidal with no harmonics. For the second part the grid is modelled as a distorted grid using the harmonic data obtained from measurements of the grid voltage at the PCC for the experimental set up.

5.5.1 With $L_g = 0.1$ mH

With the grid inductance set to 0.1 mH, the proportional gain for both control schemes is varied and the total harmonic distortion in the current is obtained for each value of K_p . The variation of the current THD with proportional gain is shown in Figure 5.7.

A lower THD of 2.19 % for a proportional gain of $K_p = 2$ is achieved with VF-DPC-SVM than with voltage based DPC-SVM for which the lowest THD achieved is 3.74 % for a proportional gain of $K_p = 1.5$. Both control schemes meet the IEEE 519 requirement of a current THD of less than 5 %.

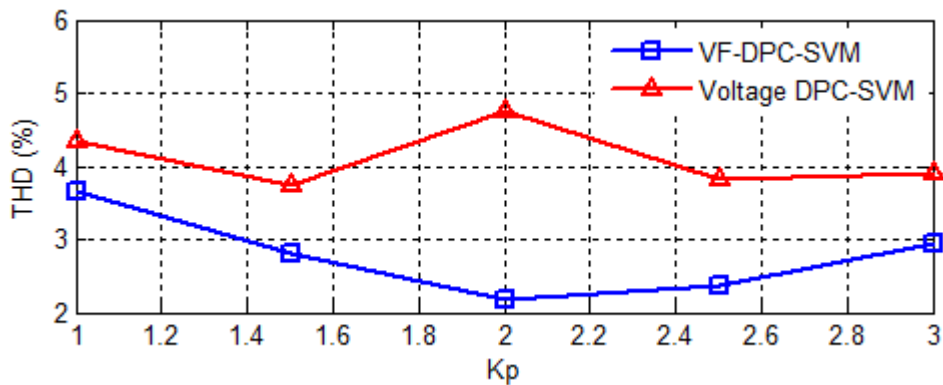


Figure 5.7 Variation of current THD with K_p for $L_g = 0.1$ mH with ideal grid voltage.

The frequency spectrum of the current with the lowest THD achieved for each method is plotted in Figure 5.8. VF-DPC-SVM has a more evenly spread harmonic spectrum, with the highest harmonics being the 5th and 7th in the low-order range while in the higher range the highest harmonics are in the range of 23rd to 32nd which is within the same range as the resonance frequency of the LCL filter. Voltage DPC-SVM has harmonics with magnitude greater than 1% of the fundamental between the 23rd and 27th harmonics. Thus, while both control schemes show good harmonic rejection in the low-frequency range, at frequencies close to the resonance frequency VF-DPC-SVM performs better.

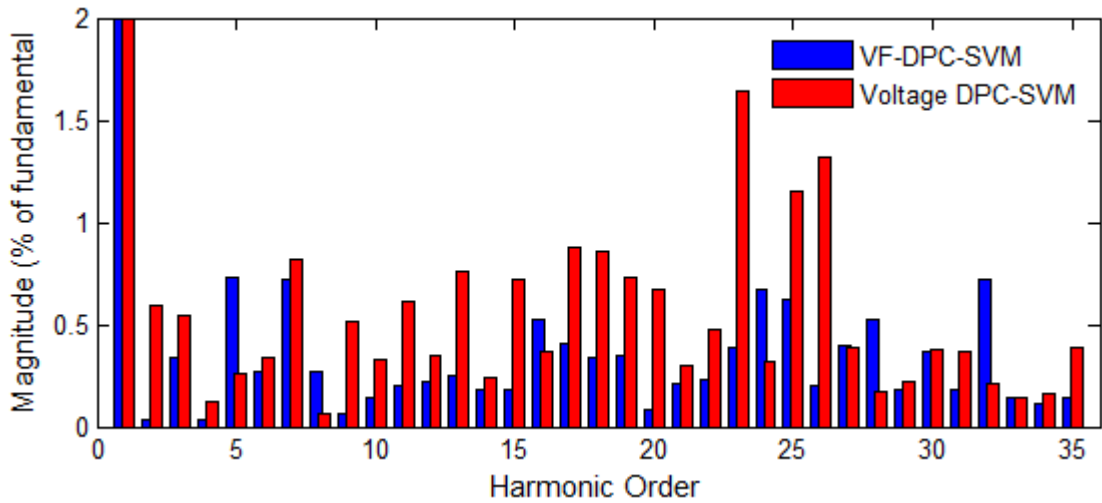


Figure 5.8 Frequency spectra of the grid current for $L_g = 0.1$ mH with ideal grid voltage.

5.5.2 With $L_g = 0.5$ mH

The variation of the current THD with proportional gain at a higher grid inductance of 0.5 mH is shown in Figure 5.9. VF-DPC-SVM shows very little variation in the THD, which is less than 2 %, for all values of K_p considered. Voltage DPC-SVM shows a wide variation for values of K_p less than 2, but less variation for values greater than 2. The lowest THDs achieved for both methods are identical.

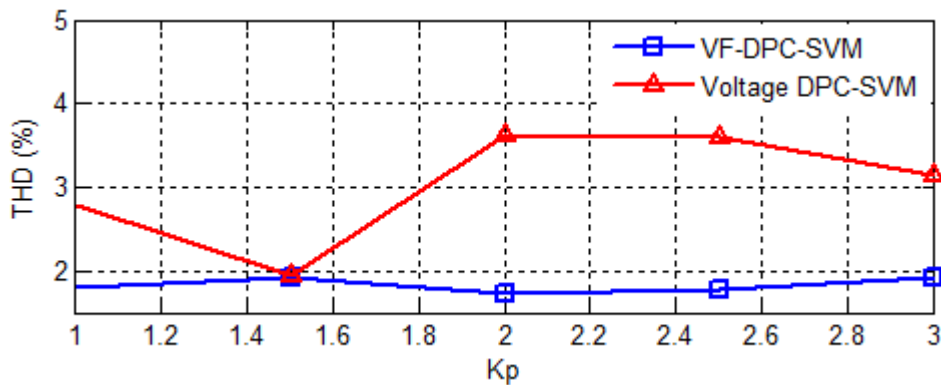


Figure 5.9 Variation of current THD with K_p for $L_g = 0.5$ mH with ideal grid voltage.

The frequency spectrum of the current with the lowest THD achieved for each method is plotted in Figure 5.10. For VF-DPC-SVM, the highest harmonics are in the lower range between the 5th and 13th, with the 5th being the highest at 0.82 %, while the higher order

harmonics are much lower, with the 18th, 19th and 21st harmonics being the only ones greater than 0.2 %. For voltage DPC-SVM, the low-order harmonics are more evenly spread, though even harmonics such as the 4th and 6th have the highest magnitudes of 0.72 % and 0.7 % respectively. The higher order harmonics are greater than for VF-DPC-SVM with the 19th and 24th harmonics being the highest with magnitudes of 0.5% and 0.35 %.

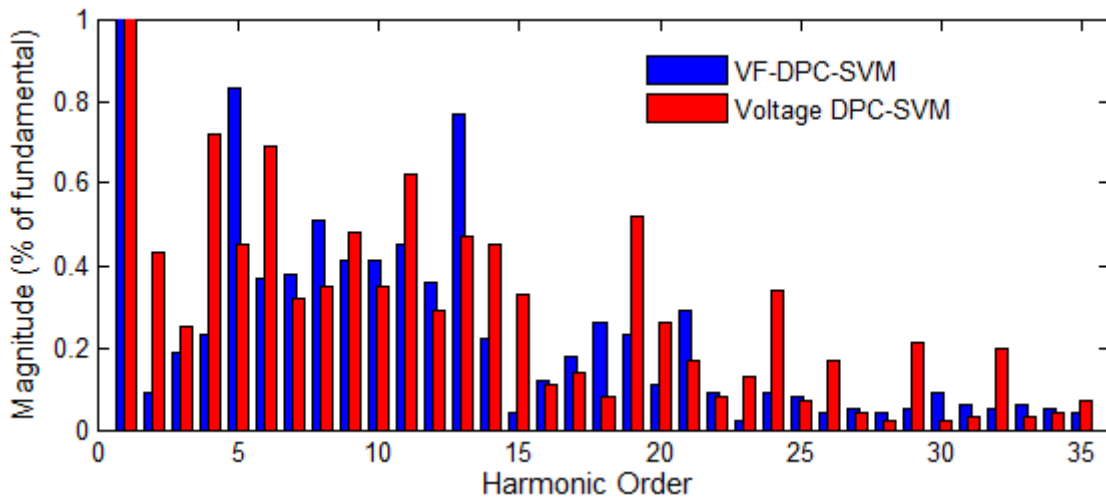


Figure 5.10 Frequency spectra of the grid current for $L_g = 0.5$ mH with ideal grid voltage.

Comparing the results for the two values of grid inductance, it can be seen that at the higher value the current is less distorted. This is because the grid impedance appears as additional impedance to that offered by the LCL filter inductors, and provides additional harmonic attenuation.

5.6 Simulation Results with Distorted Grid Voltage

The distorted grid is created by superimposing the following harmonic components on the fundamental frequency voltage: 5th harmonic of 1.81%; 7th harmonic of 2.56%; 11th harmonic of 1.21%; and 13th harmonic of 1.08%. The THD of this distorted voltage is 3.53%. These harmonics were obtained from measurement of the grid voltage at the PCC for the experimental system.

5.6.1 With $L_g = 0.1$ mH

The grid inductance is set to 0.1 mH, and the proportional gain for both control schemes is varied. The total harmonic distortion in the current is obtained for each value of K_p and is shown in Figure 5.11.

The lowest THD achieved for the current with VF-DPC-SVM is 3.57 % with $K_p = 2$, while the lowest THD achieved with voltage based DPC-SVM is 5.75 % with $K_p = 2.5$. Therefore, with a distorted grid voltage only VF-DPC-SVM achieves a THD lower than the maximum allowed by the IEEE 519.

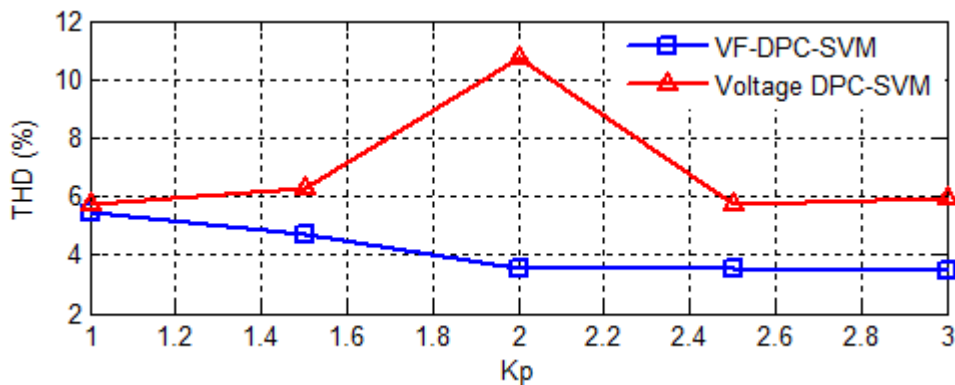


Figure 5.11 Variation of current THD with K_p for $L_g = 0.1$ mH with distorted grid voltage.

The frequency spectrum of the current with the lowest THD achieved for each method is plotted in Figure 5.12. The main harmonics present in the spectrum for VF-DPC-SVM are the 5th and the 7th with magnitudes of 1.61 % and 1.86 %, respectively. Other prominent low-order harmonics are the 11th and 13th with magnitudes less than 1%. In the resonance frequency range, the prominent harmonics are the 23rd and 28th both with magnitude less than 1 %. For voltage based DPC-SVM, the 3rd, 5th, 7th and 9th are the main low-order harmonics, with respective magnitudes of 1.69 %, 2.57 %, 2.1 % and 1.66 %. Other harmonics with magnitude greater than 1 % include the 15th and 21st. While most individual harmonics are within the limits specified by IEEE 519, the 33rd and the 35th exceed the limits with respective magnitudes of 0.78 % and 0.69 %.

Therefore, with low grid impedance, VF-DPC-SVM has a better performance than voltage based DPC-SVM when the grid voltage is distorted.

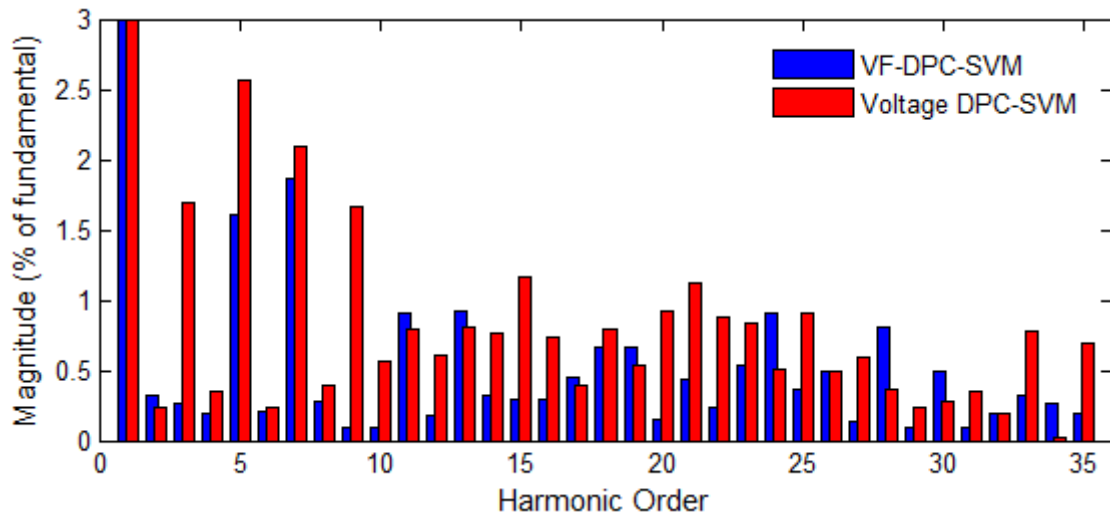


Figure 5.12 Frequency spectra of the grid current for $L_g = 0.1$ mH with distorted grid voltage.

5.6.2 With $L_g = 0.5$ mH

The grid inductance is increased to 0.5 mH and the proportional gain for each control scheme is varied and the THD of the current obtained for each control scheme is plotted against the corresponding proportional gain as shown in Figure 5.13. The lowest current THD achieved with VF-DPC-SVM is 3.54 % for $K_p = 2$, while for voltage based DPC-SVM it is 6.07 % for $K_p = 1.5$. Therefore, while both control schemes are able to achieve stability for the investigated range of K_p values, only VF-DPC-SVM achieves a THD of less than 5 %.

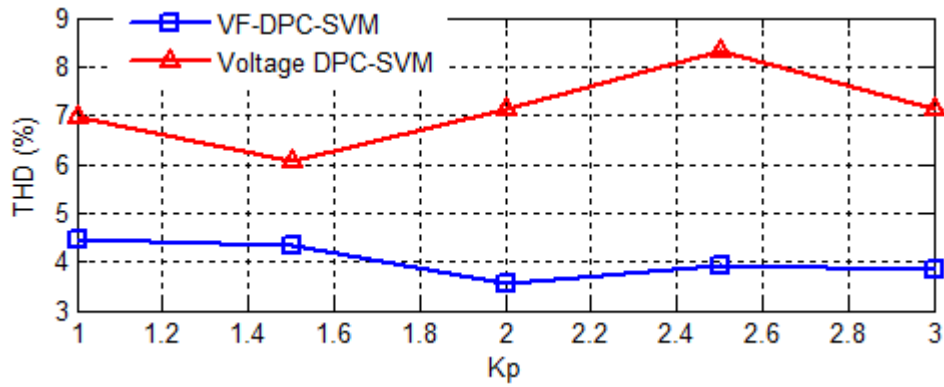


Figure 5.13 Variation of current THD with K_p for $L_g = 0.5$ mH with distorted grid voltage.

The frequency spectrum of the current with the lowest THD achieved for each method is plotted in Figure 5.14. For both control schemes the low order harmonics are more prominent than the higher order harmonics because the increased grid inductance increased the attenuation of the higher order harmonics. For VF-DPC-SVM the main harmonics are the 5th, 7th, 11th and 13th with respective magnitudes of 1.43 %, 1.99 %, 1.73 % and 1.1 %. They are all within the individual harmonic limits specified by IEEE 519. For voltage based DPC-SVM the main harmonics are the 3rd, 5th, and 7th with respective magnitudes of 1.32 %, 4.15 % and 3.53 %. The 11th and 13th are significantly less than with VF-DPC-SVM with magnitudes of 0.27 % and 0.49 % respectively.

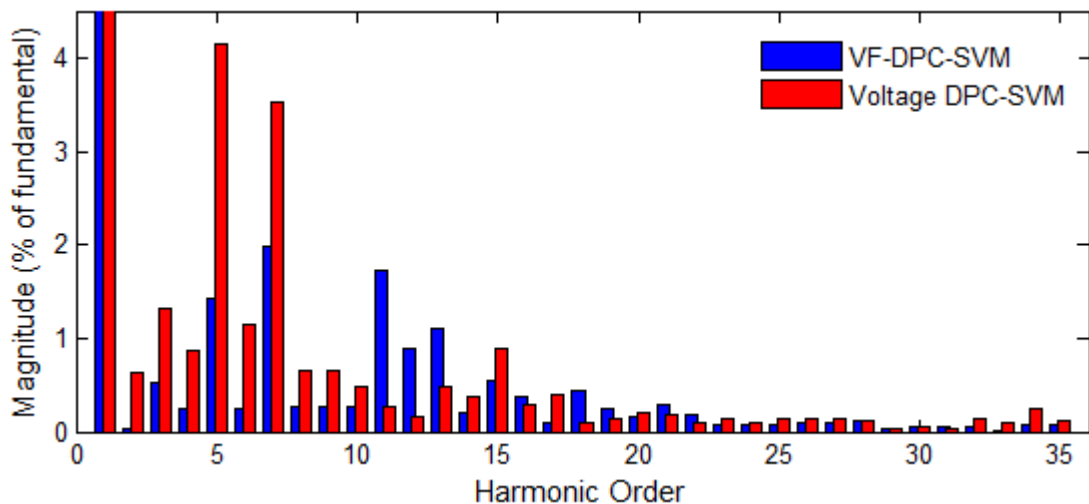


Figure 5.14 Frequency spectra of the grid current for $L_g = 0.5$ mH with distorted grid voltage.

5.7 Experimental Results

The harmonic analysis was carried out on the current obtained experimentally for both VF-DPC-SVM and voltage based DPC-SVM. The voltage at the PCC for the experimental tests has a harmonic profile similar to the one used in the simulations with a distorted grid (which was based on the harmonic spectrum of the measured voltage) and has a THD which varies between 3.20 % and 3.90 %. The grid impedance is not negligible due to the use of long connecting cables, the impedance of the variac, and the impedance of the isolation transformer. The grid impedance was estimated using the PQ variation method of grid impedance estimation described in [146]. The estimated grid resistance was $R_g = 0.35 \Omega$ and the estimated grid inductance was $L_g = 0.3 \text{ mH}$. The presence of a significant resistive component in the grid impedance is expected to have an effect on the stability of the system by indirectly acting as a passive damping resistance.

The results are divided into two parts: the first part is with the nominal grid impedance, and the second part is with an additional grid inductance of 0.3 mH.

5.7.1 With Nominal Grid Impedance

With the nominal grid impedance, the proportional gain for each control scheme was varied from 1 to 3.5 in steps of 0.5. The waveforms of the grid voltage and current for VF-DPC-SVM are shown in Figure 5.15 for $K_p = 2$. The same waveforms for voltage based DPC-SVM are shown in Figure 5.16. The variation of the current THD with the proportional gain is shown in Figure 5.17. The lowest THD obtained with VF-DPC-SVM is 2.49 % with $K_p = 3.5$, while for voltage based DPC-SVM it is 5.81 % with $K_p = 2.5$. VF-DPC-SVM achieves a THD of less than 5 % for all values of K_p considered and the THD tends to decrease as K_p is increased. On the other hand, voltage based DPC-SVM does not achieve a THD of less than 5 % for any value of K_p and there is no proportionality between the variation of K_p and the THD.

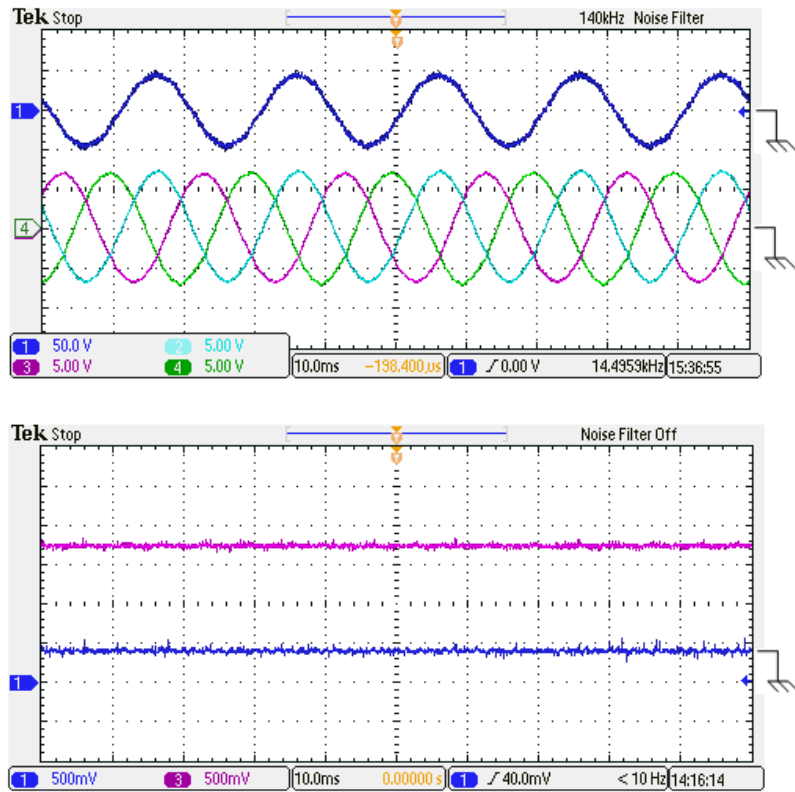


Figure 5.15 Experimental voltage (50V/div), current (5A/div) and power (200W/div) waveforms for VF-DPC-SVM with nominal grid impedance.

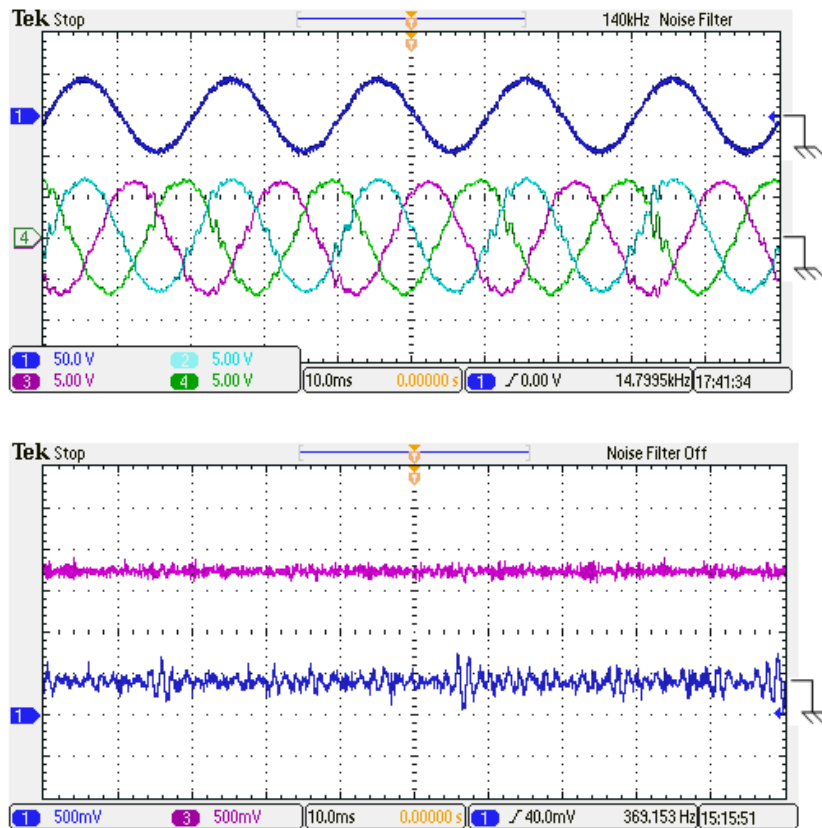


Figure 5.16 Experimental voltage (50V/div), current (5A/div) and power (200W/div) waveforms for voltage based DPC-SVM with nominal grid impedance.

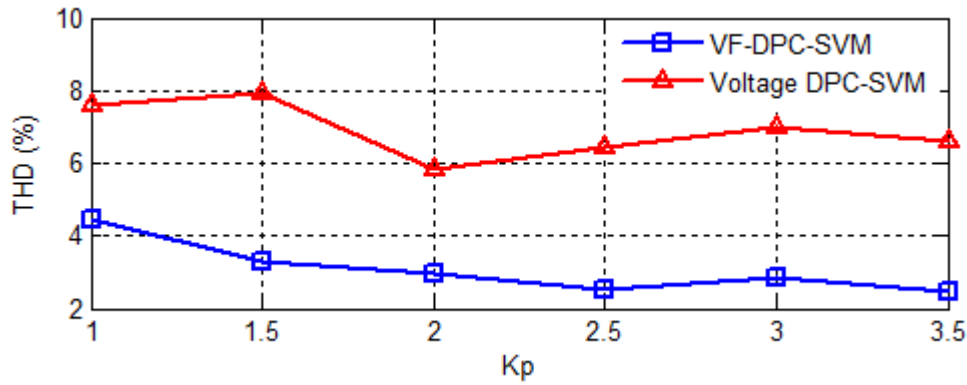


Figure 5.17 Experimental variation of current THD with K_p for a nominal grid inductance of $L_g = 0.3$ mH.

The frequency spectrum of the current with the lowest THD achieved for each method is shown in Figure 5.18. For VF-DPC-SVM the 5th, 7th, 11th, 13th and 17th harmonics have magnitudes of 0.86 %, 0.76 %, 0.26 %, 0.78 % and 0.81 %, respectively. There is also a 2nd harmonic of 0.99 %, a 3rd harmonic of 0.64 % and a 4th harmonic of 0.82 %. For voltage based DPC-SVM the main harmonics with magnitudes over 2 % are the 5th and 7th with respective magnitudes of 2.19 % and 2.44 %. Other harmonics with magnitudes greater than 1 % are the 4th, 11th, 13th, 15th, 16th and 17th. While the individual harmonics are less than the IEEE 519 limits, they are almost evenly spread throughout the frequency spectrum and this makes the overall distortion very high.

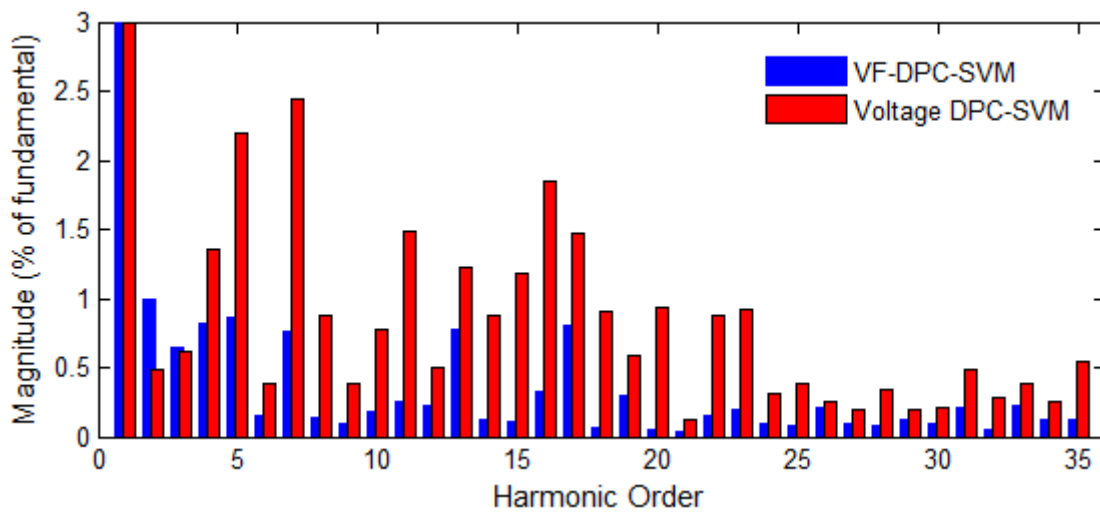


Figure 5.18 Frequency spectra of the grid current for a nominal grid inductance of $L_g = 0.3$ mH.

5.7.2 With Additional Grid Inductance

The grid inductance was increased by inserting an inductance of 0.3 mH between the LCL filter and the variac to give a total grid inductance of 0.6 mH. The voltage measurements were taken on the grid side of the LCL filter so that the additional inductance was seen as part of the grid impedance and not part of the filter. With this change, the system became unstable for voltage based DPC-SVM and the controller could not be tuned to obtain a stable response. With VF-DPC-SV, the system was stable for values of K_p starting from 1.2. The voltage, current and power waveforms obtained with $K_p = 2.5$ are shown in Figure 5.19. The variation of the current THD with the proportional gain is shown in Figure 5.20. For low values of K_p (less than 2), the THD is greater than 5 % but for values of K_p greater than 2, there is a big reduction in the THD which decreases further as K_p increases. This shows that the higher grid inductance and higher proportional gain lead to increased attenuation of harmonics.

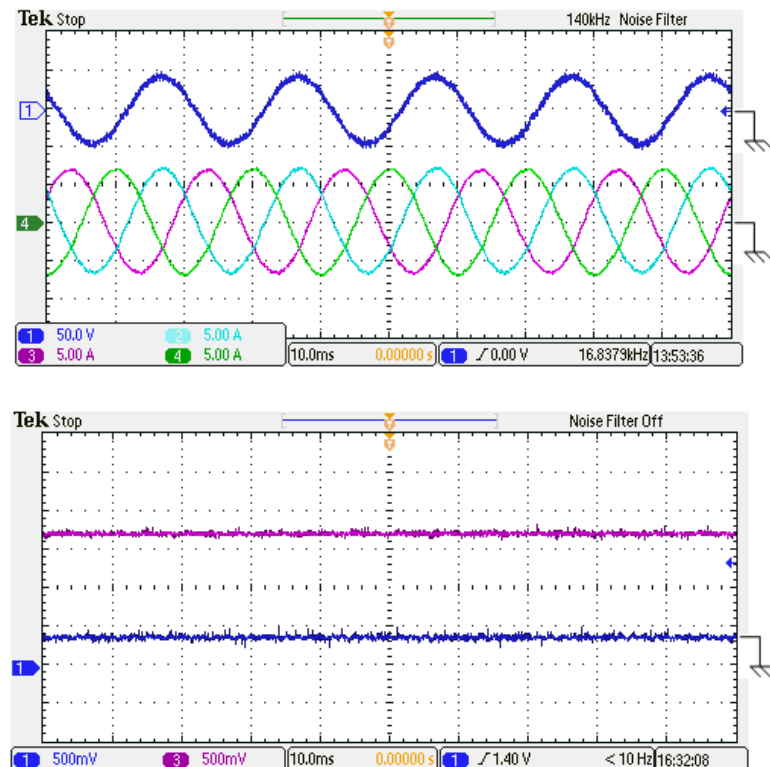


Figure 5.19 Experimental voltage (50V/div), current (5A/div) and power (200W/div) waveforms for VF-DPC-SVM with high grid inductance.

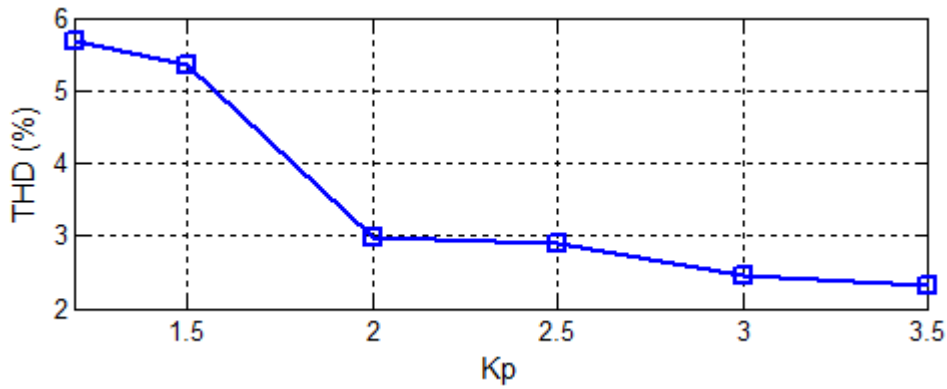


Figure 5.20 Experimental variation of current THD with K_p for a high grid inductance of $L_g = 0.6$ mH.

The frequency spectrum of the current obtained with $K_p = 3.5$ is shown in Figure 5.21. The low order harmonics from the 2nd to the 5th are quite prominent with magnitudes of between 0.47 % and 0.73 %. Outside of these the 13th harmonic has the highest magnitude of 0.88 %. Other harmonics with magnitudes greater than 0.5 % are the 7th and 17th. Beyond the 17th, all harmonics are highly attenuated with magnitudes not exceeding 0.3 %. This shows that at high values of grid inductance, the VF-DPC-SVM control scheme remains stable and with a high value of proportional gain, a very low current distortion can be achieved even if the grid voltage is distorted.

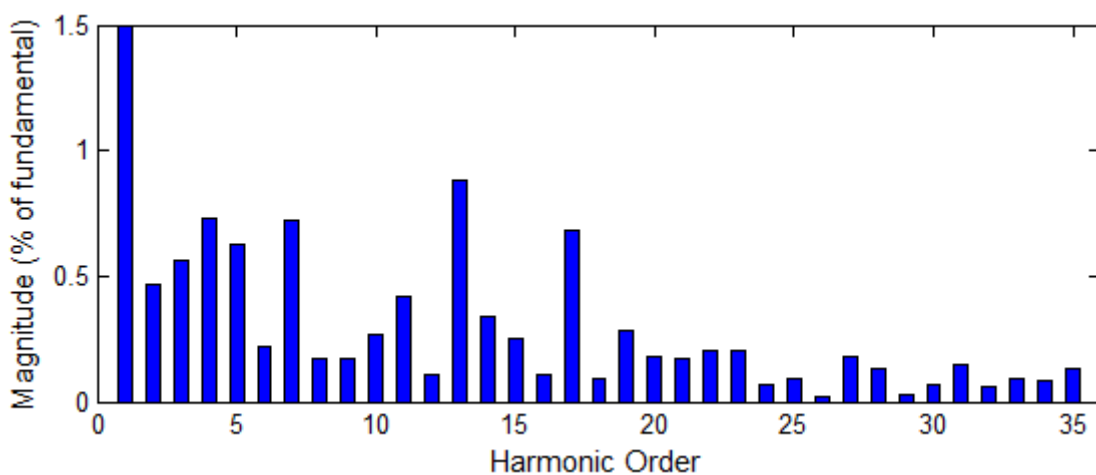


Figure 5.21 Frequency spectrum of the grid current for VF-DPC-SVM for a high grid inductance of $L_g = 0.6$ mH.

5.8 Conclusion

In this chapter, the effect of variations in grid impedance and the effect of grid voltage distortion on the converter control and the quality of the current injected to the grid was investigated. The main results are summarized below.

- The closed-loop control system is stable with varying grid inductance, despite the reduction in LCL filter resonance frequency with increasing grid inductance.
- Virtual-flux based DPC-SVM is robust to changes in grid inductance, and keeps the THD of the injected current less than 5 % for all values of grid inductance, and with grid voltage distortion. The variation in the current THD with different values of proportional gain is 1 -2 %.
- Comparatively, voltage based DPC-SVM fails to keep the THD of the injected current below 5 % when the grid voltage is distorted, and is not robust to changes in grid inductance. There is also a bigger variation in current THD with different values of proportional gain of 2-4 %.

Chapter 6 **Current Limitation during Grid Voltage Disturbances**

6.1 Introduction

With the increase in the use of renewable energy sources, the use of grid-connected voltage source converters has increased. The control of the voltage source converter is affected by the state of the grid voltage parameters such as magnitude and frequency at the point of common coupling. Under normal grid operating conditions, the grid voltage magnitude and frequency can be considered to be constant within a small allowable margin of variation. While this represents the desirable state of the grid, and is the actual operating condition most of the time, the grid experiences many disturbances which cause the voltage magnitude and frequency to vary from their expected values. The main source of grid voltage disturbances are faults. Faults in the grid can be classified as symmetrical or unsymmetrical faults. Symmetrical faults affect all the three-phase equally while unsymmetrical faults affect one or two phases. Symmetrical faults are more severe, but occur less frequently than unsymmetrical faults. Common unsymmetrical faults include single-line to ground faults, double-line faults and double-line to ground faults.

A direct consequence of faults in the grid is the flow of very high fault currents which lead to voltage dips at the point of common coupling of the VSC to the grid. A voltage dip (also known as voltage sag) is defined as a drop in the voltage magnitude to less than 0.9 pu lasting in duration from half a cycle to one minute [159]. In a direct power controlled VSC, a voltage dip will cause high currents to flow in the VSC in order to maintain the power transfer from the DC side. These currents could lead to tripping of the protective devices, thereby isolating the VSC from the grid or it could lead to damage of the semiconductor switching devices. However, due to changes in the grid codes governing the performance of grid-connected systems during grid faults, the VSC is expected to remain connected to the grid during the short duration grid disturbances [53]. Thus, control of converters during grid disturbances has become an important consideration in the design of converter control schemes.

One of the considerations in the control of grid-connected VSCs during grid faults is limiting the current to safe levels to avoid damaging the VSC. Many different approaches of current limitation during balanced and unbalanced grid faults can be found in

literature. Current limitation has been implemented in the natural reference frame [160], [161], stationary reference frame [162], [163] and synchronous reference frame [164]. Current limitation for a direct power controlled VSC is presented in [144].

Another consideration is the control of the VSC during unbalanced faults leading to unbalanced voltage dips. During unbalanced voltage dips, the presence of negative-sequence components will give rise to oscillations in the active power and reactive power, and in the grid voltage angle detected by the PLL. Conventional current control schemes such as voltage oriented control and direct power control would not be able to adequately control the current during unsymmetrical faults. A voltage oriented current control scheme suitable during unsymmetrical faults is the decoupled-double synchronous reference frame (DD-SRF) proposed in [165]. It consists of two synchronous reference frame current controllers, one rotating in the positive direction and one rotating in the negative direction. The drawback of the DD-SRF controller is that it has four PI controllers and needs two voltage angles in its implementation. An alternative to the SRF PI control is the stationary reference frame proportional-resonant (PR) control [32]. An ideal PR controller has an infinite gain at the fundamental frequency, and attenuates all other frequencies. Since both the positive and negative-sequence components have the same fundamental frequency, PR controllers are able to control unbalanced currents.

A number of control strategies for grid-connected converters during unsymmetrical grid faults have been presented in [162], [163]. The control strategies have different objectives which are achieved by the calculation of the current references using the active power and reactive power reference and the grid voltage. The main objectives include reduction or elimination of the oscillations in the active power and reactive power, and injection of balanced and sinusoidal currents. It is not possible to achieve all the objectives with the same control strategy, therefore, the chosen strategy depends on which objective is prioritized over others. The control strategies and their objectives include the instantaneous active-reactive control (IARC) which gives constant active power and reactive power, but with highly distorted and unbalanced currents; the average active-reactive control (AARC) which gives constant active power and oscillating reactive power with sinusoidal but unbalanced current; positive-negative-sequence compensation (PNSC) which gives constant reactive power and oscillating active power with sinusoidal but unbalanced currents; and the balanced positive-sequence control (BPSC) which gives active power and reactive power with reduced oscillations with balanced and sinusoidal

currents. These control strategies have also been presented in [166] where the virtual flux is used instead of the voltage to calculate the current references.

In this chapter the control of a direct power controlled VSC during symmetrical and unsymmetrical grid voltage disturbances is presented. To limit the current during voltage dips and protect the VSC, a new current limitation scheme based on limiting the active power and reactive power references is proposed. To maintain sinusoidal and balanced currents, limited to safe levels to protect the VSC during unsymmetrical faults, the controller is modified by using the positive-sequence virtual flux for synchronization and power estimation. The proposed current limitation has the advantage of directly limiting the reference powers without having to calculate new current references which makes it simpler than other current limitation schemes. While current limitation is the primary objective discussed in this chapter, it is demonstrated that the current limitation scheme can be combined with a secondary objective during unsymmetrical voltage dips. In this chapter the secondary objective is maintaining the quality of the output current, which is achieved by using the positive-sequence virtual flux (similar to the BPSC strategy).

6.2 Over-currents in Direct Power Controlled VSCs during Grid Disturbances

In a direct power controlled VSC, the magnitude of the current the VSC is delivering to the grid is proportional to the instantaneous power being delivered. During normal grid operation, the grid voltage can be assumed to be constant and therefore the current will vary proportionally with the power. If the active power losses are neglected, the active power delivered to the grid is equal to the active power on the DC side drawn from a PV array or another renewable resource. The active power reference varies as the power output of the PV array, and the current will vary proportionally. If the active power from the DC side is constant and the grid voltage suddenly decreases, but the power from the DC side does not change, therefore, to maintain the flow of active power to the grid, the grid current increases. If the VSC is already delivering close to its rated power, the rise in current could cause the protective devices to trip or cause damage to the converter switches.

The theoretical increase in current for various magnitudes of voltage dip is plotted in Figure 6.1 and it shows that for voltage dips of less than 80% the current will rise to more than 125% of its value before the voltage dip.

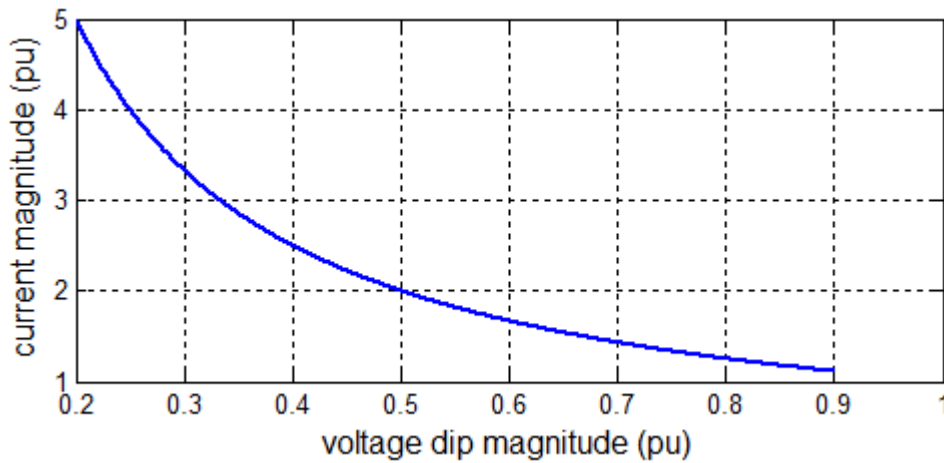


Figure 6.1 Theoretical current rise due to voltage dip.

A voltage dip of 50 % lasting for one second is applied in simulations and experiments and the resulting current rise is shown in Figure 6.2 and Figure 6.3 respectively. In the simulation, the converter is supplying rated active power while in the practical it is supplying half of rated power to avoid excessive current during the voltage dip. In both the simulation and experimental results, the current increase to twice the pre-dip current. The active power remains constant, while the reactive power is zero. This shows that the converter is able to maintain the active power flow to the grid during voltage dips but the currents will be excessive and could damage the converter switches. Thus, there is need to limit the current to a suitable level during voltage dips as described in the following section.

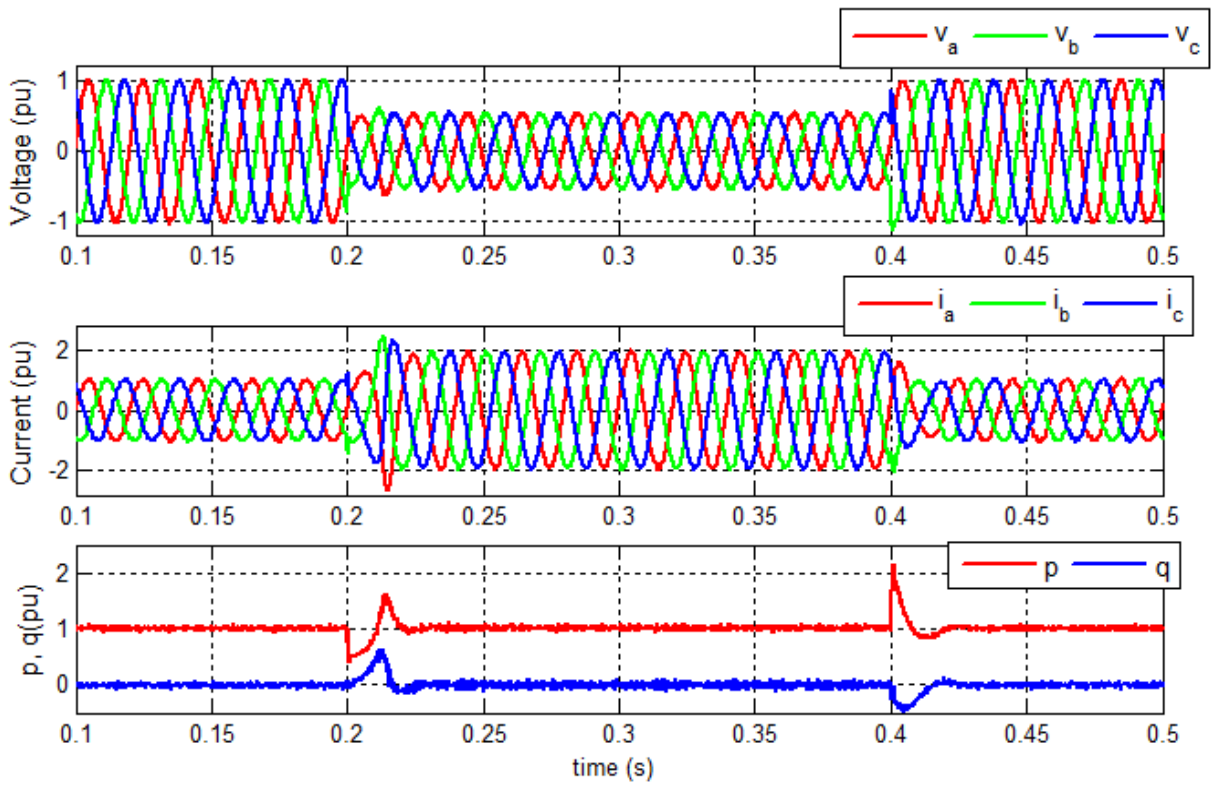


Figure 6.2 Simulated voltage dip of 50% showing current rise.

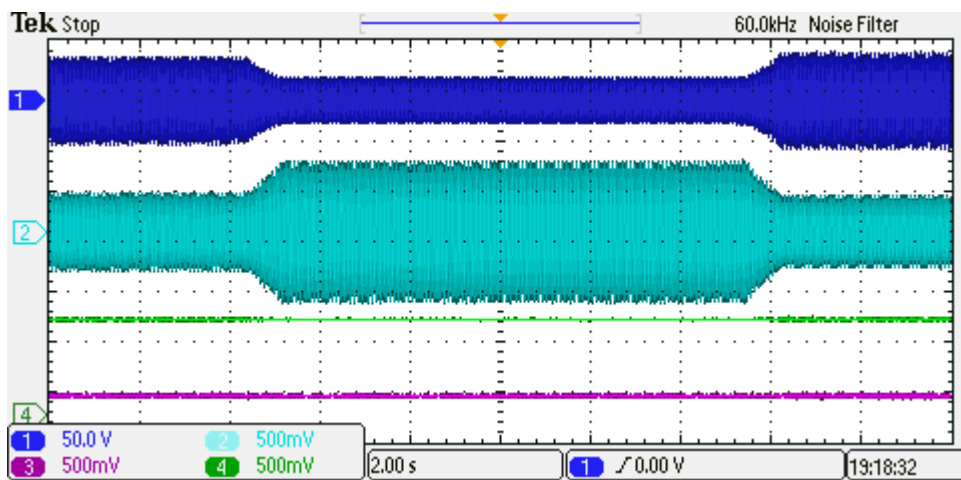


Figure 6.3 Experimental voltage dip of 50% showing current rise Upper: grid voltage (50V/div), middle: inverter current (10A/div), lower: active power and reactive power (200W/div).

6.3 Proposed Current Limitation Method

The maximum allowable current of a voltage source converter is limited by the current carrying capability of the semiconductor switches. This in turn determines the maximum power capacity of the converter at nominal voltage. During normal grid conditions, the converter can deliver rated power without exceeding its maximum current capacity because the voltage at the PCC is equal to the nominal voltage. However, if a voltage dip occurs at the PCC, the voltage becomes less than the nominal voltage and for the converter to continue delivering rated power, the current increases and it might exceed the current carrying capability of the semiconductors leading to tripping of the protective devices or damage to the converter. To prevent tripping or damage to the converter, a current limiter based on limiting the power references is proposed and implemented to limit the current during voltage dips.

In space vector form the apparent power capacity of the converter is given by

$$|\underline{S}| = \frac{3}{2} |\underline{v}_g| |\underline{i}_{L1}| \quad (6.1)$$

where $|\underline{S}|$ is the rated apparent power, $|\underline{v}_g|$ is the magnitude of the nominal grid voltage vector and $|\underline{i}_{L1}|$ is the magnitude of the inverter rated current vector.

The apparent power is also given in terms of the active power and the reactive power as

$$|\underline{S}| = \sqrt{p^2 + q^2} \quad (6.2)$$

where p is the instantaneous active power and q is the instantaneous reactive power.

From equation (6.1) the magnitude of the current vector is given by

$$|\underline{i}_{L1}| = \frac{2}{3} \frac{|\underline{S}|}{|\underline{v}_g|} \quad (6.3)$$

During a voltage dip, the magnitude of the voltage decreases below 90% of the nominal value. The reduction in the voltage will be quantified by a factor k_1 , which is defined in the equation below.

$$k_1 = \frac{|\underline{v}_{g,dip}|}{|\underline{v}_{g,ref}|} \quad (6.4)$$

where $|\underline{v}_{g,dip}|$ is the magnitude of the grid voltage during the voltage dip and $|\underline{v}_{g,ref}|$ is the nominal magnitude of the grid voltage.

Since virtual flux is used for synchronization and power estimation, k_1 can be calculated in terms of the virtual flux as

$$k_1 = \frac{|\underline{\psi}_{g,dip}|}{|\underline{\psi}_{g,ref}|} \quad (6.5)$$

where $|\underline{\psi}_{g,dip}|$ is the magnitude of the virtual flux during a voltage dip, which is detected using the virtual flux PLL described in Chapter 4, and $|\underline{\psi}_{g,ref}|$ is the nominal value of the virtual flux.

To limit the current during the voltage dip to a safe level, the power capacity of the converter should be reduced by the same factor, k_1 . Thus, the limited power capacity is given by

$$|\underline{s}_{lim}| = k_1 |\underline{s}| \quad (6.6)$$

The active power reference after limitation is given by

$$P_{ref,lim} = k_1 P_{ref} \quad (6.7)$$

Equation (6.7) is only effected when the voltage dip is less than 0.9 pu to avoid limiting the current during normal grid voltage variations.

If the converter is not supplying rated power to the VSC, it is possible to continue supplying a higher amount of power than given by equation (6.7) without overloading the VSC. A new factor k_2 which determines the capacity of the VSC being used is introduced and defined as

$$k_2 = \frac{P}{|\underline{s}|} \quad (6.8)$$

The factor k_2 is used to determine the capacity of the converter not being used for active power. When k_2 is equal to one, all the capacity of the converter is being used for active

power, and the reactive power reference is limited to zero. When k_2 less than one, the converter is supplying less than rated active power, and the remaining capacity of the converter can be used for reactive power if needed. This reactive power limitation is based on the idea presented in [167], which limits the reference reactive power to the capacity of the converter not being used for active power.

When $k_2 < 1$ and $k_1 > 0.9$, the reactive power capacity is given by

$$q_{avail} = \sqrt{|\underline{S}|^2 - p_{ref}^2} \quad (6.9)$$

And when $k_2 < 1$ and $k_1 < 0.9$, it is given by

$$q_{avail} = \sqrt{k_1^2 |\underline{S}|^2 - k_2^2 p_{ref}^2} \quad (6.10)$$

The full implementation of the current limiter is given in the flowchart of Figure 6.4.

The performance of the current limitation method is tested by implementing it in both simulation and practical set-up for a balanced voltage dip of 50%. The results are shown in Figure 6.5 and Figure 6.6 for simulation and experiment respectively.

When the voltage dip occurs, the active power reference is reduced proportionally to the voltage dip. The reactive power reference is kept at zero. Due to the reduction in active power, the current remains constant. This ensures that the current does not increase beyond the rated capacity of the converter. It should be noted that in both simulations and practical, the converter is supplied by a constant DC voltage source, and the DC voltage controller is not implemented. If the DC source is a renewable source such as a PV array, additional control measures should be put in place to protect the DC link from the residual power that is not being transferred to the grid during the voltage dip.

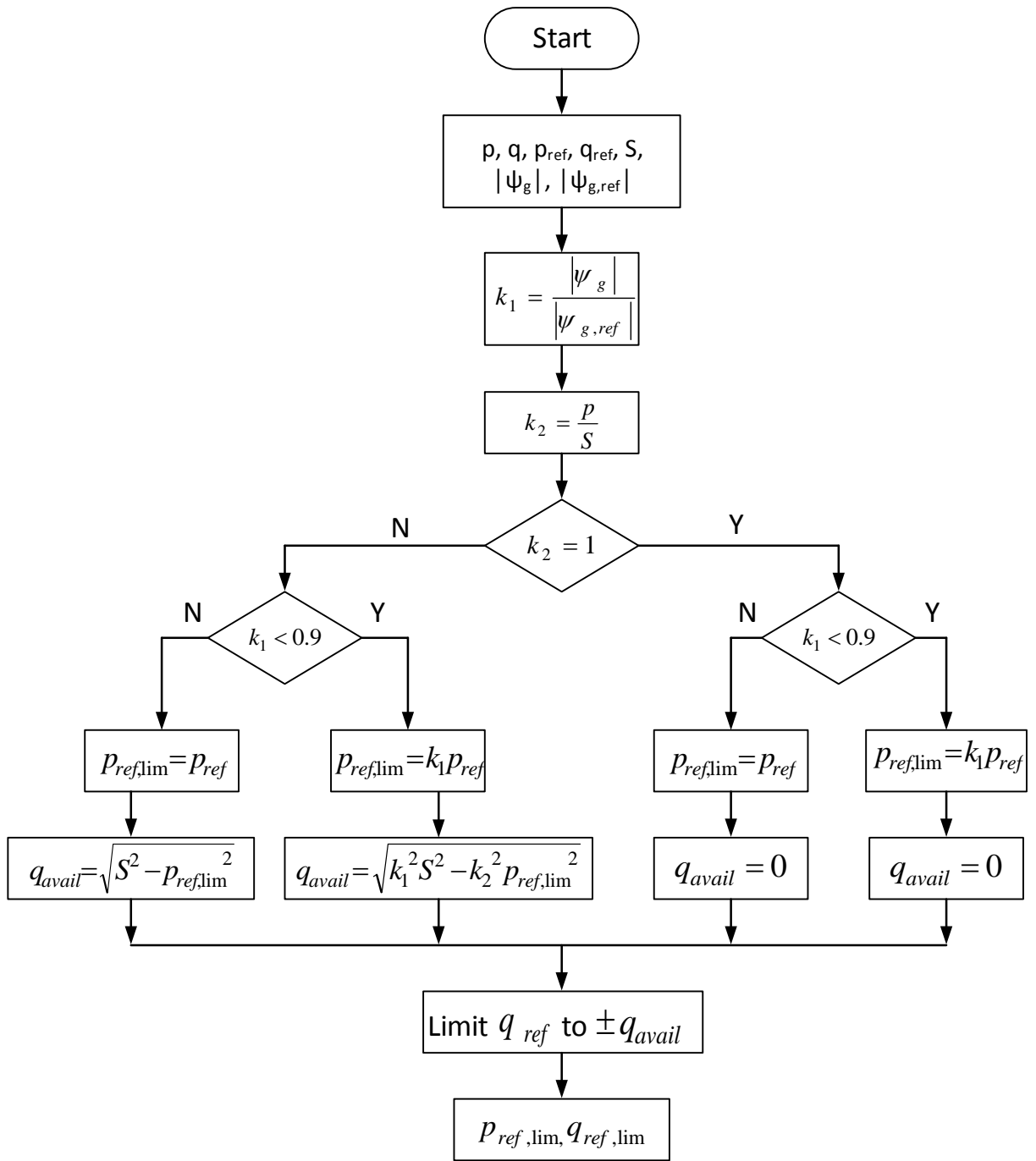


Figure 6.4 Flowchart of current limiter algorithm

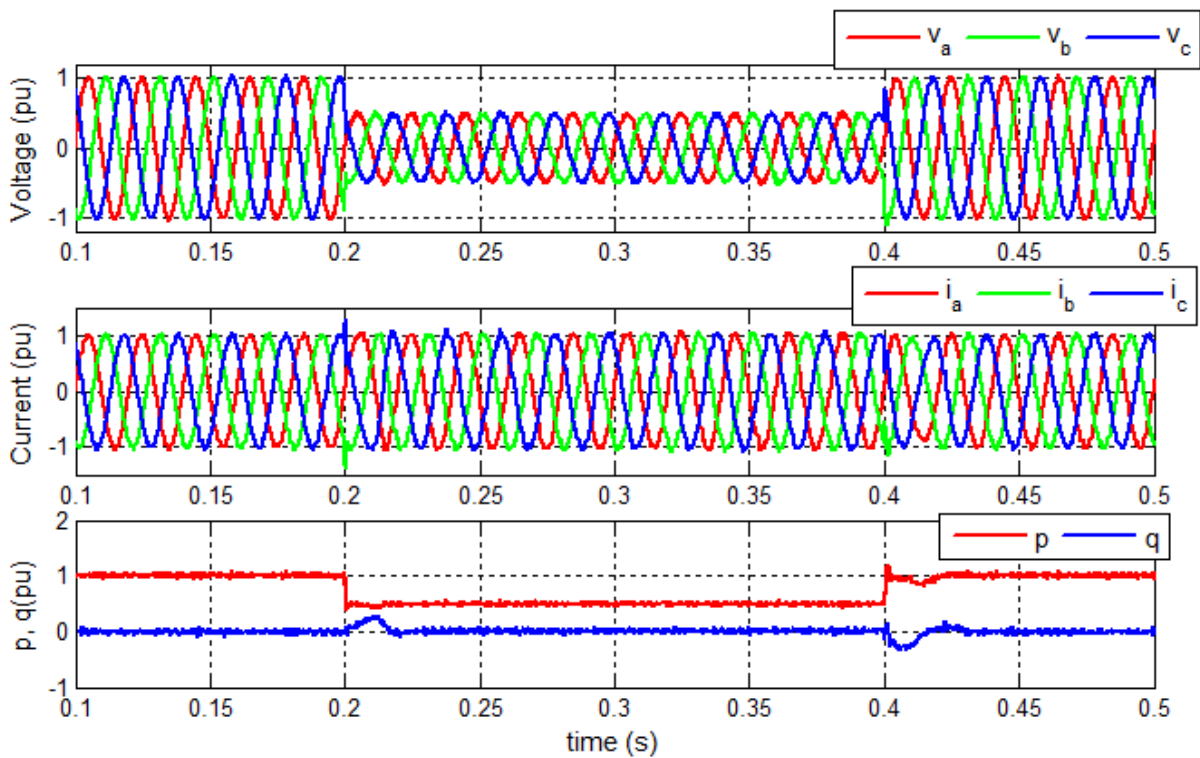


Figure 6.5 Simulation of 50% voltage dip with current limitation.

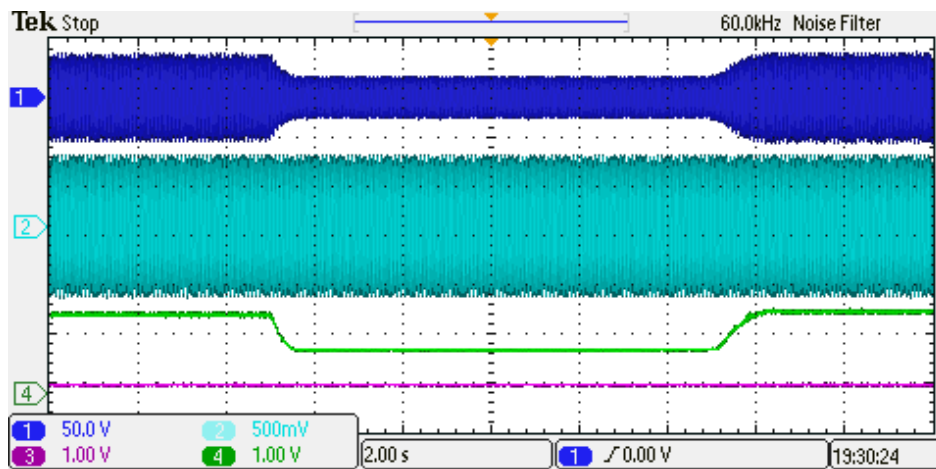


Figure 6.6 Experimental results of 50% voltage dip with current limitation. Upper: grid voltage (50V/div), middle: inverter current (10A/div), lower: active power and reactive power (250W/div).

6.4 Current Limitation during Unsymmetrical Voltage Dips

The majority of faults and hence voltage dips that occur in the grid are unsymmetrical, therefore, the proposed current limitation scheme should be extended to unsymmetrical voltage dips. In this section, the method of symmetrical components, which is used in the analysis of unsymmetrical voltages and currents is reviewed. Based on the positive-sequence and negative-sequence components, the instantaneous power equations for unsymmetrical voltages and currents are reviewed and the basis for obtaining balanced and sinusoidal currents with unsymmetrical grid voltage is presented. The estimation of the positive-sequence virtual flux from the unsymmetrical virtual flux resulting from unsymmetrical voltages is briefly outlined.

6.4.1 Symmetrical Components

The method of symmetrical components was first proposed by Fortesque and is used to analyze unbalanced three-phase system. In a set of unbalanced three-phase voltages or currents, each phase voltage or current can be decomposed into three components which are the positive-sequence component, the negative-sequence component and the zero-sequence component. The positive-sequence components form a balanced three-phase system, with 120° phase shift between phase voltages, rotating at the fundamental angular frequency with phase-sequence a-b-c. The negative-sequence components are also a balanced three-phase system rotating at the fundamental angular frequency in the opposite direction to the positive-sequence components with phase sequence a-c-b. The zero-sequence components are a set of three in-phase voltages with equal magnitude and no phase sequence. The sequence components are shown in Figure 6.7.

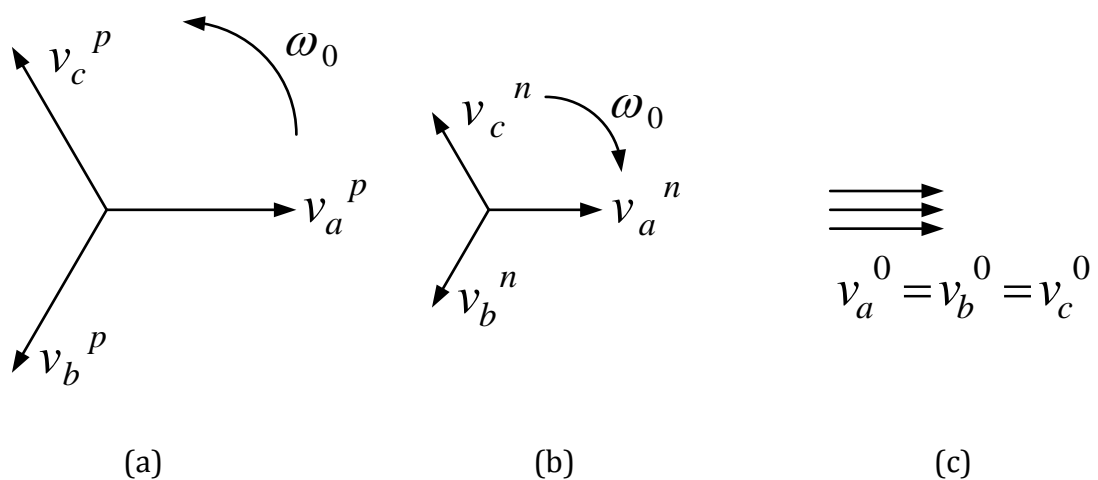


Figure 6.7 Symmetrical Components (a) positive-sequence (b) negative-sequence
(c) zero-sequence.

In an unbalanced three-phase system the phase voltages are given by

$$v_a = v_a^p + v_a^n + v_a^0 \quad (6.11)$$

$$v_b = v_b^p + v_b^n + v_b^0 \quad (6.12)$$

$$v_c = v_c^p + v_c^n + v_c^0 \quad (6.13)$$

where the superscript 'p' denotes the positive-sequence components, superscript 'n' denotes the negative-sequence components and superscript '0' denotes the zero-sequence components.

The symmetrical components in phase-a can be calculated from the phase voltages using the matrix equation below.

$$\begin{bmatrix} v_a^p \\ v_a^n \\ v_a^0 \end{bmatrix} = \frac{1}{3} \begin{bmatrix} 1 & a & a^2 \\ 1 & a^2 & a \\ 1 & 1 & 1 \end{bmatrix} \begin{bmatrix} v_a \\ v_b \\ v_c \end{bmatrix} \quad (6.14)$$

where $a = e^{j\frac{2\pi}{3}}$.

The symmetrical component voltages in phase-b and phase-c can be derived from the phase a components in equation (6.14). Similar calculations can be carried out for the current.

In a three-phase three-wire system without a neutral connection, the zero-sequence components are not present, and thus will be omitted from the following analysis.

In the stationary reference frame, the unbalanced voltages are given by

$$v_\alpha = v_\alpha^p + v_\alpha^n \quad (6.15)$$

$$v_\beta = v_\beta^p + v_\beta^n \quad (6.16)$$

Using space vectors, the unbalanced voltage vector is given by

$$\underline{v} = \underline{v}^p + \underline{v}^n = |\underline{v}^p| e^{j(\omega t + \theta_p)} + |\underline{v}^n| e^{-j(\omega t + \theta_n)} \quad (6.17)$$

where \underline{v}^p is the positive-sequence vector; \underline{v}^n is the negative-sequence vector; θ_p is the angle of the positive-sequence vector; and θ_n is the angle of the negative-sequence vector.

The symmetrical components in the stationary reference frame are given by

$$\begin{bmatrix} v_{\alpha}^p \\ v_{\alpha}^n \end{bmatrix} = \frac{1}{2} \begin{bmatrix} 1 & j \\ 1 & -j \end{bmatrix} \begin{bmatrix} v_{\alpha} \\ v_{\beta} \end{bmatrix} \quad (6.18)$$

$$\begin{bmatrix} v_{\beta}^p \\ v_{\beta}^n \end{bmatrix} = \frac{1}{2} \begin{bmatrix} -j & 1 \\ j & 1 \end{bmatrix} \begin{bmatrix} v_{\alpha} \\ v_{\beta} \end{bmatrix} \quad (6.19)$$

where the j operator denotes rotation through 90° .

In the time domain, the space vectors of the symmetrical components are given by

$$\underline{v}^p(t) = \frac{1}{2} \left[\underline{v}(t) + j\underline{v}\left(t - \frac{T}{4}\right) \right] \quad (6.20)$$

$$\underline{v}^n(t) = \frac{1}{2} \left[\underline{v}(t) - j\underline{v}\left(t - \frac{T}{4}\right) \right] \quad (6.21)$$

where T is the periodic time of the grid voltage.

Equations (6.20) and (6.21) form the basis of symmetrical component separation methods. The signal being decomposed into its symmetrical components needs to be delayed in time by a quarter of the fundamental cycle. This is equivalent to a phase shift of -90° . Any method that can achieve this delay or phase shift would be suitable for symmetrical component separation depending on their suitability in the system under consideration.

6.4.2 Instantaneous Power Equations with Unsymmetrical Voltages and Currents

The unsymmetrical grid voltage during an unsymmetrical voltage dip is given by

$$\underline{v}_g = \underline{v}_g^p + \underline{v}_g^n \quad (6.22)$$

Where \underline{v}_g^p is the positive-sequence grid voltage vector and \underline{v}_g^n is the negative-sequence grid voltage vector.

A similar expression can be written for the current injected to the grid, assuming it is unbalanced but has no harmonic distortion. This is given by

$$\underline{i}_{L2} = \underline{i}_{L2}^p + \underline{i}_{L2}^n \quad (6.23)$$

where \underline{i}_{L2} is the grid current vector; \underline{i}_{L2}^p and \underline{i}_{L2}^n are its positive and negative-sequence component vectors respectively.

By applying the instantaneous power theory [62] and expressing the voltages and currents in terms of their orthogonal stationary reference frame components, the instantaneous active power and reactive power are shown to be composed of constant and oscillating components as shown below.

$$p = P_0 + P_c \cos(2\omega t) + P_s \sin(2\omega t) \quad (6.24)$$

$$q = Q_0 + Q_c \cos(2\omega t) + Q_s \sin(2\omega t) \quad (6.25)$$

where P_0 and Q_0 are the average values of the powers; P_c , P_s , Q_c and Q_s are the amplitudes of the oscillating components of the powers.

Each of the power components can be expressed in terms of the voltage and currents components as shown below.

$$P_0 = \frac{3}{2} (v_{g\alpha}^p i_{L2\alpha}^p + v_{g\beta}^p i_{L2\beta}^p + v_{g\alpha}^n i_{L2\alpha}^n + v_{g\beta}^n i_{L2\beta}^n) \quad (6.26)$$

$$Q_0 = \frac{3}{2} (v_{g\alpha}^p i_{L2\beta}^p - v_{g\beta}^p i_{L2\alpha}^p + v_{g\alpha}^n i_{L2\beta}^n - v_{g\beta}^n i_{L2\alpha}^n) \quad (6.27)$$

$$P_c = \frac{3}{2} (v_{g\alpha}^n i_{L2\alpha}^p + v_{g\beta}^n i_{L2\beta}^p + v_{g\alpha}^p i_{L2\alpha}^n + v_{g\beta}^p i_{L2\beta}^n) \quad (6.28)$$

$$Q_c = \frac{3}{2} (v_{g\alpha}^n i_{L2\beta}^p - v_{g\beta}^n i_{L2\alpha}^p + v_{g\alpha}^p i_{L2\beta}^n - v_{g\beta}^p i_{L2\alpha}^n) \quad (6.29)$$

$$P_s = \frac{3}{2} (v_{g\alpha}^n i_{L2\alpha}^p - v_{g\beta}^n i_{L2\beta}^p - v_{g\alpha}^p i_{L2\alpha}^n + v_{g\beta}^p i_{L2\beta}^n) \quad (6.30)$$

$$Q_s = \frac{3}{2} (-v_{g\alpha}^n i_{L2\beta}^p - v_{g\beta}^n i_{L2\alpha}^p + v_{g\alpha}^p i_{L2\beta}^n + v_{g\beta}^p i_{L2\alpha}^n) \quad (6.31)$$

In the controller, the power is estimated using the grid virtual flux and the inverter current. The virtual flux estimated from the unsymmetrical grid voltage will be unsymmetrical, while the inverter current will have a similar waveform to the grid current. Thus, the estimated powers will have constant and oscillating components as given in equations (6.24) and (6.25). However, the power controllers are unable to control the oscillating powers effectively and the resulting current is unbalanced and distorted and with no current limitation its magnitude could exceed the rated current of the VSC.

To improve the power estimation and synchronization, the positive-sequence grid voltage [168], [163] or virtual flux is used [128]. The positive-sequence virtual flux based power estimation is described in more detail below.

6.4.3 Positive-sequence Virtual-flux Based Instantaneous Power Estimation

Considering only the positive-sequence virtual-flux, the estimated instantaneous powers available to the power controllers are given by

$$p = \frac{3}{2} \left(\psi_{g\alpha}^p i_{L1\beta} - \psi_{g\beta}^p i_{L1\alpha} \right) \quad (6.32)$$

$$q = \frac{3}{2} \left(\psi_{g\alpha}^p i_{L1\alpha} + \psi_{g\beta}^p i_{L1\beta} \right) \quad (6.33)$$

Since, the inverter current is balanced the grid current will be balanced as well and will not have a negative-sequence component. However, the grid voltage is unbalanced and has a negative-sequence components. Therefore, the actual power at the grid side will have oscillation arising from the interaction between the balanced current and the unbalanced voltage. The oscillating power components are given by

$$P_c = \frac{3}{2} \left(v_{g\alpha}^n i_{L2\alpha}^p + v_{g\beta}^n i_{L2\beta}^p \right) \quad (6.34)$$

$$Q_c = \frac{3}{2} \left(v_{g\alpha}^n i_{L2\beta}^p - v_{g\beta}^n i_{L2\alpha}^p \right) \quad (6.35)$$

$$P_s = \frac{3}{2} \left(v_{g\alpha}^n i_{L2\alpha}^p - v_{g\beta}^n i_{L2\beta}^p \right) \quad (6.36)$$

$$Q_s = \frac{3}{2} \left(-v_{g\alpha}^n i_{L2\beta}^p - v_{g\beta}^n i_{L2\alpha}^p \right) \quad (6.37)$$

Comparison of the magnitudes of the oscillating power components in equations (6.28)-(6.31) and those in equations (6.34)-(6.37) shows that the power oscillations are reduced by using the positive-sequence control.

6.4.4 Positive-sequence Virtual-flux Estimation

In order to use the positive-sequence component of the virtual flux for power estimation and synchronization, it has to be extracted from the unbalanced virtual flux estimated from the unbalanced grid voltage.

The positive-sequence components of the virtual flux are given by

$$\psi_{g\alpha}^p = \frac{1}{2}(\psi_{g\alpha} + j\psi_{g\beta}) \quad (6.38)$$

$$\psi_{g\beta}^p = \frac{1}{2}(-j\psi_{g\alpha} + \psi_{g\beta}) \quad (6.39)$$

where j denotes a counterclockwise vector rotation of 90° .

The phase shift of 90° can be obtained using a number of different methods presented in literature. One of these is the delayed signal cancellation method [169], [170]. In this method the phase shift is achieved by delaying a signal for a quarter of the fundamental time period. Another method is based on cascaded low-pass filters which were introduced for sequence decomposition and virtual flux estimation in [82]. This method makes use of the cascaded filters' phase shift of 90° and attenuation of 0.5 at the fundamental grid frequency. The second method, which is also used to estimate the grid virtual flux, is adopted, and its implementation is illustrated in Figure 6.8.

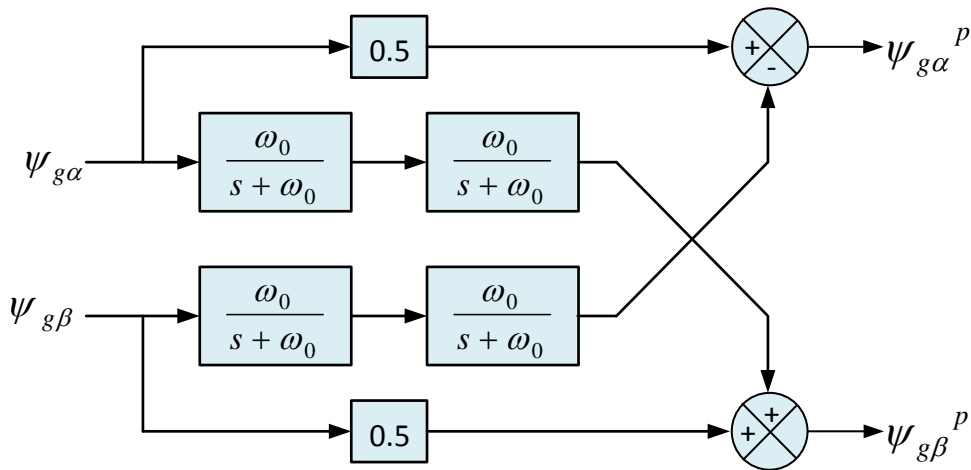


Figure 6.8 Positive-sequence VF estimation.

The positive-sequence virtual-flux is used for power estimation, synchronization and current limitation.

6.5 Experimental System for Unsymmetrical Voltage Dips

To achieve unbalanced grid voltages at the PCC, the experimental layout which is described in Chapter 4 is modified as explained below. The most common type of unsymmetrical fault is the single-line to ground fault which results in a single-phase voltage dip. The performance of the system is investigated for this type of voltage dip. To achieve a single-phase voltage dip, a single-phase variac is connected in phase-a on the grid-side of the three-phase variac. By reducing the voltage of the single-phase variac, the voltage in phase-a is reduced to give a single-phase voltage dip.

The modified connection with the single-phase variac to create an unbalanced voltage dip is shown in Figure 6.9.

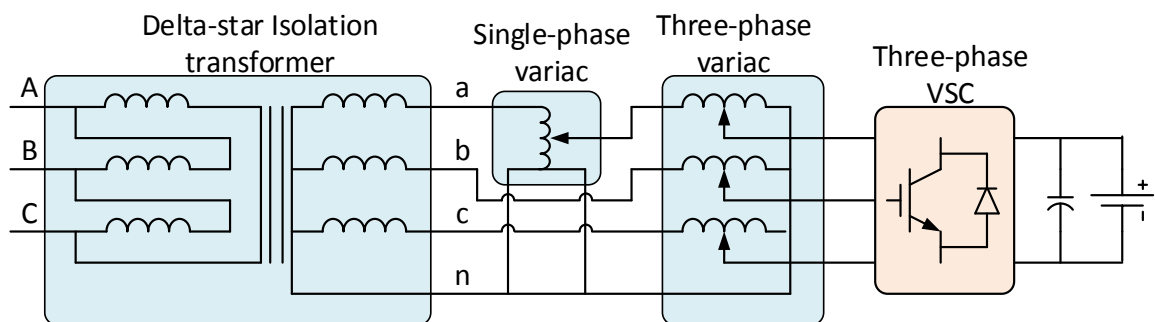


Figure 6.9 Modified connection to create single-phase voltage dips.

The block diagram of the positive-sequence virtual flux control with current limitation is shown in Figure 6.10.

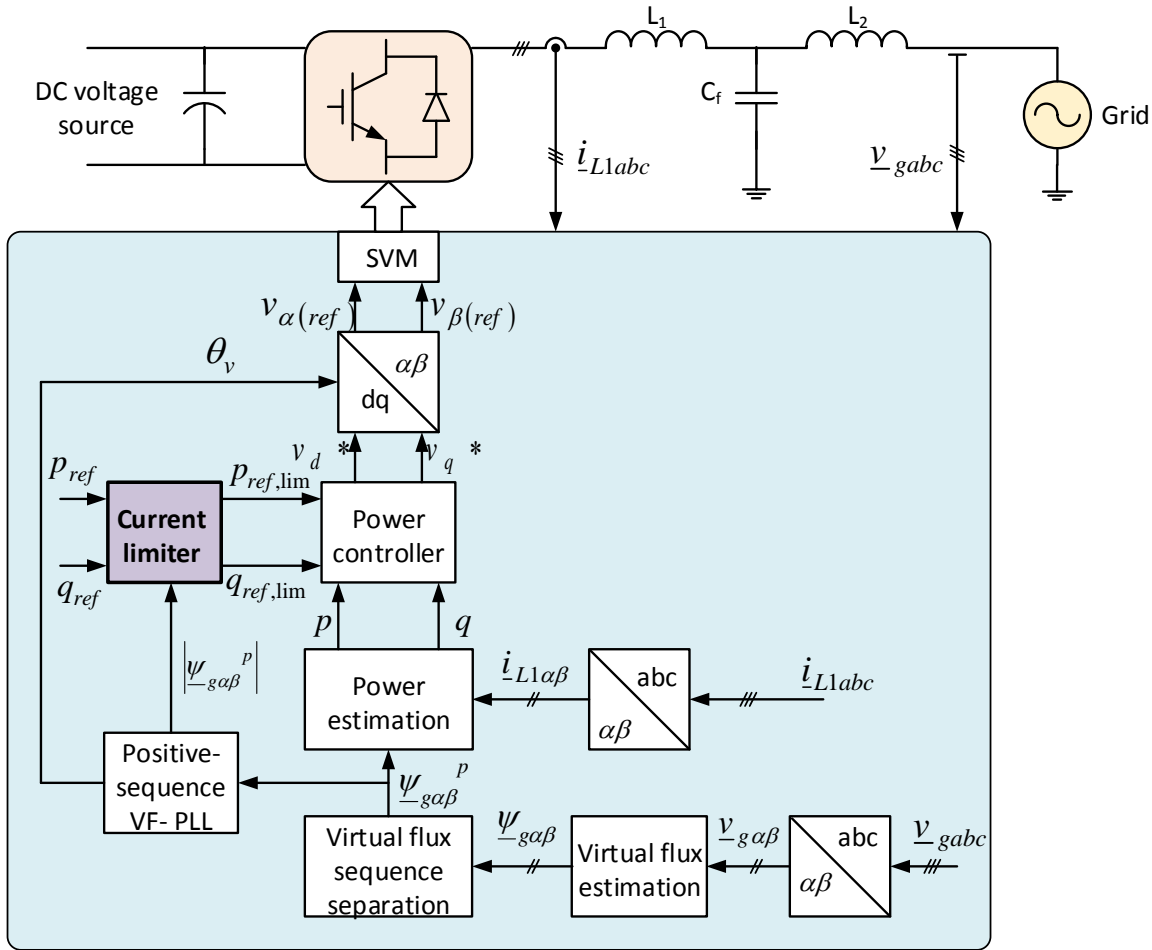


Figure 6.10 Block diagram of positive-sequence virtual-flux control with current limitation.

6.6 Experimental Results

The performance of the current limitation during unsymmetrical voltage dips was verified experimentally for different modes of operation of the VSC during a single-phase voltage dip. The following operating modes are considered:

1. When the VSC is supplying active power only.
2. When the VSC is supplying reactive power only.
3. When the VSC is supplying both active power and reactive power.

These three operating modes represent the main applications of grid-connected VSCs. For each mode of operation four different cases are considered. In the first case, the conventional VF-DPC-SVM control scheme without current limitation is used. In the second case, the conventional VF-DPC-SVM control scheme with current limitation is

used. In the third case, the positive-sequence VF control scheme without current limitation is used. In the fourth cases, the positive-sequence VF control scheme with current limitation is used.

The grid synchronization during the single-phase voltage dip of 50 % is shown in Figure 6.11 for the conventional VF-PLL and for the positive-sequence VF-PLL. The conventional VF-PLL angle shown in Figure 6.11(a) is distorted due to the non-symmetrical virtual flux with a non-circular trajectory obtained from the unsymmetrical grid voltage. This will affect the symmetry and the quality of the output current. By using the positive-sequence VF-PLL, the undistorted synchronization angle is obtained as shown in Figure 6.11(b). This is because only the positive-sequence virtual flux which is symmetrical and has a circular trajectory.

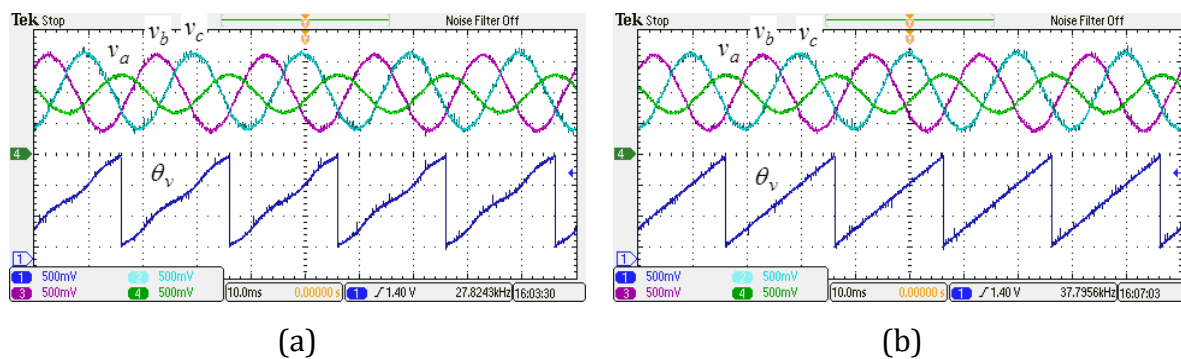


Figure 6.11 Grid voltage [30 V/div] and synchronization angle [$2\pi/3$ rad/div] during unsymmetrical voltage dip (a) virtual-flux PLL (b) positive-sequence virtual-flux PLL.

The grid currents obtained when the active power reference is set to 500 W and the reactive power reference is set to 0, are shown in Figure 6.12. The power reference is limited to 500 W to limit the over-currents likely to occur when the current limitation is not employed. Figure 6.12(a) shows the currents obtained with the conventional VF-DPC-SVM scheme. The currents are distorted and unsymmetrical, and reach a magnitude of about 12.5 A, which is over 150 % of the expected current magnitude. By including the current limitation in the conventional control, the magnitude of the currents can be significantly reduced as shown in Figure 6.12(b). However, the currents are still distorted despite having their magnitude limited to about 7.5 A. Figure 6.12(c) shows the currents obtained with the positive-sequence VF-DPC-SVM scheme. In this case, the currents are symmetrical but they are distorted and they have a magnitude of 10 A, which is 133 % of

the expected current. Figure 6.12(d) shows the currents obtained when the positive-sequence VF-DPC-SVM scheme with current limitation is used. The currents are balanced and sinusoidal and their magnitude is limited to 7.5 A. This shows that using current limitation algorithm with the positive-sequence control scheme ensures that the current does not exceed its rated value and the currents remain balanced and sinusoidal which is important in meeting the current quality requirements.

Similar results are observed in Figure 6.13 where the VSC is supplying reactive power and Figure 6.14 where it is supplying both active power and reactive power. In all cases the positive-sequence VF-DPC-SVM control scheme achieves balanced and sinusoidal currents with limited magnitude.

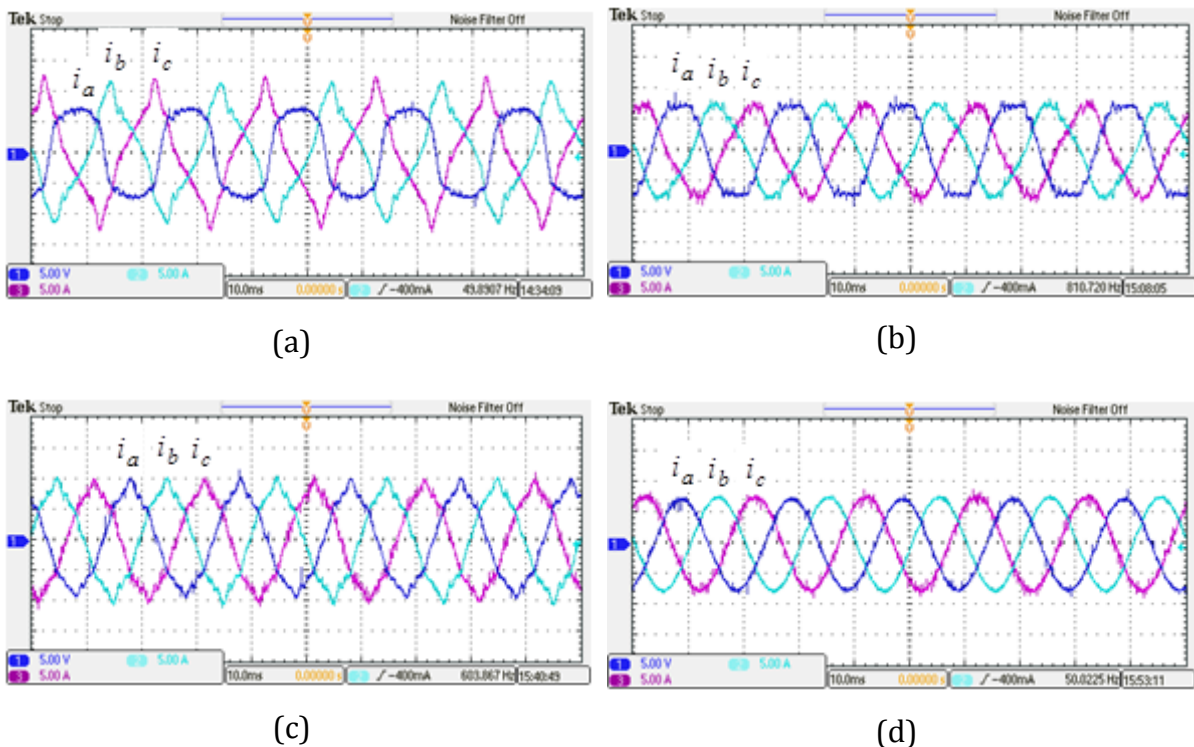
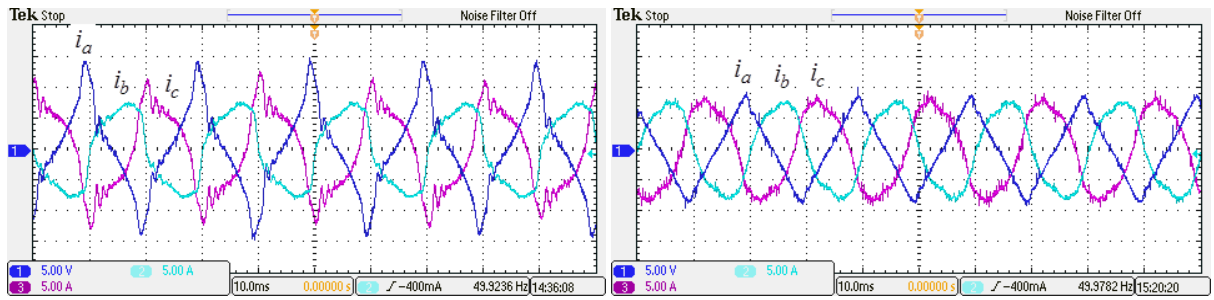
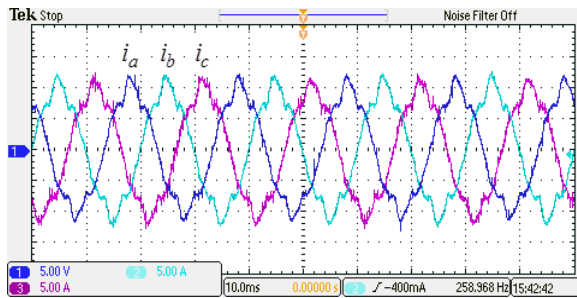


Figure 6.12 Grid currents [5 A/div] during unsymmetrical voltage dip when supplying active power (a) conventional control with no current limitation (b) conventional control with current limitation (c) positive-sequence control with no current limitation (d) positive-sequence control with current limitation.

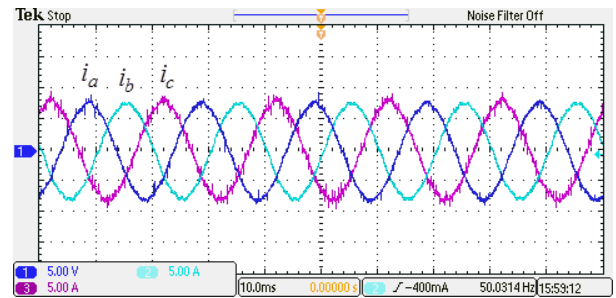


(a)

(b)

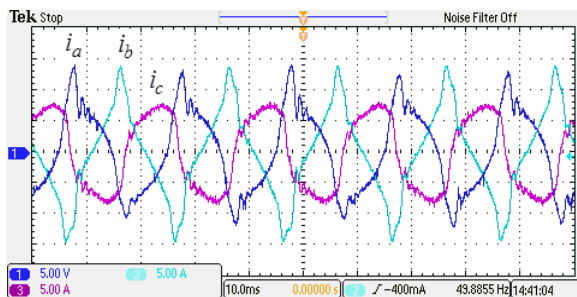


(c)

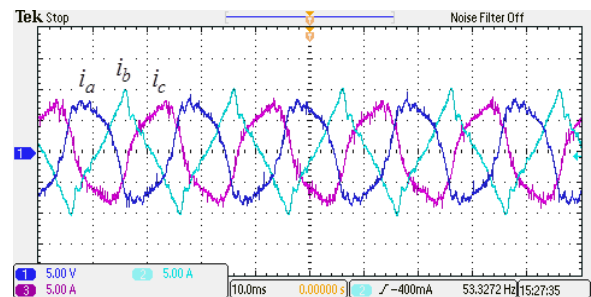


(d)

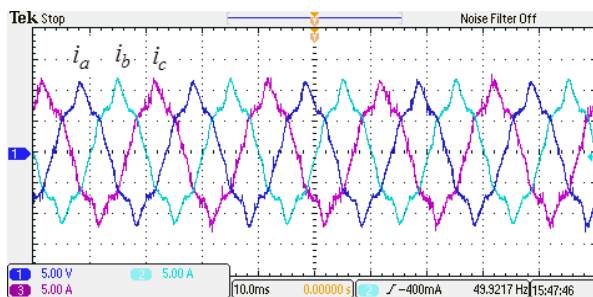
Figure 6.13 Grid currents [5 A/div] during unsymmetrical voltage dip when supplying reactive power (a) conventional control with no current limitation (b) conventional control with current limitation (c) positive-sequence control with no current limitation (d) positive-sequence control with current limitation.



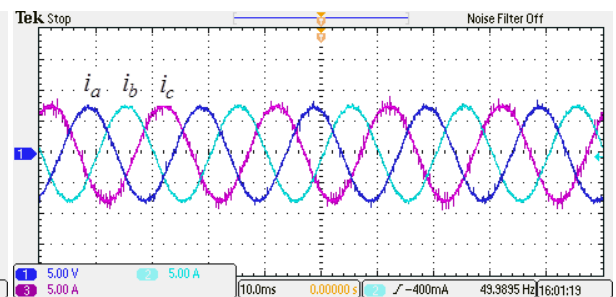
(a)



(b)



(c)



(d)

Figure 6.14 Grid currents [5 A/div] during unsymmetrical voltage dip when supplying active power and reactive power (a) conventional control with no current limitation (b) conventional control with current limitation (c) positive-sequence control with no current limitation (d) positive-sequence control with current limitation.

The results in this section show that the proposed current limitation algorithm effectively limits the current during unsymmetrical voltage dips. This has been demonstrated, for different operating modes of the VSC.

The limitations of the conventional VF-DPC-SVM control scheme during unsymmetrical voltage dips have been demonstrated. These include the inability of the VF-PLL to correctly obtain the synchronization angle. The obtained angle is distorted which leads to increased distortion in the current. The other limitation is that the output current is unsymmetrical, distorted and its magnitude increases beyond the rated capacity of the VSC. The main harmonics in the distorted current are the third harmonic and the fifth harmonic with magnitudes of more than 20 % and 5 % respectively, of the fundamental frequency component. The average current THD is 22 %. Due to the unsymmetrical nature of the current, the magnitudes of the currents in the different phases will not be equal.

With current limitation, the magnitude of the currents obtained with the conventional VF-DPC-SVM is reduced to safe levels in all the phases. Thus, the objective of current limitation is achieved. However, the currents are still unsymmetrical and distorted due to the unbalanced grid voltage and the distorted synchronization angle. There is a noticeable improvement in the current quality, with an average THD of 12%.

While the current limitation is the primary objective of this algorithm, it can be employed with a secondary control objective, in this case achieving balanced and sinusoidal currents. The average current THD achieved is less than 3 %, which is less than the allowable THD limit of 5 %. It is demonstrated that by using the positive-sequence VF-DPC-SVM control scheme without the current limitation, the currents are symmetrical but their magnitude is not limited and they are distorted. With the addition of the current limitation, the currents are balanced, sinusoidal and limited within the rated capacity of the VSC.

6.7 Conclusion

In this chapter, the control of grid-connected converters during grid voltage disturbances has been presented. The main issues considered are limiting the current to safe levels during both symmetrical and unsymmetrical voltage dips, and maintaining balanced and sinusoidal current during unsymmetrical voltage dips. A new current limiting method based on limiting the power references is proposed. The proposed scheme calculates the

fraction of the voltage remaining during a voltage dip and reduces the active power reference proportionally. The reactive power reference is reduced to the available capacity of the inverter which is not being used for active power flow. This ensures that the converter current is limited to safe levels during voltage dips thus avoiding tripping of the protective devices or damage to the converter.

The proposed scheme is implemented in experiments and it is demonstrated to be effective in limiting the current during both symmetrical and unsymmetrical voltage dips. The scheme is simple and can be easily implemented as part of an existing control scheme without adding more complexity to the system. It is very flexible and can be used together with a secondary objective during unsymmetrical voltage dips. This has been demonstrated by combining it with positive-sequence control to obtain balanced and sinusoidal currents with a THD of less than 3 % during an unsymmetrical voltage dip.

Chapter 7 Thesis Conclusions and Suggestions for Further Work

This chapter presents the main conclusions drawn from the thesis and provides some suggestions for future work.

7.1 Conclusions

In this thesis, the performance of grid-connected voltage source converters controlled using virtual-flux direct power control with space vector modulation has been investigated, and new schemes have been proposed to improve the performance of the system. The main contributions of the thesis are summarized in the following points.

- Stability analysis of the closed-loop power controller with an LCL filter.

From the stability analysis in Chapter 3, it is established that the instability problem caused by the resonance of the LCL filter can be mitigated by passive damping, active damping or by the positioning of the current sensors on the inverter side of the LCL filter. It has been demonstrated by using pole-zero plots that having the current sensors on the inverter side results in a stable system without using any form of damping for all values of proportional gain. The advantage of this method is that it does not use any additional passive components and does not require any modification to the controller, thus it does not reduce the power efficiency of the system and it does not increase the controller complexity.

- Compensation of reactive power error caused by using inverter side current for power estimation

A consequence of having the current sensors on the inverter side is a mismatch in the estimated reactive power and the reactive power at the PCC due to the reactive power output of the filter capacitor. To compensate for this difference in reactive power, a new error compensation scheme was proposed and implemented in Chapter 4. The proposed scheme does not need any additional voltage or current sensors. The grid side current which is needed for the estimation of the capacitor current is estimated from the power references and the grid virtual flux. Implementation of the scheme

achieves unity power factor at the PCC when the reactive power reference is zero for all values of active power.

- Investigation of the robustness of the system with the undamped LCL filter to variations in grid impedance and grid voltage distortion

The use of an undamped LCL filter raises the question of how robust the system would be in a grid with a varying grid impedance and with grid voltage distortion. The effect of grid impedance variation and grid voltage distortion on the stability and the performance of the system was investigated in Chapter 5. The investigation focused on the variation in grid inductance, which has a bigger effect on system stability and performance than the grid resistance. The stability analysis shows that the system will be stable for a wide range of proportional gain and a wide range of grid inductance values. Comparison of virtual-flux based and voltage based DPC-SVM showed that the latter was more robust to grid inductance variations and was able to maintain the current THD below 5 % when the grid voltage was distorted.

- Current limitation during symmetrical and unsymmetrical voltage dips

The control of the VSC during voltage dips presents a challenge of excessive current magnitudes, and unbalanced and distorted line currents. In Chapter 6, a new current limiting algorithm is developed and implemented to limit the magnitude of the current during voltage dips. Additionally, the positive-sequence component of the virtual-flux is used for synchronization and power estimation. With these improvements, experimental results show that the VSC currents are limited in magnitude during symmetrical voltage dips. In addition, during unsymmetrical voltage dips, the currents are balanced and have a THD of less than 3 %.

Overall, it can be concluded that VF-DPC-SVM is a stable and robust control scheme with good rejection of grid voltage harmonics. It is flexible, and this makes it easy to implement additional functions such as the reactive power error compensation, current limitation and positive-sequence control, without the system becoming too complicated.

7.2 Suggestions for Further Work

In this thesis some interesting new modifications to the basic VF-DPC-SVM scheme have been proposed to improve its performance. The investigation has been based on the two-

level VSC which is limited to low voltage applications. For medium and high voltage applications multi-level converters are preferred. The performance of the control schemes proposed in this thesis has not been considered for multi-level converters and this could be investigated in future.

The VF-DPC-SVM scheme has been shown to be stable and robust to changes in the grid conditions even when used with an undamped LCL filter. The robustness and performance of the fixed control parameter scheme can be compared to an adaptive control scheme in which an online grid impedance estimation algorithm can be used to track the changes in the grid inductance and use the estimated impedance to work out optimal values of the controller parameters. In addition, an adaptive harmonic compensation scheme can be incorporated into the control system to further improve its performance with grid voltage distortion.

The current limitation algorithm introduced in Chapter 6 has been implemented with a variable DC voltage source whose output power follows the active power reference. In a real system, the DC side of the converter is fed from a renewable energy source, with a DC voltage controller and a maximum power point tracker. The active power from the renewable energy source cannot be reduced instantaneously, and a lowering of the active power reference by the current limiter would lead to a mismatch between the DC power and the AC power, and the excess power could lead to an increase of the DC link voltage which could damage the DC link capacitors. To avoid this, the action of the current limiter should be coordinated with the DC voltage controller, and the DC link should be protected from excessive voltage. For low power systems, a braking chopper can be used to dissipate the excess power, while for high power systems, the excess power can be channelled to an energy storage device for future use.

References

- [1] WWEA. (2016, 25th February). *The World sets New Wind Installations Record: 63,7 GW New Capacity in 2015*. Available: <http://www.wwindea.org/the-world-sets-new-wind-installations-record-637-gw-new-capacity-in-2015/>
- [2] IEA-PVPS, "Survey Report of Selected IEA Countries between 1992 and 2014," International Energy Agency (IEA)2015.
- [3] "Worldwide electricity production from renewable energy sources: Stats and figures series ", Observ'ER, Ed., 2013 ed, 2013.
- [4] S. O. Gaëtan Masson, Manoël Rekinger. (2014). *Global Market Outlook for Photovoltaics 2014-2018*. Available: http://www.cleanenergybusinesscouncil.com/site/resources/files/reports/EPIA_Global_Market_Outlook_for_Photovoltaics_2014-2018_-_Medium_Res.pdf
- [5] "Technology Roadmap Solar Photovoltaic Energy," International Energy Agency (IEA), Paris, 2014.
- [6] R. I. (RENI), "PV power plants 2012 industry guide," 2012.
- [7] T. Pultarova. (2015) East Africa's first large-scale solar plant online. *Engineering and Technology Magazine*. Available: <http://eandt.theiet.org/news/2015/feb/solar-power-rwanda.cfm>
- [8] T. Geury, S. Pinto, and J. Gyselinck, "Three-phase power controlled PV current source inverter with incorporated active power filtering," in *Industrial Electronics Society, IECON 2013 - 39th Annual Conference of the IEEE*, 2013, pp. 1374-1379.
- [9] C. Klumpner, "A New Single-Stage Current Source Inverter for Photovoltaic and Fuel Cell Applications using Reverse Blocking IGBTs," in *Power Electronics Specialists Conference, 2007. PESC 2007. IEEE*, 2007, pp. 1683-1689.
- [10] A. C. Kyritsis, N. P. Papanikolaou, E. C. Tatakis, and J. C. Kobougias, "Design and control of a current source flyback inverter for decentralized grid-connected photovoltaic systems," in *Power Electronics and Applications, 2005 European Conference on*, 2005.
- [11] J. Glasdam, J. Hjerrild, L. H. Kocewiak, and C. L. Bak, "Review on multi-level voltage source converter based HVDC technologies for grid connection of large offshore wind farms," in *Power System Technology (POWERCON), 2012 IEEE International Conference on*, 2012, pp. 1-6.
- [12] Yasmeena and G. T. R. Das, "A structural & operational comparative study of converter topologies & analysis of MMC for high voltage applications," in *Circuit, Power and Computing Technologies (ICCPCT), 2015 International Conference on*, 2015, pp. 1-8.
- [13] "IEEE Standard for Interconnecting Distributed Resources with Electric Power Systems," *IEEE Std 1547-2003*, pp. 1-28, 2003.
- [14] "IEEE Recommended Practice and Requirements for Harmonic Control in Electric Power Systems - Redline," in *IEEE Std 519-2014 (Revision of IEEE Std 519-1992) - Redline*, ed, 2014, pp. 1-213.
- [15] "Limits for harmonic currents produced by equipment connected to public low-voltage systems with input current > 16 A and ≤ 75 A per phase," in *IEC 61000-3-12:2011*, ed: IEC, 2013, pp. 1-30.
- [16] M. Lindgren and J. Svensson, "Control of a voltage-source converter connected to the grid through an LCL-filter-application to active filtering," in *Power Electronics*

Specialists Conference, 1998. PESC 98 Record. 29th Annual IEEE, 1998, pp. 229-235 vol.1.

- [17] T. Instruments, "TMS320F28335 Digital Signal Controllers (DSCs) Data Manual," *accessible through www.ti.com*, 2010.
- [18] N. Hamrouni, M. Jraidi, and A. Cherif, "New control strategy for 2-stage grid-connected photovoltaic power system," *Renewable Energy*, vol. 33, pp. 2212-2221, 2008.
- [19] G. Feng, L. Ding, P. C. Loh, T. Yi, and W. Peng, "Indirect dc-link voltage control of two-stage single-phase PV inverter," in *Energy Conversion Congress and Exposition, 2009. ECCE 2009. IEEE, 2009*, pp. 1166-1172.
- [20] S. Jain and V. Agarwal, "A Single-Stage Grid Connected Inverter Topology for Solar PV Systems With Maximum Power Point Tracking," *IEEE Transactions on Power Electronics*, vol. 22, pp. 1928-1940, 2007.
- [21] T. F. Wu, C. H. Chang, L. C. Lin, and C. L. Kuo, "Power Loss Comparison of Single- and Two-Stage Grid-Connected Photovoltaic Systems," *IEEE Transactions on Energy Conversion*, vol. 26, pp. 707-715, 2011.
- [22] R. Kadri, J. P. Gaubert, and G. Champenois, "An Improved Maximum Power Point Tracking for Photovoltaic Grid-Connected Inverter Based on Voltage-Oriented Control," *IEEE Transactions on Industrial Electronics*, vol. 58, pp. 66-75, 2011.
- [23] V. Minambres-Marcos, E. Romero-Cadaval, M. A. Guerrero-Martinez, M. I. Milanés-Montero, and I. I. E. Society, "Three-phase Single Stage Photovoltaic Inverter with Active Filtering Capabilities," in *38th Annual Conference on Ieee Industrial Electronics Society*, ed New York: Ieee, 2012, pp. 5253-5258.
- [24] IEEE, "IEEE 929-2000: Recommended Practice for Utility Interface of Photovoltaic (PV) Systems," ed, 2000.
- [25] Z. Ozkan and A. M. Hava, "Energy conversion efficiency of single-phase transformerless PV inverters," in *Electrical and Electronics Engineering (ELECO), 2013 8th International Conference on*, 2013, pp. 283-287.
- [26] M. Armstrong, D. J. Atkinson, C. M. Johnson, and T. D. Abeyasekera, "Auto-Calibrating DC Link Current Sensing Technique for Transformerless, Grid Connected, H-Bridge Inverter Systems," *IEEE Transactions on Power Electronics*, vol. 21, pp. 1385-1393, 2006.
- [27] Z. Tao, H. Guofeng, C. Min, and X. Dehong, "A novel control strategy to suppress DC current injection to the grid for three-phase PV inverter," in *Power Electronics Conference (IPEC-Hiroshima 2014 - ECCE-ASIA), 2014 International*, 2014, pp. 485-492.
- [28] Y. P. Siwakoti and G. E. Town, "Three-phase transformerless grid connected Quasi Z-Source Inverter for solar photovoltaic systems with minimal leakage current," in *Power Electronics for Distributed Generation Systems (PEDG), 2012 3rd IEEE International Symposium on*, 2012, pp. 368-373.
- [29] R. Teodorescu, M. Liserre, and P. Rodriguez, *Grid Converters for Photovoltaic and Wind Power Systems*: Wiley, 2011.
- [30] M. P. Kazmierkowski and L. Malesani, "Current control techniques for three-phase voltage-source PWM converters: a survey," *IEEE Transactions on Industrial Electronics*, vol. 45, pp. 691-703, 1998.
- [31] V. Blasko and V. Kaura, "A new mathematical model and control of a three-phase AC-DC voltage source converter," *IEEE Transactions on Power Electronics*, vol. 12, pp. 116-123, 1997.
- [32] H. Cha, T. K. Vu, and J. E. Kim, "Design and control of Proportional-Resonant controller based Photovoltaic power conditioning system," in *Energy Conversion Congress and Exposition, 2009. ECCE 2009. IEEE, 2009*, pp. 2198-2205.

- [33] L. Yumei, B. Rui, W. Daoqian, M. Wenge, and W. Lin, "Proportional-resonant control method of three-phase grid-connected inverter," in *Control and Decision Conference (2014 CCDC), The 26th Chinese*, 2014, pp. 4797-4800.
- [34] T. Noguchi, H. Tomiki, S. Kondo, and I. Takahashi, "Direct power control of PWM converter without power-source voltage sensors," *IEEE Transactions on Industry Applications*, vol. 34, pp. 473-479, 1998.
- [35] M. Malinowski, G. Marques, M. Cichowlas, and M. P. Kazmierkowski, "New direct power control of three-phase PWM boost rectifiers under distorted and imbalanced line voltage conditions," in *Industrial Electronics, 2003. ISIE '03. 2003 IEEE International Symposium on*, 2003, pp. 438-443 vol. 1.
- [36] G. Saccomando and J. Svensson, "Transient operation of grid-connected voltage source converter under unbalanced voltage conditions," in *Industry Applications Conference, 2001. Thirty-Sixth IAS Annual Meeting. Conference Record of the 2001 IEEE*, 2001, pp. 2419-2424 vol.4.
- [37] I. Agirman and V. Blasko, "A novel control method of a VSC without AC line voltage sensors," *IEEE Transactions on Industry Applications*, vol. 39, pp. 519-524, 2003.
- [38] F. Blaabjerg, R. Teodorescu, M. Liserre, and A. V. Timbus, "Overview of Control and Grid Synchronization for Distributed Power Generation Systems," *IEEE Transactions on Industrial Electronics*, vol. 53, pp. 1398-1409, 2006.
- [39] C. Klumpner, M. Liserre, and F. Blaabjerg, "Improved control of an active-front-end adjustable speed drive with a small de-link capacitor under real grid conditions," in *Power Electronics Specialists Conference, 2004. PESC 04. 2004 IEEE 35th Annual*, 2004, pp. 1156-1162 Vol.2.
- [40] M. Malinowski, M. P. Kazmierkowski, S. Hansen, F. Blaabjerg, and G. D. Marques, "Virtual-flux-based direct power control of three-phase PWM rectifiers," *IEEE Transactions on Industry Applications*, vol. 37, pp. 1019-1027, 2001.
- [41] V. Kaura and V. Blasko, "Operation of a phase locked loop system under distorted utility conditions," in *Applied Power Electronics Conference and Exposition, 1996. APEC '96. Conference Proceedings 1996., Eleventh Annual*, 1996, pp. 703-708 vol.2.
- [42] A. Timbus, M. Liserre, R. Teodorescu, and F. Blaabjerg, "Synchronization methods for three phase distributed power generation systems - An overview and evaluation," in *Power Electronics Specialists Conference, 2005. PESC '05. IEEE 36th*, 2005, pp. 2474-2481.
- [43] N. Anani, O. Al-Kharji AlAli, M. Al-Qutayri, and S. Al-Araji, "Synchronization of a renewable energy inverter with the grid," *Journal of Renewable and Sustainable Energy*, vol. 4, 2012.
- [44] M. Boyra and J. L. Thomas, "A review on synchronization methods for grid-connected three-phase VSC under unbalanced and distorted conditions," in *Power Electronics and Applications (EPE 2011), Proceedings of the 2011-14th European Conference on*, 2011, pp. 1-10.
- [45] M. A. G. de Brito, L. Galotto, L. P. Sampaio, G. de Azevedo e Melo, and C. A. Canesin, "Evaluation of the Main MPPT Techniques for Photovoltaic Applications," *IEEE Transactions on Industrial Electronics*, vol. 60, pp. 1156-1167, 2013.
- [46] M. A. Elgendy, B. Zahawi, and D. J. Atkinson, "Assessment of the Incremental Conductance Maximum Power Point Tracking Algorithm," *EEE Transactions on Sustainable Energy*, vol. 4, pp. 108-117, 2013.
- [47] M. A. Elgendy, B. Zahawi, and D. J. Atkinson, "Evaluation of perturb and observe MPPT algorithm implementation techniques," in *Power Electronics, Machines and Drives (PEMD 2012), 6th IET International Conference on*, 2012, pp. 1-6.

- [48] M. A. Elgendy, B. Zahawi, and D. J. Atkinson, "Comparison of Directly Connected and Constant Voltage Controlled Photovoltaic Pumping Systems," *IEEE Transactions on Sustainable Energy*, vol. 1, pp. 184-192, 2010.
- [49] T. Esum and P. L. Chapman, "Comparison of Photovoltaic Array Maximum Power Point Tracking Techniques," *IEEE Transactions on Energy Conversion*, vol. 22, pp. 439-449, 2007.
- [50] G. A. Kern, "SunSine300, utility interactive AC module anti-islanding test results," in *Photovoltaic Specialists Conference, 1997., Conference Record of the Twenty-Sixth IEEE, 1997*, pp. 1265-1268.
- [51] F. De Mango, M. Liserre, A. D. Aquila, and A. Pigazo, "Overview of Anti-Islanding Algorithms for PV Systems. Part I: Passive Methods," in *Power Electronics and Motion Control Conference, 2006. EPE-PEMC 2006. 12th International, 2006*, pp. 1878-1883.
- [52] F. De Mango, M. Liserre, and A. D. Aquila, "Overview of Anti-Islanding Algorithms for PV Systems. Part II: Active Methods," in *Power Electronics and Motion Control Conference, 2006. EPE-PEMC 2006. 12th International, 2006*, pp. 1884-1889.
- [53] E. Troester, "New German Grid Codes for Connecting PV Systems to the Medium Voltage Power Grid," in *2nd International Workshop on Concentrating Photovoltaic Power Plants, Darmstadt, Germany, 2009*.
- [54] S. Hyo-Ryong, K. Gyeong-Hun, J. Seong-Jae, K. Sang-Yong, P. Sangsoo, P. Minwon, *et al.*, "Harmonics and reactive power compensation method by grid-connected Photovoltaic generation system," in *Electrical Machines and Systems, 2009. ICEMS 2009. International Conference on, 2009*, pp. 1-5.
- [55] X. Yan, L. M. Tolbert, D. T. Razy, and J. D. Kueck, "Nonactive-Power-Related Ancillary Services Provided by Distributed Energy Resources," in *Power Engineering Society General Meeting, 2007. IEEE, 2007*, pp. 1-7.
- [56] R. K. Varma, B. Das, I. Axente, and T. Vanderheide, "Optimal 24-hr utilization of a PV solar system as STATCOM (PV-STATCOM) in a distribution network," in *Power and Energy Society General Meeting, 2011 IEEE, 2011*, pp. 1-8.
- [57] S. Buso, L. Malesani, and P. Mattavelli, "Comparison of current control techniques for active filter applications," *IEEE Transactions on Industrial Electronics*, vol. 45, pp. 722-729, 1998.
- [58] L. Malesani and P. Tomasin, "PWM current control techniques of voltage source converters-a survey," in *Industrial Electronics, Control, and Instrumentation, 1993. Proceedings of the IECON '93., International Conference on, 1993*, pp. 670-675 vol.2.
- [59] M. P. Kazmierkowski, R. Krishnan, and F. Blaabjerg, *Control in Power Electronics: Selected Problems*: Academic Press, 2002.
- [60] S. Buso and P. Mattavelli, *Digital Control in Power Electronics: Lectures on Power Electronics* vol. 1: Morgan & Claypool, 2006.
- [61] M. Malinowski, M. P. Kazmierkowski, and A. M. Trzynadlowski, "A comparative study of control techniques for PWM rectifiers in AC adjustable speed drives," *IEEE Transactions on Power Electronics*, vol. 18, pp. 1390-1396, 2003.
- [62] H. Akagi, E. H. Watanabe, and M. Aredes, *Instantaneous Power Theory and Applications to Power Conditioning*: Wiley, 2007.
- [63] B. K. Bose, *Power electronics and variable frequency drives: technology and applications*: IEEE Press, 1997.
- [64] A. Tripathi and P. C. Sen, "Comparative analysis of fixed and sinusoidal band hysteresis current controllers for voltage source inverters," *IEEE Transactions on Industrial Electronics*, vol. 39, pp. 63-73, 1992.

- [65] H. Rashid, *Power Electronics: Circuits, Devices, and Applications*: Pearson/Prentice Hall, 2004.
- [66] J. Holtz, "Pulsewidth modulation-a survey," *IEEE Transactions on Industrial Electronics*, vol. 39, pp. 410-420, 1992.
- [67] L. A. Serpa, S. D. Round, and J. W. Kolar, "A Virtual-Flux Decoupling Hysteresis Current Controller for Mains Connected Inverter Systems," in *Power Electronics Specialists Conference, 2006. PESC '06. 37th IEEE*, 2006, pp. 1-7.
- [68] L. Malesani and P. Tenti, "A novel hysteresis control method for current-controlled voltage-source PWM inverters with constant modulation frequency," *IEEE Transactions on Industry Applications*, vol. 26, pp. 88-92, 1990.
- [69] R. Gabriel, W. Leonhard, and C. J. Nordby, "Field-Oriented Control of a Standard AC Motor Using Microprocessors," *IEEE Transactions on Industry Applications*, vol. IA-16, pp. 186-192, 1980.
- [70] I. Takahashi and T. Noguchi, "A New Quick-Response and High-Efficiency Control Strategy of an Induction Motor," *IEEE Transactions on Industry Applications*, vol. IA-22, pp. 820-827, 1986.
- [71] I. Takahashi and Y. Ohmori, "High-performance direct torque control of an induction motor," *IEEE Transactions on Industry Applications*, vol. 25, pp. 257-264, 1989.
- [72] T. Ohnishi, "Three phase PWM converter/inverter by means of instantaneous active and reactive power control," in *Industrial Electronics, Control and Instrumentation, 1991. Proceedings. IECON '91., 1991 International Conference on*, 1991, pp. 819-824 vol.1.
- [73] M. Malinowski, "Sensorless control strategies for three-phase PWM rectifiers," PhD Thesis, Faculty of Electrical Engineering, Institute of Control and Industrial Electronics, Warsaw university of Technology, 2001.
- [74] J. Alonso-Marti, x, nez, J. Carrasco, and S. Arnaltes, "Table-Based Direct Power Control: A Critical Review for Microgrid Applications," *IEEE Transactions on Power Electronics*, vol. 25, pp. 2949-2961, 2010.
- [75] A. Bouafia, J. P. Gaubert, and F. Krim, "Analysis and design of new switching table for direct power control of three-phase PWM rectifier," in *Power Electronics and Motion Control Conference, 2008. EPE-PEMC 2008. 13th*, 2008, pp. 703-709.
- [76] T. Yi, W. Jiuhe, L. Tao, and W. Lei, "Research on direct power control technology of three-phase boost type PWM rectifiers based on twelve voltage space vectors," in *Computer Design and Applications (ICCD), 2010 International Conference on*, 2010, pp. V3-133-V3-136.
- [77] M. Malinowski, M. Jasinski, and M. P. Kazmierkowski, "Simple direct power control of three-phase PWM rectifier using space-vector modulation (DPC-SVM)," *IEEE Transactions on Industrial Electronics*, vol. 51, pp. 447-454, 2004.
- [78] M. P. Kazmierkowski, M. Jasinski, and G. Wrona, "DSP-Based Control of Grid-Connected Power Converters Operating Under Grid Distortions," *IEEE Transactions on Industrial Informatics*, vol. 7, pp. 204-211, 2011.
- [79] Y. Zhang and C. Qu, "Direct Power Control of a Pulse Width Modulation Rectifier Using Space Vector Modulation Under Unbalanced Grid Voltages," *IEEE Transactions on Power Electronics*, vol. 30, pp. 5892-5901, 2015.
- [80] G. Yu, Y. Wang, S. Ma, and L. Zhang, "Research of Direct Power Control of PWM rectifier based on virtual flux," in *Electrical Machines and Systems (ICEMS), 2014 17th International Conference on*, 2014, pp. 775-779.
- [81] J. L. Duarte, A. Van Zwam, C. Wijnands, and A. Vandenput, "Reference frames fit for controlling PWM rectifiers," *IEEE Transactions on Industrial Electronics*, vol. 46, pp. 628-630, 1999.

- [82] A. Kulka, " Sensorless Digital Control of Grid Connected Three-Phase Converters for Renewable Sources," PhD, Department of Electric Power Engineering, Norwegian University of Science and Technology, Trondheim, 2009.
- [83] S. Bhattacharya, A. Veltman, D. M. Divan, and R. D. Lorenz, "Flux-based active filter controller," *IEEE Transactions on Industry Applications*, vol. 32, pp. 491-502, 1996.
- [84] L. Hao, T. Guojun, F. Jinghuan, and W. Xuanqin, "Study of multi-level rectifier in high power system based on a novel virtual flux observer," in *Power Electronics and Motion Control Conference, 2009. IPEMC '09. IEEE 6th International*, 2009, pp. 1618-1621.
- [85] T. Guojun, L. Hao, F. Jinghuan, and L. Meng, "Study of Multi-level Active Power Filter Control without phase-locked-loop," in *Power and Energy Engineering Conference (APPEEC), 2010 Asia-Pacific*, 2010, pp. 1-4.
- [86] J. A. Suul and T. Undeland, "Flexible reference frame orientation of Virtual Flux-based Dual Frame Current controllers for operation in weak grids," in *PowerTech, 2011 IEEE Trondheim*, 2011, pp. 1-8.
- [87] M. Malinowski, M. P. Kazmierkowski, and A. Trzynadlowski, "Review and comparative study of control techniques for three-phase PWM rectifiers," *Mathematics and Computers in Simulation*, vol. 63, pp. 349-361, 11/17/ 2003.
- [88] L. A. Serpa, S. Ponnaluri, P. M. Barbosa, and J. W. Kolar, "A Modified Direct Power Control Strategy Allowing the Connection of Three-Phase Inverters to the Grid Through LCL Filters," *IEEE Transactions on Industry Applications*, vol. 43, pp. 1388-1400, 2007.
- [89] P. Cortes, M. P. Kazmierkowski, R. M. Kennel, D. E. Quevedo, and J. Rodriguez, "Predictive Control in Power Electronics and Drives," *IEEE Transactions on Industrial Electronics*, vol. 55, pp. 4312-4324, 2008.
- [90] A. Sikorski, "Current controller minimizing the switching number of the VS-PWM inverter devices for AC motor drive application," in *Industrial Electronics, 1996. ISIE '96., Proceedings of the IEEE International Symposium on*, 1996, pp. 493-498 vol.1.
- [91] S. Vazquez, A. Marquez, R. Aguilera, D. Quevedo, J. I. Leon, and L. G. Franquelo, "Predictive Optimal Switching Sequence Direct Power Control for Grid-Connected Power Converters," *IEEE Transactions on Industrial Electronics*, vol. 62, pp. 2010-2020, 2015.
- [92] O. Kukrer, "Discrete-time current control of voltage-fed three-phase PWM inverters," *IEEE Transactions on Power Electronics*, vol. 11, pp. 260-269, 1996.
- [93] Y. Sheng-Ming and L. Chen-Haur, "A deadbeat current controller for field oriented induction motor drives," *IEEE Transactions on Power Electronics*, vol. 17, pp. 772-778, 2002.
- [94] S. Buso, S. Fasolo, and P. Mattavelli, "Uninterruptible power supply multi-loop control employing digital predictive voltage and current regulators," in *Applied Power Electronics Conference and Exposition, 2001. APEC 2001. Sixteenth Annual IEEE*, 2001, pp. 907-913 vol.2.
- [95] P. Eichenberger and M. Junger, "Predictive vector control of the stator voltages for an induction machine drive with current source inverter," in *Power Electronics Specialists Conference, 1997. PESC '97 Record., 28th Annual IEEE*, 1997, pp. 1295-1301 vol.2.
- [96] M. Depenbrock, "Direct self-control (DSC) of inverter-fed induction machine," *IEEE Transactions on Power Electronics*, vol. 3, pp. 420-429, 1988.

- [97] E. Flach, R. Hoffmann, and P. Mutschler, "Direct mean torque control of an induction motor," in *European Conference on Power Electronics and Applications*, 1997, pp. 3.672-3.677.
- [98] J. Rodriguez, J. Pontt, C. A. Silva, P. Correa, P. Lezana, P. Cortes, *et al.*, "Predictive Current Control of a Voltage Source Inverter," *IEEE Transactions on Industrial Electronics*, vol. 54, pp. 495-503, 2007.
- [99] J. Rodriguez, J. Pontt, P. Cortes, and R. Vargas, "Predictive Control of a Three-Phase Neutral Point Clamped Inverter," in *Power Electronics Specialists Conference, 2005. PESC '05. IEEE 36th*, 2005, pp. 1364-1369.
- [100] P. Antoniewicz and M. P. Kazmierkowski, "Virtual-Flux-Based Predictive Direct Power Control of AC/DC Converters With Online Inductance Estimation," *IEEE Transactions on Industrial Electronics*, vol. 55, pp. 4381-4390, 2008.
- [101] L. A. Serpa, "Current control strategies for multilevel grid connected inverters," Diss., Eidgenössische Technische Hochschule ETH Zürich, Nr. 17463, 2007, 2007.
- [102] A. Bozicek, B. Blazic, and I. Papic, "Mathematical modeling and current control of a voltage source converter," in *Universities Power Engineering Conference, 2008. UPEC 2008. 43rd International*, 2008, pp. 1-5.
- [103] M. Liserre, F. Blaabjerg, and S. Hansen, "Design and control of an LCL-filter-based three-phase active rectifier," *IEEE Transactions on Industry Applications*, vol. 41, pp. 1281-1291, 2005.
- [104] M. Liserre, F. Blaabjerg, and A. Dell'Aquila, "Step-by-step design procedure for a grid-connected three-phase PWM voltage source converter," *International Journal of Electronics*, vol. 91, pp. 445-460, 2004.
- [105] A. A. Rockhill, M. Liserre, R. Teodorescu, and P. Rodriguez, "Grid-Filter Design for a Multimegawatt Medium-Voltage Voltage-Source Inverter," *IEEE Transactions on Industrial Electronics*, vol. 58, pp. 1205-1217, 2011.
- [106] K. H. Ahmed, S. J. Finney, and B. W. Williams, "Passive Filter Design for Three-Phase Inverter Interfacing in Distributed Generation," in *Compatibility in Power Electronics, 2007. CPE '07*, 2007, pp. 1-9.
- [107] C. Wessels, J. Dannehl, and F. W. Fuchs, "Active damping of LCL-filter resonance based on virtual resistor for PWM rectifiers - stability analysis with different filter parameters," in *Power Electronics Specialists Conference, 2008. PESC 2008. IEEE*, 2008, pp. 3532-3538.
- [108] W. Gullvik, L. Norum, and R. Nilsen, "Active damping of resonance oscillations in LCL-filters based on virtual flux and virtual resistor," in *Power Electronics and Applications, 2007 European Conference on*, 2007, pp. 1-10.
- [109] W. Xuehua, B. Chenlei, R. Xinbo, L. Weiwei, and P. Donghua, "Design Considerations of Digitally Controlled LCL-Filtered Inverter With Capacitor-Current-Feedback Active Damping," *IEEE Journal of Emerging and Selected Topics in Power Electronics*, vol. 2, pp. 972-984, 2014.
- [110] B. Chenlei, R. Xinbo, W. Xuehua, L. Weiwei, P. Donghua, and W. Kailei, "Design of injected grid current regulator and capacitor-current-feedback active-damping for LCL-type grid-connected inverter," in *Energy Conversion Congress and Exposition (ECCE), 2012 IEEE*, 2012, pp. 579-586.
- [111] J. Dannehl, M. Liserre, and F. W. Fuchs, "Filter-Based Active Damping of Voltage Source Converters With LCL Filter," *IEEE Transactions on Industrial Electronics*, vol. 58, pp. 3623-3633, 2011.
- [112] R. Pena-Alzola, M. Liserre, F. Blaabjerg, M. Ordonez, and T. Kerekes, "Self-commissioning Notch Filter for Active Damping in Three Phase LCL-filter Based Grid-tie converter," *IEEE Transactions on Power Electronics*, vol. PP, pp. 1-1, 2014.

- [113] M. Liserre, A. D. Aquila, and F. Blaabjerg, "Genetic algorithm-based design of the active damping for an LCL-filter three-phase active rectifier," *IEEE Transactions on Power Electronics*, vol. 19, pp. 76-86, 2004.
- [114] D. Ricchiuto, M. Liserre, T. Kerekes, R. Teodorescu, and F. Blaabjerg, "Robustness analysis of active damping methods for an inverter connected to the grid with an LCL-filter," in *Energy Conversion Congress and Exposition (ECCE), 2011 IEEE*, 2011, pp. 2028-2035.
- [115] R. Teodorescu, F. Blaabjerg, M. Liserre, and A. Dell'Aquila, "A stable three-phase LCL-filter based active rectifier without damping," in *Industry Applications Conference, 2003. 38th IAS Annual Meeting. Conference Record of the*, 2003, pp. 1552-1557.
- [116] G. Escobar, M. J. Lopez-Sanchez, D. F. Balam-Tamayo, J. A. Alonzo-Chavarria, and J. M. Sosa, "Inverter-side current control of a single-phase inverter grid connected through an LCL filter," in *Industrial Electronics Society, IECON 2014 - 40th Annual Conference of the IEEE*, 2014, pp. 5552-5558.
- [117] T. Yi, L. Poh Chiang, W. Peng, C. Fook Hoong, and G. Feng, "Exploring Inherent Damping Characteristic of LCL-Filters for Three-Phase Grid-Connected Voltage Source Inverters," *IEEE Transactions on Power Electronics*, vol. 27, pp. 1433-1443, 2012.
- [118] M. Jasinski, "Direct power and torque control of AC/DC/AC converter-fed induction motor drives," *Faculty of Electrical Engineering, PhD. Thesis, Warsaw University of Technology*, 2005.
- [119] The Mathworks, "MATLAB," vol. R2012a, ed. Natick, Massachusetts, USA, 2012.
- [120] C. A. Rabbath and N. Léchevin, *Discrete-Time Control System Design with Applications*: Springer New York, 2013.
- [121] J. Lettl, J. Bauer, and L. Linhart, "Comparison of different filter types for grid connected inverter," *PIERS Proceedings, Marrakesh, Morocco*, 2011.
- [122] S. V. Araujo, A. Engler, B. Sahan, and F. Antunes, "LCL filter design for grid-connected NPC inverters in offshore wind turbines," in *Power Electronics, 2007. ICPE '07. 7th International Conference on*, 2007, pp. 1133-1138.
- [123] D. Kun, B. XinGao, L. HaiHao, and P. Tao, "A MATLAB-Simulink-Based PV Module Model and Its Application Under Conditions of Nonuniform Irradiance," *Energy Conversion, IEEE Transactions on*, vol. 27, pp. 864-872, 2012.
- [124] F. M. González-Longatt, "Model of photovoltaic module in matlab," *II CIBELEC*, vol. 2005, pp. 1-5, 2005.
- [125] IEC, "IEC 60725:2012: Consideration of reference impedances and public supply network impedances for use in determining disturbance characteristics of electrical equipment having a rated current ≤ 75 A per phase," ed: BSI Standards Limited, 2012.
- [126] N. R. N. Idris and A. H. M. Yatim, "An improved stator flux estimation in steady-state operation for direct torque control of induction machines," *IEEE Transactions on Industry Applications*, vol. 38, pp. 110-116, 2002.
- [127] H. Jun and W. Bin, "New integration algorithms for estimating motor flux over a wide speed range," *IEEE Transactions on Power Electronics*, vol. 13, pp. 969-977, 1998.
- [128] J. A. Suul, A. Luna, P. Rodriguez, and T. Undeland, "Voltage-Sensor-Less Synchronization to Unbalanced Grids by Frequency-Adaptive Virtual Flux Estimation," *IEEE Transactions on Industrial Electronics*, vol. 59, pp. 2910-2923, 2012.
- [129] U. K. Legislation, "The Electricity Safety, Quality and Continuity Regulations 2002," ed, 2002, p. 14.

- [130] National Grid, "The Grid Code," United Kingdom, 2013.
- [131] F. Mur, V. Cardenas, J. Vaquero, and S. Martinez, "Phase synchronization and measurement digital systems of AC mains for power converters," in *Power Electronics Congress, 1998. CIEP 98. VI IEEE International*, 1998, pp. 188-194.
- [132] J. W. Choi, Y. K. Kim, and H. G. Kim, "Digital PLL control for single-phase photovoltaic system," *Electric Power Applications, IEE Proceedings -*, vol. 153, pp. 40-46, 2006.
- [133] S. K. Chung, "Phase-locked loop for grid-connected three-phase power conversion systems," *Electric Power Applications, IEE Proceedings -*, vol. 147, pp. 213-219, 2000.
- [134] L. N. Arruda, S. M. Silva, and B. J. C. Filho, "PLL structures for utility connected systems," in *Industry Applications Conference, 2001. Thirty-Sixth IAS Annual Meeting. Conference Record of the 2001 IEEE*, 2001, pp. 2655-2660 vol.4.
- [135] C. Se-Kyo, "A phase tracking system for three phase utility interface inverters," *IEEE Transactions on Power Electronics*, vol. 15, pp. 431-438, 2000.
- [136] B. P. McGrath, D. G. Holmes, and J. J. H. Galloway, "Power converter line synchronization using a discrete Fourier transform (DFT) based on a variable sample rate," *IEEE Transactions on Power Electronics*, vol. 20, pp. 877-884, 2005.
- [137] H. Guan-Chyun and J. C. Hung, "Phase-locked loop techniques. A survey," *IEEE Transactions on Industrial Electronics*, vol. 43, pp. 609-615, 1996.
- [138] P. Rodriguez, J. Pou, J. Bergas, J. I. Candela, R. P. Burgos, and D. Boroyevich, "Decoupled Double Synchronous Reference Frame PLL for Power Converters Control," *IEEE Transactions on Power Electronics*, vol. 22, pp. 584-592, 2007.
- [139] H. Akagi, Y. Kanazawa, and A. Nabae, "Instantaneous Reactive Power Compensators Comprising Switching Devices without Energy Storage Components," *IEEE Transactions on Industry Applications*, vol. IA-20, pp. 625-630, 1984.
- [140] H. Akagi, S. Ogasawara, and K. Hyosung, "The theory of instantaneous power in three-phase four-wire systems: a comprehensive approach," in *Industry Applications Conference, 1999. Thirty-Fourth IAS Annual Meeting. Conference Record of the 1999 IEEE*, 1999, pp. 431-439 vol.1.
- [141] T. Furuhashi, S. Okuma, and Y. Uchikawa, "A study on the theory of instantaneous reactive power," *IEEE Transactions on Industrial Electronics*, vol. 37, pp. 86-90, 1990.
- [142] P. Fang Zheng and L. Jih-Sheng, "Generalized instantaneous reactive power theory for three-phase power systems," *IEEE Transactions on Instrumentation and Measurement*, vol. 45, pp. 293-297, 1996.
- [143] Y. Xu, L. M. Tolbert, J. N. Chiasson, J. B. Campbell, and F. Z. Peng, "A generalised instantaneous non-active power theory for STATCOM," *IET Electric Power Applications*, vol. 1, pp. 853-861, 2007.
- [144] J. Reese, R. Lohde, and F. W. Fuchs, "FRT capability of direct power controlled converters connected by an actively damped LCL-filter for wind power applications," in *Power Electronics and Applications (EPE 2011), Proceedings of the 2011-14th European Conference on*, 2011, pp. 1-10.
- [145] G. Hong Soo, M. Armstrong, and B. Zahawi, "The effect of grid operating conditions on the current controller performance of grid connected photovoltaic inverters," in *Power Electronics and Applications, 2009. EPE '09. 13th European Conference on*, 2009, pp. 1-8.
- [146] M. Ciobotaru, R. Teodorescu, P. Rodriguez, A. Timbus, and F. Blaabjerg, "Online grid impedance estimation for single-phase grid-connected systems using PQ

- variations," in *Power Electronics Specialists Conference, 2007. PESC 2007. IEEE*, 2007, pp. 2306-2312.
- [147] Y. Shuitao, L. Qin, F. Z. Peng, and Q. Zhaoming, "A Robust Control Scheme for Grid-Connected Voltage-Source Inverters," *IEEE Transactions on Industrial Electronics*, vol. 58, pp. 202-212, 2011.
- [148] M. Liserre, R. Teodorescu, and F. Blaabjerg, "Stability of photovoltaic and wind turbine grid-connected inverters for a large set of grid impedance values," *IEEE Transactions on Power Electronics*, vol. 21, pp. 263-272, 2006.
- [149] E. Romero-Cadaval, G. Spagnuolo, L. Garcia Franquelo, C. A. Ramos-Paja, T. Suntio, and W. M. Xiao, "Grid-Connected Photovoltaic Generation Plants: Components and Operation," *Industrial Electronics Magazine, IEEE*, vol. 7, pp. 6-20, 2013.
- [150] G. K. Singh, "Power system harmonics research: a survey," *European Transactions on Electrical Power*, vol. 19, pp. 151-172, 2009.
- [151] S. Ponnaluri, A. Brickwedde, and R. W. De Doncker, "Overriding individual harmonic current control with fast dynamics for UPS with nonlinear loads," in *Power Electronics and Drive Systems, 2001. Proceedings, 2001 4th IEEE International Conference on*, 2001, pp. 527-532 vol.2.
- [152] "Assessment of low frequency electromagnetic immunity and emission requirements for dispersed generation systems in LV networks," in *IEC 61000-3-15:2011*, ed, 2011, pp. 1-54.
- [153] A. E. Emanuel and J. A. Orr, "Fryze's power definition: Some limitations," in *Harmonics and Quality of Power (ICHQP), 2012 IEEE 15th International Conference on*, 2012, pp. 518-522.
- [154] V. Staudt, "Fryze - Buchholz - Depenbrock: A time-domain power theory," in *Nonsinusoidal Currents and Compensation, 2008. ISNCC 2008. International School on*, 2008, pp. 1-12.
- [155] J. L. Willems, "Budeanu's Reactive Power and Related Concepts Revisited," *IEEE Transactions on Instrumentation and Measurement*, vol. 60, pp. 1182-1186, 2011.
- [156] D. Jeltsema, "Budeanu's concept of reactive and distortion power revisited," in *Nonsinusoidal Currents and Compensation (ISNCC), 2015 International School on*, 2015, pp. 1-6.
- [157] L. S. Czarnecki, "What is wrong with the Budeanu concept of reactive and distortion power and why it should be abandoned," *IEEE Transactions on Instrumentation and Measurement*, vol. IM-36, pp. 834-837, 1987.
- [158] P. Fang Zheng, G. W. Ott, Jr., and D. J. Adams, "Harmonic and reactive power compensation based on the generalized instantaneous reactive power theory for three-phase four-wire systems," *IEEE Transactions on Power Electronics*, vol. 13, pp. 1174-1181, 1998.
- [159] "IEEE Recommended Practice for Monitoring Electric Power Quality," *IEEE Std 1159-2009 (Revision of IEEE Std 1159-1995)*, pp. c1-81, 2009.
- [160] J. Seong-Jeub and F. C. Lee, "Three control strategies for a three-leg AC-DC converter under unbalanced AC voltage condition," in *Industrial Electronics Society, 2003. IECON '03. The 29th Annual Conference of the IEEE*, 2003, pp. 186-191 vol.1.
- [161] O. Ojo and W. Zhiqiao, "A new controller for three-phase boost rectifiers lacking balance in source voltages and impedances," in *Applied Power Electronics Conference and Exposition, 2005. APEC 2005. Twentieth Annual IEEE*, 2005, pp. 508-514 Vol. 1.
- [162] P. Rodriguez, G. Medeiros, A. Luna, M. C. Cavalcanti, and R. Teodorescu, "Safe current injection strategies for a STATCOM under asymmetrical grid faults," in

- Energy Conversion Congress and Exposition (ECCE), 2010 IEEE, 2010, pp. 3929-3935.*
- [163] P. Rodriguez, A. V. Timbus, R. Teodorescu, M. Liserre, and F. Blaabjerg, "Flexible Active Power Control of Distributed Power Generation Systems During Grid Faults," *IEEE Transactions on Industrial Electronics*, vol. 54, pp. 2583-2592, 2007.
 - [164] C. Du, M. H. J. Bollen, E. Agneholm, and A. Sannino, "A New Control Strategy of a VSC-HVDC System for High-Quality Supply of Industrial Plants," *IEEE Transactions on Power Delivery*, vol. 22, pp. 2386-2394, 2007.
 - [165] M. Reyes, P. Rodriguez, S. Vazquez, A. Luna, J. M. Carrasco, and R. Teodorescu, "Decoupled Double Synchronous Reference Frame current controller for unbalanced grid voltage conditions," in *Energy Conversion Congress and Exposition (ECCE), 2012 IEEE, 2012, pp. 4676-4682.*
 - [166] J. A. Suul, "Control of Grid Integrated Voltage Source Converters under Unbalanced Conditions: Development of an On-line Frequency-adaptive Virtual Flux-based Approach," PhD Thesis, NTNU, 2012.
 - [167] F. Mulolani, M. Armstrong, and B. Zahawi, "Modeling and simulation of a grid-connected photovoltaic converter with reactive power compensation," in *Communication Systems, Networks & Digital Signal Processing (CSNDSP), 2014 9th International Symposium on, 2014, pp. 888-893.*
 - [168] R. Kabiri, D. G. Holmes, and B. P. McGrath, "Control of Active and Reactive Power Ripple to Mitigate Unbalanced Grid Voltages," *IEEE Transactions on Industry Applications*, vol. 52, pp. 1660-1668, 2016.
 - [169] J. Svensson, M. Bongiorno, and A. Sannino, "Practical Implementation of Delayed Signal Cancellation Method for Phase-Sequence Separation," *IEEE Transactions on Power Delivery*, vol. 22, pp. 18-26, 2007.
 - [170] R. Cardenas, M. Diaz, F. Rojas, and J. Clare, "Fast Convergence Delayed Signal Cancellation Method for Sequence Component Separation," *IEEE Transactions on Power Delivery*, vol. 30, pp. 2055-2057, 2015.
 - [171] H. R. Karshenas and H. Saghafi, "Basic Criteria in Designing LCL Filters for Grid Connected Converters," in *2006 IEEE International Symposium on Industrial Electronics, 2006, pp. 1996-2000.*

Appendix A. Transformations for Three-Phase Systems

Coordinate transformations are used to convert quantities from one reference frame to another, in order to simplify controller design for three-phase drives and grid connected converters. The main transformations are from three-phase to vector components on a stationary reference frame, and from a stationary reference frame to a rotating reference frame. In this appendix these transformations are presented.

A.1 Three-phase to Stationary Reference Frame Transformation

A three-phase system of voltages, currents or fluxes can be expressed as a space vector in a stationary reference frame usually known as the $\alpha - \beta$ reference frame by using

$$\underline{x} = x_\alpha + jx_\beta = K(x_a + ax_b + a^2x_c) \quad (\text{A.1})$$

where $a = e^{j\frac{2\pi}{3}}$ and $a^2 = e^{-j\frac{2\pi}{3}}$.

The factor K can be chosen depending on the required scaling of the quantities. The most common choices are $K = 2/3$ for an amplitude invariant transformation and $K = \sqrt{2/3}$ for a power invariant transformation. The amplitude invariant transformation is used in this thesis. A three-phase three-wire system is used throughout; therefore, there is no zero-sequence component.

In matrix form, this transformation, also commonly called the Clarke transformation is given by

$$\begin{bmatrix} x_\alpha \\ x_\beta \end{bmatrix} = \frac{2}{3} \begin{bmatrix} 1 & -\frac{1}{2} & -\frac{1}{2} \\ 0 & \frac{\sqrt{3}}{2} & -\frac{\sqrt{3}}{2} \end{bmatrix} \begin{bmatrix} x_a \\ x_b \\ x_c \end{bmatrix} \quad (\text{A.2})$$

The inverse transformation is given by

$$\begin{bmatrix} x_a \\ x_b \\ x_c \end{bmatrix} = \begin{bmatrix} 1 & 0 \\ -\frac{1}{2} & \frac{\sqrt{3}}{2} \\ -\frac{1}{2} & -\frac{\sqrt{3}}{2} \end{bmatrix} \begin{bmatrix} x_\alpha \\ x_\beta \end{bmatrix} \quad (\text{A.3})$$

The transformation is illustrated in the vector diagram of Figure A.1.

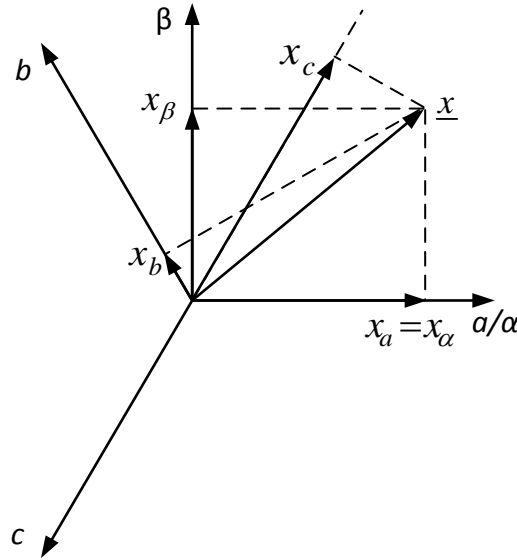


Figure A.1 Vector diagram space vector transformation of three-phase quantities

A.2 Stationary to Rotating Reference Frame Transformation

The complex space vector in the stationary reference frame can be expressed in a rotating reference frame. The rotating reference frame is usually called the $d-q$ reference frame or the synchronous reference frame (SRF). If the angular speed of the reference frame is equal to the angular speed of the space vector, the components of the space vector on the rotating reference frame will be DC quantities. This transformation makes the analysis and control of AC machines and grid-connected converters easier and makes it possible to use PI controllers without facing the drawback of a steady-state error which is encountered when PI controllers are used to control AC quantities.

The transformation is given by

$$\underline{x}^{dq} = e^{-j\theta} \underline{x}^{\alpha\beta} \quad (\text{A.4})$$

where the superscripts dq and $\alpha\beta$ represent the rotating reference frame and the stationary reference frame respectively, and $\theta = \int \omega dt$ is the angle of the reference space vector.

The reference space vector is usually chosen to be a voltage, or a virtual flux for grid-connected converters or the air-gap flux in an AC machine.

In matrix form, the transformation, which is commonly called the Park transformation, is given by

$$\begin{bmatrix} x_d \\ x_q \end{bmatrix} = \begin{bmatrix} \cos \theta & \sin \theta \\ -\sin \theta & \cos \theta \end{bmatrix} \begin{bmatrix} x_\alpha \\ x_\beta \end{bmatrix} \quad (\text{A.5})$$

The inverse transformation from the rotating reference frame to the stationary reference frame is given by

$$\underline{x}^{\alpha\beta} = e^{j\theta} \underline{x}^{dq} \quad (\text{A.6})$$

In matrix form, the inverse Park transformation is given by

$$\begin{bmatrix} x_\alpha \\ x_\beta \end{bmatrix} = \begin{bmatrix} \cos \theta & -\sin \theta \\ \sin \theta & \cos \theta \end{bmatrix} \begin{bmatrix} x_d \\ x_q \end{bmatrix} \quad (\text{A.7})$$

The transformations between the stationary and the rotating reference frames are illustrated in Figure A.2.

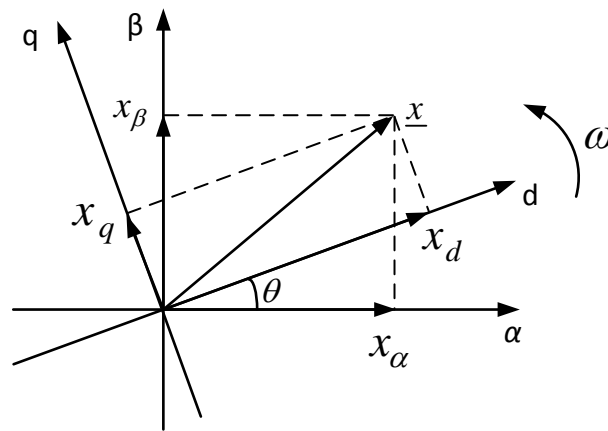


Figure A.2 Vector diagram showing the stationary and rotating reference frames

A.3 Transformations for Unsymmetrical Systems

The phase voltages in a three-phase system are given by

$$v_a = \hat{V}_a \cos(\omega t - \gamma_a) \quad (\text{A.8})$$

$$v_b = \hat{V}_b \cos\left(\omega t - \frac{2\pi}{3} - \gamma_b\right) \quad (\text{A.9})$$

$$v_c = \hat{V}_c \cos\left(\omega t + \frac{2\pi}{3} - \gamma_b\right) \quad (\text{A.10})$$

where \hat{V}_a , \hat{V}_b and \hat{V}_c are the magnitudes of the phase-a, phase-b and phase-c voltages respectively and γ_a , γ_b and γ_c are their respective phase angles.

If the magnitudes and the phase angles of the phase voltages are not equal, they are said to be unbalanced or unsymmetrical.

The voltage vector of an unbalanced three-phase three-wire system is the sum of two vectors rotating in opposite directions and can be written as

$$\underline{v} = \underline{v}^p + \underline{v}^n = |\underline{v}^p| e^{j(\omega t + \gamma_p)} + |\underline{v}^n| e^{-j(\omega t + \gamma_n)} \quad (\text{A.11})$$

where \underline{v}^p and \underline{v}^n are the positive-sequence vector and the negative-sequence vector respectively; γ_p and γ_n are their respective phase angles.

When the unbalanced voltage vector is transformed to the rotating reference frame aligned with the positive-sequence vector, the resulting SRF vectors are given by

$$\underline{v}^{dqp} = e^{-j\omega t} |\underline{v}^p| e^{j(\omega t + \gamma_p)} = |\underline{v}^p| e^{j\gamma_p} \quad (\text{A.12})$$

$$\underline{v}^{dqn} = e^{-j\omega t} |\underline{v}^n| e^{-j(\omega t + \gamma_n)} = |\underline{v}^n| e^{-j(2\omega t + \gamma_n)} \quad (\text{A.13})$$

where \underline{v}^{dqp} is the positive-sequence vector in the rotating reference frame and \underline{v}^{dqn} is the negative-sequence vector in the rotating reference frame.

Equations (A.12) and (A.13) show that when transformed to a rotating reference frame aligned with the positive-sequence, the positive-sequence vector will have a rotating frequency of 0, thus it will be a DC quantity, while the negative-sequence vector will be rotating at a frequency of 2ω . This explains the oscillations in the power at twice the fundamental frequency when the grid voltage is unbalanced.

Appendix B. Per-unit System

The per-unit system is widely used in power systems, electrical machines and control systems to simplify analysis and allow comparison of results over a wide range of power and voltage ratings. The basis of the per-unit system is the expression of quantities as fractions of pre-selected values known as the base quantities. In this appendix, the base values for the per-unit system used to present simulation results in this thesis are defined.

The base power and the base voltage are chosen to be equal to the rated power and the rated voltage of the system. The rated power of the system is 100 kW, therefore the base power is

$$S_{base} = 100 \text{ kVA} \quad (\text{B.1})$$

It should be noted that the same base power applies for apparent power, active power and reactive power.

The rated voltage of three-phase systems is given as the rms value of the line-line voltage V_L and this is usually chosen as the base voltage. However, in this thesis the amplitude of the phase voltage is chosen as the base voltage. Therefore, the base voltage is given by

$$V_{base} = \sqrt{\left(\frac{2}{3}\right)} V_L \quad (\text{B.2})$$

The base angular frequency is selected to be equal to the nominal angular frequency of the grid voltage. That is

$$\omega_{base} = 2\pi f \quad (\text{B.3})$$

where f is the nominal frequency of the grid voltage in Hz.

The base current is defined as the peak value of the line current and is given by

$$I_{base} = \frac{S_{base}}{\left(\frac{3}{2}\right) V_{base}} \quad (\text{B.4})$$

The base impedance is given by

$$Z_{base} = \frac{V_{base}}{I_{base}} \quad (\text{B.5})$$

The base inductance is given by

$$L_{base} = \frac{Z_{base}}{\omega_{base}} \quad (B.6)$$

The base capacitance is given by

$$C_{base} = \frac{1}{\omega_{base} Z_{base}} \quad (B.7)$$

With these definitions, the base values used in simulations are given in Table B.1.

Table B.1 Base Values used in Simulations

Parameter	Base Value
Power	100 kW
Voltage	338.85 V
Frequency	314.16 rad/s
Current	196.75 A
Impedance	1.722 Ω
Inductance	5.5 mH
Capacitance	1800 μ F

Appendix C. LCL Filter Design

This appendix presents the design procedure of the LCL filter. This procedure is used to determine the LCL filter parameters used in simulations and experiments. The design considerations for LCL filters are given in a number of publications among them [103], [104], [171].

The total voltage drop across the filter inductors should not exceed 10% of the nominal voltage. Having a high voltage drop would require a higher DC link voltage to compensate for the voltage drop and prevent the current controller from saturating. The resistance of the inductors can be neglected. Therefore, the total inductance is given by

$$L_{1(pu)} + L_{2(pu)} \leq 0.1L_{base} \quad (C.1)$$

Where $L_{1(pu)}$ is the inverter-side inductor in per-unit, $L_{2(pu)}$ is the grid-side inductor in per-unit and L_{base} is the base value of the inductance.

The converter-side inductor, L_1 is calculated first using the equation

$$L_1 = \frac{V_{dc}}{8f_{sw}\Delta i_{L1}} \quad (C.2)$$

where V_{dc} is the DC link voltage, f_{sw} is the switching frequency and Δi_{L1} is the ripple in the inverter current, usually chosen to be between 10 % and 20 % of the rated current.

The filter capacitor is selected next. The limitation on its value is that it should not cause a reduction in power factor of more than 5 % at rated power. Thus, the filter capacitor is selected as a fraction of the base capacitance, x , limited to

$$C_f \leq 0.05C_{base} \quad (C.3)$$

where C_f is the filter capacitor and C_{base} is the base capacitance.

The grid side inductor is designed to further attenuate high frequency harmonics.

The transfer function of the filter from the inverter current to the grid current is given by

$$\frac{I_{L2}(s)}{I_{L1}(s)} = \frac{1}{L_2 C_f s^2 + 1} \quad (C.4)$$

From equation (C.4), the harmonic attenuation of the grid side current at the switching frequency can be obtained as

$$\frac{I_{L2}(\omega_{sw})}{I_{L1}(\omega_{sw})} = \frac{1}{|1 - rL_1C_f\omega_{sw}^2|} \quad (C.5)$$

where $r = L_2/L_1$ is the ratio of the grid side inductor to the inverter side inductor and ω_{sw} is the switching frequency in rad/s.

After determining a suitable value for L_2 the resonance frequency of the filter is calculated. The upper and lower limits for the resonance frequency are given by

$$10f < f_{res} < 0.5f_{sw} \quad (C.6)$$

The step by step design process is given in the flow chart in Figure C.1.

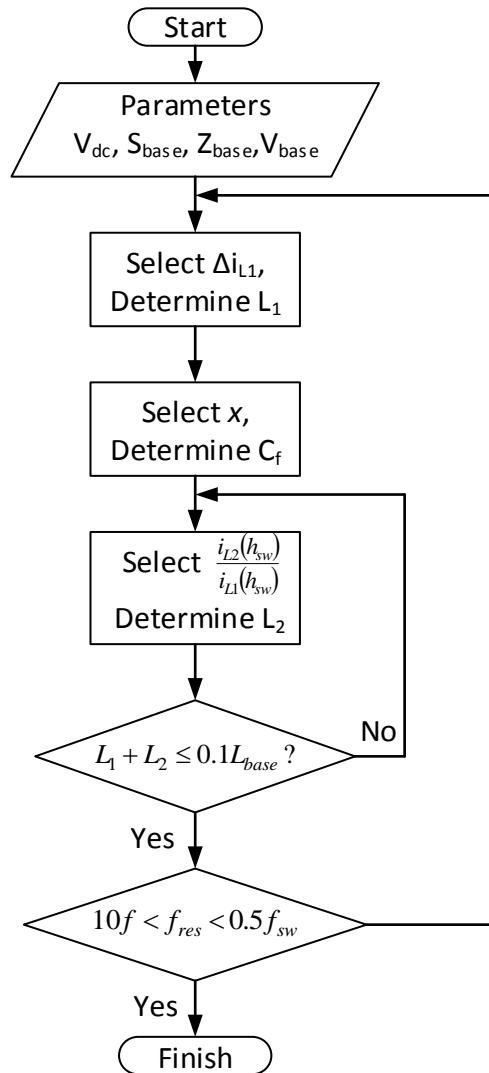


Figure C.1 Flow chart of LCL Filter Design

The LCL filter parameters used in simulations and experiments are given in Table C.1.

Table C.1 LCL filter parameters used in simulations and experiments

	Simulation		Experimental	
L_1	0.35 mH	0.06 pu	0.5 mH	0.063 pu
L_2	0.1 mH	0.018 pu	0.15 mH	0.018 pu
C_f	90 μ F	0.05 pu	20 μ F	0.015 pu
f_{sw}	10 kHz		10 kHz	
f_{res}	1.9 kHz		3.3 kHz	

Appendix D. Power Flow between the VSC and the Grid

In this appendix, equations that give the flow of active power and reactive power between the VSC and the grid are derived in terms of the voltage and the total impedance between the VSC and the grid. The following assumptions are made:

- The voltages and the current are assumed to be purely sinusoidal with no harmonic distortion; therefore, rms value based phasor analysis will be used.
- The three-phase system is balanced; therefore, per-phase analysis is used.
- The effect of the filter capacitor of the LCL filter is negligible at the fundamental frequency; therefore, it is not considered.

The single-phase equivalent circuit of the grid-connected VSC is shown in Figure D.1.

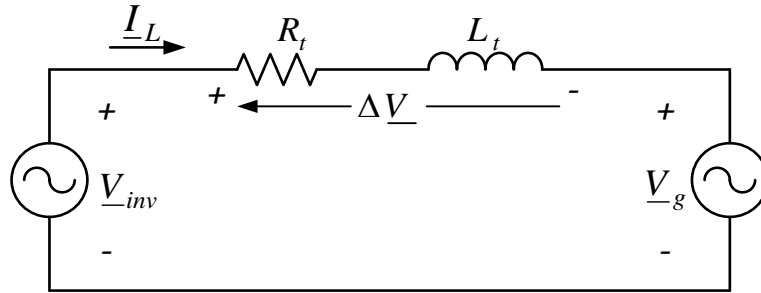


Figure D.1

The inverter voltage is defined in phasor notation as

$$\underline{V}_{inv} = |\underline{V}_{inv}| e^{j\delta} \quad (D.1)$$

where δ is the angle between the inverter voltage and the grid voltage.

The grid voltage is defined as

$$\underline{V}_g = |\underline{V}_g| e^{j0} = |\underline{V}_g| \quad (D.2)$$

The current flowing from the inverter to the grid is given by

$$\underline{I}_L = \frac{\underline{V}_{inv} - \underline{V}_g}{R + j\omega L} \quad (D.3)$$

where R and L are the total resistance and total inductance respectively between the VSC and the grid, including that of the filter, and the grid impedance; ω is the angular frequency of the grid voltage.

Substituting equations (D.1) and (D.2) into equation (D.3) and expanding gives

$$\underline{I}_L = \frac{R|V_{inv}| \cos \delta + \omega L|V_{inv}| \sin \delta - R|V_g|}{R^2 + \omega^2 L^2} + j \frac{R|V_{inv}| \sin \delta - \omega L|V_{inv}| \cos \delta + \omega L|V_g|}{R^2 + \omega^2 L^2} \quad (D.4)$$

The complex apparent power flow between the inverter and the grid is given by

$$\underline{S} = \underline{V}_g \underline{I}_L^* \quad (D.5)$$

where \underline{I}_L^* is the complex conjugate of the current and is given by

$$\underline{I}_L^* = \frac{R|V_{inv}| \cos \delta + \omega L|V_{inv}| \sin \delta - R|V_g|}{R^2 + \omega^2 L^2} - j \frac{R|V_{inv}| \sin \delta - \omega L|V_{inv}| \cos \delta + \omega L|V_g|}{R^2 + \omega^2 L^2} \quad (D.6)$$

Substituting equation (D.6) into equation (D.5) the complex power is obtained as

$$\underline{S} = \frac{R|V_{inv}| |V_g| \cos \delta + \omega L|V_{inv}| |V_g| \sin \delta - R|V_g|^2}{R^2 + \omega^2 L^2} - j \frac{R|V_{inv}| |V_g| \sin \delta - \omega L|V_{inv}| |V_g| \cos \delta + \omega L|V_g|^2}{R^2 + \omega^2 L^2} \quad (D.7)$$

The active power is defined as the real part of the complex power and is given by

$$P = \frac{R|V_{inv}| |V_g| \cos \delta + \omega L|V_{inv}| |V_g| \sin \delta - R|V_g|^2}{R^2 + \omega^2 L^2} \quad (D.8)$$

The reactive power is defined as the imaginary part of the complex power and is given by

$$Q = \frac{\omega L|V_{inv}| |V_g| \cos \delta - R|V_{inv}| |V_g| \sin \delta - \omega L|V_g|^2}{R^2 + \omega^2 L^2} \quad (D.9)$$

In high power VSCs connected to strong grids the impedance between the VSC and the grid is predominantly inductive, and the resistance can be neglected.

With the resistance neglected, equations (D.8) and (D.9) simplify to

$$P = \frac{|V_{inv}| |V_g| \sin \delta}{\omega L} \quad (D.10)$$

$$Q = \frac{|V_g| (|V_{inv}| \cos \delta - |V_g|)}{\omega L} \quad (D.11)$$

Since the angle δ is usually small, equations (D.10) and (D.11) can be simplified to the approximate but simpler form given by

$$P \approx \frac{|V_{inv}| |V_g|}{\omega L} \delta \quad (D.12)$$

$$Q \approx \frac{|V_g| (|V_{inv}| - |V_g|)}{\omega L} \approx \frac{|V_g| \Delta|V|}{\omega L} \quad (D.13)$$

where $\Delta|V|$ is the difference in magnitude between the inverter voltage and the grid voltage.

In low power VSCs connected to weak grids, the resistive component of the impedance has a significant magnitude and should not be neglected. To determine the effect of this resistive component, the inductance is set to zero and equations (D.8) and (D.9) simplify to

$$P = \frac{|V_g| (|V_{inv}| \cos \delta - |V_g|)}{R} \quad (D.14)$$

$$Q = \frac{-|V_{inv}| |V_g|}{R} \sin \delta \quad (D.15)$$

For a small value of δ equations (D.14) and (D.15) can be written in approximate form as

$$P \approx \frac{|V_g| (|V_{inv}| - |V_g|)}{R} \approx \frac{|V_g| \Delta|V|}{R} \quad (D.16)$$

$$Q \approx \frac{-|V_{inv}| |V_g|}{R} \delta \quad (D.17)$$

Equations (D.10) to (D.17) show the relationship between the power flow, voltage and impedance. If the impedance is predominantly inductive, active power flow is proportional to the angle between the grid voltage and the inverter voltage; while reactive power flow is proportional to the difference between the inverter voltage and the grid voltage. If the impedance is predominantly resistive, the active power flow is proportional to the difference between the inverter voltage and the grid voltage; while reactive power flow is proportional to the angle between the grid voltage and the inverter voltage. These equations can be used to obtain an estimate of the grid impedance by injecting a known amount of active power or reactive power and noting the change in voltage. A grid impedance estimation method based on these equations is presented in [146]. The equations can also be used to estimate the voltage regulation capability of a grid-connected VSC.

The variation of voltage magnitude with active power and reactive power injection respectively is shown in Figure D.2 for an inductive grid impedance and Figure D.3 for a resistive grid impedance. The change in voltage due to active power injection is denoted by ΔV_p and the change in voltage due to reactive power injection is denoted by ΔV_q .

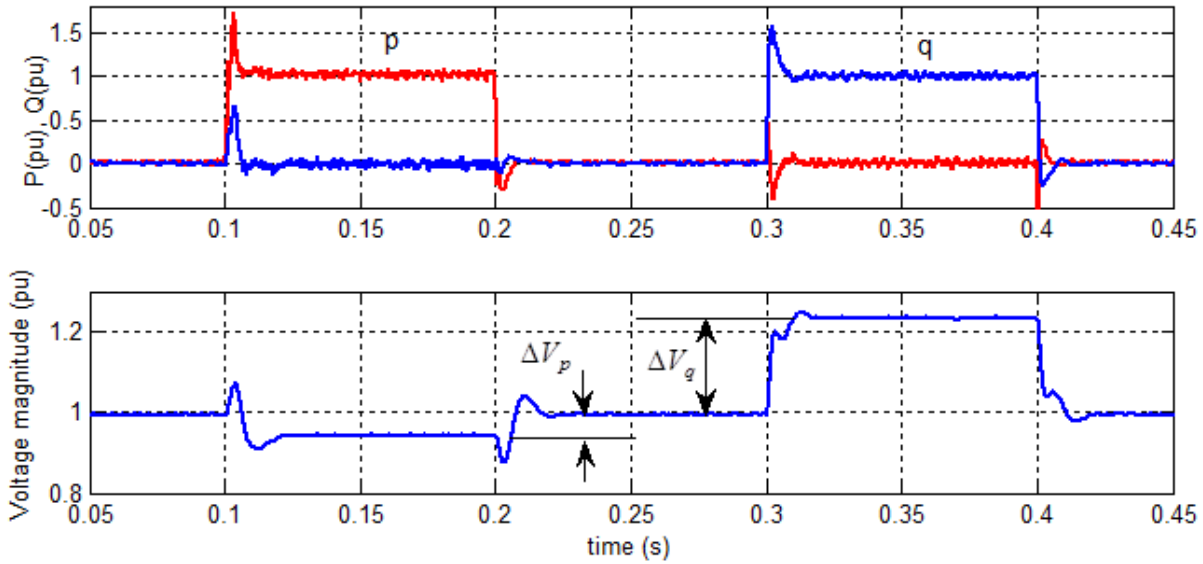


Figure D.2 Variation of voltage with active and reactive power with inductive grid impedance

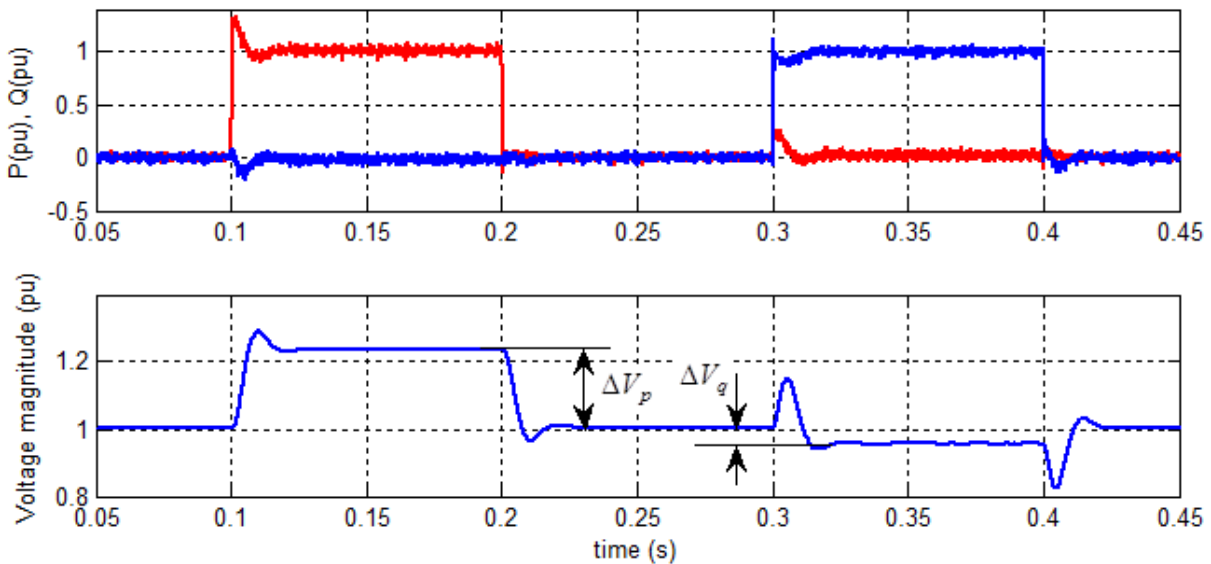


Figure D.3 Variation of voltage with active and reactive power with resistive grid impedance

Appendix E. List of Equipment

Table E.1 List of Equipment

Equipment	Type
DC Power Supply	LAB/SM 3300
Oscilloscope	Tektronix DPO2014B
Power Analyser	Yokogawa PZ4000
Isolated Voltage probe	Pico TA041 differential probe
Current probe	Tektronix A622
Voltage probe	Tektronix P3010
Voltage sensor	AD251AY isolation amplifier
Current sensor	CAS 6-NP LEM current transducer